CAUSAL INFINITESIMAL MODELING OF NONLINEAR IMPULSIVE SYSTEMS AND SAFE PATH PLANNING IN ROBOTICS

A Dissertation
Presented to
The Academic Faculty

By

Nak-seung Patrick Hyun

In Partial Fulfillment
of the Requirements for the Degree
Doctor of Philosophy in the
School of Electrical and Computer Engineering

Georgia Institute of Technology

August 2018

CAUSAL INFINITESIMAL MODELING OF NONLINEAR IMPULSIVE SYSTEMS AND SAFE PATH PLANNING IN ROBOTICS

Approved by:

Dr. Erik I. Verriest, Advisor
School of Electrical and Computer Engineering
Georgia Institute of Technology

Dr. Patricio A. Vela
School of Electrical and Computer Engineering
Georgia Institute of Technology

Dr. Luca Dieci
School of Mathematics
Georgia Institute of Technology

Dr. Magnus Egerstedt
School of Electrical and Computer Engineering
Georgia Institute of Technology

Dr. Panagiotis Tsiotras
School of Aerospace Engineering
Georgia Institute of Technology

Date Approved: May 30, 2018

La nature ne fait jamais des sauts

Gottfried Leibniz

To my parents, Oh Seok Hyun and Jong Hee Chyun

ACKNOWLEDGEMENTS

According to Aristotle, everything happens for a reason. My journey in graduate school was all about finding the reason for my being, and with help and support from numerous people, I was able to finish the first chapter of my life, attaining my Ph.D. degree. The goal of this note is to acknowledge everyone who helped me through this long journey.

First of all, I would like to express my deepest gratitude to my advisor, Professor Erik I. Verriest, for patiently guiding me on the right path in my research, and teaching me how to think differently. Over the years, I was constantly amazed by his passion for creating new ideas in science and mathematics, and brainstorming sessions with his new ideas on the whiteboard were always full of excitement. The best lesson I learned from Dr. Verriest is to dare to think differently when it comes to researchand painting. Not only did he share his bold ideas, but he also showed me how each new idea can be analytically justified, which stimulated me to become more critically creative in research. I shall always remember the motto of the MAthematical Systems Theory (MAST) laboratory: "*To have a great idea, you need many ideas*", and "*first principles*." In addition, I would also like to thank Professor Patricio A. Vela, who substantially helped me with researching robotics motion planning. Dr.Vela was always open to the new ideas and guided me to make the ideas applicable to the robotics problem. His critical assessment on writing a paper helped me enormously on giving a good flow to the paper. Besides the research, I enjoyed the dinner at Manuel with Dr. Verriest and Mrs. Verriest, and the coffee breaks with Dr. Vela. I was fortunate to work with both advisors, and hoping my thesis will become a pivoting point to have more collaboration in the future.

Also, I was able to meet many mentors during my Ph.D. study. First, I would like to thank Professor Magnus Egerstedt for teaching me how to become a professional researcher and encouraging me to improve for the better. His visions in research and approaches on how to deliver the research to help others inspired me in setting what the ultimate goal of

the research should be. I would also like to thank the committee members, Professor Luca Dieci and Professor Panagiotis Tsiotras, for valuable discussions in the future direction of the research. Also, I want to thank Professor Aaron Ames for teaching nonlinear systems, and his encouragement and comments after the Ph.D. proposal, and Professor Wassim M. Haddad for his support in the last two months. Also, I want to thank Professor Mary Ann Weitnauer, Professor Anthony Yezzi, and Professor Yi-Chang James Tsai, who helped me discover many research areas in communications and computer visions in the first and second years. One good thing about studying at Georgia Tech was that I was able to pursue a master's degree in mathematics. I want to thank Professor Michael Loss and Professor Plamen Iliev for teaching functional analysis, which helped me significantly in learning the mathematical system theory. Also, I want to thank Dr. Yuval Peres at Microsoft Research (MSR) for hosting the visit to MSR and for the valuable discussions in research with future career advice.

I also want to thank my lab mates and fellow graduate students I met at Georgia Tech. First, many thanks go to my friend and former labmate, Basit Memon, for being my sounding board and enjoyable conversationalist during coffee breaks and dinner. I also want to thank my friend and colleague Vishal Murali for becoming my new sounding board after Basit and the constructive math discussions we had in the past year. Outside of the lab, I would like to thank Jaeha Kung, Duckhwan Kim, and our team, HYPEN 9, who made my life at Georgia Tech enjoyable and unforgettable. Also, I want to thank my soul friend, Billy Kihei, and all the members of the Korea University alumni association for always supporting me ever since the first year, especially, many thanks to Chunjae Yoo, who provided me a comfy stay when I was visiting back to Atlanta for writing the thesis. Besides the people I met in Atlanta, I also want to thank my old friends in Korea for always being there to support me, even though I had not been able to attend their weddings in Korea: Seungchan Kim, Hojung Nam, Bongchun Hur, Hyundong Kim, Moonki Choi, Jooncheol Shin, Donghoon Shin, Soyeon Park, Jabeom Koo, and Jungyoon Choo.

The most precious things sometimes come at the least expected time. During my third years at Georgia Tech, I am glad that I was able to answer Jaewon Shim's call, which led me to meeting my wife, Ain Chung. Ever since then, we have spent time together in Atlanta and New York, and also we were fortunate to meet our undoubtedly gorgeous cat, Haru. With them, I could be myself and was able to enjoy doing the research and living life at the same time. The best part of our life together was meeting our son, Teo Hyun. As luck would have it, everything went smoothly, and Teo's presence was a significant driving force to make it to this point. Without Ain's sacrifices, I would not have completed my thesis. Ain is the best in every aspect. I would also like to thank my in-laws, Hyunsook Shin, Hosung Chung, Hyein Chung, and Jiin Chung, for their enormous help in raising Teo.

Finally, I want to thank my parents, Oh-seok Hyun and Jong-Hee Chyun, and my sister, Nak-hee Hyun. This thesis is dedicated to my parents, who showed me the path in academia since I was a child. They respected my decisions and embraced me when I pursued what I believed in. As I grew up, I observed how my father critically analyzed problems in economics and how my mother engaged in teaching and mentoring students. I am very proud to follow their path in research and want to thank both of them for indirectly teaching me about the ultimate pleasure of being creative in life. Also, I want to thank my sister for passing on her wisdom and giving me her honest advice on how to manage life. The same thanks go to my brother-in-law, Jipyung Kim, for being a great supporter, and my lovely niece, Insuh Kim, and nephew, Injoon Kim, for making me smile.

Lastly, I would like to especially thank my grandmother, Youngja Kim, for always praying for me since I was a child. She is always in my heart, and I believe that her prayer is the reason why I was able to meet great people and finish my very first Ph.D. degree.

TABLE OF CONTENTS

LIST OF TABLES

LIST OF FIGURES

LIST OF SYMBOLS AND ABBREVIATIONS

$\langle r; s \rangle$	A geometric sequence: $\{s \cdot r^n\}_n$ for $s, r \in \mathbb{R}$
$\mathbb{R}^{\mathbb{R}}$	The set of real valued functions on domain $\mathbb{R}$
σ_t	An evaluation operator: $\sigma_t(f) = f(t)$ for $f : \mathbb{R} \to \mathbb{R}$
$\{a_n\}_n$	A real valued sequence: $a_n \in \mathbb{R}$ for all $n \in \mathbb{N}$
$C(\mathbb{R})$	The set of real valued continuous functions
$C^1(\mathbb{R})$	The set of real valued continuously differentiable functions
$D^1(\mathbb{R})$	The set of real valued right differentiable functions
$PC(\mathbb{R})$	The set of real valued piecewise continuous functions
S_α	A scaling operator: $S_\alpha(f)(t) = f(\alpha t)$
T_α	A translation operator: $T_\alpha(f)(t) = f(t - \alpha)$
CoM	Center of Mass
EoM	Equations of Motion
FTC	Fundamental Theorem of Calculus
GODE	Generalized Ordinary Differential Equation
GRL	Generalized Root Locus
HFM	Harmonic Field Method

KGF	Krylov Generalized Function
NSA	Nonsatandard Analysis
ODE	Ordinary Differential Equation
PDE	Partial Differential Equation
PFM	Potential Field Method
RL	Root Locus

SUMMARY

Modeling mechanical systems is a mathematical abstraction of describing the relation between the *cause* (e.g. a force and inertia) and the resulting motions. Depending on the assumptions simplifying the model, and the mathematical framework chosen to describe the model, different aspects of the behavior of systems can be analyzed. The objective of this thesis is to create new mathematical frameworks which respects the microscopic feature (e.g. impulsive contact force modeling) and the macroscopic behavior (e.g. safe trajectory planning).

In the first part of the thesis, the microscopic modeling of an impact phase in mechanical systems, which interact with rigid environments, is considered. Since the impact on the hard ground changes the velocities of the part contacting the surface almost instantaneously, the contact force model is often omitted by assuming the amount of change is known a priori. For this reason, this type of model is called an *effect* model, and the dynamics involves discrete reset maps. However, it is preferable to engage the *cause* in the model to respect the underlying physics. The model containing the force term is denoted as a *causal* model in this thesis. Intuitively, it is attempting to model the contact force as a singular function defined in distribution theory, the most appreciated way of describing the singular behavior in physics and engineering. Unfortunately, the singular function defined in distribution theory has a limitation that the multiplication between a nonsmooth function and the singular function may not be well-defined, which occurs often in the mechanical systems written as a nonlinear affine form. The objective of the first part is to develop a new mathematical framework which makes the causal modeling feasible for systems with jumps using a well-defined singular functions. To do so, a new generalized function theory, entitled as *Krylov generalized function* (KGF) theory, is developed within the framework provided by nonstandard analysis (NSA), which properly defines the infinitesimals and infinitely large numbers to extend the real space. First, an algebraically structured multi-

dimensional space is constructed to define the domain of the generalized function, and the fundamental operations, such as differentiation and integration, are proposed to formally define a generalized singular function. Next, a generalized ordinary differential equation (GODE) is considered to apply KGF theory to the causal modeling of mechanical systems with jumps.

In the second part of the thesis, the macroscopic view in motion planning of mechanical systems is considered in the sense that the control is used to avoid a collision (microscopic phase) with the environment while driving the system to a desired configuration. The objective of the second part is to find an analytic framework to either generate safe trajectories for point mass robots or to find analytic conditions capturing the collision between rectangular bodies in planar space, and cuboid bodies in three-dimensional space. As opposed to sampling-based planning (SBP) method in motion planning, the analytic framework could enhance the accuracy of designing the safe trajectories. In this thesis, inspired by algebraic and geometric properties of polynomials, a new paradigm of considering the position of point robots, and approximating the boundary or surface of the full body robot is proposed. A robot's center of mass (CoM) position is considered as a root of some polynomial, and the trajectory is generated by smoothly controlling the coefficients of the polynomials. The basic rule is to follow the generalized root locus (GRL) principle used in the control theory for a completely different purpose. Later, multiple robots are also identified with the polynomials, and the assignment free formation controller is designed following the GRL principles. Furthermore, the full body of rectangular or cuboid shaped robot is analytic approximated by one level set of weighted L_p norm. By using this approximation, an collision avoidance constraint is proposed by a set of equalities and inequalities, which does not include any slack integer variables. Finally, an analytic surface model for bendable cuboid robot is proposed by extending the weighted L_p norm in the polar coordinates. The proposed analytic constraints are used to form a general Bolza type of optimal path planning problem, and the numerical solution is obtained to validate the model.

CHAPTER 1
INTRODUCTION

Newton's law of motion provides fundamental rules on how a force and inertia would change the motion of an object. Along with more generalized methods to model a mechanical system such as an energy-based method in Lagrangian mechanics and a momentum based method in Hamiltonian mechanics, many areas of fundamental mathematics have been developed from infinitesimal calculus to differential geometry. By using the well established mathematical tools, modeling of a real-world problem is then about finding reasonable assumptions which simplify the problem, and articulating a justification of the model within a rigorous mathematical framework. The philosophy of this thesis is to yield different aspects in modeling the mechanical systems from a microscopic view (e.g. contact mechanics) to the macroscopic view (e.g. robotics path planning) by introducing a set of new mathematical frameworks.

1.1 Causal modeling of Impulsive Affine Systems

A *causal* model of mechanical systems is usually given by a dynamics of the system containing the force terms, which follows Newton's law, as opposed to kinematics which only describes the behavior of the motion without considering the force that causes the motion. As the mathematical modeling is a logical abstraction of the physics of nature, it will always be preferable to design a causal model which considers the origin of the desired behavior.

The *causality* of the model can be determined by the level of assumptions made for the simplification. There is always a tradeoff between the scope and the accuracy of the model but some assumptions, made directly on the motion itself, may ignore the underlying physics, and so the overall dynamical model fails to be a *causal* one. For example,

modeling the dynamics of walking gaits for a biped robot requires considering the contact forces which are exerted by a rigid ground, the foot is interacting with. However, the contact force modeling is often ignored by assuming the foot immediately stops after the impact on the ground. See the discussion on the assumptions of the impact model for biped robot in [1]. For these reasons, this type of modeling is denoted as an *effect* model, which contains a continuous dynamics and a discrete system that represents instantaneous jumps in the states. The rational of these assumptions will be reviewed again in Chapter 2.

Also, the causal modeling may be difficult depending on which mathematical framework is chosen to describe the motion. Especially, a causal modeling of mechanical systems which interact with the rigid environment by an impacting behavior may require designing a contact force only defined in a very short duration of time. Therefore, it is natural to model the contact force by a singular delta function in the context of the Schwartz distribution theory in [2], which formally defines the delta function introduced by Paul Dirac in quantum mechanics, [3]. The formal definition and the theories of the singular function will be reviewed in Chapter 2. The causal model for an impulsive system is easily realized in linear systems by solving the instantaneous reachability problem in [4]. A linear combination of the higher derivatives of a delta function, which is well defined in the distribution theory, can be used to change the state instantaneously to the desired state if the system is completely reachable. However, the dynamics for mechanical systems are mostly in nonlinear affine form, and the use of Schwartz distributions in nonlinear systems may be ill-posed since the multiplication between singular functions cannot be well defined. Even the multiplication of a nonsmooth function and a singular function is not well defined. Therefore, most of the work on modeling the singular control in nonlinear system theory has been done by first regularizing the singular control input, and pursue a limit solution of the regularized system. Although the limit solution provides a generalized solution of impulse-driven systems, the limiting process itself lacks physical meaning.

The main difficulties in using the distributional delta function to nonlinear system the-

ory are that it is not a regular function defined on the real line, and so the pointwise evaluation is meaningless. The singular function can only be utilized by its axiomatic properties in distribution theory. The question is then if a space denser than a real space can be constructed where the delta function can be defined pointwise. The answer is yes, and it was the motivation to develop a new field of mathematics called the *Nonstandard analysis* (NSA), [5], created by Abraham Robhinson in the 1960s. Initially, the calculus was based on the infinitesimal elements, *something that is smaller than any assignable element*, as introduced by Cauchy, Leibniz, and Newton in the 17th century. However, infinitesimals were eventually removed in the analysis as the concept would not be formally defined. The infinitesimal calculus was replaced by the calculus based on a constructive number system, which was formulated by Cantor, Dedekind and others in 19th century. Weierstrass invented the formulation of limits using (ϵ, δ) arguments. Since then, it became a dominant way of dealing with functions in calculus up to today. Only three hundred years after, Robinson was first to rigorously define an infinitesimal quantity, and extend the standard real spaces using the modern logic systems. The extended real space is called *hyperreal space*, which will be formally introduced in Chapter 2. Also, a more interesting history of NSA can be found in [6].

The objective of the first part of the thesis is to build up from first principles to create a new mathematical framework which makes the causal modeling feasible using the generalized singular functions. A new algebraically structured extended real space embedded in the hyperreal space is proposed in this thesis, where the independent variable (usually time) is now decomposed into the standard part and infinitesimal parts. The infinitesimal parts of the time are also decomposed based on the ordering property in NSA. The generalized function is then defined on the proposed extended real space, and generalized fundamental operations including differentiation and integration are introduced. The algebraically structured infinitesimal space enables the singular delta function to be evaluated pointwise, and so the fundamental shape of the singular functions can be found, which will be used to

model the contact force. This new space is called a *Krylov hyperreal space* as the process of generating the space resembles the successive operation of Krylov subspace in linear algebra, and the new generalized function theory will be denoted as *Krylov generalized function* (KGF) theory. The detailed construction of KGF theory is explained in Chapter 3.

Next, the generalized ordinary differential equation (GODE) is proposed, and the KGF theory-based solution is sought in Chapter 4. Two problems are considered in this thesis. The first problem is to find a causal representation of a given effect model which the generalized solution for the corresponding causal GODE would be identical if it is evaluated in the standard time. The second problem is to design a contact force which either generates the same desired jump as in the effect model or generates different jump but with relaxed assumptions than the ones in the effect model. The first problem is more general than the second one since it is a question of if it is possible to find the GODE which follows the effect model without considering the actual physics. In contrast, the second problem actually considers the causal modeling of the mechanical systems with jumps by designing the singular contact force.

As such, this first part breaks new ground in mathematical theory and systems applications and necessarily goes down to basics with a revolutionary viewpoint, albeit not as revolutionary as Kalman's introduction of the state space, [7], or Willems's behavioral theory, [8].

1.2 Safe Trajectory Planning

In contrast to the mechanical systems which need contact with its environments to navigate the world, there are many applications where collisions with the obstacles needs to be avoided, i.e. controlling a drone or an autonomous vehicle. Therefore, the path planner must design a trajectory of the robot which avoids collision with other obstacles or robots. A classical way to find safe configurations is through the *configuration space approach*, which transfers the rigid body path planning problem to a point mass problem by enlarging

the obstacle with the robot for every orientation. One popular approach on constructing the configuration space is the sampling-based planning (SBP) method. The SBP first samples the configuration space, and explores a path connecting the sampled points. See the survey of the sampling-based planning in [9], and more in the book [10]. In the second part of this thesis, instead of working on the sampled configuration space, an analytical way to model the path planning problem is proposed. The objective is either to find a set of smooth vector fields which all generates the collision free trajectories or to find a set of analytic constraints on the configuration of the robots which represents the collision avoidance. By using the algebraic and geometric properties of the polynomial, new frameworks for path planning methods are introduced.

First, an algebraic property of a single variable polynomial is used to generate a safe trajectory for a point mass robot in the planar space. The location of the robot is identified as a complex root for some polynomial, and the trajectory is generated by tracking the roots of updated polynomials. Inspired by the root locus method in control theory, which is used for a completely different purpose, the trajectory of the robot is generated by following the generalized root locus. A formal definition of generalized root locus will be introduced in Chapter 5. By placing more stationary roots inside the obstacles, a safety region around the obstacles is generated, and the root locus path starting from the robot's initial location does not go into the safety region. The generalized root locus method produces a set of safe trajectories. An optimal path planning problem is then considered which minimize the final arrival time to the target point among those safe trajectories. Furthermore, the root locus based path planning algorithm can be applied to generate trajectories for multiple robots to achieve a cooperative goal of making a formation without any specific target assignment on each robot.

Next, a geometric property of a multi-variable polynomial is used to find a collision avoidance condition for full body robot. The configuration space is not constructed in this case, and so the geometry of the robot is taken into account directly when deriving the

safety conditions. Especially, a rectangular robot in planar space and a cuboid robot in three-dimensional space are considered, for which the analytic safe configuration is usually constructed by introducing slack integer variables that makes the problem NP-hard. The boundary or surface of the robot is approximated by the one level set of weighted L_p norm. The formal definition of the weighted L_p norm is introduced in Chapter 6. The distance from the rectangular robot to the obstacle can be defined by measuring the weighted L_p norm from the center of the robot to the closest point on the obstacle. A direct method finds a set of inequalities by measuring the distances from possible collision points, and use it as a safety constraint for solving a general Bolza type of optimization problem. The direct method is then generalized by formulating a two-staged optimization problem, which includes a constraint that depends on a solution to the closest point problem. By analytically deriving the necessary and sufficient conditions, the safety condition is given as a set of equalities and inequalities. Furthermore, an analytic surface model for a bendable cuboid is designed by considering the weighted L_p norm in the polar coordinates. The curvature parameter controls the bending of the robot, and the analytic safety conditions for the bendable cuboid is also derived. This bendable cuboid robot structure opens up the possibilities of finding the analytic safety conditions for continuum mechanics in [11, 12] and a soft bendable finger in [13].

1.3 Organization of the Thesis

The thesis is organized as follows. Part I contains three chapters which consider the causal modeling problem of impulsive affine systems. The mathematical preliminaries and background of the causal modeling is explained in Chapter 2, and the Krylov generalized function (KGF) theory is introduced in Chapter 3. An application to the impulsive affine systems using KGF theory is covered in Chapter 4. Part II contains three chapters which considers the safe trajectories generation in robotics using algebraic and geometric properties of polynomials. The root locus based point mass robot planning is considered in

Chapter 5, and the full body robot path planning is considered in Chapter 6 and Chapter 7, where the generalized weighted L_p method including bendable robot path planning is considered in Chapter 7. Finally, the conclusion of the thesis and the future research direction is summarized in Chapter 8.

Part I

Causal Modeling of Impulsive Affine Systems- A Nonstandard Analysis Approach

CHAPTER 2

MATHEMATICAL PRELIMINARIES AND BACKGROUND

In this chapter, some mathematical background material for the causal impulsive modeling problem is introduced. First, in § 2.1, the impulsive affine systems are reviewed in the context of Lagrangian mechanics considering the contact force. Based on the assumption of the behavior during the contact, two different means of modeling the impulsive behavior are reviewed: one is impulsive effect modeling, and the other is causal impulsive modeling. In addition, the classical distributional definition of a singular function is introduced, and the Schwartz impossibility theorem is recalled to illustrate the difficulties with its applications in nonlinear systems. Next, in § 2.2, the fundamental definitions and theorems for NSA are reviewed with its applications in engineering. Finally, three basic operators, a scaling, translation, and evaluation operators commonly used in this thesis are formally defined in § 2.3.

2.1 Impulsive Affine Systems

In this section, the background of mechanical systems modeling problem is considered. In § 2.1.1, the equations of motion of mechanical systems are derived using Lagrangian mechanics, and formulated in the affine form. Next, an impulsive effect modeling is reviewed in § 2.1.2, and causal impulsive modeling is reviewed in § 2.1.3.

2.1.1 Lagrangian Mechanics

Classical mechanics mainly studies the motion of a finite number of point mass particles. Each rigid component of the multibody mechanical systems is approximated by a point mass particle located at the center of mass (CoM) position of the component where the mass at the CoM can be computed by the integral of the mass distribution of the compo-

nent. Therefore, the multibody system is often modeled by multi-linked point masses. For example, a two link compass gait passive walker in [14] is modeled with three point mass particles, and a five link bipedal robot in [15] is modeled with four point mass particles. Every particle follows Newton's law of motion in the global inertial frame with the constraint on the interconnection, and the equation of motion (EoM) can be derived in many different ways. In this section, the EoM is derived using the Lagrangian analysis in generalized coordinates. A basic reference to the classical mechanics is [16]. More intuitive explanation of Lagrangian mechanics can be found in [17]. In addition, the kinematics and dynamics of rigid body motion with respect to the body frame is detailed in [18]. This section gives a summary of deriving the dynamics of actuated mechanical systems interacting with the rigid environment.

Let the multi-link rigid body system be approximated by n particles, $\{r_i\}_{i=1}^n \subset \mathbb{R}^3$ in the global inertial frame, with the interconnection between particles satisfying the constraints,

$$g_j(r_1, \cdots, r_n) = 0$$

for $j = 1, \cdots, k$ for some $k < n$. A constraint which only consists of the position of the particles is called *holonomic*. The minimum number of coordinates to represent the motion is called the *degree of freedom*. Since the particle needs to satisfy k holonomic constraints, its $3n$ coordinates are not independent, and may be reduced to $3n - k$ independent coordinates. Let $d := 3n - k$ be the degree of the freedom. By introducing d new *generalized coordinates*, $\{q_l\}_{l=1}^d$, the original coordinates can be represented by

$$\begin{aligned} r_1 &= \eta_1(q_1, \cdots, q_d) \\ &\vdots \\ r_N &= \eta_N(q_1, \cdots, q_d) \end{aligned}$$

where η_i are smooth transformations for $i = 1, \cdots, N$. Let $r = (r_1, \cdots, r_N) \in \mathbb{R}^{3n}$ and

$q = (q_1, \cdots, q_d) \in \mathbb{R}^d$ be the augmented state, and set $r = \eta(q)$ by using the component-wise transformations.

The Lagrangian analysis is based on the energy of the system. Let $K(r, \dot{r})$ be the kinetic energy of the n particles, and $U(r)$ be the potential energy. The Lagrangian of the system is defined as

$$L(r, \dot{r}) := K(r, \dot{r}) - U(r). \tag{2.1}$$

The kinetic energy of n particles in the global frame can be written as

$$K(r, \dot{r}) = \frac{1}{2} \sum_{i=1}^{n} m_i \dot{r}_i^T \dot{r}_i$$

By using the generalized coordinate q, the kinetic energy K_q can also be defined in the q coordinates,

$$K_q(q, \dot{q}) := K(\eta(q), \dot{\eta(q)}) = \frac{1}{2} \sum_{i=1}^{n} m_i \dot{\eta}_i(q)_i^T \dot{\eta}_i(q)_i = \frac{1}{2} \dot{q}^T M(q) \dot{q} \tag{2.2}$$

where $M(q) \in \mathbb{R}^{d \times d}$ is the inertia matrix defined with

$$M(q)_{ab} = \sum_{i=1}^{n} m_i \partial \eta_i(q) / \partial q_a \cdot \partial \eta_i(q) / \partial q_b$$

for the (a, b) element. The inertia matrix can be understood as a mass matrix for the generalized coordinates. The following is true for the inertia matrix.

Lemma 1 ([18]). *$M(q)$ is symmetric and positive definite.*

Proof. See Lemma 4.2 in [18] □

Let $V(q) := U(\eta(q))$ be the potential function in the generalized coordinates, then the Lagrangian in the generalized coordinate is given by

$$L(q, \dot{q}) := \frac{1}{2} \dot{q}^T M(q) \dot{q} - V(q). \tag{2.3}$$

Let $F_i : \mathbb{R} \to \mathbb{R}^3$ be the external force acting on the $i-$th particle in the global inertial frame, then the generalized force for $j-$th generalized coordinates is defined as

$$Q_j := \sum_{i=1}^{n} F_i \cdot \partial \eta_i(q)/\partial q_j. \tag{2.4}$$

Let $Q : \mathbb{R}^d \to \mathbb{R}^d$ be the augmentation of generalized forces,

$$Q(q) = (Q_1(q), \cdots, Q_d(q))^T.$$

The equation of motion is now specified by the *Euler-Lagrange equation*,

$$d(L_{\dot{q}}(q, \dot{q}))/dt - L_q(q, \dot{q}) = Q, \tag{2.5}$$

where $L_{\dot{q}}(q, \dot{q}) := \partial L(q, \dot{q})/\partial \dot{q}$ and $L_q(q, \dot{q}) := \partial L(q, \dot{q})/\partial q$.

By directly computing the Euler-Lagrange equation using (2.3), the dynamics can be written as

$$M(q)\ddot{q} + C(q, \dot{q})\dot{q} + G(q) = Q \tag{2.6}$$

where $C(q, \dot{q}) \in \mathbb{R}^{d \times d}$ is known as the Coriolis matrix and $C(q, \dot{q})\dot{q}$ gives the Coriolis and centrifugal force terms in the generalized coordinates, and $G(q) \in \mathbb{R}^d$ contains gravity and other position dependent force terms acting on the generalized coordinates.

If the q were chosen as the relative joint angle of manipulators or biped robots as in [15], then the actuation is by the torque controls on the joint space. The external torque can be regard as a generalized forces through the actuation matrix $B \in \mathbb{R}^{d \times m}$ where m is the number of actuators, and the dynamics becomes

$$M(q)\ddot{q} + C(q, \dot{q})\dot{q} + G(q) = Bu, \tag{2.7}$$

where $u : \mathbb{R} \to \mathbb{R}^m$ is the control signals from m actuators. If the rank of B is full, then the

system is *fully actuated*, and if the rank is less than d, then the system is *underactuated*.

Lagrangian Mechanics with Contact Force

Suppose that a rigid mechanical system interacts with the rigid environment, then there exist a point on the robot's surface which is in contact with the rigid surface. This contact point can be represented by the generalized coordinate, and let $z(q) \in \mathbb{R}^3$ be the contact point in the global coordinate with some smooth function, $z : \mathbb{R}^d \to \mathbb{R}^3$. For example, this point of contact could be understood as a point foot of a bipedal robot in [15]. An analysis of multiple contact points can be found in [19].

Let $dz_q : \mathbb{R}^d \to \mathbb{R}^3$ be the differential of z at $q \in \mathbb{R}^d$ after considering the chart transformation to the Eucledian space. The generalized velocities, $\dot{z}$, can be derived as

$$\dot{z}(q) = dz_q(\dot{q}) = J(q)\dot{q}, \tag{2.8}$$

where $J(q) := \nabla z(q) \in \mathbb{R}^{3\times d}$ is the Jacobian of z at q. Let $F_c \in \mathbb{R}^3$ denote the contact force acting on the point $z(q)$, then the generalized force $F_c(q) \in \mathbb{R}^d$ can be computed by using (2.4),

$$F_c(q) := J(q)^T F_c. \tag{2.9}$$

The Euler-Lagrange equation containing the contact force is then given by

$$M(q)\ddot{q} + C(q,\dot{q})\dot{q} + G(q) = Bu + J(q)^T F_c. \tag{2.10}$$

Nonlinear Affine Systems

Now by using Lemma 1, the second order dynamics for d degrees of freedom, assuming the contact force F_c is applied to the point $z(q)$, can be rewritten as

$$\ddot{q} = -M(q)^{-1}C(q,\dot{q})\dot{q} - M(q)^{-1}G(q) + M(q)^{-1}Bu + M(q)^{-1}J(q)^T F_c,$$

and by augmenting the state $x := (q, \dot{q})^T \in \mathbb{R}^{2d}$, the dynamics can be formed as a nonlinear affine system form,

$$\dot{x} = \quad f(x) + g(x)u + g_c(x)F_c \tag{2.11}$$

$$\dot{x}(0) = \quad \begin{pmatrix} q_0 \\ v_0 \end{pmatrix} \tag{2.12}$$

such that

$$f(x) := \quad \begin{pmatrix} \dot{q} \\ -M(q)^{-1}C(q,\dot{q})\dot{q} - M(q)^{-1}G(q) \end{pmatrix}$$

$$g(x) := \quad \begin{pmatrix} \mathbf{0}_{d\times m} \\ M(q)^{-1}B \end{pmatrix}$$

$$g_c(x) := \quad \begin{pmatrix} \mathbf{0}_{d\times 3} \\ M(q)^{-1}J(q)^T \end{pmatrix},$$

with $(q_0, v_0) \in \mathbb{R}^d \times \mathbb{R}^d$ as a initial condition and $\mathbf{0}_{d\times m} \in \mathbb{R}^{d\times m}$ and $\mathbf{0}_{d\times 3} \in \mathbb{R}^{d\times 3}$ are zero matrices.

Therefore, the nonlinear affine system in (2.11) appears commonly in modeling the multi-rigid body robotics applications. In the following sections, the nonlinear affine system in this form is considered. The applications of the impulsive affine system are not only restricted to mechanical systems but also involve biological systems and circuit designs such as an impulsive control of a predator and prey model in [20] and a biomedical application of cancer therapy in [21], and a reset circuit design using a clegg integrator in [22].

2.1.2 Impulsive Effect Modeling

If there were no contact, then $F_c = 0$ in (2.11). The non-zero contact force occurs only if some part, $z(q)$, of the robot's body interacts with the environment, e.g, ground or other rigid robots. This contact event can be captured by first formally defining the contact surface.

Let $h : \mathbb{R}^d \to \mathbb{R}$ be a gap function (Definition 1.8 in [23]), which represents the distance between the possible contact surface to $z(q)$. For example, if the ground surface is modeled by the (x, y) plane in the global frame, $h(q) := a^T z(q)$ represents the distance of the point foot $z(q)$ to the ground, where $a = [0, 0, 1]^T$ is a normal vector to the flat ground. Then, the contact surface is modeled as a hypersurface induced by a smooth gap function,

$$S_q := \{q \in \mathbb{R}^d | h(q) = 0\}. \tag{2.13}$$

Suppose that the ground is also rigid, and so an additional *unilateral constraint* can be assumed for the feasible configurations of the robot,

$$S_q^+ := \{q \in \mathbb{R}^d | h(q) \geq 0\}. \tag{2.14}$$

In addition, assuming that the contact force does not pull to the ground but only pushes in the outer normal direction, the following inequality condition can be imposed,

$$\begin{cases} h(q) \geq 0 \wedge F_c \geq 0 \\ h(q) F_c = 0 \end{cases}. \tag{2.15}$$

This condition is so called a *linear complimentarity problem* (LCP). See the great details on the LCP in [23].

Since the contact behavior depends on the relative kinematics between the rigid body and the ground model, the non-zero ground reaction force is initiated if the relative velocity

of the contact point to the ground is decreasing at the moment of the contact (when $h(q) = 0$). Therefore, the following switching surface considering the relative velocity is defined,

$$S := \{x \in \mathbb{R}^{2d} | h(q) = 0, \nabla h(q) \cdot \dot{q} < 0\}, \tag{2.16}$$

and so if $x \in S$, then the collision is initiated, and the non-zero contact force in (2.11) should be considered.

Let $\tau > 0$ be the time when $q(\tau) \in S$, and let $q(\tau+) = \lim_{t \overset{>}{\to} \tau} q(t)$ is the right limit to τ. Since the rigid ground (unilateral constraint) is assumed, the robot cannot penetrate the surface, and so either the collision should be inelastic, $\nabla h(q(\tau+)) \cdot \dot{q}(\tau+) = 0$, or elastic $\nabla h(q(\tau+)) \cdot \dot{q}(\tau+) > 0$. If the contact force is bounded, $||F_c|| < M$, then there must be a penetration to the surface which violates the *modeling assumption*. Therefore, there exist an immediate change in the velocities, $\dot{q}(\tau-)$ and $\dot{q}(\tau+)$, driven by some *impulsive contact force*.

Assumptions and the Reset Map

The impulsive effect modeling is one way to approximate the behavior of the velocity jump due to the impulsive contact force without explicitly explaining impulsive forces but rather assuming or predicting some conditions during the impact to derive the updated velocity. Several assumptions during the contact has been studied in [19] such as

- Case 1: No rebound and no slipping along the surface
- Case 2: No rebound but slipping along the surface is allowed

The Case 1 is used for a point foot collision to the ground in the biped locomotion research, [15, 24]. See more papers in the tutorial, [1], and Case 2 is used when the friction is considered in [25]. The no slip and no rebound conditions determine the inelastic collision, where the foot velocity after the impact remains zero, $\dot{z}(q(\tau+)) = 0$. With some other assumptions such as the actuator not exerting impulsive controls, and the immediate release

of the other foot from the ground, a reset map can be obtained using the conservation of angular momentum about the contact foot position. Following the notation and procedure in [15], let $q_e := (q, z(q)) \in \mathbb{R}^{d+3}$ be the new set of generalized coordinates, then the dynamics with the foot can be expressed using the Lagrangian,

$$M_e(q_e)\ddot{q_e} + C_e(q_e, \dot{q_e})\dot{q_e} + G_e(q_e) = B_e u + J_e(q_e)^T F_c,$$

where the subscript e indicates that each matrix is different from (2.10). The overall impusive reset can be written as

$$\begin{pmatrix} M_e(q_e) & -J_e(q_e)^T \\ J_e(q_e) & 0_{3\times d} \end{pmatrix} \begin{pmatrix} \dot{q}_e(\tau+) \\ \Lambda \end{pmatrix} = \begin{pmatrix} M_e(q)\dot{q}(\tau) \\ 0 \end{pmatrix} \tag{2.17}$$

where $\Lambda := \int_{\tau}^{\tau+} F_c(t)dt$ is the impulse effect during the contact. By using the Schur complement [26], if $J_e(q_e)$ has full rank, the velocity reset map can be uniquely and algebraically defined as

$$\dot{q}_e(\tau+) := (I - M_e(q_e)^{-1}J_e(q_e)^T(J_e(q_e)M_e(q_e)^{-1}J_e(q_e)^T)^{-1}J_e(q_e))\dot{q}_e(\tau-) \tag{2.18}$$

or

$$\Delta\dot{q}_e(\tau) = -M_e(q_e)^{-1}J_e(q_e)^T(J_e(q_e)M_e(q_e)^{-1}J_e(q_e)^T)^{-1}J_e(q_e)\dot{q}_e(\tau-), \tag{2.19}$$

where $\Delta\dot{q}_e(\tau) := \dot{q}_e(\tau+) - \dot{q}_e(\tau-)$ is the state dependent jump in the generalized velocities.

Basically, the impulsive effect model assumes that there exists an impulsive contact force which creates the jump, and augments the law of the model with the provided reset

map to approximate the dynamics. In general, the following equation is considered,

$$\begin{cases} \dot{x} = f(x) + g(x)u & \text{for } x \notin S \\ \Delta x(\tau) = R(x(\tau-)) & \text{for } x(\tau-) \in S, \end{cases} \tag{2.20}$$

for some smooth function $R : \mathbb{R}^{2d} \to \mathbb{R}^{2d}$. This impulsive effect systems are a subclass of hybrid systems where the dynamics of motions are modeled with a continuous vector field in the presence of jumps. The classical formalism on impulsive differential equations and their dynamics can be found in [27, 28, 29] and [30]. Generally, there are two types of impulsive system; one with the time of jumping events specified and the other where switching times are implicitly determined by additional state dependent equations as in (2.20). The formulation of the impulsive affine system equation with a prescribed time sequence of jumps are given as

$$\begin{cases} \dot{x}(t) = f(x(t)) + g(x(t))u(t) & \text{if } t \notin \mathcal{T} \\ \Delta x(\tau) = R(x(\tau-)) & \text{if } \tau_i \in \mathcal{T}, \end{cases} \tag{2.21}$$

where $\mathcal{T} := \{\tau_i\}_{i=1}^{\infty} \subset \mathbb{R}_+$ is the monotonically increasing time sequence of jumps where $\lim_{k\to\infty} t_k = \infty$. The sufficient conditions for the existence and uniqueness of (2.21) are shown in [27] which generally depends on Lipschitz conditions for the right hand side of (2.21) on each interval, and boundedness of the function R.

Example 1: Horizontal Bouncing Ball

Suppose that a ball is moving on a one dimensional horizontal frictionless space. In this example, consider the elastic collision, which bounces off immediately after the impact. By assuming the coefficient of restitution $\gamma \in (0, 1)$ is empirically modeled using the experimental results in [31]. The state space is defined by $(x(t), v(t))^T$, where $x(t)$ is the position, and $v(t)$ is the velocity of the ball. Fig 2.1 graphically shows the reference frame

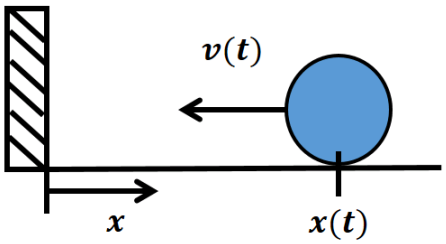

Figure 2.1: Horizontal bouncing ball

for x, and we assume that the ball is a point mass, $m = 1$, and so the ball hits the wall when $x(t) = 0$. Let $X = (x_1, x_2)^T \in \mathbb{R}^2$ be the state space where $x_1 := x$ and $x_2 := v$. The impulsive effect model of this system with the restitution coefficient, is given by

$$\begin{cases} \dot{X}(t) = \begin{pmatrix} 0 & 1 \\ 0 & 0 \end{pmatrix} X(t) & \text{if } X(t) \notin S \\ \Delta X(t) = \begin{pmatrix} 0 \\ -(\gamma+1)x_2(t-) \end{pmatrix} & \text{if } X(t) \in S \end{cases} \tag{2.22}$$

where the switching surface is $S := \{X \in \mathbb{R}^2 | x_1 = 0 \wedge x_2 < 0\}$, and $\Delta X(t)$ represents the difference, $X(t+) - X(t-)$. The jump equation can also be written as $x_2(t+) = -\gamma x_2(t-)$ where $x_2(t+)$ and $x_2(t-)$ are defined as the right limit and the left limit of x_2 at time t.

Example 2: Compass Gait Passive Walker

The compass gait model in the planar space is shown in Figure 2.2. The center of mass of each leg is represented by the particle with mass m, and the center of mass for the hip, with mass M, is located at joint. Let $l = a + b$, and assume that during the swinging phase the stance foot is fixed, and since the length of the leg and the joints are fixed, the degree of the freedom is 2. Let the generalized coordinate to be $q = (\theta_{sw}, \theta_{st})^T$, then the inertia matrix

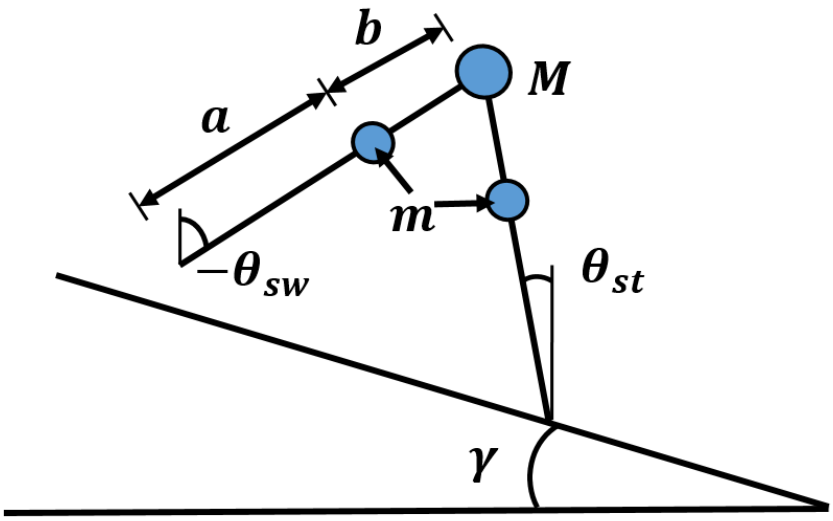

Figure 2.2: The compass gait

$M(q)$, and the Coriolis matrix, $C(q)$, and the gravity term $G(q)$ in (2.12) is given by

$$M(q) := \begin{pmatrix} mb^2 & -mbl\cos(\theta_{st}-\theta_{sw}) \\ -mbl\cos(\theta_{st}-\theta_{sw}) & (M+m)l^2+ma^2 \end{pmatrix} \tag{2.23}$$

$$C(q,\dot{q}) := \begin{pmatrix} 0 & mlb\sin(\theta_{st}-\theta_{sw})\dot{\theta}_{st} \\ -mlb\sin(\theta_{st}-\theta_{sw})\dot{\theta}_{sw} & 0 \end{pmatrix} \tag{2.24}$$

$$G(q) := \begin{pmatrix} mbg\sin(\theta_{sw}) \\ -g((M+m)l+ma)\sin(\theta_{st}) \end{pmatrix} \tag{2.25}$$

$$B(q) := \begin{pmatrix} 1 \\ -1 \end{pmatrix}. \tag{2.26}$$

The contact surface can be defined with $h(q) = 2\gamma+\theta_{sw}+\theta_{st}$, and let $z(q) \in \mathbb{R}^2$ represents the end of the swing leg, and $a = (1, 1/\tan(\gamma))$ be the normal direction to the slope, then the switching surface is defined as,

$$S := \{q \in \mathbb{R}^2 | h(q) = 0 \wedge \dot{z}(q)^T a < 0\}. \tag{2.27}$$

By using the assumption that the collision of the swing leg to the ground is inelastic (no slip and no rebound), and the stance leg does not interact with the ground during the impact, the unique reset map can be derived using (2.19) by deriving the Lagrangian for $q_e := (q, z(q))$. The compass gait dynamics contains natural passive stable periodic orbit for some narrow γ values around 3 degree. Detailed analysis of the passive periodic orbits are shown in [14].

2.1.3 Causal Impulsive Modeling

Contact Force

The assumptions during the impact in the impulsive effect model simplify the problem but it is not the most accurate model. The no slip assumption which helps to find the unique reset map can be easily violated in practice due to softness of the foot or the ground model, or the finite friction. Painleve's paradox explains that a simple rod must be sliding along the surface otherwise it will penetrate the ground. In addition, even with infinite friction there may be sliding. See [32] for the ambiguity of the outcome of the collision for different cases in legged locomotion with infinite friction.

More complicated but accurate analysis can be done by modeling the contact force directly. Generalized contact force using the nonlinear spring and damper model is reviewed in [33]. In these models, the slight violation to the unilateral constraint is allowed, and therefore the contact force is modeled as a function of the relative indentation, δ. Hunt and Crossley investigate the nonlinear viscous-elastic element to model the contact force as

$$F_c := K\delta^n + D\dot{\delta}, \tag{2.28}$$

see Chapter 3 in [33] for more details. This contact force model was applied in the biped robot design in [34]. The duration of the contact is assumed to be small but not of measure zero, and so the contact force is point-wise well defined but the differential equation would be stiff.

Generalized Functions

Instead of modeling the contact force as a regular function for a short duration, the singular function, as known as the Dirac delta function, introduced but not justified by Dirac in quantum mechanics and used in many engineering text book, may be used to generate the jump behavior in the velocity domain. In 1950s, Laurent Schwartz was the first to unambiguously formulate the theory of distributions, which contains a proper definition for a delta function. See [35] for more details in the generalized function theory, and [2] by Israel Halperin, based on Lectures by Laurent Schwartz. In distribution theory, a 'well-behaved' function, $\varphi : \mathbb{R} \to \mathbb{R}$, is defined as an infinitely differentiable function with a compact support: $\{x \in \mathbb{R} | \varphi(x) \neq 0\}$ is bounded on $\mathbb{R}$. These functions are called *test functions*, and $\mathcal{D}$ is denoted as a set of such test functions. The generalized functions are defined as continuous linear functionals on $\mathcal{D}$, and the set of generalized function is denoted as $\mathcal{D}'$. If f is locally integrable, then the corresponding generalized function F is given as

$$F(\varphi) := (f, \varphi) = \int_{\mathbb{R}} f(x)\varphi(x)dx \tag{2.29}$$

for all $\varphi \in \mathcal{D}$. The function, F, that can be expressed as in (2.29) is called a *regular* function. Suppose that a generalized function, δ, is given, such that $\delta(\varphi) := \varphi(0)$ for all $\varphi \in \mathcal{D}$, then it can be shown that δ is a continuous linear functional on $\mathcal{D}$. However, there does not exist a locally integrable function f which satisfies $\delta(\varphi) = \int_{\mathbb{R}} f(x)\varphi(x)dx$. The function $F \in \mathcal{D}'$ which cannot be expressed as in (2.29) is called a *singular* function. Therefore, the delta function is a well defined singular function in distribution theory. The derivative of generalized function, $F \in \mathcal{D}'$, can be also defined as

$$F'(\varphi) := -F(\varphi') \tag{2.30}$$

where ϕ' is a derivative of $\phi \in \mathcal{D}$. If F is regular differentiable function, then (2.30) can be verified by using the integration by parts of (2.29). Furthermore, in distribution theory, every generalized function is differentiable any number of times since the generalized derivative is properly defined. Therefore, one can show that the generalized derivative of the Heaviside function H, such that it is zero for $x < 0$, and one for $x \geq 0$, is equal to the delta function.

However, a major problem of using Schwartz distributions in nonlinear system theory is that the set of generalized functions cannot acquire the structure of an associative algebra.

Theorem 1 ([36])**.** *Let A be an algebra containing the algebra $C(\mathbb{R})$ of all continuous functions on $\mathbb{R}$ as a subalgebra. Let us assume that the constant function $1 \in C(\mathbb{R})$ is the unit element in A. Further assume that $D : A \to A$ is the distributional derivative and satisfying the Leibniz's rule. Then one has $D^2(|x|) = 0$*

Proof. See Chapter 1.3 in [37]. □

This is called a *Schwartz impossibility theorem* shown in [36] by Schwartz. In addition, the simple Leibniz product rule does not hold in distribution theory. For example, since H, H^2 and H^3 are pointwise equivalent, they are all equal to H in distribution theory. Assume that the Leibniz rule holds, then their distributional derivatives satisfies $\delta = 2H\delta = 3H\delta$, and so $(1/2)\delta = (1/3)\delta$, which is not true since δ is not equal to a zero function in distribution. See more details in [37].

The deficiency in Schwartz distribution theory has been overcome in the 80s by the New Generalized Function (NGF) theory proposed by Colombeau in [38] and [39]. The NGF space is constructed as a quotient algebra where Leibniz's rule holds for its generalized derivative operator. One of the key properties of Colombeau algebra is that the two functions, H^n and H, in the previous example, are different in NGF but two functions can be weakly equal to each other: Roughly speaking, there exist two equalities, one is a strong equality which distinguishes H^n with H and the other is a weak equality denoted

as $H^n \approx H$: the weak equality holds if $(H^n - H, \varphi)$ equals to zero for all $\varphi \in \mathcal{D}$ in usual distributional sense. See more details in Chapter 2 of [39]. The Colombeau algebra has inspired many physical models involving the partial differential equations such as the impulsive gravitational wave equation in [40] and others reported in [37].

Alternatively, it was shown in [41] and in [42] that the theory of Colombeau algebra can be interpreted in the language of nonstandard analysis (NSA) which was first introduced by Robinson in [5]. The NSA is revisited in § 2.2 with more details. The nonstandard analysis extends the real numbers to the *hyperreals*, denoted as ${}^*\mathbb{R}$, where the infinitesimals are well defined elements in hyperreals. In NSA, similar to Colombeau algebra, two Heaviside functions, H^n and H, are not equal from a microscopic viewpoint near the infinitesimals in hyperreals. See the tutorials of the construction of Heaviside functions in [43].

Limit Solution

A constructive way of eliminating the reset equation in (2.20) was proposed in [44] by identifying the states, before and after the jump. By using this identification, the quotient domain of the system is constructed, and a gluing homeomorphism is introduced to show that the resulting system has a continuous but possibly nonsmooth solution which can be inverted back to the discontinuous solution of the original hybrid system. The gluing homeomorphism has also been used in [45] to design the observer for the hybrid system. After transferring the hybrid system to the discontinuous system, the absolutely continuous solution can be obtained in terms of Caratheodory solution or Filippov solutions. See [46] and [47] for absolutely continuous solutions. Although, the gluing method can remove the jump equation from the impulsive system equation, it does not provide a proper framework of controlling the jumps.

On the other hand, instead of removing the jump equation by simply matching two states in (2.20), modeling the contact force as a singular function or singular measure has been actively studied. This is essentially different from the contact force model in [33], as

the impact duration would be regard as measure zero. The main goal is to properly define the generalized ordinary differential equation (GODE) which can generate a solution of bounded variation; roughly speaking the piecewise continuous solutions. The most studied two forms of GODE are written as

$$Dx = f(x) + g(x)u_s \tag{2.31}$$

$$dx = f(x)dt + g(x)du, \tag{2.32}$$

where Dx is the distributional derivative of x, u_s is a generalized singular delta function, and u is of bounded variation and the derivative of u can also be understood as a singular function. If (2.31) is linear, then the solution can be sought in distribution theory. However, if g is not constant and depends on the state x, then one cannot simply use the distributional singular function due to Theorem 1 (the Schwartz impossibility theorem). Therefore, most research is based on a measure differential equations (MDE) using (2.32), where the measure is decomposed into a continuous part and atomic part: Dirac delta measure. See chapter 1 in [23]. The integral solutions of MDE of (2.32) are computed by constructing an auxiliary ODE at the exact moment of the impact. This auxiliary ODE depends on the total variation of u, and roughly speaking it relaxes $g(x)$ to be continuous when it is multiplied by the Dirac delta measure. Many results in [23, 48, 49, 50] have shown that this integral solution is equivalent to the limit of sequence of solutions, which is generated by applying continuously differentiable controls, $\{u_i\}_{i=1}^{\infty}$, to (2.32) where the control sequences converge to u almost everywhere. Another interesting approach is the so called graph completion method in [51], which defines a parameterized curve function, $\gamma : [0, 1] \to [0, T] \times \mathbb{R}$, that continuizes the discontinuous graph $(t, u(t))$, and applies γ as a control input to an extended MDE of (2.32). Similar to the MDE solution, the authors of [51] seek for a continuously differentiable sequence of functions which converges to the graph completion, γ, and find the limiting solution. Further generalization of the graph completion method can

be found in [49, 52]. See also [53, 54] for the sequence approximation for singular function u_s in (2.31).

Independently, the authors of [55, 50] constructed so called active singularities which model the contact force in a singular phase of the mechanical system. They used a penalty method which allows the violation of the unilateral constraints of the collision, and introduce a sequentially approximated penetration of the boundary constraint. During this penetration phase, the singular control can be modeled, and used to generate different jump behavior. Similar to the work in [55], the proposed singular function in this thesis is motivated by the mechanical impact models but rather not seeking for the limiting solution. In this thesis, a new definition for the generalized function is proposed, which the singular function is point wise well defined, to find the generalized solution for GODE in (2.31). The evaluation of the proposed solution at the real-valued time, $t \in \mathbb{R}$, will be equivalent to the discontinuous solution in classical impulsive system.

2.2 Nonstandard Analysis

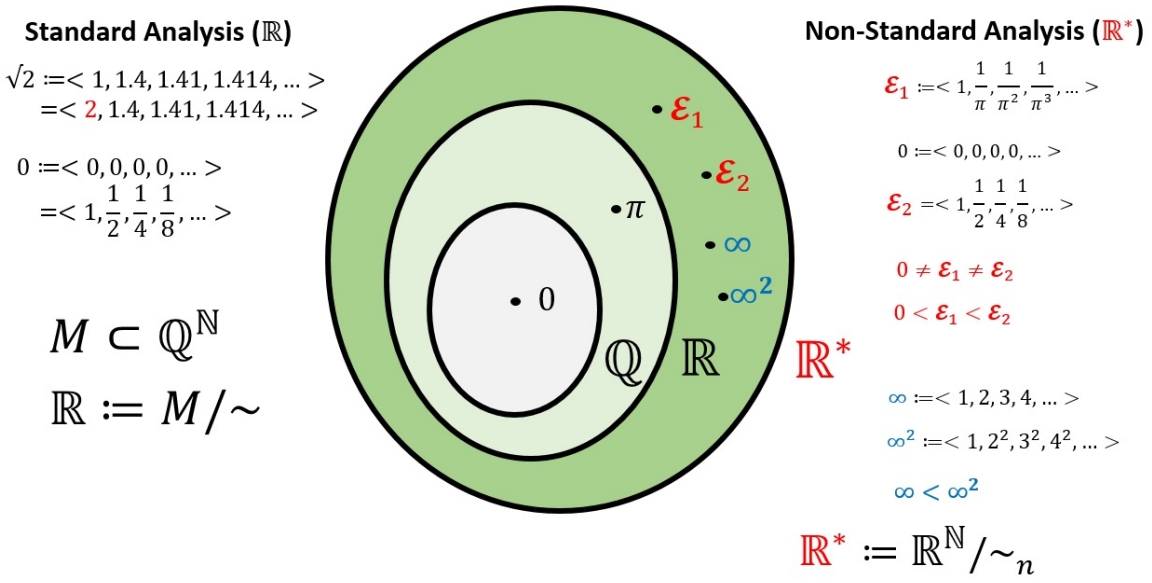

Figure 2.3: Hyperreal diagram.

In this section, the notation of Nonstandard Analysis (NSA) introduced in [6] is used.

NSA is motivated from the Cantor's construction of the reals, $\mathbb{R}$, from the rational numbers, $\mathbb{Q}$, by taking the equivalence classes of the space of rational valued Cauchy sequences. The equivalence relation was defined such that two rational Cauchy sequences are equal if and only if the difference sequence of two rational Cauchy sequences is converging to zero. Similarly, NSA defines a proper extension to the real space, $\mathbb{R}$, via the set of real-valued sequences, $\mathbb{R}^N$. The main difference between Cantor's extension and the extended reals in NSA is that NSA does not identify two sequences with its limit points but rather it distinguishes two sequences which converge to the same limit point by comparing the number of agreement indexes of two sequences. If the number of agreement indexes is *large enough*, then two sequences are equal, otherwise two sequences are different. The concept of large enough agreement indexes is properly defined by the *filter* concept in set theory. As a result, NSA introduces many distinct sequences converging to zero with different rates of convergence, where each sequence is called as an *infinitesimal*. The key feature is that the infinitesimal proposed by Cauchy and Leibniz can now be formally defined as an element in the extended real space. In addition, the extended real space contains diverging sequences which may correspond to positive infinity or negative infinity. Two diverging sequences are also distinguished by the rate of divergence after properly comparing the number of agreement indexes of two sequences. The summary of the difference between the standard analysis and NSA is shown in Figure 2.3, where ϵ_1 and ϵ_2 are both infinitesimal but not equal. In the standard analysis both sequences are identified with 0. Also, two different infinities are shown in Figure 2.3 where the two can be distinguished using the ordering property. The formal construction is reviewed in this section with more details.

In addition, NSA was also used in the control theory, e.g. an optimal control problem in stochastic systems with Brownian motion in [56]. The construction of Brownian motion is very clear in the hyperreal space since the Brownian motion can be viewed as an infinitesimal random walk where the infinitesimal is a well defined element in NSA. Furthermore, NSA is used in singular perturbation analysis for slow and fast systems due to its obvious

advantage in using the infinitesimal calculus. See [57] for its use in the feedback control of slow and fast feedback model, and [58] for its use in rigorously analyzing the Canard phenomenon in the bifurcation of slow and fast systems. Also see [59] for the peaking phenomenon in NSA framework, and general intuition of the usage of NSA to control theory. In addition, the author in [60] has also considered the pointwise evaluation of the singular function for the initial value problem of impulsive ordinary differential equations where the jump occurs an infinitesimal time after the initial time.

However, the hyperreals, the extended reals in NSA, are not the minimal extension of the reals, which include many redundant infinitesimals to represent the generalized functions. The redundancy of infinitesimals prevents the space from having a constructive property such as having a countable basis which generates the the whole hyperreals as a vector space over a field, $\mathbb{R}$. Therefore, in this thesis, a countably infinite basis is constructed, which generates not the whole space but the reduced extension of reals, denoted as $\mathbb{K}$, which is a proper extension of the reals but not equal to the hyperreals. A new generalized function on $\mathbb{K}$ is the proposed, which still distinguishes H^n and H but has a more algebraically constructed setup. Two function can also be different not only by comparing the shape in microscopic view near infinitesimals but also by defining on a different basis in $\mathbb{K}$.

Hyperreals

Let $\mathcal{P}(\mathbb{N})$ be the power set on $\mathbb{N}$. A *filter* on $\mathbb{R}^{\mathbb{N}}$ is a nonempty collection of $\mathcal{F} \subset \mathcal{P}(\mathbb{N})$ which satisfies the first two axioms.

- If $A, B \in \mathcal{F}$, then $A \cap B \in \mathcal{F}$
- If $A \in \mathcal{F}$ and $A \subset B \subset \mathbb{N}$, then $B \in \mathcal{F}$
- For any $A \subset \mathbb{N}$, either $A \in \mathcal{F}$ or $A^c \in \mathcal{F}$

A proper filter is a filter, $\mathcal{F}$, which does not include an empty set, $\emptyset$. By using the second axiom, it can be shown that $\mathcal{F} = \mathcal{P}(\mathbb{N})$ holds if and only if $\emptyset$ is in $\mathcal{F}$ by the second axiom.

An *ultrafilter* is a proper filter which also satisfies the last axiom. An ultrafilter defined by $\mathcal{F} := \{A \in \mathcal{P}(\mathbb{N}) : i \in A\}$ for some $i \in \mathbb{N}$ is called a *principal ultrafilter* generated by i. Observe that a nonprincipal ultrafilter must contain all cofinite filters which are defined by $\{A \in \mathcal{P}(\mathbb{N}) : A^c \text{ is finite}\}$ otherwise it will be a principal ultrafilter.

Proposition 1 ([6])**.** *Any infinite set has a nonprincipal ultralfilter on it.*

Proof. See the Corollary $2.6.2$ in [6]. □

The existence of the nonprincipal ultrafilter is a necessary part for the construction of the extended real space. Therefore, the filter mentioned in this article will refer to a nonprincipal ultrafilter.

In addition, it can be shown that the equivalence relation $\cong$ on $\mathbb{R}^{\mathbb{N}}$,

$$\{r_n\}_n \sim \{s_n\}_n \text{ if and only if } \{n \in \mathbb{N} : r_n = s_n\} \in \mathcal{F} \tag{2.33}$$

is well defined where $\mathcal{F}$ is the nonprincipal ultrafilter on $\mathbb{N}$, and $\{r_n\}_n$ and $\{s_n\}_n$ are in $\mathbb{R}^{\mathbb{N}}$. The two axioms of the filter validate the transitive relation condition for equivalence. The rough idea that two sequences coincide on large enough indexes is now translated into the rigorous statement that the set of agreement indexes should be in the nonprincipal ultrafilter. As mentioned before, all cofinite sets are in the nonprincipal ultrafilter, and so if two sequences are equal for infinitely many indexes then two sequences are belong to the same equivalence class. Let the equivalence class of a sequence $\{r_n\}_n \in \mathbb{R}^{\mathbb{N}}$ be denoted as $\langle r \rangle$ or $\langle r_n \rangle$.

Definition 1. *The quotient set* ${}^*\mathbb{R} \coloneqq \{\langle r \rangle : \{r_n\}_n \in \mathbb{R}^{\mathbb{N}}\}$ *is called the extended real space or* hyperreal space*, and the members of* ${}^*\mathbb{R}$ *are called* hyperreal numbers*.*

Since $\mathbb{R}^{\mathbb{N}}$ can have a sequence with repeated elements, the real space $\mathbb{R}$ is a proper subspace of ${}^*\mathbb{R}$. Furthermore, ${}^*\mathbb{R}$ is endowed with algebraic structure by defining addition

and multiplication for $\langle r\rangle, \langle s\rangle \in {}^*\mathbb{R}$ with

$$\langle r\rangle + \langle s\rangle = \langle r_n + s_n\rangle \tag{2.34}$$

$$\langle r\rangle \cdot \langle s\rangle = \langle r_n \cdot s_n\rangle \tag{2.35}$$

and an order relation, $<$, by

$$\langle r\rangle < \langle s\rangle \text{ if and only if } \{n \in \mathbb{N} : r_n < s_n\} \in \mathcal{F}. \tag{2.36}$$

The algebraic structure of ${}^*\mathbb{R}$ enables to show that ${}^*\mathbb{R}$ is the ordered field.

Theorem 2 (Hyperreal space as a ordered field)**.** *The hyperreal space,* $({}^*\mathbb{R}, +, \cdot, <)$*, is an ordered field with zero* $\langle 0\rangle$ *and unity* $\langle 1\rangle$

Proof. See Theorem $3.6.1$ in [6]. □

One of the strong benefits of having an extended real space is that now there exist elements which are infinitesimally small and also there exist unbounded numbers.

Definition 2 (Infinitesimal, limited, and unlimited number)**.** *An element* $\langle \epsilon_n\rangle \in {}^*\mathbb{R}$ *is called* infinitesimal *if* $A = \{n \in \mathbb{N} : |\epsilon_n| < r\}$ *is cofinite for any positive real* $r \in \mathbb{R}^+$*, and* $\langle 0\rangle < \langle |\epsilon_n|\rangle$*. An element* $b := \langle b_n\rangle$ *is* limited *if there exist* $M > 0$ *such that* $\langle |b_n|\rangle < \langle M\rangle$*. An element* $\langle E_n\rangle \in {}^*\mathbb{R}$ *is called* unlimited *if* $\langle |E_n|\rangle > \langle r\rangle$ *for any* $r \in \mathbb{R}$*.*

For example, $\langle 1/n\rangle$ is an infinitesimal since for any positive real number r there exist $N \in \mathbb{N}$ such that if $n > N$, then $1/n < r$. Similarly, any converging sequence which has its limit point at 0 can be regarded as an infinitesimal element in ${}^*\mathbb{R}$, and so there exist uncountably many infinitesimals in ${}^*\mathbb{R}$.

In addition, there are two more important definitions for particular subsets of ${}^*\mathbb{R}$ which will be used in the next section.

Definition 3 (halo and shadow)**.** *Given a hyperreal number $b \in {}^*\mathbb{R}$, a subset $hal(b) \subset {}^*\mathbb{R}$ is called* halo *of b if $hal(b) = \{c \in {}^*\mathbb{R} : b - c$ is infinitesimal$\}$, and $c \in \mathbb{R}$ is called a* shadow *of b if $b - c$ is infinitesimal, and we denote it as $sh(b)$.*

By the definition, $hal(0)$ is a set of infinitesimals, and if $sh(b)$ exist for some $b \in {}^*\mathbb{R}$, then $sh(c) = sh(b)$ for all $c \in hal(b)$. Let $\mathbb{L} \subset {}^*\mathbb{R}$ be a set of limited hyperreals, then there exists a shadow point, $sh(b)$, at any given hyperreal $b \in \mathbb{L}$, and this point can be uniquely defined.

2.3 Preliminary Notions of Basic Operators

Four basic operators are defined, and their commutative properties are summarized, which were first introduced in [61].

Definition 4 (Evaluation functional)**.** *A functional, $\sigma_t : \mathbb{R}^{\mathbb{R}} \to \mathbb{R}$ is called an evaluation functional at time $t \in \mathbb{R}$ if $\sigma_t(x) = x(t)$ for every function $x \in \mathbb{R}^{\mathbb{R}}$.*

By using the evaluation functional, a translation operator and a scaling operator on an arbitrary function are also defined.

Definition 5 (Translation operator and scaling operator)**.** *Let $\alpha \in \mathbb{R}$ be a fixed constant. Operators, $T_\alpha : \mathbb{R}^{\mathbb{R}} \to \mathbb{R}^{\mathbb{R}}$ and $S_\alpha : \mathbb{R}^{\mathbb{R}} \to \mathbb{R}^{\mathbb{R}}$, are called translation and scaling operators which shifts and factor α, respectively, if $\sigma_t(T_\alpha x) = \sigma_{t-\alpha}(x)$ and $\sigma_t(S_\alpha x) = \sigma_{\alpha t}x$ for $\forall x \in \mathbb{R}^{\mathbb{R}}$ and $\forall t \in \mathbb{R}$.*

The right limit of the derivative operator introduced by Ulysse Dini is also defined. See the extension of Dini operator in [62]. The following definition uses the evaluation and translation operators.

Definition 6 (Differential operator)**.** *An operator, $D : D^1(\mathbb{R}) \to D^1(\mathbb{R})$ is denoted as* right derivative *operator with right limit, if $\sigma_t(Dx) = \sigma_t(\lim_{s \underset{>}{\to} 0}(T_{-s}x - x)/s)$ for $\forall x \in D^1(\mathbb{R})$ and $\forall t \in \mathbb{R}$.*

The next Lemma shows the commutation of these operators. Fix $\alpha, \beta \in \mathbb{R}$ to be a constant.

Lemma 2. *(a)* $S_\alpha \circ S_\beta = S_\beta \circ S_\alpha = S_{\alpha\beta}$

(b) $T_\alpha \circ T_\beta = T_\beta \circ T_\alpha = T_{\alpha+\beta}$

(c) $S_\alpha \circ T_\beta = T_{\frac{\beta}{\alpha}} \circ S_\alpha$

(d) $D \circ S_\alpha = \alpha S_\alpha \circ D$

Proof. The proofs are immediate from the definition. □

In the following chapter, the basic operators are used to notationally simplify the geometric sequences, which plays a fundamental role in defining the extended real spaces embedded in the hypererals. Furthermore, a new generalized function is defined on the extended real space using the sequence of the above basic operators in Definition 4 and Definition 5. A new singular function is then generalized by using the sequence of Dini operators acting on a function composed of the scaling and translation operators. The principles in Lemma 2 is used to define the generalized derivatives for the new generalized functions properly. Note that, especially, the evaluation operator seems to be obvious and redundant, but it helps to understand what a point-wise defined function means in the new generalized function theory.

CHAPTER 3

KRYLOV GENERALIZED FUNCTION THEORY

This chapter develops two key contributions for (1) constructing a new countably infinite-dimensional subspace of ${}^*\mathbb{R}$, and (2) introducing a new generalized function on the proposed space. The advantage of having a hyperreal space is to capture more details than standard $\mathbb{R}$ space by introducing the infinitesimals and unlimited numbers. However, a function defined on the hyperreal space should also be evaluated at every point, infinitesimally separated from all real values, and so the constructive way to point-wise define a generalized function on hyperreal space is not practical. Therefore, in § 3.1, a new extended real space is proposed, which can be decomposed into the real part and infinitesimal parts with a countably infinite basis depending on the convergence rate. This space is denoted as a *Krylov space*. The name is inspired by the Krylov subspace method in numerical linear algebra since a successive composition of scaling operators is required to generate the space. More precise definition and useful theorems will be shown in § 3.1.

In § 3.2, a new generalized function defined on the Krylov space is proposed, and in § 3.2.1, a non-classical sampling method is introduced by using the shadow operation in Definition 3 to map a proposed hyperreal valued function to a real valued function. A geometric interpretation of this function and the sampling process is also analyzed. In § 3.2.2, a fundamental shape of the discontinuous function in the infinitesimal space is introduced which plays a key role on the *continuization* of the discontinuous function in Krylov space. Roughly speaking, the fundamental shape represents the evaluation of the discontinuous function at each point infinitesimally away from the discontinuity, which smoothly connects the left limit and the right limit of the function in infinitesimal time. In addition, a bump shape function which represents the infinitesimal changes for absolutely continuous function is also considered. A rigorous definition and detailed analysis can be found in

the following subsections. In § 3.2.3 and 3.2.4, a set of Heaviside functions generated by a different continuization process is proposed, and used to construct a general piecewise continuous function on Krylov space. In § 3.2.5 and 3.2.6 an extended differential and integration of the new generalized function is proposed, and it is used to generate singular delta functions on the Krylov space in 3.2.8.

3.1 Krylov Hyperreal Space

First, pick $\alpha > 1$. The basic concepts are defined as follows.

Definition 7. *($\mathbb{K}_i$-sequence and $\mathbb{K}_i$ space)*
Given $i \in \mathbb{Z}$. A sequence $\langle r_n \rangle \in {}^*\mathbb{R}$ is called a $\mathbb{K}_i$-sequence if there exist $s \in \mathbb{R}$ such that $r_n = s(1/\alpha^i)^n$ for all $n \in \mathbb{N}$. Furthermore, a subset $\{x \in {}^*\mathbb{R} | x$ is a $\mathbb{K}_i$-sequence$\}$, is called $\mathbb{K}_i$ space.

Let $x \in \mathbb{K}_i$, then, by using the $\langle \cdot ; \cdot \rangle$ notation to represent a geometric sequence, there exist $s \in \mathbb{R}$ such that $x = \langle (1/\alpha)^i ; s \rangle$. In the rest of the thesis, this notation is used to represent Krylov sequences.

Observe that each $\mathbb{K}_i$ space forms one dimensional vector space over $\mathbb{R}$ and has the following properties.

Proposition 2. *$\mathbb{K}_i \subset hal(0)$ for all $i \in \mathbb{N}\backslash\{0\}$ and $\mathbb{K}_0$ is identified with $\mathbb{R}$.*

Proof. Let $i = 0$. If $x \in \mathbb{K}_i$ then $x = \langle 1; s \rangle$ for some $s \in \mathbb{R}$ so $\mathbb{K}_0 \subset \mathbb{R}$. The other inclusion is obvious. Now pick $i \in \mathbb{N}\backslash\{0\}$. Let $x \in \mathbb{K}_i$ then there exist $s \in \mathbb{R}$ such that $x - 0 = \langle (1/\alpha)^i ; s \rangle$ and since $\alpha > 1$, $x - 0$ is an infinitesimal and so $x \in hal(0)$ □

Since each $\mathbb{K}_i$ is spanned by one basis vector, we define the element, $e_i = \left\langle (\frac{1}{\alpha})^i ; 1 \right\rangle$, as an *i-th Krylov basis* vector.

Lemma 3. *$e_i \cdot e_j = e_{i+j}$ for all $i, j \in \mathbb{Z}$ with product defined in (2.35).*

Proof. Pick i and j in $\mathbb{Z}$, then $e_i = \langle (1/\alpha)^i; 1\rangle$ and $e_j = \langle (1/\alpha)^j; 1\rangle$. By using the sequence multiplication in the hyppereals, $e_i \cdot e_j = \left\langle 1, (1/\alpha)^{i+j}, (1/\alpha)^{2(i+j)}, \cdots \right\rangle = e_{i+j}$ holds. $\square$

A space generated by a set of Krylov basis vectors $\{e_i\}_{i=0}^N$ is then considered.

Definition 8. *($\mathbb{K}^N$ space)*
A set $\mathbb{K}^N = \{x \in {}^*\mathbb{R} | x = \sum_{i=0}^N s_i \cdot e_i$ where $\{s_i\}_{i=0}^N \subset \mathbb{R}\}$ with addition is called $\mathbb{K}^N$ space where $N \in \mathbb{N}$.

This space can also be written as $\oplus_{i=0}^N \mathbb{K}_i$ where $\oplus$ is a direct sum. By the definition of the $\mathbb{K}^N$ space, it can be shown that $e_i \in \mathbb{K}_i \subset \mathbb{K}^i$, and $\mathbb{K}^{i-1} \subset \mathbb{K}^i$ for all $i \in \{1, \cdots, N\}$. Therefore, $e_i \in \mathbb{K}^N$ for all $i \in \{0, \cdots, N\}$. The next Proposition shows that $\{e_i\}_{i=0}^N$ forms a basis for $\mathbb{K}^N$ space.

Proposition 3. *$\{e_i\}_{i=0}^N$ are linearly independent in $\mathbb{K}^N$.*

Proof. Suppose that $\{e_i\}_{i=0}^N$ are linearly dependent then there exist $\{s_i\}_{i=0}^N \subset \mathbb{R}$ such that $\sum_{i=0}^N s_i \cdot e_i = 0$ and $s_j \neq 0$ for some j. In addition, for large $M \in \mathbb{N}$, we can choose N elements in the sequence such that $VS = 0$ where

$$V = \begin{pmatrix} 1 & 1 & \cdots & 1 \\ \frac{1}{\alpha}^M & (\frac{1}{\alpha})^{2M} & \cdots & (\frac{1}{\alpha})^{NM} \\ \vdots & \vdots & \ddots & \vdots \\ (\frac{1}{\alpha})^{NM} & (\frac{1}{\alpha})^{2NM} & \cdots & (\frac{1}{\alpha})^{N^2M} \end{pmatrix}, S = \begin{pmatrix} s_1 \\ \vdots \\ s_N \end{pmatrix}.$$

Since V is a Vandermonde matrix and $\{(1/\alpha)^i\}_i$ are all distinct values, V is invertible and so $s_j = 0$. This gives a contradiction. $\square$

However, the space $\mathbb{K}^N$ is not closed under the multiplication since $e_N \cdot e_N = e_{2N}$ which is not in $\mathbb{K}^N$. Next, the space which contains all $\mathbb{K}_N$ sequences is introduced.

Definition 9. *($\mathbb{K}$ space)*

A set $\mathbb{K} = \{x \in {}^*\mathbb{R} | x = \sum_{i=0}^{\infty} s_i \cdot e_i$ where $\{s_i\}_{i=0}^{\infty} \in l_1\}$ is called a Krylov hyperreal space where l_1 is a space of absolutely summable real valued sequence.

The space $\mathbb{K}$ is a well defined space. Let $\langle x_n \rangle \in \mathbb{K}$ then $x_n = \sum_{i=0}^{\infty} s_i/\alpha^{ni}$ and so $x_n \leq \sum_{i=0}^{\infty} |s_i| < \infty$ for all n since $\alpha > 1$ and $\{s_i\}_i$ is in l_1. In addition, $\mathbb{K}$ is a vector space over $\mathbb{R}$ since l_1 is a vector space over the same field. Furthermore, by Lemma 3, and the fact that $l_1 \subset l_\infty$ in Proposition 6.11 of [63], one can easily check that $\mathbb{K}$ is an algebra, which means that if t_1^* and t_2^* are in $\mathbb{K}$, then $t_1^* t_2^*$ are also in $\mathbb{K}$. Therefore, the space is closed under multiplication, and $\mathbb{K}$ is a commutative ring. The infinite summation of infinitesimals with l_1 coefficient has been shown to be also infinitesimal in [64].

In addition, $\mathbb{K}$ is a unique factorization domain as a consequence of the Problem 11.2.10 in [65]. One conjecture is that the further generalization on $\mathbb{K}$ by including unlimited elements such as $e_{-i} := \langle \alpha^i; 1 \rangle$ for $i > 0$ will render the space a subfield of ${}^*\mathbb{R}$. This is left as a conjecture since it is not required in the application to the impulsive system modeling. The codomain of the hyperreal functions proposed in the next subsection will be the whole hyperreal space, ${}^*\mathbb{R}$, and the domain will be in $\mathbb{K}$. Therefore, division of two functions is still well defined in the whole space, ${}^*\mathbb{R}$. To motivate more on the generalized $\mathbb{K}$ for further interest, the basic idea of the proving the generalized $\mathbb{K}$ to be a subfield will be similar to showing that the ring of formal Laurent series over a field is a field.

Proposition 4. *If $t^* \in \mathbb{K}$, then the representation with $\{s_i\}_{i=0}^{\infty}$ is unique up to its equivalence in ${}^*\mathbb{R}$. See the equivalence relation in (2.33).*

Proof. We have seen that the series $\sum_{i=0}^{\infty} s_i \cdot e_i$ is element-wise convergent in ${}^*\mathbb{R}$ since $\{s_i\}_i \in l_1$. Therefore, it is sufficient to show that such representation is unique. Pick $x \in \mathbb{K}$. Suppose there exist $\{a_i\}_i$ and $\{b_i\}_i \in l_1$ such that $x = \sum_{i=0}^{\infty} a_i \cdot e_i = \sum_{i=0}^{\infty} b_i \cdot e_i$. Let $c_i = a_i - b_i$ for all i then $\{c_i\}_i$ is also in l_1. By the definition of equality, a set $B := \{n \in \mathbb{N} | \sum_{i=0}^{\infty} c_i/\alpha^{ni} = 0\}$ is contained in the nonprincipal ultrafilter. Therefore, the set contains a monotonically increasing sequence $n_k \subset \mathbb{N}$. Suppose that $\{a_i\}_i \neq \{b_i\}_i$,

then there exist $M \in \mathbb{N}$ such that $a_M \neq b_M$. This shows that $c_M \neq 0$, and so

$$c_M = -\sum_{i=0}^{M-1} c_i \alpha^{n_k(M-i)} - \sum_{i=M+1}^{\infty} c_i \alpha^{-n_k(i-M)}$$

for all k. Let $A := |\sum_{i=M+1}^{\infty} c_i \alpha^{-n_k(i-M)}|$, then by the triangular inequality, we have

$$|c_M + \sum_{i=0}^{M-1} c_i \alpha^{n_k(M-i)}| \leq A \leq \sum_{i=M+1}^{\infty} |c_i \alpha^{-n_k(i-M)}| \leq \sum_{i=M+1}^{\infty} |c_i| < \infty,$$

for all k. Since $\alpha > 1$ and the above is true for all monotonically increasing $\{n_k\}_k$, it holds that $c_i = 0$ for all i from 0 to $M-1$, and so $0 < |c_M| \leq A$. Now, suppose there exist another $M_1 > M$ such that $c_{M_1} \neq 0$, then, by the same reasoning, $c_M = 0$. This gives a contradiction, and so $c_j = 0$ for all $j > M$, which leads to the conclusion that $\sum_{i=0}^{\infty} c_i \frac{1}{\alpha^{ni}} = c_M/\alpha^{nM} \neq 0$ for all n. This gives a contradiction since B is in the nonprincipal ultrafilter. Hence, $\{a_i\}_{i=0}^{\infty} = \{b_i\}_{i=0}^{\infty}$. □

By having the unique representation of the Krylov hyperreals, the space can be identified as a countably infinite dimensional space. For example, suppose that $t^* \in \mathbb{K}$ is given such that $t^* = s_0 e_0 + s_1 e_1$ for some $s_0, s_1 \in \mathbb{R}$. Since e_1 is in $\mathbb{K}_1$, by Proposition 2, e_1 is an infinitesimal, and so $sh(t^*) = s_0$ for all $s_1 \in \mathbb{R}$. Proposition 3 states that e_0 and e_1 are independent, which gives an algebraic structure of the Krylov hyperreal space. Similarly, if $t^* = s_0 e_0 + \sum_{i=1}^{N} s_i e_i$ for $N \in \mathbb{N}$ and $\{s_i\}_{i=0}^{N} \subset \mathbb{R}$, then the shadow of t^* is still infinitesimal apart from s_0, and so $sh(t^*) = s_0$. By following Proposition 3, $\mathbb{K}^N$ can be identified with $\mathbb{R}^N$, and so any finite dimensional vector space is isomorphic to a subspace of $\mathbb{K}$.

The Krylov space diagram in Figure 3.1 shows the graphical set inclusion representation compared to the hypperreal diagram in Figure 2.3. There exist elements in the hyperreal such that are not in the Krylov space but the Krylov space is still *large enough* to include the real numbers with structured infinitesimals. The Krylov sequences, e_i, are independent of each other, and the ordering property shows that e_j gets closer to 0 as j increases, which

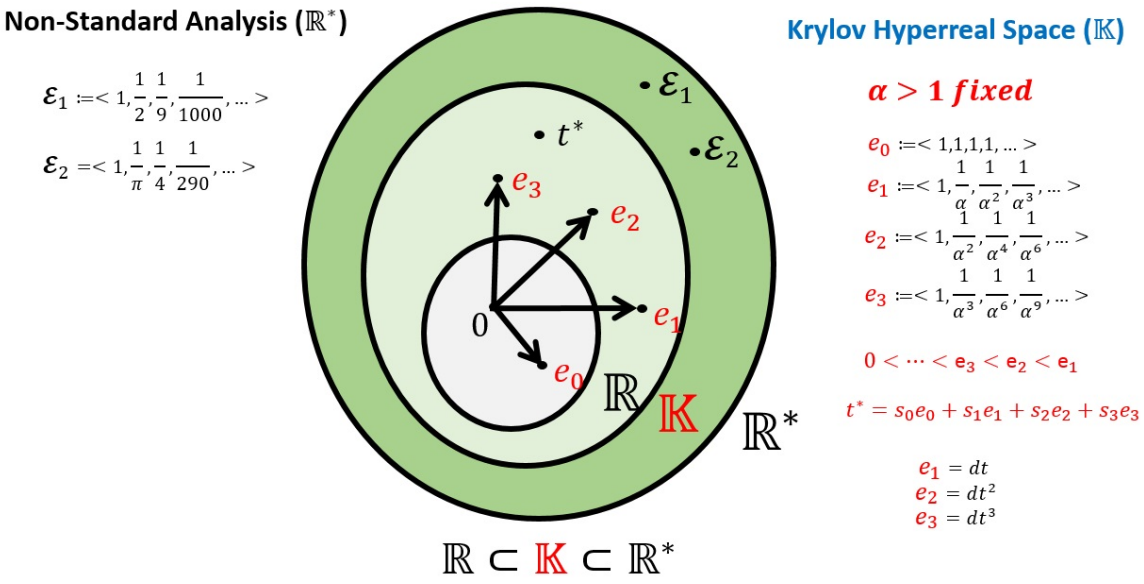

Figure 3.1: Krylov Space diagram.

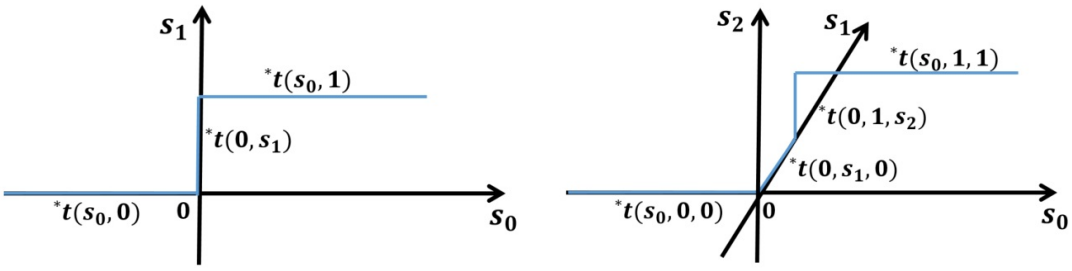

(a) s_0 and s_1 time line

(b) s_0, s_1 and s_2 insensible time line

Figure 3.2: Geometric interpretation of sensible and insensible time

inspires the rate of convergence in the following definitions.

3.1.1 Geometric Interpretations

In system theoretic modeling, functions of time are an ubiquitous concept. Here the usual time is extended.

Definition 10. *(Insensible and sensible time) Given a $t^* \in \mathbb{K}$ with a representation, $\{s_i\}_i \in l_1$. The component s_0 is called* sensible *time of t^*, and s_i is called* insensible *time of t^* with $1/\alpha^i$ as a* rate of convergence.

A geometric interpretation of the insensible time line is shown for the example where

$t^* = s_0 e_0 + s_1 e_1$ in Figure 3.2. The axis of s_0 represents the sensible time line of $\mathbb{R}$, and the other axes of s_1 and s_2 represent the insensible time line. By taking the shadow operation, one can project t^* to its corresponding sensible time, s_0. An example in Figure 3.2a shows that $t^* = 0 \cdot e_0 + s_1 e_1$ with $s_1 \in [0, 1]$ can be identified with the blue line with ${}^*t(0, s_1)$ labels on s_1 axis, and $t^* = s_0 e_0 + 1 e_1$ with $s_0 \in [0, \infty)$ can be identified with the blue line with ${}^*t(s_0, 1)$ label. The change, ${}^*t(0, s_1)$, in s_1 axis is orthogonal to s_0 axis, which shows the infinitesimal changes from its shadow point, 0, on the sensible time line. An example of a further extended insensible time with faster rate of convergence is shown in Figure 3.2b. Both directions in s_1 and s_2 axes are orthogonal to the sensible time line, and so the change only amounts to an infinitesimal difference from its shadow point. This algebraically extended insensible time line is used to give a non unique definition for a Heaviside function, which plays a crucial role in finding the causal representation of impulsive effect systems.

3.2 Krylov Functions

Symbol	Description
σ_t	Evaluation operator (Definition 4)
S_α	Scaling operator (Definition 5)
T_β	Translation operator (Definition 5)

Table 3.1: Summary of basic operators

In the rest of Section 3.2, a generalized function is defined on the Krylov space, $\mathbb{K}$. The basic operators frequently used in the following sections are recapitulated in Table 3.1. First, the general hyperreal valued function on ${}^*\mathbb{R}$ is defined, and it is narrowed down to its restriction to $\mathbb{K}$.

Definition 11. *(Hyperreal function and Krylov function)*
A mapping $F : {}^*\mathbb{R} \to {}^*\mathbb{R}$ is called a hyperreal valued function. If there exist a sequence of functions, $\{f_n\}_n \subset \mathbb{R}^{\mathbb{R}}$, such that $\sigma_{t^*} F \stackrel{\text{def}}{=} \langle f_n(t_n) \rangle$ where $t^* \in {}^*\mathbb{R}$ and $t^* = \langle t_n \rangle$. The hyperreal valued function is written as $F := \langle f_n \rangle$. In addition, the restriction of F to the Krylov space, $\mathbb{K}$, is called a Krylov function.

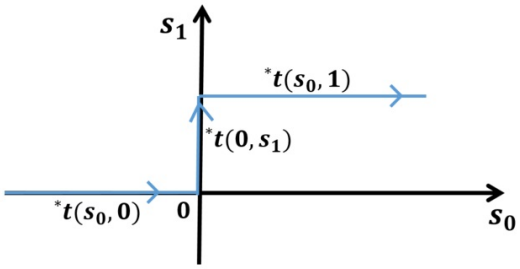

(a) s_0 and s_1 directed time line

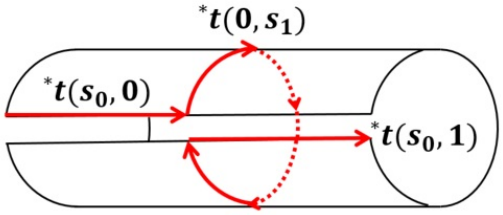

(b) Cylindrical representation of s_0 and s_1 directed time line

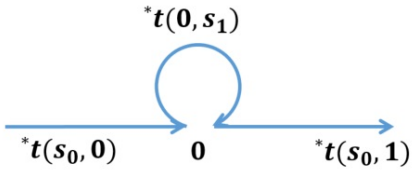

(c) s_0 and s_1 extended time line

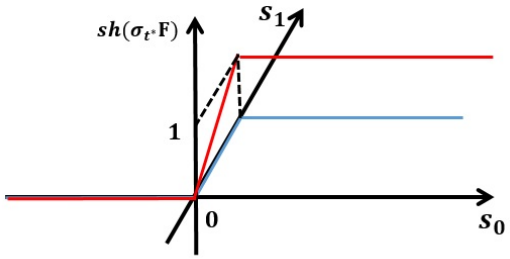

(d) Krylov function on (s_0, s_1) space

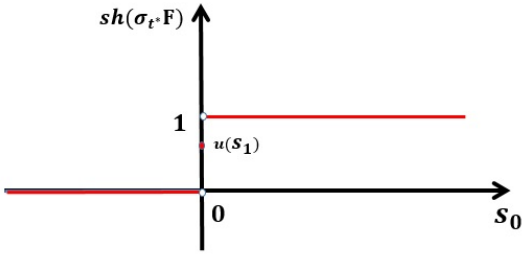

(e) $\mathbb{R}$- sampled Krylov function

Figure 3.3: Geometric interpretation of extended time, and Krylov Heaviside function

The new evaluation operator σ_{t^*} is denoted as a *hyperreal evaluation*. The set of hyperreal functions includes the usual extended function in nonstandard analysis since any repeated sequence $\{f_n\}_n$ where $f_n = f$ for all n can generate the extended function. Suppose that f is continuous and $t^* \in \mathbb{K}$, then the evaluation of the function F, $\sigma_{t^*}F = \langle f(t_n)\rangle$, is a limited sequence. By using the fact that every limited sequence has a shadow point, it can be shown that the shadow evaluation of F, $sh(\sigma_{t^*}F)$, at $t^* \in hal(s)$ is equal to $f(s)$, and this is true for all $s \in \mathbb{R}$.

3.2.1 Sampling of Krylov Functions

In this section, we introduce the method of restricting a Krylov function into the corresponding real valued function.

Definition 12. *($\mathbb{R}$-sampling)*
Given a Krylov function $F : \mathbb{K} \to {}^*\mathbb{R}$ generated by a pointwise convergent sequence of continuous functions, a mapping $f : \mathbb{R} \to \mathbb{R}$ is called $\mathbb{R}$-sampled function of F if, for any given $s_0 \in \mathbb{R}$, the evaluation $f(s_0)$ is equal to $sh(\sigma_{t^*}F)$ for some $t^* \in \mathbb{K} \cap hal(s_0)$.

Here is an example for the $\mathbb{R}$-sampled Krylov function: Let $u(t) = t\chi_{[0,1]}(t) + \chi_{[1,\infty)}(t)$ where χ is a characteristic function. Recall that S_{α^n} is a scaling operator with a scale α^n. See the definition of scaling operator in Section 2.3. Now define a Krylov function as $F = \langle S_{\alpha^n} u \rangle$ for some $\alpha > 1$. The $\mathbb{R}$-sampled function f of F can be characterized by an evaluation of $sh(\sigma_{t^*}F)$ where $t^* \in \mathbb{K}$. Let $\{s_i\} \in l_1$ be the representation of t^*. By expanding this Krylov Hyperreal number, $t^* = s_0 \cdot e_0 + \sum_{i=1}^{\infty} s_i \cdot e_i$,

$$\sigma_{t^*}F = \left\langle u(\alpha^n s_0 + s_1 + \sum_{i=2}^{\infty} s_i/\alpha^{n(i-1)}) \right\rangle$$

holds. Since $\alpha > 1$, the evaluation at each time depends on the s_0 values. If $s_0 < 0$, then there exists a big $N > 0$ such that if $n > N$, then $\alpha^n s_0 + s_1 + \sum_{i=2}^{\infty} s_i/\alpha^{n(i-1)} < 0$ and so, by the definition of u,

$$\sigma_{t^*}F = \langle 0 \rangle$$

holds. Similarly, for $s_0 > 0$, it is obvious that

$$\sigma_{t^*}F = \langle 1 \rangle$$

holds. In the case when $s_0 = 0$, by the direct computation,

$$\sigma_{t^*}F = \left\langle u(s_1 + \sum_{i=2}^{\infty} s_i/\alpha^{n(i-1)}) \right\rangle$$

holds. Since $\langle s_i \rangle_i \in l_1$ and u is a continuous function, the sequence $\sigma_{t^*}F$ and $\langle u(s_1) \rangle$ has an infinitesimal difference. In other words, there exists a $\mathbb{R}$-sampled function f defined as follows,

$$f(s_0) = sh(\sigma_{t^*}F) = \begin{cases} 0 & s_0 < 0 \\ u(s_1) & s_0 = 0 \\ 1 & s_0 > 0 \end{cases} \tag{3.1}$$

This $\mathbb{R}$-sampled function f is not unique since $f(0)$ can take any value of $u(s_1) \in [0, 1]$. However, all the $\mathbb{R}-$sampled functions are equal almost everywhere to the point wise convergent limit, $\lim_{n\to\infty} S_{\alpha^n} u$, which is the Heaviside function.

Geometric views of this example are given in Figure 3.3d and Figure 3.3e. The extended Heaviside function is *continuously* connected from 0 to 1 in a first insensible time line s_1 as shown in Figure 3.3d. The shape of the connection is a ramp function, u, which was chosen in the example. Once it processes through the $\mathbb{R}-$ sampling of the Krylov function F, the usual Heaviside function is obtained with a point value different at 0 in the sensible time. Figure 3.3e shows the sampled Krylov function.

Conversely, starting from a discontinuous Heaviside function in sensible time, the function can be extended by a continuous connection from 0 to 1 in the insensible time defined on $\mathbb{K}$. For example, define a topological space, $\mathbb{R} \times [0, 1]$, by using the product topology. This is the space where each sensible time in $\mathbb{R}$ extends to $[0, 1]$ in its insensible direction (s_1-axis). The geometric shape of this space is cylindrical as shown in Figure 3.3b. The red curve on this cylinder is now called an *extended time*. The topology on the extended time can also be induced by the subspace topology from the original space, $\mathbb{R} \times [0, 1]$. The continuization of the discontinuous function can be well defined on the extended time

line using the subspace topology, which is graphically shown in Figure 3.3d. Equivalently, the cylindrical representation of the extended time can be viewed in two dimensional space with a circle attached to a point at 0, which is illustrated in Figure 3.3c. Therefore, the reverse procedure of $\mathbb{R}$-sampling can be interpreted as an interpolation process at 0 in sensible time within the insensible time of $[0, 1]$. The generalized extended time can be taken as a curve in $\mathbb{R} \times [0, 1]^{\mathbb{N}}$.

Interestingly, a geometric point of view of the continuization in the hybrid system was also analyzed in [66] by using a gluing homeomorphism which basically identifies two disjoint points, $x(t_i-)$ with $x(t_i+)$. The main difference in the gluing method, and the Krylov based approach is that the Krylov approach defines the function more precisely in the insensible time, whereas the other method ignores the connection.

3.2.2 Shape Functions

Here, the space of shape functions is defined which characterizes continuous behavior at the discontinuity of the Heaviside function.

Definition 13. *(Shape function)*
A function $u \in C(\mathbb{R})$ is called a shape function if there exists a function $p \in C^1(\mathbb{R})$ where p is strictly monotonic in $[0, 1]$ such that $p(0) = 0$ and $p(1) = 1$, so that $u = \chi_{(0,1)}p + \chi_{[1,\infty)}$.

A typical example for the shape function is by choosing p as a monomial of t with a degree greater than or equal to one. In the previous example, a ramp was chosen, $p(t) = t$. Let U be the space of the shape functions then the multiplication operator is closed in U, and so any multiplication of shape functions is still a shape function.

3.2.3 Fundamental Krylov Operators

In this section, an extended scaling operator and an extended shifting operator acting on the Krylov function are introduced. Suppose that $\mathcal{F}^*$ is a set of Krylov functions.

Definition 14. *($S_{<\alpha;1>}$ and $T_{<\alpha;1>}$ operator)*
A mapping $S_{<a_n>} : \mathcal{F}^* \to \mathcal{F}^*$, where $\langle a_n \rangle \in \mathbb{K}$, is called a Krylov scaling operator if, given $F \in \mathcal{F}^*$ where $F = \langle f_n \rangle$, the evaluation of $S_{<a_n>}(F)$ is $\langle S_{a_n} f_n \rangle$. Similarly, a mapping $T_{<\tau_n>} : \mathcal{F}^* \to \mathcal{F}^*$, where $\langle \tau_n \rangle \in \mathbb{K}$, is called a Krylov shifting operator if, given $F \in \mathcal{F}^*$ where $F = \langle f_n \rangle$, the evaluation of $T_{<\tau_n>}(F)$ is $\langle T_{\tau_n} f_n \rangle$.

In the previous example, the ramp shape function $\langle u \rangle$ is defined as $u(t) = t\chi_{[0,1]}(t) + \chi_{[1,\infty)}(t)$, and the Krylov function is given by $F = \langle S_{\alpha^n} u \rangle$. By using the Krylov scaling operator, a compact expression of sequence of scaled function can be written as

$$F := S_{<\alpha;1>}(\langle u \rangle).$$

The next Proposition helps to construct further generalized piecewise continuous functions.

Proposition 5. *(a)* $S_{<\alpha;1>} \circ S_{<\beta;1>} = S_{<\alpha\beta;1>}$
(b) $S_{<\alpha;1>} \circ S_{<\beta;1>} = S_{<\beta;1>} \circ S_{<\alpha;1>}$
(c) $T_{<\gamma;\beta>} \circ S_{<\alpha;1>} = S_{<\alpha;1>} \circ T_{<\gamma\alpha;\beta>}$

Proof. (a) Pick $F = \langle f_n \rangle$ such that $F \in \mathcal{F}^*$. We have $S_{<\beta;1>}F = \langle S_{\beta^n} f_n \rangle$ and so $(S_{<\alpha;1>} \circ S_{<\beta;1>})F = \langle S_{\alpha^n}(S_{\beta^n} f_n) \rangle = \left\langle S_{(\alpha\beta)^n} f_n \right\rangle$. Therefore, $S_{<\alpha;1>} \circ S_{<\beta;1>}F = S_{<\alpha\beta;1>}F$.
(b) Since (a) is true, (b) follows.
(c) Pick $F = \langle f_n \rangle$ such that $F \in \mathcal{F}^*$. We have $S_{<\alpha;1>}F = \langle S_{\alpha^n} f_n \rangle$ and so $T_{<\gamma;\beta>} \circ S_{<\alpha;1>}F = \langle T_{\gamma^n\beta}(S_{\alpha^n} f_n) \rangle = \langle (S_{\alpha^n} \circ T_{\alpha^n\gamma^n\beta}) f_n \rangle = (S_{<\alpha;1>} \circ T_{<\alpha\gamma;\beta>})F$. Hence, $T_{<\gamma;\beta>} \circ S_{<\alpha;1>} = S_{<\alpha;1>} \circ T_{<\alpha\gamma;\beta>}$. □

3.2.4 Krylov Heaviside Functions

In this section, the generalized Heaviside function on the Krylov space is introduced using the shape function and the Krylov operators. Suppose that a shape function u is given, then by using the Krylov scaling operator, one can create a sequence of functions, $S_{<\alpha;1>}u$, where each function can be indexed by n, and as n goes to infinity the function converges

pointwise to the unit step function. Similarly, one can define another sequence of functions, $S_{<\alpha^2;1>}u$, with the same shape but with a faster scaling rate of α^2. It will be shown that two sequences of functions are both Krylov functions, and they are not equal in Krylov space but the $\mathbb{R}-$sampling of each function is the unit step function. This process is generalized by defining the Heaviside function as an element in the range of Krylov scaling operators where the domain was restricted to the shape space.

Definition 15. *(Krylov Heaviside function)*
A function $F \in \mathcal{F}^*$ is called a Krylov Heaviside *function if there exist a shape function u and $N \in \mathbb{Z}$ such that $F = S_{<\alpha^N;1>}u$. In addition, α^N is called a* rate *or* continuization rate *of F.*

Let $\mathbb{H}$ to be a set of all Krylov Heaviside functions and $H \in \mathbb{H}$.

Theorem 3. *$\mathbb{R}$-sampled function for all $H \in \mathbb{H}$ is the Heaviside function.*

Proof. Since H is a hyperreal function and the shape function u is continuous, $\sigma_{t^*}S_{\langle\alpha^N;1\rangle}u$ is limited and converges to $u(s_0)$ for $t^* = \sum_{i=0}^{\infty} s_i \cdot e_i$ where $\{s_i\} \in l_1$. If t^* is such that $sh(t^*) < 0$, then $sh(\sigma_{t^*}H)$ equals 0, and for the case when $sh(t^*) > 0$, $sh(\sigma_{t^*}H)$ equals 1. This confirms that for any shape function u, the $\mathbb{R}$-sampled function is the Heaviside function. □

Suppose that H_1 and H_2 are Krylov Heaviside functions that $H_1 = S_{<\alpha;1>}u$ and $H_2 = S_{<\alpha^2;1>}w$ where u and w are the shape functions, then a new Krylov Heaviside function can be defined by multiplying H_1 and H_2: $H = H_1H_2$. The direct evaluation of H at $t^* = s_0e_0 + s_1e_1 + s_2e_2$ gives

$$\begin{aligned}\sigma_{t^*}H &= \langle u(\alpha^n s_0 + s_1 + s_2/\alpha^n)\rangle \cdot \left\langle w(\alpha^{2n}s_0 + \alpha^n s_1 + s_2)\right\rangle \\ &= \left\langle u(\alpha^n s_0 + s_1 + s_2/\alpha^n) \cdot w(\alpha^{2n}s_0 + \alpha^n s_1 + s_2)\right\rangle\end{aligned}$$

Therefore, if $s_0 < 0$, then $\sigma_{t^*}H = \langle 0\rangle$, and if $s_0 > 0$, then $\sigma_{t^*}H =< 1 >$. Let $s_0 = 0$,

then if $s_1 > 0$, then $\sigma_{t^*}H = \langle u(\alpha^n s_0 + s_1 + s_2/\alpha^n)\rangle$, and if $s_1 < 0$, then $\sigma_{t^*}H = \langle 0\rangle$. Lastly, let $s_1 = 0$, then if $s_2 < 0$, then $\sigma_{t^*}H = \langle 0\rangle$, and if $s_2 > 0$, then $\sigma_{t^*}H \cong \langle 0\rangle$ where $\cong$ means $\sigma_{t^*}H \in hal(0)$. This implies that $H \cong H_1$ or $\sigma_{t^*}H \cong \sigma_{t^*}H_1$ for all $t^* \in \mathbb{K}$. The next Lemma generalizes this example.

Lemma 4 (Multiplication of Krylov Heaviside Functions)**.** *If H_1 and H_2 are Krylov Heaviside functions with $H_1 = S_{<\alpha^j;1>}u$ and $H_2 = S_{<\alpha^k;1>}w$ for some $j \leq k$, and u and w are shape functions, then $H_1 \cdot H_2 \cong H_1$ for $j < k$, and $H_1 \cdot H_2 = S_{<\alpha^k;1>}u \cdot w$ for $j = k$.*

The proof of the Lemma can be shown with the same procedure with the σ_{t^*} evaluation shown in the previous example. The interpretation of this Lemma is that the multiplication of two Heaviside functions with different rate of convergence is identical to the Krylov Heaviside function with the slower rate almost everywhere in $\mathbb{K}$. This Lemma helps to simplify the process in solving differential equation in the following sections.

3.2.5 Krylov Differentiation

In this section, an extended differential operator acting on Krylov functions is introduced, and one example of a singular function as an extended derivative of the Krylov Heaviside function is considered. In NSA, differentiability of a real valued function, $f : \mathbb{R} \to \mathbb{R}$, at $t \in \mathbb{R}$ can be checked on its hyperreal extension, $F := \langle f\rangle$. For every infinitesimal $\epsilon := \langle \epsilon_n\rangle \in hal(0)$, if there exist $L \in \mathbb{R}$ such that

$$\frac{\sigma_{\langle t\rangle+\epsilon}F - \sigma_{\langle t\rangle}F}{\epsilon} \cong L, \tag{3.2}$$

then f is differentiable at t.

Suppose that f is a differentiable function, and let f' be its derivative, then the above L is equal to $f'(t)$. By replacing L by $f'(t)$, and letting $g := \langle f'\rangle$ be the hyperreal extension

function of f', then we have

$$\frac{\sigma_{\langle t\rangle+\epsilon}F - \sigma_{\langle t\rangle}F}{\epsilon} - \sigma_{\langle t\rangle}(g) = \left\langle \frac{\sigma_{t+\epsilon_n}f - \sigma_t f}{\epsilon_n} - \sigma_t f' \right\rangle$$

The right hand side of the above equation is an infinitesimal by following the classical definition of a differentiable function in standard analysis. By using the right differential operator, D, defined in Definition 6, the above equation can be rewritten as

$$\frac{\sigma_{\langle t\rangle+\epsilon}F - \sigma_{\langle t\rangle}F}{\epsilon} \cong \sigma_{\langle t\rangle}g = \sigma_{\langle t\rangle}\left\langle Df\right\rangle \tag{3.3}$$

for all $t \in \mathbb{R}$.

Observe that the above generalization to the hyperreal function was valid if the original function f was differentiable. In the case when f is not differentiable or even discontinuous, only evaluating the right derivative of the function f will not give a proper generalization of the differential. For example, let $H : \mathbb{R} \to \mathbb{R}$ be a Heaviside function where $H(0) := 1$, then H is right differentiable, and $DH \equiv 0$, which is not desired since a singular delta function is expected. Therefore, one fundamental idea of the distribution theory lies in generalizing the differential operator. However, as it was mentioned in § 2.1.3, the set of Schwartz distributions does not form an algebra, which makes it infeasible to use the Schwartz theory directly for nonlinear systems.

In this section, the differential operator is generalized by enlarging the domain of the operator to the Krylov function space. The benefit of this formalism is that the generalized derivative is point-wise well defined as oppose to the functional form in the theory of distributions. This makes the multiplication of a Heaviside function and a singular function possible. Furthermore, the powers of delta can be well defined in the proposed framework. The formal definition of the generalized differential is given as follows. Recall that $\mathcal{F}^*$ is a space of Krylov functions, and D' is a set of right differentiable functions from $\mathbb{R}$ to $\mathbb{R}$.

Definition 16 (Generalized Differential D^*)**.** *Let $f \in \mathcal{F}^*$ such that there exist $\{f_n\}_n \subset D'$*

satisfying $\sigma_{t^*} f = \langle \sigma_{t_n} f_n \rangle$ *where* $t^* = \langle t_n \rangle \in \mathbb{K}$*, then* $D^* : \mathcal{F}^* \to \mathcal{F}^*$ *defined as* $\sigma_{t^*} D^* f := \langle \sigma_{t_n} D f_n \rangle$ *for each* $t^* \in \mathbb{K}$ *is called generalized differential.*

If $F \in \mathcal{F}^*$ is chosen to be the hyperreal extension of a differentiable function f, then the shadow of the generalized differential $sh(D^*F)$ is equivalent to f' as shown in (3.3).

Even if F is not a hyperreal extension of some standard differentiable function, the above definition is close to the definition in NSA. Suppose that the original differentiation in NSA is given by the operator $D_{\epsilon^*} : \mathcal{F}^* \to \mathcal{F}^*$ where $\epsilon^* = \langle \epsilon_n \rangle$ is a fixed infinitesimal, which is defined as

$$D_{\epsilon^*} F := 1/\epsilon^* (\mathcal{T}_{-\epsilon^*} F - F). \tag{3.4}$$

The hyperreal evaluation is then

$$\sigma_{t^*} D_{\epsilon^*} F = \left\langle \frac{f_n(t_n + \epsilon_n) - f_n(t_n)}{\epsilon_n} \right\rangle.$$

The following theorem shows the well-posedness of the generalized differential in Definition 16.

Theorem 4. *If* $\epsilon^* \in hal(0)$*, then* $\sigma_{t^*}(D^*F - D_{\epsilon^*}F) \cong 0$.

Proof. By directly evaluating at $t^* \in {}^*\mathbb{R}$,

$$\sigma_{t^*}(D^*F - D_{\epsilon^*}F) = \left\langle Df_n(t_n) - \frac{f_n(t_n + \epsilon_n) - f_n(t_n)}{\epsilon_n} \right\rangle = \langle Df_n(t_n) - Df_n(t_n + \epsilon_n') \rangle$$

for some $0 < \epsilon_n' < \epsilon_n$ at each n by the Mean Value Theorem in the standard analysis. Since this is true for all n, the new sequence, $\langle \epsilon_n' \rangle$, is a positive infinitesimal. By the right continuity of Df_n at t_n, for every $r > 0$, there exist $\delta_r > 0$ such that if $\alpha_r < \delta_n$, then

$$|Df_n(t_n) - Df_n(t_n + \alpha_r)| < r.$$

Since $\langle \epsilon'_n \rangle$ is infinitesimal, there exist $N > 0$ such that $\epsilon'_m < \delta_r$ for all $m > N$. Therefore,

$$\sigma_{t^*}(D^*F - D_{\epsilon^*}F) < \langle r \rangle$$

holds for all $r > 0$. □

More interesting results can be shown when F is chosen to be a non differentiable function such as a Krylov Heaviside function.

Singular Function Induced by Ramp Shape Function

Let H_u be a Krylov Heaviside function and u be a ramp shape function defined by $u(t) = t\chi_{[0,1]}(t) + \chi_{[1,\infty)}(t)$. The right derivative of u can be written as $Du = \chi_{[0,1)} = h - T_1 h$ where $h : \mathbb{R} \to \mathbb{R}$ is a standard Heaviside function. Observe that Du is a piecewise continuous function, and so it can be also written as a linear summation of the delayed Krylov Heaviside function. Pick the same ramp shape function for Du as well, then we have $Du = (I - T_{\langle 1;1 \rangle})S_{\langle \alpha;1 \rangle}u$ where I is an identity operator. By applying the composition rule in Proposition 5 and commutation rule in Lemma 2,

$$\begin{aligned}
\delta_u = D^*H_u = D^*S_{\langle \alpha;1 \rangle}u &= \langle \alpha; 1 \rangle \, S_{\langle \alpha;1 \rangle}Du \\
&= \langle \alpha; 1 \rangle \, S_{\langle \alpha;1 \rangle}(I - T_{\langle 1;1 \rangle})S_{\langle \alpha;1 \rangle}u \\
&= \langle \alpha; 1 \rangle \, (S_{\langle \alpha^2;1 \rangle} - T_{\left\langle \frac{1}{\alpha};1 \right\rangle}S_{\langle \alpha^2;1 \rangle})u \\
&= \langle \alpha; 1 \rangle \, (I - T_{\left\langle \frac{1}{\alpha};1 \right\rangle})S_{\langle \alpha^2;1 \rangle}u.
\end{aligned}$$

holds. This δ_u function is derived from a particular type of Krylov Heaviside function in which the shape function u was the ramp function. Different types of singular functions can also be derived by choosing different shape functions. See § 3.2.8 for the generalization. In the reset of this section, δ will represent the singular function δ_u without the subscript.

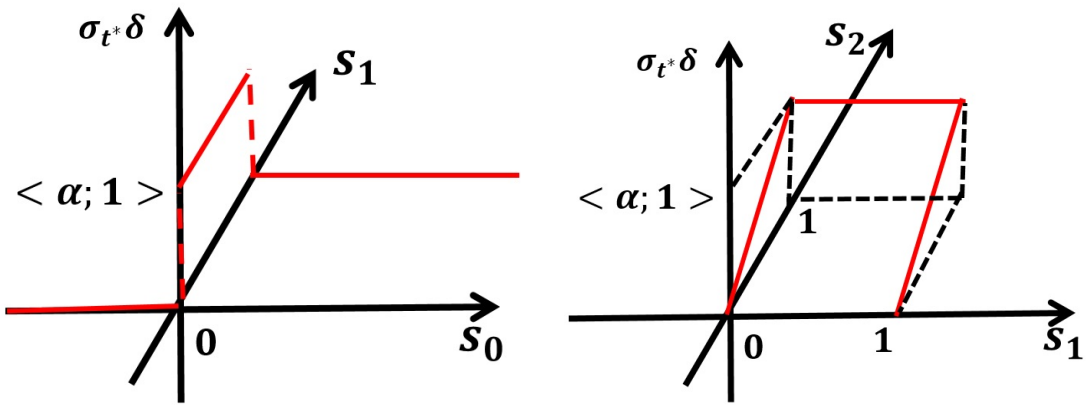

(a) s_0 and s_1 time line (b) s_1 and s_2 time line

Figure 3.4: Geometric interpretation of delta function

Similarly, the powers and the derivatives of above δ function are defined,

$$\delta^n = \langle \alpha^n; 1\rangle \, (I - T_{\left\langle \frac{1}{\alpha};1\right\rangle}) S_{\langle \alpha^2;1\rangle} u^n \tag{3.5}$$

$$(D^*)^n\delta = \left\langle \alpha^{2n+1}; 1\right\rangle \, (\prod_{i=0}^{n}(I - T_{\left\langle \frac{1}{\alpha^{i+1}};1\right\rangle})) S_{\langle \alpha^{2n+1};1\rangle} u, \tag{3.6}$$

for all $n \in \mathbb{N}$ where $(D^*)^n$ represents the $n-$th self composition of the generalized differential, D^*. It is interesting to see that the rate of the Krylov Heaviside function, $S_{\langle \alpha^{2n+1};1\rangle} u$, appearing in δ function is α^2 which is faster than the rate, α, of H. The interpretation of the faster rate is that the H function gets continuized in the e_1 space, the first infinitesimal time axis, while the δ function gets continuized in the e_2 space, the second infinitesimal time axis. The geometrical interpretation of the continuized delta function is shown in Figure 3.4

This shows that the continuization of the function is not only applied for regular discontinuous function but also applied to the singular function in the Krylov space, $\mathbb{K}$. Another remark on Eq. (3.5) is that the powers of δ do not change the continuization rate of δ function, but the higher derivative increases the rate as a function of n. The compact form of the generalized singular function with Krylov operators in Eq. (3.5) is used to solve the impulsive affine system in the next chapter.

3.2.6 Krylov Integration

In this section, inverse to the differentiation, an extended integration is introduced by using the sequence of integration operators. The integration is intuitively more understandable since the integration of the regular function would be regular, and the integral of a singular function would be also regular if the usual *delta function* is considered. To formally introduce the integral operator, let $t^* \in {}^*\mathbb{R}$ be fixed, and let $L(\mathbb{R})$ be a set of Lebesgue integrable function. The integral operator is introduced below.

Definition 17 (Generalized Integral $I^*_{t^*}$)**.** *Let $f \in \mathcal{F}^*$ such that there exist $\{f_n\}_n \subset L(\mathbb{R})$ satisfying $\sigma_{s^*} f = \langle \sigma_{s_n} f_n \rangle$ where $s^* = \langle s_n \rangle \in \mathbb{K}$, then $I^*_{t^*} : \mathcal{F}^* \to \mathcal{F}^*$ defined as $\sigma_{s^*} I^*_{t^*} f := \left\langle \int_{t_n}^{s_n} f_n(\tau) d\tau \right\rangle$ for each $s^* \in \mathbb{K}$ is called the generalized integral of f.*

The following two examples validate that the integral of the delta function induced by the Krylov Heaviside function reconstruct the original Krylov Heaviside function.

Example: (Integral of the delta function with a ramp shape function) In § 3.2.5, a new generalized singular delta function was defined as a Krylov function. This example shows the generalized integral of the singular delta function. Let Du be the right derivative of the ramp shape function, u, then the integral of δ in (3.5) with power 1, is given by

$$\begin{aligned}
\sigma_{s^*} I^*_{t^*} \delta : &= \langle \alpha; 1 \rangle \left\langle \int_{t_n}^{s_n} Du(\alpha^n \tau) d\tau \right\rangle \\
&= \langle \alpha; 1 \rangle \left\langle 1/\alpha^n \int_{\alpha^n t_n}^{\alpha^n s_n} Du(\tau) d\tau \right\rangle \\
&= \left\langle \int_{\alpha^n t_n}^{\alpha^n s_n} Du(\tau) d\tau \right\rangle
\end{aligned}$$

Suppose that $t_n = \tau_0 + \tau_1/\alpha^n$ and $s_n = \zeta_0 + \zeta_1/\alpha^n$ such that $t_n < s_n$, then

$$\sigma_{s^*} I^*_{t^*} \delta := \left\langle \int_{\alpha^n \tau_0 + \tau_1}^{\alpha^n \zeta_0 + \zeta_1} Du(\tau) d\tau \right\rangle.$$

If $\zeta_0 < 0$, then $\sigma_{s^*} I^*_{t^*} \delta = \langle 0 \rangle$ since $\sigma_{s^*} Du = 0$ for $s^* < 0$. Also, if $\tau_0 > 0$, then there exist $N > 0$ such that if $m > N$, then $\alpha^m \tau_0 + \tau_1 > 1$, and $\sigma_{s^*} I^*_{t^*} \delta = \langle 0 \rangle$. This is expected since if the interval of integration does not contain 0, then the integral of delta function is equal to zero.

If $\tau_0 < 0 < \zeta_0$, then there exist $N > 0$ such that if $m > N$, then $\alpha^m \tau_0 + \tau_1 < 0$ and $\alpha^m \zeta_0 + \zeta_1 > 1$, and so $\sigma_{s^*} I^*_{t^*} \delta = \langle 1 \rangle$. Interestingly, if $\zeta_0 = 0$, and $\zeta_1 \in [0, 1]$, then $\sigma_{s^*} I^*_{t^*} \delta = \langle \zeta_1 \rangle$. In summary, for $t^* < 0$, the integral of this δ function is give by,

$$\sigma_{s^*} I^*_{t^*} \delta = \begin{cases} \langle 0 \rangle \text{ if } \zeta_0 < 0 \\ \langle \zeta_1 \rangle \text{ if } \zeta_0 = 0 \text{ and } \zeta_1 \in [0, 1] \\ \langle 1 \rangle \text{ if } \zeta_0 > 0 \end{cases} . \tag{3.7}$$

Therefore, the Heaviside function with the ramp shape function at the first infinitesimal axis, e_1, is reconstructed.

Example: (Integral of a delta function with a quadratic shape function) As discussed in § 3.2.2, the space of shape functions is closed under multiplication, and so $u_1(t) = \chi_{(0,1)} t^2 + \chi_{[1,\infty)} t$ also represents the continuization between 0 and 1 in the first infinitesimal axis, e_1. Let $H_1 := S_{\langle \alpha; 1 \rangle} u_1$ be another Krylov Heaviside function with a quadratic shape function. The right derivative of this quadratic u shows $Du_1(t) = 2t \chi_{[0,1]} t$, and so different singular delta function can be derived using the generalized differential in Definition 16, given by

$$\delta_1 := \langle \alpha; 1 \rangle \left(I - T_{\left\langle \frac{1}{\alpha}; 1 \right\rangle} \right) S_{\langle \alpha; 1 \rangle} Du_1 \tag{3.8}$$

The direct computation of the integral shows that

$$\sigma_{s^*} I^*_{t^*} \delta_1 = \begin{cases} \langle 0 \rangle \text{ if } \zeta_0 < 0 \\ \langle \zeta_1^2 \rangle \text{ if } \zeta_0 = 0 \text{ and } \zeta_1 \in [0,1] \\ \langle 1 \rangle \text{ if } \zeta_0 > 0 \end{cases} . \tag{3.9}$$

Therefore, the Heaviside function with the quadratic shape function at the first infinitesimal axis, e_1, is reconstructed. These two examples are generalized in the next fundamental theorem of calculus (FTC) in Krylov generalized function theory.

Theorem 5 (The First Fundamental Theorem of Calculus in Krylov generalized function theory)**.** *Suppose that $f^* \in \mathcal{F}^*$ is given by $f_n \in L(\mathbb{R})$ for all n, then*

$$D^* \circ I^*_{t^*} f^* \cong f^*. \tag{3.10}$$

Proof. By following the definition of generalized differentiation and integration, pick $s^* \in {}^*\mathbb{R}$, then

$$\sigma_{s^*} D^* \circ I^*_{t^*} f^* = \left\langle \sigma_{s_n} D(\int_{t_n}^{\cdot} f_n(\tau) d\tau) \right\rangle = \langle \sigma_{s_n} f_n \rangle = \sigma_{s^*} \langle f_n \rangle$$

The equality holds by using the fundamental theorem of calculus in the standard analysis for each n. □

The second FTC theorem shows the opposite composition of differential and integration operators.

Theorem 6 (The Second Fundamental Theorem of Calculus in Krylov generalized function theory)**.** *Suppose that $f^* \in \mathcal{F}^*$ is given by $f_n \in D^1(\mathbb{R})$ for all n, then*

$$I^*_{t^*} \circ D^* f^* \cong f^* + c^*. \tag{3.11}$$

for some $c^* \in {}^*\mathbb{R}$.

Proof. By following the definition of generalized differentiation and integration, pick $s^* \in {}^*\mathbb{R}$, then

$$\sigma_{s^*} I^*_{t^*} \circ D^* f^* = \left\langle \int_{t_n}^{s_n} Df_n(\tau) d\tau) \right\rangle = \langle \sigma_{s_n} f_n - \sigma_{t_n} f_n \rangle = \sigma_{s^*} f^* - \sigma_{t^*} f^*$$

The equality holds by using the fundamental theorem of calculus in the standard analysis for each n, and by letting $c^* := -\sigma_{t^*} f^*$, the theorem holds. □

3.2.7 Generalized Nonsmooth Functions

By using Proposition 5, it can be shown that the $\mathbb{R}$-sampled function of $T_{<1;\beta>}H$ where $\beta \in \mathbb{R}$ is a β-shifted Heaviside function. Any generalized piecewise function can now be defined using the Krylov Heaviside function.

Definition 18. *A linear combination of shifted Krylov Heaviside functions and a continuous function is called a generalized piecewise continuous function.*

Suppose that x is a real valued piecewise continuous function, then x can be decomposed into two parts,

$$x = x_c + \sum_{i=1}^{N} a_i T_{\tau_i} S_{\langle \alpha^{n(i)};1 \rangle} u_i, \tag{3.12}$$

where x_c is a continuous function, $\{\tau_i\}_{i=1}^N$ are points of discontinuity, and $\{a_i\}_{i=1}^N$ are the amount of jumps where N is the total number of discontinuity. The function, u_i, and $n(i)$ represents the corresponding shape function, and the convergence rate, respectively, for each i. Observe that the Krylov Heaviside part in Eqn (3.12) contains the shape function which shows how the discontinuous points will be connected in insensible time. In addition, the derivative of the Heaviside part can be obtained from the shape definition but the continuous part does not have the information on how the connection will be made for $\dot{x_c}$ in insensible time. If x_c has a point that is not differentiable, then the Eqn (3.12) is insufficient to generalize the derivative of the x in insensible time. Therefore, a new shape function which can generalize a continuous but nonsmooth function is introduced.

Self returning shape function (bump)

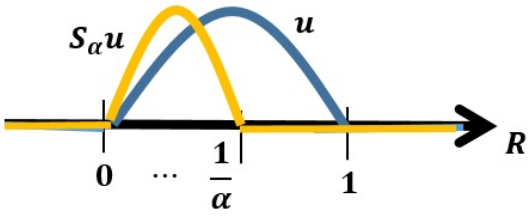

(a) An example of new shape function $u(t) = \chi_{(0,1)} sin(\pi t)$

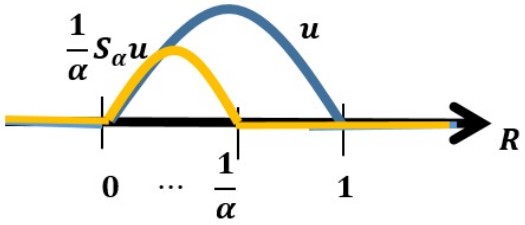

(b) A sequence of shape function with regulated amplitude.

Figure 3.5: Example for the shape function, and the effect of Krylov scaling operation

The main objective of introducing the shape function in Definition 13 is to find a continuous connection between two discontinuous points, and make the limit of the Krylov scaling operator act on the shape function convergence point-wise to a Heaviside function in sensible time. For example, let $f_n = S_{\alpha^n} u$ where $u(t) = \chi_{(0,1)} t + \chi_{[1,\infty)}$ is the ramp shape function, then we have $\lim_{n\to\infty} f_n(t) = 1$ for all $t > 0$, and $\lim_{n\to\infty} f_n(t) = 0$ for all $t \leq 0$. This convergence result guarantees that the discontinuity model in (3.12) will generate the desired jump for x in sensible time.

Similar to the construction of the original shape function, we introduce a new shape function which connects from $u(0) = 0$ to $u(1) = 0$. The goal is to find a smooth connection between the left derivative and right derivative of a non differentiable function, x_c, in insensible time. For example, $u(t) = \chi_{(0,1)} \sin(\pi t)$ can be a new shape function since $u(0+) = \sin(0) = 0$ and $u(1-) = \sin(\pi) = 0$. By the mean value theorem, there exist

at least one point t_1 in $(0,1)$ such that $\dot{u} = 0$. Therefore, except for the trivial solution where $u \equiv 0$, there must be a bump within $(0,1)$. A graphical representation of this example is shown in Fig 3.5a. A new shape function is now introduced by using this necessary conditions on returning to zero.

Definition 19. *(Bump shape function)*

A function $u \in C(\mathbb{R})$ is called a bump shape *function if there exist a function $p \in C^1(\mathbb{R})$ such that $p(0) = 0$ and $p(1) = 0$ and $u = \chi_{(0,1)}p$.*

Generalized nonsmooth function

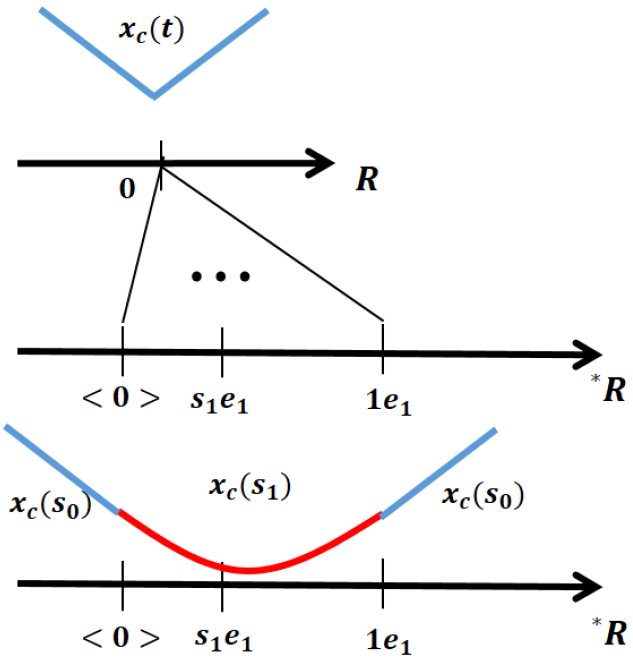

Figure 3.6: A geometrical view of generalized nonsmooth function

Suppose that x_c in Eqn (3.12) is continuous but not differentiable at $t = 0$, and the left limit $\dot{x}_c(0-)$, and the right limit $\dot{x}_c(0+)$ of the derivatives exist but not equal. The objective of this section is to properly define the generalized form for x_c using the new shape function in Definition 19, which will end up having a smooth connection between the discontinuity of derivatives.

First, consider a motivating counter example for the generalization of the absolutely continuous function. Suppose one were to take,

$$\overline{x}_c := x_c(t) + S_{\langle\alpha;1\rangle}u \tag{3.13}$$

as an analogy of constructing Krylov Heaviside function by directly applying the Krylov scaling operator to the new bump shape function u. The generalized derivative of $\overline{x}_c$ at $t = 0$ is defined as $D^*\overline{x}_c = S_{\langle\alpha;1\rangle}Du$. Direct evaluation of $D^*\overline{x}_c$ at $t^* = 0e_0 + s_1e_1$ for some $s_1 \in (0, 1)$ gives $\sigma_{t^*}D\overline{x}_c := \langle\alpha; 1\rangle \langle\alpha; Du(s_1)\rangle$. However, this shows that $D^*\overline{x}_c$ goes to infinity since $\langle\alpha; Du(s_1)\rangle$ is not an infinitesimal, and so x_c is not continuous, which contradicts the fact that x_c is continuous. Therefore, (3.13) is not a generlization of the absolutely continuous function. A remedy to this problem is by defining the generalized $\overline{x}_c$ in the next form.

$$\overline{x}_c := x_c(t) + \langle 1/\alpha; 1\rangle\, S_{\langle\alpha;1\rangle}u. \tag{3.14}$$

For example, suppose that $x_c(t)$ is given as in the top graph in Fig 3.6 that x_c is differentiable everywhere except at $t = 0$. The direct evaluation of the above function at Krylov time, $t^* = s_0e_0 + s_1e_1$, gives

$$\begin{aligned} \sigma_{t^*}\overline{x}_c : &= \sigma_{t^*}(x_c) + \sigma_{t^*}(\langle 1/\alpha; 1\rangle\, S_{\langle\alpha;1\rangle}u) \\ &= \sigma_{t^*}x_c + \epsilon \end{aligned}$$

where $\epsilon \in hal(0)$ is an infinitesimal. The equality holds since u is continuous and it is bounded on $[0, 1]$, which then the multiplication with $\langle 1/\alpha; 1\rangle$ makes the right term be an infinitesimal. Therefore, the $\mathbb{R}$-sampling of $\overline{x}_c$ is equivalent to x_c in the real time. The only requirement for the bump shape function u is to satisfy the boundary conditions: $Du(0)$ and $Du(1)$ should be equal to $\dot{x}_c(0-)$ and $\dot{x}_c(0+)$, respectively.

Now define a generalized derivative of Eqn (3.14) at the non-differentiable point $sh(t^*) =$

0, and evaluate at $t^* = 0e_0 + s_1 e_1$ for $s_1 \in (0, 1)$, then

$$\begin{aligned} \sigma_{t^*} D^* \overline{x}_c : &= \sigma_{t^*}(\langle 1/\alpha; 1\rangle \langle \alpha; 1\rangle S_{\langle \alpha;1\rangle} Du) \\ &= \sigma_{t^*}(S_{\langle \alpha;1\rangle} Du) \\ &= Du(s_1). \end{aligned}$$

By using this generalized derivative, we now define a generalized nonsmooth function as an extension to Definition 18,

$$x = x_c + \sum_{i=1}^{M} T_{k_i} \langle 1/\alpha; 1\rangle S_{\langle \alpha;1\rangle} w_i + \sum_{i=1}^{N} a_i T_{\tau_i} S_{\left\langle \alpha^{n(i)};1\right\rangle} u_i, \tag{3.15}$$

where M is the number of non differentiable point of x_c, and $\{w_i\}_{i=1}^{M}$ are corresponding bump shape functions. Since the smooth change in the derivative is now well defined, the point-wise evaluation of the composition between a δ function in Eqn (3.5), and a non smooth function x in Eqn (3.14) is well-defined, and it can be use to solve the generalized ordinary differential equation in the next chapter.

3.2.8 Generalized Singular Functions

In this section, the process of generating the singular delta function is generalized. An example of the generalized singular delta function was shown in (3.5) by differentiating Krylov Heaviside function with a ramp shape functions. In fact, the ramp shape function represents the integral of the constant function in the first infinitesimal time as shown in Figure 3.4. In this section, a new singular shape function is introduced to generalize the *shape* of the function values in the first infinitesimal domain. This function would represent the impulsive force profile in the *insensible time*. The integral of the singular shape function would then demonstrate the continuization between the velocity jumps in impulsive effect models.

First, inspired by the derivative of the ramp function, the truncation function, $g \in \mathbb{F}^*$, is defined as

$$g^* := (I - T_{\langle 1;1\rangle})S_{\langle \alpha;1\rangle}u \tag{3.16}$$

where u is the ramp shape function.

Definition 20. *A function $h^* \in \mathcal{F}^*$ is called a singular shape function if there exists a non-negative function $p \in C(\mathbb{R})$ such that $\int_0^1 p(\tau)d\tau = 1$, and $h^* := g^*p^*$ where $p^* = \langle p\rangle$ is the extension of p.*

Observe that, by taking the $\mathbb{R}$ sampling of g^*, the following holds:

$$sh(\sigma_{t^*}g^*) = \begin{cases} 0 & \text{if } sh(t^*) \notin (0,1) \\ 1 & \text{if } sh(t^*) \in (0,1) \end{cases},$$

and so $sh(\sigma_{t^*}g^*) = \chi_{(0,1)}$ holds almost everywhere. Similarly, by taking the $\mathbb{R}$ sampling of h^* in Definition 20, the following holds,

$$sh(\sigma_{t^*}h^*) = \begin{cases} 0 & \text{if } sh(t^*) \notin (0,1) \\ \sigma_{sh(t^*)}p & \text{if } sh(t^*) \in (0,1) \end{cases}.$$

Now, take the generalized integral of h^* from the reference time at $\langle 0\rangle$, and $\mathbb{R}-$sample the integral function. Let $t := sh(t^*)$, then the following holds:

$$sh(\sigma_{t^*}I^*_{\langle 0\rangle}h^*) = \begin{cases} 0 & \text{if } t < 0 \\ \int_0^t p(\tau)d\tau & \text{if } t \in [0,1] \\ 1 & \text{if } t \geq 1 \end{cases}.$$

Therefore, the shape function in Definition 13 can be induced by the integral of the singular shape function h^*. Let the corresponding shape function to be h such that $\sigma_t h :=$

$sh(\sigma_{t^*} I^*_{\langle 0\rangle} h^*)$, and so the Krylov Heaviside function with the shape function h can be defined as

$$H_h := S_{\langle \alpha;1\rangle} h.$$

since h and $I^*_{\langle 0\rangle} h^*$ are infinitesimally apart, by the definition of the $\mathbb{R}-$ sampling, consider the following generalized Heaviside function,

$$H_{h^*} := S_{\langle \alpha;1\rangle} I^*_{\langle 0\rangle} h^*.$$

Now, by directly computing the generalized derivative of this function and using Lemma 2, Proposition 5, and Theorem 5, the singular delta function can be derived,

$$\begin{aligned}
D^* H_{h^*} &= D^* S_{\langle \alpha;1\rangle} I^*_{\langle 0\rangle} h^* \\
&= \langle \alpha;1\rangle \, S_{\langle \alpha;1\rangle} D^* I^*_{\langle 0\rangle} h^* \\
&= \langle \alpha;1\rangle \, S_{\langle \alpha;1\rangle} h^* \\
&= \langle \alpha;1\rangle \, S_{\langle \alpha;1\rangle} g^* p^* \\
&= \langle \alpha;1\rangle \, S_{\langle \alpha;1\rangle} g^* S_{\langle \alpha;1\rangle} p^* \\
&= \langle \alpha;1\rangle \left(S_{\langle \alpha;1\rangle} (I - T_{\langle 1;1\rangle}) S_{\langle \alpha;1\rangle} u \right) \left(S_{\langle \alpha;1\rangle} p^* \right) \\
&= \langle \alpha;1\rangle \left((I - T_{\left\langle \frac{1}{\alpha};1\right\rangle}) S_{\langle \alpha^2;1\rangle} Du \right) \left(S_{\langle \alpha;1\rangle} p^* \right)
\end{aligned}$$

The singular delta function derived in (3.5) is the special case when p is chosen to be constant 1 function. The $\mathbb{R}-$sampling of the singular shape function h^* is zero in the sensible time $t \neq 0$, and it can be only nonzero during the first insensible axis, e_1. Therefore, the generalized singular function associated with the singular shape function is now introduced.

Definition 21. *The function $\delta \in \mathcal{F}^*$ is called a* generalized singular function *with a singular*

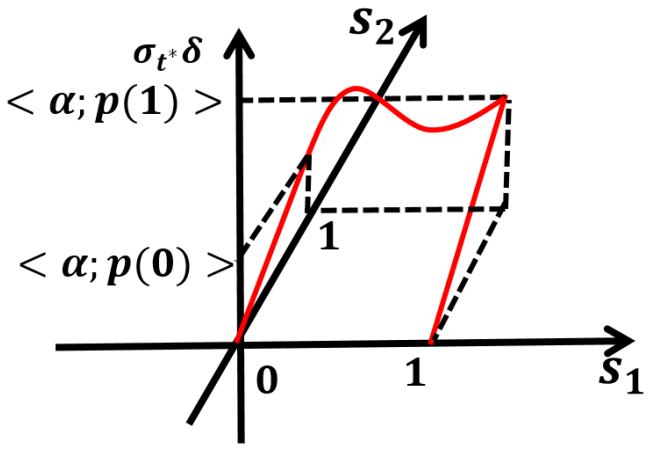

Figure 3.7: A geometrical view of generalized singular function

shape h *if* h^* *is the singular shape function, and* h *is* $\mathbb{R}-$*sampled function of* h^* *such that*

$$\delta := \langle \alpha; 1 \rangle \left((I - T_{\left\langle \frac{1}{\alpha}; 1 \right\rangle}) S_{\langle \alpha^2; 1 \rangle} u \right) (S_{\langle \alpha; 1 \rangle} p^*). \tag{3.17}$$

The geometrical interpretation of the generalized singular function is shown in Figure 3.7. An example of the generalized singular function is plotted on s_1 domain, and the singular shape function scaled with infinitely large number $\langle \alpha; 1 \rangle$ is drawn in the first infinitesimal axis, e_1. The evaluation of the generalized singular function at the infinitesimal is infinitely large, but it is zero in any sensible time except at 0.

CHAPTER 4

APPLICATION TO IMPULSIVE SYSTEM MODELING

In this chapter, the Krylov generalized function (KGF) theory is applied to generate impulsive causal modeling. See the background for the impulsive causal modeling problem in § 2.1.3. While ill-posed in the distribution theory, The pointwise multiplication between a singular function and a nonsmooth function is well defined in KGF theory. Therefore, it is possible to directly apply the generalized singular function as a impulsive force input to the nonlinear affine system in (2.31). By using the generalized nonsmooth function description in (3.15), the generalized solution to the ordinary differential equation is sought. The generalized solution contains the jump (discontinuity) which can be resolved by taking $\mathbb{R}-$sampling of the generalized solution. In addition, the solution contains the continuization between the jumps in insensible time, which follows the system dynamics. Therefore, the Krylov generalized function theory not only generates the solution with discontinuity but also respects the physics model in the insensible time to create such jumps.

This chapter is organized as follows. In § 4.1, the generalized solution is sought to the ordinary differential equation using the generalized differential operators. Three cases are studied to find the singular control in the right hand side of ODE which could generate a desire jump. In § 4.3, the affine dynamics of the mechanical system is considered to model the contact force which generate the desired jump. A causal impulsive contact force modeling for the bouncing ball model in § 2.1.2 and the compass gait walker model are considered in § 2.1.2.

4.1 Ordinary Differential Equations

In this section, a generalized impulsive affine system equation is introduced by using the generalized differential, D^*, and its particular solution is presented. Consider the gene-

ralized scalar ordinary differential equation (ODE) with an initial condition at $-\epsilon$ where $\epsilon := \langle \epsilon_n \rangle$ is some positive infinitesimal:

$$\begin{cases} D^*x^* = f(x^*) + g(x^*) \cdot u^* \\ \sigma_{-\epsilon}x^* = \langle c_n \rangle \end{cases} \tag{4.1}$$

where f and g are smooth functions in $C^1(\mathbb{R})$, and $\langle c_n \rangle$ is a limited hyperreal that $sh(\langle c_n \rangle) = c$ for some $c \in \mathbb{R}$, and $u^* \in \mathcal{F}^*$ is the generalized control input to the system.

If $u^* := \langle y \rangle$ is a hyperreal extension of some continuous function $y \in C(\mathbb{R})$, then the above initial value problem is equivalent to

$$\begin{cases} \dot{x} = f(x) + g(x) \cdot y \\ x(0) = c \end{cases} \tag{4.2}$$

by using (3.3). The conditions for the existence of the solution are equivalent to the classical ones in ordinary differential equation. Suppose that $x_p : [0, T] \to \mathbb{R}$ is the solution to (4.2), then the hyperreal extension to $x = \langle x_p \rangle$ is the solution to (4.1). On each evaluation of $t^* \in \mathbb{K}$, the equality holds up to its equivalence class in the filter, which gives non-uniqueness of the solution to (4.1) in $\mathcal{F}^*$. However, all the $\mathbb{R}-$sampled solutions should be equal to x_p.

More interesting results can be shown when u^* is chosen to be a generalized singular Krylov function proposed in the previous chapter. In this section, the generalized singular function in (3.17) is used for $u^* = \delta$, and a solution is proposed in terms of the linear combination of the continuous part and the Krylov Heaviside function part. More precisely, the proposed solution can be written as $x^* = x_c^* + a_0 \cdot H$ where a_0 is the jump at time $t = 0$, x_c^* is the extension of the continuous function, x^*, and H is the Krylov Heaviside function.

Remark: Similar to the Caratheodory solution in the standard analysis (see [46]), which provides the absolute continuous solution, the weak solution to (4.1) can also be

analyzed. By following the fundamental theorem of calculus in Theorem 6, the solution x^* to (4.1) evaluated at $s^* := \langle s_n \rangle$ should satisfy

$$\sigma_{s^*}(I^*_{-\epsilon} \circ D^* x^*) = \sigma_{s^*} x^* - \sigma_{-\epsilon} x^*.$$

Let $x^* := \langle x_n \rangle$ be the solution and the $u^* := \langle u_n \rangle$ be the generalized control input, then by taking the generalized integral to the right hand side of (4.1), the following integral equation should hold for the solution x^*,

$$\langle x_n(s_n) \rangle = \langle x_n(\epsilon_n) \rangle + \left\langle \int_{\epsilon_n}^{s_n} f(x_n(\tau)) + g(x_n(\tau)) u_n(\tau) \right\rangle. \tag{4.3}$$

The equality holds up to the equivalence set of the ultrafilter, where the ultrafilter contains the cofinite set. Therefore, the solution in (4.3) includes the extension of the absolutely continuous solutions of the standard Caratheodory type where the equality is for almost everywhere with respect to Borel measure. In this thesis, instead of pursuing the weak solution of (4.3) type, a direct solution to the (4.1) is considered using the generalized derivative, and the inverse mapping of Krylov scaling operators.

In the following subsection, a generalized solution to the (4.1) is analyzed by separating the solution to the sensible part and the insensible part.

4.1.1 Sensible Part of the Solution

By evaluating (4.1) for $t^* \in \mathbb{K}$ in two cases $t^* < 0$, and $sh(t^*) > 0$, the following holds,

$$\begin{cases} \sigma_{t^*}(D^* x) = \sigma_{t^*}(f(x)) \quad \text{if } t^* < 0 \\ x(0 - \epsilon) = \langle c_n \rangle \end{cases} \tag{4.4}$$

$$\begin{cases} \sigma_{t^*}(D^* x) = \sigma_{t^*}(f(x)) \quad \text{if } sh(t^*) > 0. \end{cases} \tag{4.5}$$

In both cases, (4.4) and (4.5) are non-impulsive ODEs, and there exist a continuous solution, $x_{c1} : [-T, 0) \to \mathbb{R}$ and $x_{c2} : (0, T] \to \mathbb{R}$ for some $T > 0$, respectively. Different from (4.4), the initial value for (4.5) is not given yet since the initial condition $x_{c2}(0+) = \lim_{h \geq 0} sh(x(\langle h \rangle))$ is undetermined until the solution to (4.1) for $t^* \in \{t^* \in hal(0) : t^* > 0\}$ is found. Suppose that an initial condition $x_{c2}(0+)$ is given, then a continuous function can be constructed as

$$x_c := x_{c1}\chi_{[-T,0)} + (x_{c2} - x_{c2}(0+) + x_{c1}(0-))\chi_{[0,T]}$$

on $[-T, T]$. Since the difference,

$$x_c - x_{c2} = x_{c2}(0+) - x_{c1}(0-),$$

is constant on $[0, T]$, by the fundamental theorem of calculus, x_c is also a solution to (4.5). Therefore, the Krylov function $\langle x_c \rangle$ is a solution to (4.1) for every t^* belonging in the following set,

$$\{t^* \in \mathbb{K} \cap [-T, T] : t^* < 0 \vee sh(t^*) > 0\}.$$

An interpretation of the continuous part, x_c, is that if there were no jumps in the solution to (4.1), then $x_{c2}(0+) = x_{c1}(0-)$, and so x_c itself is the solution to (4.1) meaning the impulsive input u^* was ineffective in sensible time. However, since the system is driven by a generalized singular function δ, which is understood as an impulsive contact force, it is possible to have a jump on the state variable. In this case, the solution x_c is not sufficient to characterize the jump behavior in the insensible time. Therefore, the following more detailed behavior of the solution at the infinitesimal moment of the impact is necessary.

4.1.2 Insensible Part of the Solution

Suppose that there is a jump, $a_0 = x_{c2}(0+) - x_{c1}(0-)$, in sensible time, then a generalized piecewise continuous function can be written as

$$x = x_c + a_0 \cdot S_{\langle \alpha^N ; 1 \rangle} w \tag{4.6}$$

for some $N \in \mathbb{N}$, and shape function w. The generalized derivative of (4.6) is given by

$$D^* x := Dx_c + a_0 \left\langle \alpha^N ; 1 \right\rangle S_{\langle \alpha^N ; 1 \rangle} Dw$$

assuming that x_c is right differentiable. In order to have the equality hold in (4.1), the unlimited numbers $\left\langle \alpha^N ; 1 \right\rangle$ and $\langle \alpha ; 1 \rangle$ should be matched, in other words, N should be equal to 1 since the generalized singular function in (3.17) is used for u^*.

In addition, if the solution x contains a singular part, then $D^* x$ should contain some generalized derivatives of δ function defined in (3.5). Observe that the continuization rate for the first derivative corresponds to α^3. However, the continuization rate of the powers of δ function remains at α^2 in (3.5), and the multiplication of two Heaviside functions should not increase the continuization rate by Lemma 4, and so the right hand side (RHS) of (4.1) should have at most α^2 for the continuization rate. This shows that the RHS cannot describe the details of the derivatives of delta at the continuization rate α^3. Hence, the solution x should not contain the singular part for (4.1).

Finally, by evaluating (4.1) at $t^* \in \{t^* \in \mathbb{K} \cap hal(0) : t^* > 0\}$ with the proposed solution, it is possible to convert the generalized impulsive affine system into a classical non-impulsive differential equation for the shape function w with the two point boundary conditions $w(0) = 0$ and $w(1) = 1$. Since there are two unknowns for w and the jump a_0, this two point boundary problem will uniquely determine the two unknowns. In the next section, three cases are analyzed with the detailed derivation of the differential equation for

the shape function.

4.2 Causal Representation of Impulsive Effect Model

In this section, a causal representation of a given impulsive effect model in (2.21) is considered, where for simplicity, assume that the single jump occurs at t=0.

Problem 1 (Causal representation of impulsive effect model)**.** *Given an impulsive effect model in (2.21) without the actuation part, find the equivalent causal model with generalized singular input on the right hand side such that two solutions are equivalent in the sensible time. In summary, find* $g(x)$ *and the singular input* u^* *showing the following,*

$$\begin{cases} \dot{x} = f(x) \\ \Delta x(0) = R(x(0-)) \end{cases} \iff \begin{cases} D^*x = f(x) + g(x)u^* \end{cases} .$$

This problem is more general than the causal contact force modeling problem in (2.11) since the question of the causal representation of the impulsive effect model is whether if one can find a $g(x)$ and the singular input u^* which generate the same jump as in (2.21).

4.2.1 Case 1: Scalar System

Suppose that an impulsive effect equation where $f(x,u) \equiv 0$ and $x(\tau+) = x(\tau-) \cdot e$ in (2.21) is given such that τ_i is the sensible time for the discontinuity, then the jump is proportional to the state, and so the linear model with the singular control cannot be applied. Therefore, the objective is to find the equivalent causal system by using the Krylov generalized functions.

$$\begin{cases} \dot{x} = 0 \\ \Delta x(0) = (e-1)x(0-) \end{cases} \iff \begin{cases} D^*x = g(x)\delta \end{cases} \tag{4.7}$$

The goal is to find the causal bilinear representation by properly defining $g(x)$ and the singular control δ as defined in the previous section. Let $x(0-) \in \mathbb{R}$ be the initial condition such that $x(0-) \neq 0$. The generalized solution has a form such that

$$x(t) = x_c(t) + a_0 \cdot S_{\langle \alpha;1 \rangle} w$$

and the generalized singular function with the constant singular shape function is used,

$$\delta = \langle \alpha; 1 \rangle \, (I - T_{\langle 1/\alpha;1 \rangle}) S_{\langle \alpha^2;1 \rangle} u$$

where u is the ramp shape function, $u(t) = t\chi_{[0,1]}(t) + \chi_{[1,\infty)}(t)$.

Pick $g(x) := x$, then the right hand side and the left hand side of the GODE in (4.7) are

$$\begin{aligned} x\delta &= x_c \cdot \langle \alpha; 1 \rangle \, (I - T_{\left\langle \frac{1}{\alpha};1 \right\rangle}) S_{\langle \alpha^2;1 \rangle} u + a_0 S_{\langle \alpha;1 \rangle} w \cdot \langle \alpha; 1 \rangle \, (I - T_{\left\langle \frac{1}{\alpha};1 \right\rangle}) S_{\langle \alpha^2;1 \rangle} u \\ D^* x &= D x_c + a_0 \, \langle \alpha; 1 \rangle \, S_{\langle \alpha;1 \rangle} D w \end{aligned}$$

First observe that the evaluation at $t^* \in \mathbb{K}$ for $sh(t^*) \neq 0$, gives that $\sigma_{t^*} \dot{x_c} = 0$, which after $\mathbb{R}-$sampling, it shows that x_c is a constant function. Therefore, $x_c(t) = x(0-)$ holds for all t. Now by factoring out the unlimited number, $\langle \alpha; 1 \rangle$, the equation is reduced to

$$a_0 S_{\langle \alpha;1 \rangle} D w = x_c \cdot (I - T_{\left\langle \frac{1}{\alpha};1 \right\rangle}) S_{\langle \alpha^2;1 \rangle} u + a_0 S_{\langle \alpha;1 \rangle} w \cdot (I - T_{\left\langle \frac{1}{\alpha};1 \right\rangle}) S_{\langle \alpha^2;1 \rangle} u$$

Taking the left inverse of Krylov scaling operator, $S_{\langle 1/\alpha;1 \rangle}$, the above equation can be simplified to

$$a_0 D w = x_c \cdot (I - T_{\langle 1;1 \rangle}) S_{\langle \alpha;1 \rangle} u + a_0 w \cdot (I - T_{\langle 1;1 \rangle}) S_{\langle \alpha;1 \rangle} u$$

Therefore, the right hand side is equal to $x(0-) + a_0 w(t)$ for all t^* such that $sh(t^*) \in (0, 1)$ since $x_c(t) = x(0-)$. In addition, the right hand side is equal to 0 for $sh(t^*) \notin (0, 1)$ which coincides with the condition for the shape function w. The continuous differential equation

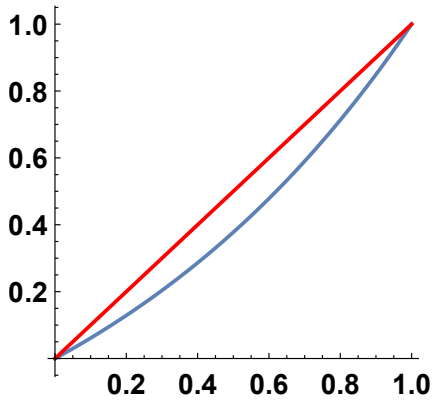

(a) Shape functions

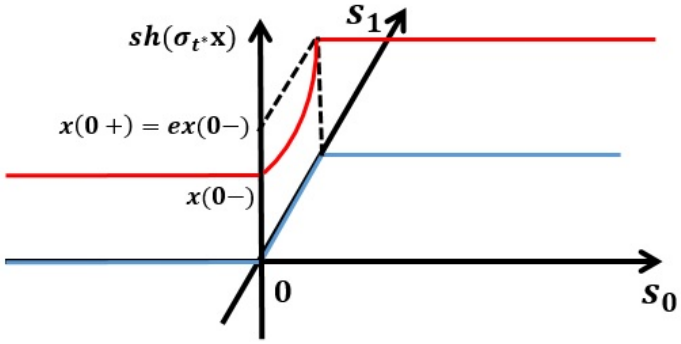

(b) Generalized solution

Figure 4.1: Solution to the scalar example

is then given as

$$Dw = \frac{x(0-)}{a_0} + w,$$

with $w(0) = 0$ and $w(1) = 1$. Solving this differential equation leads to

$$\begin{aligned} w(t) &= x(0-)(e^t - 1)/a_0 \\ a_0 &= x(0-)(e - 1). \end{aligned}$$

Now the resulting jump equation can be written as

$$x(0+) = x(0-) \cdot e \text{ or } \Delta x(0) = (e-1)x(0-)$$

By using the Krylov based approach, the equivalent causal equation, $g(x) = x$, is

found, and the corresponding shape function w defined in *insensible* time at the discontinuity is derived. The plot of two different shape functions in the interval $[0, 1]$ is shown in Figure 4.1a where w is obtained from the solution, and u is given as a ramp. The trajectory in the extended time is shown in Figure 4.1b.

4.2.2 Case 2: Multi-dimensional Dynamics

In this subsection, an n-dimensional linear impulsive system with state dependent jump is considered. Let $A, C \in \mathbb{R}^{n\times n}$, and $X \in \mathbb{R}^n$. For simplicity, assume that the jump occurs at time $t = 0$.

$$\begin{cases} \dot{X} = AX \\ \Delta X(0) = CX(0-) \end{cases} \iff \begin{cases} D^*X = AX + BX\delta \end{cases} \tag{4.8}$$

Similarly, as in the previous case, the goal is to find $B \in \mathbb{R}^{n\times n}$, which generates the same jump when the singular control δ defined in (3.5) is applied. Since the original continuous dynamics has smooth vector field, the generalized solution will be $X := X_c + A_0 S_{\langle\alpha;1\rangle} w$ where $X_c \in C(\mathbb{R})^n, A_0 \in \mathbb{R}^{n\times n}$ and $w \in C(\mathbb{R})^n$ is a multi-dimensional shape function. Suppose that $\delta = \langle\alpha; 1\rangle (I - T_{\langle 1/\alpha;1\rangle}) S_{\langle\alpha^2;1\rangle} u$, and the shape function is defined as a ramp function: $u(t) = t\chi_{[0,1]}(t) + \chi_{[1,\infty)}(t)$.

The right hand side and the left hand side are,

$$\begin{aligned} AX + BX\delta &= A(X_c + A_0 S_{\langle\alpha;1\rangle} w) + BX_c \cdot \langle\alpha; 1\rangle (I - T_{\left\langle \frac{1}{\alpha};1\right\rangle}) S_{\langle\alpha^2;1\rangle} u \\ &\quad + BA_0 S_{\langle\alpha;1\rangle} w \cdot \langle\alpha; 1\rangle (I - T_{\left\langle \frac{1}{\alpha};1\right\rangle}) S_{\langle\alpha^2;1\rangle} u \end{aligned} \tag{4.9}$$

$$D^*X = DX_c + A_0 \langle\alpha; 1\rangle S_{\langle\alpha;1\rangle} Dw \tag{4.10}$$

Observe that if $sh(t^*) \neq 0$, then $\sigma_{t^*}\dot{X} \cong \sigma_{t^*}\dot{X}_c$, and

$$\sigma_{t^*}(AX + BX\delta) = \begin{cases} \sigma_{t^*}(AX_c) & \text{if } sh(t^*) < 0 \\ \sigma_{t^*}(AX_c) + AA_0\mathbf{1} & \text{if } sh(t^*) > 0 \end{cases}$$

where $\mathbf{1} \in \mathbb{R}^n$ is a vector with all the elements equal to 1. Therefore, a differential equation for X_c in sensible time can be formulated as,

$$\dot{X}_c(t) = \begin{cases} AX_c(t) & \text{if } t < 0 \\ AX_c(t) + AA_0\mathbf{1} & \text{if } t > 0 \end{cases}.$$

Since X_c is continuous at 0, the continuous part of the solution must hold $X_c(0-) = X_c(0+)$. In addition, the initial condition of the generalized solution, $X(0-)$, and the initial condition for X_c are equivalent by the matching requirement. The solution for X_c is then,

$$X_c(t) = \begin{cases} e^{At}X_c(0-) & \text{if } t < 0 \\ e^{At}X_c(0-) + (e^{At} - I)A_0\mathbf{1} & \text{if } t \geq 0 \end{cases}.$$

Now, evaluate $t^* \in \mathbb{K}$ when $sh(t^*) = 0$. By factoring out the unlimited number $\langle \alpha; 1 \rangle$ in (4.9) and (4.10), the following holds,

$$A_0 S_{\langle \alpha;1 \rangle} Dw = BX(0-)(I - T_{\left\langle \frac{1}{\alpha};1 \right\rangle})S_{\langle \alpha^2;1 \rangle}u + BA_0 S_{\langle \alpha;1 \rangle} w \cdot (I - T_{\left\langle \frac{1}{\alpha};1 \right\rangle})S_{\langle \alpha^2;1 \rangle}u.$$

By using Proposition 5, Lemma 4 and taking the left inverse of Krylov scaling operator, the equation can further simplified to,

$$\begin{aligned} A_0 Dw &= BX(0-)S_{\left\langle \frac{1}{\alpha};1 \right\rangle}(I - T_{\left\langle \frac{1}{\alpha};1 \right\rangle})S_{\langle \alpha^2;1 \rangle}u \\ &\quad + BA_0 S_{\left\langle \frac{1}{\alpha};1 \right\rangle} S_{\langle \alpha;1 \rangle} w \cdot S_{\left\langle \frac{1}{\alpha};1 \right\rangle}(I - T_{\left\langle \frac{1}{\alpha};1 \right\rangle})S_{\langle \alpha^2;1 \rangle}u. \\ &= BX(0-)(I - T_{\langle 1;1 \rangle})S_{\langle \alpha;1 \rangle}u + BA_0 w \cdot (I - T_{\langle 1;1 \rangle})S_{\langle \alpha;1 \rangle}u. \end{aligned}$$

Let $t^* = 0 \cdot e_0 + s_1 e_1$. If $s_1 < 0$ or $s_1 > 1$, then $A_0 Dw = 0$ which coincides with the definition of the shape function. Therefore, the algebraic differential equation is derived, in insensible s_1 time axis, by

$$\begin{cases} A_0 \dot{w} = BX(0-) + BA_0 w \\ w(0) = 0, w(1) = \mathbf{1} \end{cases} . \tag{4.11}$$

Since the goal is to find the generalized bilinear system to generate the same jump $CX(0-)$, which was given as initial model, the general solution to (4.11) satisfies the equation

$$\begin{cases} A_0 w(s_1) = (e^{Bs_1} - I)X(0-) & \text{for } s_1 \in (0,1) \\ CX(0-) = A_0 \mathbf{1} = (e^B - I)X(0-) \end{cases} . \tag{4.12}$$

In case when $n = 1$, (4.12) corresponds to the solution in the previous scalar case with $A = 0$. The solution in (4.12) is the generalization to the $n-$dimensional case, and by having a solution for $B \in \mathbb{R}^{n \times n}$ and w function, a causal representation of the impulsive system in (4.8) is derived. There is more: If A_0 is invertible, then one can uniquely find the shape function w by having

$$w(s_1) = A_0^{-1}(e^{Bs_1} - I)X(0-).$$

4.2.3 Case 3: Horizontal Bouncing Ball Problem

In this example, a simple one dimensional horizontal bouncing ball problem is considered. The impulsive effect model is introduced in (2.22). The discussion of the scalar case with the bilinear control showed that if the jump is proportional to the prior state of the impact without the sign changes, then there exists a simple bilinear singular controller which represents the same effect. However, the bouncing ball is a typical example of when the velocity before and after the jump switches its sign. Here, the frictionless motion is considered. As

shown in Figure 2.1, a ball is moving on a horizontal frictionless surface where the wall is located at $x = 0$. The coefficient of restitution, γ is given as a constant in $(0, 1)$ interval. Let $X(t) \in \mathbb{R}^2$ for all $t \in \mathbb{R}$ where $X(t) = [x(t), v(t)]^T$, and $x(t)$ represents the position of the ball, and $v(t)$ represents the velocity of the ball at time t. Assume that the impact with the wall occurred at time $t = 0$, then the effect dynamics can be written as

$$\begin{cases} \dot{X} = \begin{pmatrix} 0 & 1 \\ 0 & 0 \end{pmatrix} X \\ \Delta v(0) = -(1+\gamma)v(0-) \end{cases} \iff D^*X = \begin{pmatrix} 0 & 1 \\ 0 & 0 \end{pmatrix} X + BX\delta. \tag{4.13}$$

The goal is to find proper B, and δ which generate the same effect equation. First, the singular shape function for δ is chosen to be a constant function and so it is induced by the ramp shape Heaviside function as defined in (3.5). The result of the n-dimensional case can be directly applied by choosing,

$$A = \begin{pmatrix} 0 & 1 \\ 0 & 0 \end{pmatrix}, C = \begin{pmatrix} 0 & 0 \\ 0 & -1-\gamma \end{pmatrix}.$$

Now, solve for B from the boundary condition of the shape function, (4.12),

$$\left(e^B - \begin{pmatrix} 1 & 0 \\ 0 & -\gamma \end{pmatrix} \right) X(0-) = 0. \tag{4.14}$$

Suppose that

$$e^B = \begin{pmatrix} a & b \\ c & d \end{pmatrix}$$

then by substituting to (4.14), $b = 0$, and $d = -\gamma$ hold since $x(0-) = x(0+) = 0$ at the impact with the wall. The values for a and c are free. Let $a = -\gamma$ and $c = 0$, then the

model B can be designed such that

$$B = \begin{pmatrix} \ln(\gamma) & \pi \\ -\pi & \ln(\gamma) \end{pmatrix}.$$

Therefore, the corresponding causal representation can be expressed as a bilinear singular control form by

$$D^*X = AX + \begin{pmatrix} \ln(\gamma) & \pi \\ -\pi & \ln(\gamma) \end{pmatrix} X\delta. \tag{4.15}$$

In sensible time, the trajectory of (4.15) shows an equivalent jump equation as in (4.13). More interestingly, in insensible time (s_1-axis), the dynamics are governed by the B matrix, and spirals inward to the origin. Therefore, (4.12) can now be written as

$$A_0 w(s_1) = (\gamma^{s_1} \begin{pmatrix} \cos(\pi s_1) & -\sin(\pi s_1) \\ \sin(\pi s_1) & \cos(\pi s_1) \end{pmatrix} - I)X(0-) \tag{4.16}$$

for all $s_1 \in (0, 1)$. The solution for the jump model A_0 can also be non uniquely determined and paired with the solution of the shape w by solving (4.16). The solution for A_0 in $CX(0-) = A_0\mathbf{1}$ can be non-uniquely found. Here, choose A_0 to be

$$A_0 = \begin{pmatrix} 1 & -1 \\ 0 & (-1-\gamma)v(0-) \end{pmatrix},$$

then $w = [w_1, w_2]^T$ can be solved. The solution for the shape functions is

$$w_1(s_1) = w_2(s_1) - \gamma^{s_1}\sin(\pi s_1) \tag{4.17}$$

$$w_2(s_1) = (\gamma^{s_1} cos(\pi s_1) - 1)/(-\gamma - 1) \tag{4.18}$$

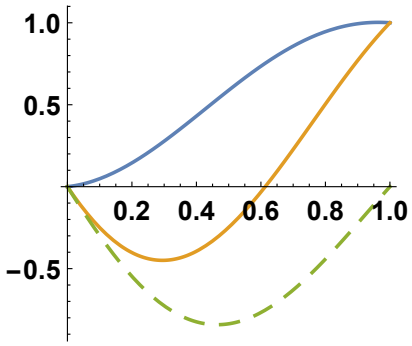

(a) Shpae functions: w_1, w_2 and $w_1 - w_2$

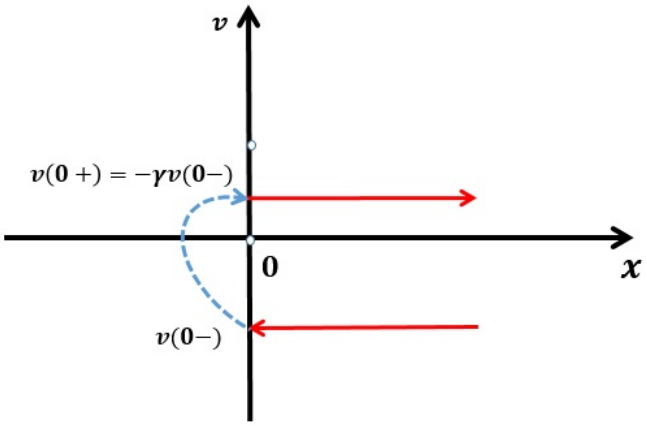

(b) Sensible and insensible state-space trajectory

Figure 4.2: Solution to the bouncing ball example

The plots of w_1 and w_2 when $\gamma = 0.7$ are shown in Figure 4.2a with a brown and blue solid line, respectively. As in the original model, (4.13), the jump only occurs in the velocity state, and so w_1 is not actually a shape function (since it is not a monotonically increasing function), but the difference between $w_1 - w_2$ has a meaning. The general causal solution for the first state can be written as

$$x(t) = -v(0-)t + S_{\langle\alpha;1\rangle}(w_1 - w_2)$$

where $w_1(0) - w_2(0) = 0$ and $w_1(1) - w_2(1) = 0$. However, the state $x(t)$ in the insensible time $t^* = s_1 e_1$ shows that $\sigma_{t^*} x = w_1(s_1) - w(s_2) = -\gamma^{s_1} \sin(\pi s_1)$, and it is shown in Figure 4.2a with a green dashed line. The figure implies that in the insensible time period,

the position has been slightly moved to the negative side while it slowed down the speed of the ball, and pushes the ball back into the reverse direction. The trajectory in the state-space of this insensible time motion is shown in Figure 4.2b. The dashed blue line shows the state transition in the insensible time, and the solid red represents the motion in sensible time. This is an example of the bump shape, $w_1 - w_2$, of the position, $x(t)$, in insensible time considered in [67], and Definition 19.

This example, together with the previous example on the scalar case, shows that in order to switch the sign of the state in a causal way, it is not possible to gradually change the state in the insensible time by passing through the equilibrium point. Therefore, in order to find a causal model which generates the sign change, one needs to think of expanding the state space into the higher dimensional space, and consider finding an infinitesimal trajectory as shown in Figure 4.2b that detours the equilibrium point.

4.3 Causal Modeling of Impulsive Forces

In contrast to the causal representation problem defined in Problem 1, the *impulsive contact force* modeling with the Krylov generalized function is considered in this section. The nonlinear affine system driven by the Lagrangian analysis in (2.11) is used. Different from Problem 1, the actuation $g_c(x)$ is fixed, and the objective is to find a *proper* generalized singular function which represent the impulsive contact force. In particular, the singular contact force satisfying one of the followings is pursued: The singular contact force should

1. generate the same desired jump as in the impulsive effect model in (2.21),

2. or generate different jump but with more relaxed assumptions than no slip condition in § 2.1.2.

In this section, two examples are considered. First, the horizontal bouncing ball problem is analyzed now by deriving the contact force directly without finding the constant B matrix as shown in (4.15). A nonlinear visco-elastic model to generate the impulsive force

is introduced. Next, the singular contact force model for the passive compass gait walker is analyzed by relaxing the non-slip assumption, and consideration of the softness of the point foot. The infinitesimally soft foot is modeled by using two geometrically constrained springs. The singular shape function is then proposed at the end.

4.3.1 Horizontal Bouncing Ball

An impulsive effect model for frictionless horizontal bouncing ball is given in (2.22). The objective in this section is to find a generalized singular function, u^*, such that the solution of the following generalized ODE (GODE) in sensible time is equivalent to (2.22). The GODE is given as

$$\dot{X}(t) = \begin{pmatrix} 0 & 1 \\ 0 & 0 \end{pmatrix} X + \begin{pmatrix} 0 \\ 1 \end{pmatrix} u^* \tag{4.19}$$

where u^* is the generalized singular function.

Physically inspired model

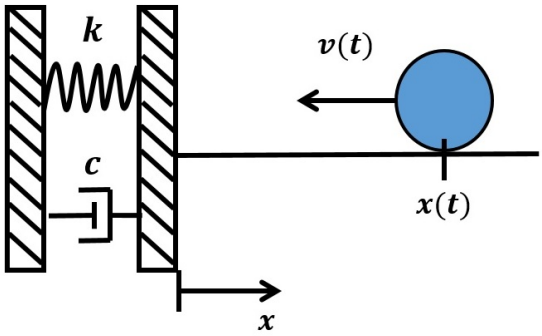

Figure 4.3: Insensible regularization for horizontal bouncing ball

A physically inspired contact force model is proposed with a nonlinear spring and damper having position dependent coefficients, $k(x_1)$ and $c(x_1)$, respectively, as shown in Figure 4.3. These coefficients are modeled as unlimited numbers when $x_1 = 0$, which repre-

sents the hard wall model in sensible time. On the other hand, these coefficients can also be understood as a sequence of nonlinear state dependent spring and damper in insensible time. Therefore, the suggested generalized force is modeled as

$$
\begin{aligned}
u^* &= -k(x_1)x_1 - c(x_1)x_2 && (4.20)\\
k(x_1) &= \frac{\pi^2}{1-\zeta^2}\delta^2(x_1) && (4.21)\\
c(x_1) &= \frac{2\pi\zeta}{1-\zeta^2}\delta(x_1), && (4.22)
\end{aligned}
$$

where ζ corresponds to the damping ratio of the insensible spring and damper model. By choosing $\zeta = -\ln(\gamma)/\pi$, the total system is underdamped with $\zeta \in (0,1)$ for $\gamma \in (e^{-\pi}, 1)$. In the next section, it is shown that this Krylov-based state dependent singular control, (4.20), generates the same jump in the velocity as in (2.22). In the proposed model, the constant singular shape function for δ is used, which is defined in (3.5) by choosing the power $n = 1$. In addition, the δ^2 defined in Eqn (3.5) is used.

Krylov-based solution

In this section, the generalized solution of (4.19) with an initial condition $X(t_0) = (x_0, v_0)^T$ where $x_0 > 0$ and $v_0 < 0$ is pursued. The initial condition represents that the ball initially moves towards the wall with constant velocity, and so $x_1(t) = v_0(t - t_0) + x_0$. The initial time for the collision is at $t_1 = t_0 - x_0/v_0$. For simplicity, assume that $t_0 = x_0/v_0 < 0$ so that $t_1 = 0$, and assume that $\gamma \in (e^{-\pi}, 1) = (0.043, 1)$ to make the system under-damped. By using the general form of the non-smooth formation in (3.15), the following solution is proposed,

$$
\begin{aligned}
x_1 &= x_{c1} + \langle 1/\alpha; 1\rangle\, S_{\langle\alpha;1\rangle} w_1 && (4.23)\\
x_2 &= x_{c2} + a_1 S_{\langle\alpha;1\rangle} w_2 && (4.24)
\end{aligned}
$$

where w_1 is some bump shape function, w_2 is the original shape function, x_{c1} and x_{c2} are continuous functions, and a_1 is the corresponding instantaneous jump of x_2 in the system. Let $X_c = (x_{c1}, x_{c2})$, then by taking the generalized derivative, the following holds:

$$\dot{X} = \dot{X}_c + \begin{pmatrix} S_{\langle\alpha;1\rangle} D w_1 \\ a_1 \langle\alpha;1\rangle S_{\langle\alpha;1\rangle} D w_2 \end{pmatrix}. \tag{4.25}$$

The right hand side of (4.19) can also be computed as

$$\begin{pmatrix} x_{c2} + a_1 S_{\langle\alpha;1\rangle} w_2 \\ -k(x_1)x_1 - c(x_1)x_2 \end{pmatrix}. \tag{4.26}$$

Now evaluate (4.25) and (4.26) at the Krylov time $t^* = s_0 e_0 + s_1 e_1$, and solve for a_1, w_1, w_2, x_{c1}, and x_{c2} by using the boundary conditions for the shape functions,

$$w_1(0) = w_1(1) = w_2(0) = 0, w_2(1) = 1,$$

and the initial condition, $x_1(0-) = 0$ and $x_2(0-) = v_0$.

First, suppose that $sh(t^*) < 0$, then

$$\dot{X}_c = \begin{pmatrix} x_{c2} \\ 0 \end{pmatrix}$$

holds, which gives $x_{c2}(t) = v_0$ and so $x_{c1}(t) = v_0 t$ for sensible time $t < 0$. Similarly, suppose that $sh(t^*) > 0$, then

$$\dot{X}_c = \begin{pmatrix} x_{c2} + a_1 \\ 0 \end{pmatrix}$$

holds, which gives $x_{c2}(t) = v_0$ and so $x_{c1}(t) = (v_0 + a_1)t$ for sensible time $t > 0$.

Now for the case in the insensible time $t^* = 0e_0 + s_1 e_1$ where $s_1 \in (0, 1)$, the generali-

zed derivative for x_1 gives that

$$S_{\langle\alpha;1\rangle} Dw_1 = v_0 + a_1 S_{\langle\alpha;1\rangle} w_2$$

so by taking the left inverse operator, $S_{\langle 1/\alpha;1\rangle}$,

$$Dw_1 = a_1 w_2 + v_0 \tag{4.27}$$

holds. Similarly, by multiplying $(1/a_1) \cdot \langle 1/\alpha; 1\rangle \, S_{\langle 1/\alpha;1\rangle}$ to the left and right for $\dot{x}_2$,

$$\begin{aligned} Dw_2 = \; & -\tfrac{\langle 1/\alpha;1\rangle S_{\langle 1/\alpha;1\rangle} k(x_1)}{a_1} \cdot (S_{\langle 1/\alpha;1\rangle} x_{c1} + \langle 1/\alpha; 1\rangle \, w_1) \\ & -\tfrac{\langle 1/\alpha;1\rangle S_{\langle 1/\alpha;1\rangle} c(x_1)}{a_1} \cdot (S_{\langle 1/\alpha;1\rangle} x_{c2} + a_1 w_2), \end{aligned}$$

holds. Since the desired jump, a_1, is $-(\gamma+1)v_0$ in (2.22), assume that $v_0 + a_1 > 0$ holds. Simplify the above equation further by evaluating $\langle 1/\alpha; 1\rangle \, S_{\langle 1/\alpha;1\rangle} \delta(x_1)$ at $t^* = 0e_0 + s_1 e_1$, then

$$\begin{aligned} \sigma_{s_1 e_1} \langle 1/\alpha; 1\rangle \, S_{\langle 1/\alpha;1\rangle} \delta(x_1) &= \sigma_{s_1 e_1} \langle 1/\alpha; 1\rangle \, S_{\langle 1/\alpha;1\rangle} (\langle \alpha; 1\rangle \, (I - T_{\left\langle \frac{1}{\alpha};1\right\rangle}) S_{\langle \alpha^2;1\rangle} u \circ x_1) \\ &= \sigma_{s_1 e_1} (I - T_{\langle 1;1\rangle}) S_{\langle \alpha;1\rangle} u \circ x_1 \\ &= 1, \end{aligned}$$

holds for all $s_1 \in (0,1)$ since $x_1(s_1) = (v_0 + a_1)s_1 > 0$. Similarly, $\langle 1/\alpha; 1\rangle \, S_{\langle 1/\alpha;1\rangle} \delta^2(x_1)$ is evaluated at $t^* = 0e_0 + s_1 e_1$ as

$$\begin{aligned} \sigma_{s_1 e_1} \langle 1/\alpha; 1\rangle \, S_{\langle 1/\alpha;1\rangle} \delta^2(x_1) &= \sigma_{s_1 e_1} \langle 1/\alpha; 1\rangle \, S_{\langle 1/\alpha;1\rangle} (\left\langle \alpha^2; 1\right\rangle \, (I - T_{\left\langle \frac{1}{\alpha};1\right\rangle}) S_{\langle \alpha^2;1\rangle} u^2 \circ x_1) \\ &= \sigma_{s_1 e_1} \langle \alpha; 1\rangle \, (I - T_{\langle 1;1\rangle}) S_{\langle \alpha;1\rangle} u^2 \circ x_1 \\ &= \langle \alpha; 1\rangle \, . \end{aligned}$$

Therefore, Dw_2 is now simplified to

$$\begin{aligned} Dw_2 &= -\frac{\pi^2 \langle \alpha; 1 \rangle}{a_1(1-\zeta^2)} \cdot (0 + \langle 1/\alpha; 1 \rangle w_1) - \frac{2\pi\zeta}{a_1(1-\zeta^2)} \cdot (v_0 + a_1 w_2) \\ &= -\frac{\pi^2}{a_1(1-\zeta^2)} w_1 - \frac{2\pi\zeta}{a_1(1-\zeta^2)}(v_0 + a_1 w_2). \end{aligned}$$

By augmenting (4.27), the ordinary differential equation for the shape functions is derived,

$$\begin{pmatrix} \dot{w}_1 \\ \dot{w}_2 \end{pmatrix} = \begin{pmatrix} 0 & a_1 \\ -\frac{\pi^2}{a_1(1-\zeta^2)} & -\frac{2\pi\zeta}{(1-\zeta^2)} \end{pmatrix} \begin{pmatrix} w_1 \\ w_2 \end{pmatrix} + \begin{pmatrix} v_0 \\ -\frac{2\pi\zeta v_0}{a_1(1-\zeta^2)} \end{pmatrix}.$$

The two point boundary condition for w_1 and w_2 gives a unique solution,

$$\begin{aligned} w_1(s_1) &= \frac{v_0}{\pi} e^{-\pi\zeta s_1} \sin(\pi s_1) \\ w_2(s_1) &= \frac{-v_0(1 + e^{-\pi\zeta s_1}(\zeta \sin(\pi s_1) - cos(\pi s_1)))}{a_1} \end{aligned}$$

As expected, the bump shape function w_1 matches the zero boundary conditions, $w_1(0) = w_2(0) = 0$. By matching the boundary condition for the original shape function, w_2, it can be shown that

$$\begin{aligned} w_2(0) &= 0 \\ w_2(1) &= -v_0(1 + e^{-\pi\zeta})/a_1 \\ &= 1 \end{aligned}$$

holds. Therefore,

$$a_1 = -v_0(1 + e^{-\pi\zeta}) = -v_0(1 + e^{\ln(\gamma)}) = -(1+\gamma)v_0$$

holds since $\zeta = -\ln(\gamma)/\pi$ was given initially. By substituting a_1 to generate the solution

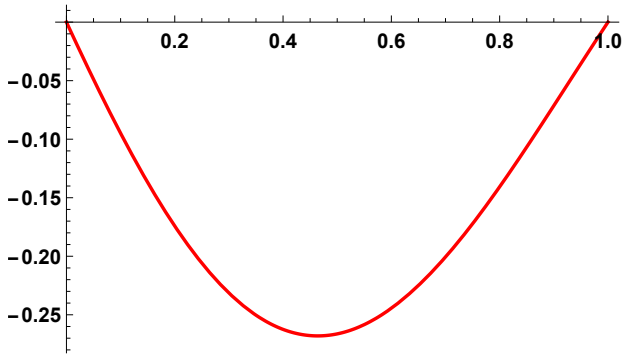

(a) Bump shape for w_1

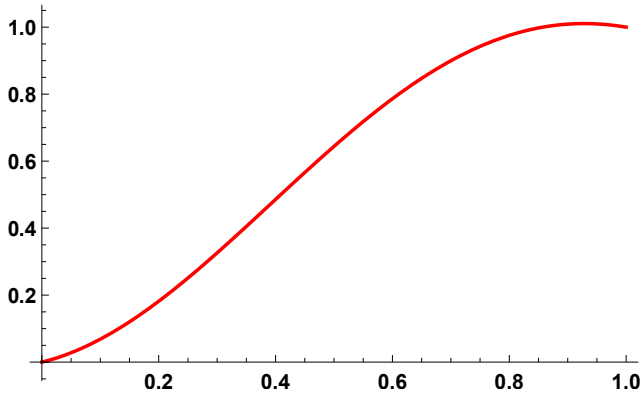

(b) Shape function for w_2

Figure 4.4: Graphs of the solution, w_1 and w_2

for w_2,

$$w_2(s_1) = \frac{1 + e^{-\pi\zeta s_1}(\zeta \sin(\pi s_1) - cos(\pi s_1))}{1+\gamma}.$$

is obtained. This shows that the shape function w_2 smoothly connects from 0 to 1 in insensible time $s_1 \in (0,1)$, and the generated jump in the velocity domain is $\Delta x_2(t) = -(1+\gamma)v_0$, which is the desired jump in (2.22). The graph of the bump shape function, w_1, is shown in Figure 4.4a.

In addition, the necessary condition for the correct bump shape function holds since $\dot{w}_1(0) = v_0 = \dot{x}_1(0-)$ and $\dot{w}_1(1) = a_1 + v_0 = -\gamma v_0 = \dot{x}_1(0+)$. The negative value of w_1 shape function shows that in insensible time the ball moves towards to the negative value, and pulls it back to the original position at $s_1 = 1$.

4.3.2 Compass Gait Walker with Infinitesimal Foot

In the previous bouncing ball example, the generalized singular contact force produces the same jump as described in the impulsive effect model. In contrast, a singular contact force model is studied here which generates a different jump than the impulsive effect model in (2.19). There are two assumptions in the impulsive effect model make the reset map algebraically computable for the compass gait walker model in § 2.1.2. One is that the robot has a *point foot*, and the other is that the collision is inelastic such that the point foot cannot slip after the collision: the foot velocity becomes zero immediately. In this section, these two assumptions are relaxed by supposing that the size of the foot is not equal to zero but it is infinitesimal, and that elastic components exist in the infinitesimal foot model which smoothly stop the foot.

Infinitesimal Foot Model

In the swing phase, the degrees of freedom is two by fixing the stance foot while swinging. In this section, it is assumed that there exist an elastic foot with sole length $L > 0$ which is connected to the end of the swinging leg. The model of the foot is shown in Figure 4.5b. This foot composed of two springs which are attached to the end of the foot, and the angle between the two springs are fixed at 90 degrees. Refer to the end of the swing leg on top of the foot as the *tipping point*. Observe that this geometric constraint on the position of the springs is holonomic, and confines the movement of the tipping point to slide on the semicircle shown in Figure 4.5 with the dashed line.

In this walking model, three assumptions are made at the insensible moment of the impact.

Assumption 1 (Flat foot landing)**.** *The foot always lands flat to the ground.*

Assumption 2 (Inelastic collision of the sole to the ground)**.** *After the sole of the foot lands on the ground, the sole stays adhere to the ground.*

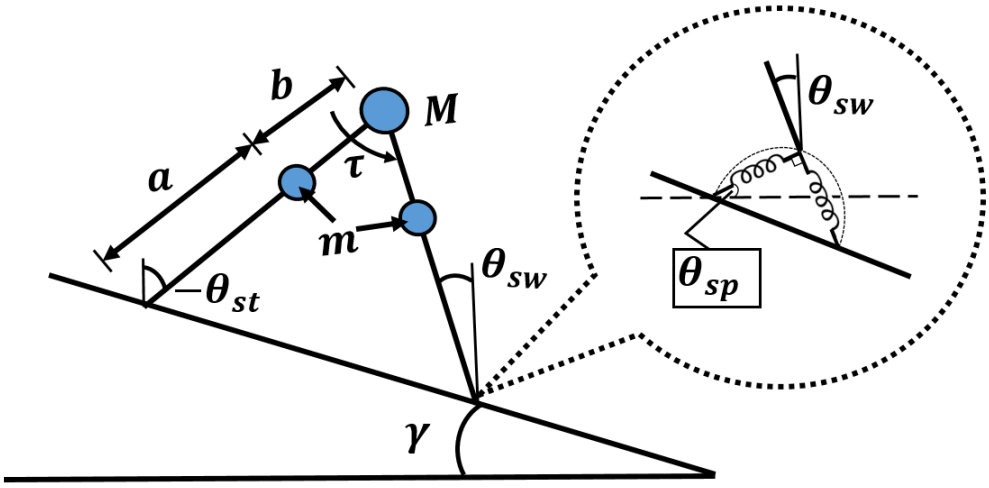

(a) Infinitesimal foot model before the impact

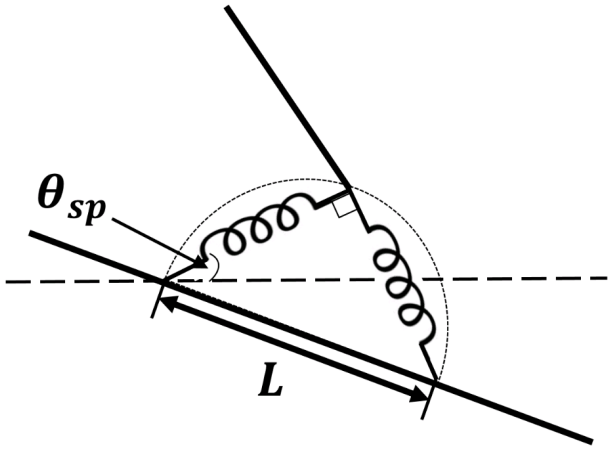

(b) Infinitesimal foot

Figure 4.5: Infinitesimal foot model

Assumption 3 (Arriving on the tangent plane)**.** *The velocity of the tipping point at the impact is in tangent to the holonomic surface.*

It is important to remark that the second assumption is different from the no slip assumption in § 2.1.2 since the *tipping point*, which is the point foot in the effect model, can still slide on the semi-circle. This model is inspired by the softness of human fingers where the elastic components imitate the behavior of the soft skin. The finger can always slightly move even when it is contacted to some rigid surface. The elastic foot in this section is a simplified model of the point foot which respects the softness at the tip. In addition, by

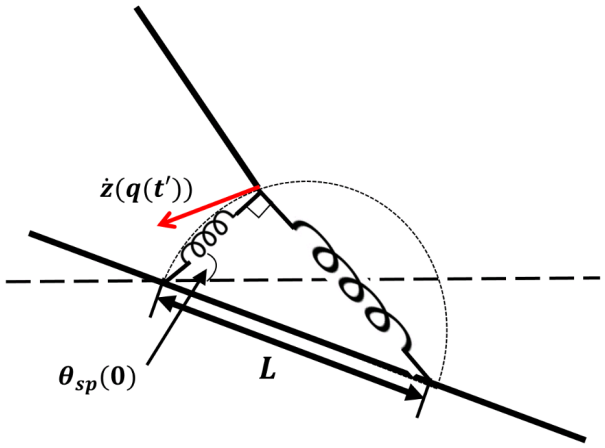

Figure 4.6: Initial condition satisfying the holonomic constraint

having the third assumption, there is no impulsive effect due to the holonomic constraint of the foot. This is shown in Figure 4.6 that the velocity of the tipping point is in the tangent to the semi circle at the moment of the impact.

Now, choose

$$L = l\epsilon \tag{4.28}$$

where $\epsilon > 0$ is the infinitesimal, and let k be the spring constant. Similar to the nonlinear singular spring model in (4.20), choose k to be infinitely large number,

$$k = \beta/\epsilon^2 \tag{4.29}$$

for some limited constant $\beta > 0$. Since the length of the spring is bounded by L, the potential energy for the both spring would be also bounded by $1/2\beta l^2$. Therefore, by using this infinitesimal foot model, the spring stores the finite energy in a very short time, which represents the impulsive behavior generated by the singular contact force acting on the tipping point.

Impact Phase

In the effect model, the impacting behavior occurs when the swinging leg touches the ground, and the velocity of the point foot is pointed towards the ground. Graphically it is shown in Figure 4.5a. In the infinitesimal foot model, a different switching surface is used since the foot cannot penetrate the ground. Suppose that $z(q)$ represents the tipping point coordinate where q is the generalized coordinate of the swinging phase, and $\dot{z}(q)$ represents the corresponding velocity of the tipping point. At each point $q \in S_q^+$ where S_q^+ is the feasible configuration in (2.14), there exist a unique semi-circle which the bottom part touches the flat ground with diameter $L'(z(q), \dot{z}(q)) > 0$ as shown in Figure 4.6. Therefore, as the swinging foot get close to the switching surface S in the effect model, there always exist a configuration q such that $L'(z(q), \dot{z}(q)) = L$. Let t' be the switching time satisfing

$$L'(z(q(t')), \dot{z}(q(t'))) = L.$$

After $t \geq t'$, the system enters the impact phase. In this impact phase, although there are two additional spring components, the total degrees of freedom becomes three due to the holonomic constraints and Assumption 2. The generalized coordinate is defined as

$$q := \begin{pmatrix} \theta_{sw} \\ \theta_{st} \\ \theta_{sp} \end{pmatrix} \tag{4.30}$$

where θ_{sp} is the angle of the first spring to the horizontal axis as shown in Figure 4.6, and the origin is at the heel of the foot on the ground. Let

$$(x_F(t'), y_F(t')) := z(q(t')) - (x_m(q(t'), y_m(q(t'))$$

be the tipping point coordinates in the new coordinate system where $(x_m(q(t')), y_m(q(t'))$ is the heel location (backend with respect to the motion) and $z(q(t'))$ is the tipping point in the previous coordinates (swinging phase). Observe that $(x_F(t'), y_F(t'))$ is on the holonomic surface of the foot.

Now the initial conditions in the impact phase are given as

$$q(0) := \begin{pmatrix} \overline{\theta}_{sw}(t') \\ \overline{\theta}_{st}(t') \\ \arctan\left(y_F(t')/x_F(t')\right) \end{pmatrix} \tag{4.31}$$

where $\overline{\theta}_{sw}$ and $\overline{\theta}_{st}$ are the generalize coordinates in the swinging phase, and the generalized initial velocities are given as

$$\dot{q}(0) := \begin{pmatrix} \dot{\overline{\theta}}_{sw}(t') \\ \dot{\overline{\theta}}_{st}(t') \\ 1/(x_F(t')^2 + y_F(t')^2)(x_F(t')\dot{\overline{z}}_y - y_F(t')\dot{\overline{z}}_x) \end{pmatrix} \tag{4.32}$$

where $(\dot{\overline{z}}_x, \dot{\overline{z}}_y)$ is the tipping point velocity $\dot{z}(q(t'))$ in the swinging phase. The initial tipping point velocity is graphically shown in Figure 4.6.

The position of the tipping point, CoM of legs, and CoM of the hip are now represented by the new generalized coordinates,

$$\begin{cases} z_x(q) = L\cos(\theta_{sp} + \gamma)\cos(\theta_{sp}) \\ z_y(q) = L\cos(\theta_{sp} + \gamma)\sin(\theta_{sp}) \end{cases} \tag{4.33}$$

$$\begin{cases} x_1(q) = z_x(q) - a\sin(\theta_{sw}) \\ y_1(q) = z_y(q) + a\cos(\theta_{sw}) \end{cases} \tag{4.34}$$

$$\begin{cases} x_M(q) = x_1(q) - b\sin(\theta_{sw}) \\ y_M(q) = y_1(q) + b\cos(\theta_{sw}) \end{cases} \tag{4.35}$$

$$\begin{cases} x_2(q) = x_M(q) + b\sin(\theta_{st}) \\ y_2(q) = y_M(q) - b\cos(\theta_{st}) \end{cases} \tag{4.36}$$

where (4.33) shows the tipping point coordinate, (4.34) is the swing leg CoM coordinate, (4.35) is the hip coordinate, and (4.36) is the stance leg coordinate.

Suppose that the spring have the natural length $l_0 := L/\sqrt{2}$, and k is the spring coefficient for both springs, then the potential energy and kinetic energy can be written as

$$\begin{aligned} V(q) &:= mg(y_1(q) + y_2(q)) + Mgy_M(q) + \frac{1}{2}k(L\cos(\theta_{sp}+\gamma) - l_0)^2 \\ &\quad + \frac{1}{2}k(L\sin(\theta_{sp}+\gamma) - l_0)^2 \\ K(q) &:= \frac{1}{2}(m(\dot{x}_1(q)^2 + \dot{y}_1(q)^2) + m(\dot{x}_2(q)^2 + \dot{y}_2(q)^2) + M(\dot{x}_M(q)^2 + \dot{y}_M(q)^2)). \end{aligned}$$

The equation of motion is then derived using the Lagrangian method described in § 2.1.1. The full equation of nonlinear affine form in (2.11) is not shown in this thesis but it can be derived analytically using symbolic solvers.

Now, the total force acting on the tipping point can be computed as

$$F_T(q) := -kL((\cos(\theta_{sp}+\gamma) - 1/\sqrt{2}) - (\sin(\theta_{sp}+\gamma) - 1/\sqrt{2}))\cos(\theta_{sp}) \tag{4.37}$$

$$F_N(q) := -kL((\cos(\theta_{sp}+\gamma) - 1/\sqrt{2}) + (\sin(\theta_{sp}+\gamma) - 1/\sqrt{2}))\sin(\theta_{sp}) \tag{4.38}$$

where $F_T(q)$ and $F_N(q)$ are horizontal and vertical component of the force, respectively. Since k and L is a function of ϵ in (4.29) and (4.28), the contact force can also be represen-

ted in terms of ϵ,

$$F_T^{(\epsilon)}(q) := \sqrt{2}\frac{l\beta}{\epsilon}\sin(\theta_{sp}+\gamma-\pi/4))\cos(\theta_{sp}) \tag{4.39}$$

$$F_N^{(\epsilon)}(q) := \sqrt{2}\frac{l\beta}{\epsilon}(1-\sin(\theta_{sp}+\gamma+\pi/4))\sin(\theta_{sp}). \tag{4.40}$$

Observe that if $\gamma = 0$, then $F_N^{(\epsilon)}$ represents the normal force to the surface, and it is non-negative since $\theta_{sp} \in (0, \pi/2)$. The actual normal force for $\gamma > 0$ can be computed as

$$F_T^{(\epsilon)}(q)\sin(\gamma) + F_N^{(\epsilon)}(q)\cos(\gamma). \tag{4.41}$$

Since the force is depending only on the lengths of two springs, it can be shown that the normal force is always non-negative. This non-negative condition is valid since the ground contact force should only push and not pull the robot as given in (2.15).

In the impact phase, the infinitesimal foot will first compress the spring to *stop* the tipping point. The impact phase will last until the tipping point stop moving, which can be interpreted as the point foot has been stop in the original effect model. The time derivative of the tipping point is computed as

$$\begin{aligned}\dot{z}_x(q) &= -L\sin(2\theta_{sp}+\gamma)\dot{\theta}_{sp}\\ \dot{z}_y(q) &= L\cos(2\theta_{sp}+\gamma)\dot{\theta}_{sp}.\end{aligned}$$

Therefore, the velocity of the tipping point is zero if and only if $\dot{\theta}_{sp} = 0$. Let $t_1(\epsilon)$ be the first time that $\dot{\theta}_{sp} = 0$, then the contact force $F_c^{(\epsilon)}(t) = (F_T^{(\epsilon)}(q(t)), F_N^{(\epsilon)}(q(t)))$ is defined for $t \in [0, t_1(\epsilon)]$, where $F_T^{(\epsilon)}$ and $F_N^{(\epsilon)}$ are defined in (4.39) and (4.38), respectively.

Let $\epsilon := \langle\epsilon_n\rangle$ be the representation of the infinitesimal ϵ, then it is obvious that $t_1(\epsilon_n)$ monotonically decreases to zero as ϵ_n approaches to zero since the spring constant gets

infinitely large. The impulse due to the contact force can be computed as

$$\begin{aligned}\Lambda_T^{\epsilon_n} &:= \int_0^{t_1(\epsilon_n)} F_T^{\epsilon_n}(t)dt \\ \Lambda_N^{\epsilon_n} &:= \int_0^{t_1(\epsilon_n)} F_N^{\epsilon_n}(t)dt\end{aligned}$$

for each $n \in \mathbb{N}$.

By taking the generalized integral evaluated at $t_1(\epsilon)$, the following holds,

$$\begin{aligned}\Lambda_T^{\epsilon} &:= \left\langle \int_0^{t_1(\epsilon_n)} F_T^{\epsilon_n}(t)dt \right\rangle \\ \Lambda_N^{\epsilon} &:= \left\langle \int_0^{t_1(\epsilon_n)} F_N^{\epsilon_n}(t)dt \right\rangle .\end{aligned}$$

Since the stored energy in the spring is bounded, the impulses, Λ_T^{ϵ} and Λ_N^{ϵ} are limited, and so a nonzero shadow point exists. By formulating the generalized integral equation as in (4.3), a sequence of differential equations can be obtained, and the weak solution can be pursued.

In addition, the structure of the normal contact force $F_N^{(\epsilon)}$ resembles the generalized singular function in (20) such that the amplitude is infinitely large by $1/\epsilon$, and the envelope is non negative. The envelope can be understood as a singular shape function defined in Definition 20. Now, by properly choosing $\alpha := 1/t_1(\epsilon_n)$ for some n, one can approximate the singular control force in the form of (3.17).

Remark. It is important to mention that, for each fixed ϵ_n, the tipping point is moving. Therefore, the assumption used in the impulsive effect method, i.e. the preservation of the angular momentum about the point foot, does not hold anymore since the point foot (the axis of rotation) is not in the inertial frame. Suppose the $\overline{p}$ is the center of mass location of the compass gait robot, and the $z(q)$ be the tipping point, then the angular momentum in

the non-inertial frame is computed as

$$L_r := L_{cm} + (\overline{p} - z(q)) \times (2m + M)\dot{\overline{p}} - (\overline{p} - z(q)) \times (2m + M)\dot{z}(q),$$

where L_{cm} is the angular momentum about the center of mass and $\times$ is the cross product. The last term involving $\dot{z}(q)$ terms is generated by the fictitious torque which is only considered in the non-inertial frame. Therefore, for given ϵ_n, the final generalized velocities for q will be changed due to this fictitious torque.

Back to Swinging Phase

Once the tipping point is stopped, the generalized velocity is computed accordingly for each ϵ_n. By relabeling the swinging and stance leg as in [15], the swinging phase is re-initiated with a new *velocity reset* in sensible time. Therefore, a new reset map is defined by solving the impact phase model for $[0, t_1(\epsilon_n)]$ time,

$$\dot{\overline{q}}_{sw}(0) = \langle \dot{q}_{st}(t_1(\epsilon_n)) \rangle \tag{4.42}$$

$$\dot{\overline{q}}_{st}(0) = \langle \dot{q}_{sw}(t_1(\epsilon_n)) \rangle \tag{4.43}$$

where q is the generalized coordinate in impact phase, and $\overline{q}$ is the generalized coordinate in the swinging phase.

Simulation

Symbol	m	M	a	b	γ
Values	5kg	10kg	0.5m	0.5m	2 degree

Table 4.1: Parameters for the compass gait

In this section, a numerical example for a specific choice of ϵ_n is considered. The parameters used in the compass gait problem are given in Table 4.1. Let the initial conditions

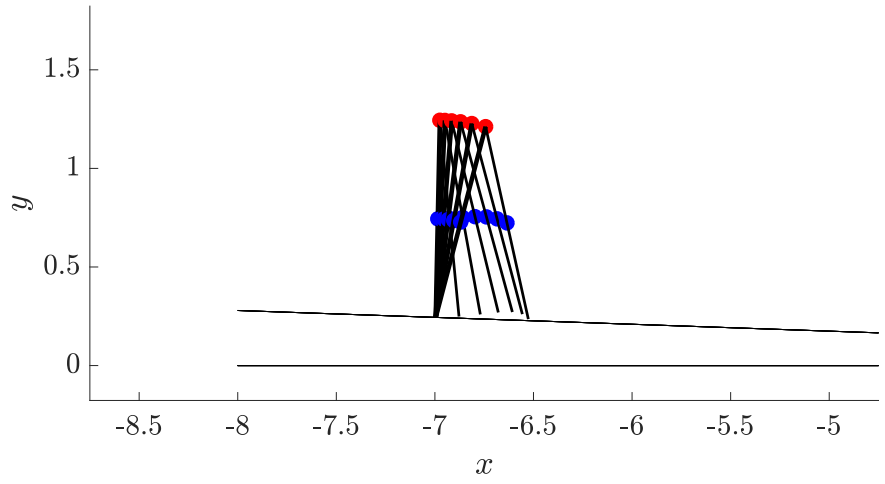

Figure 4.7: The first swinging phase.

be given as

$$\begin{aligned} \theta_{sw}(0) &= 0 \\ \theta_{st}(0) &= 0 \\ \dot{\theta}_{sw}(0) &= 2 \\ \dot{\theta}_{st}(0) &= -0.4. \end{aligned}$$

Let $\epsilon_n = 0.001$, and $\beta = 550$, then the corresponding foot length, and the spring constant are given as

$$\begin{aligned} L &= 0.001\ m \\ k &= 5.5 \times 10^8\ Nm^{-1}. \end{aligned}$$

The simulation for the first swinging phase is shown in Figure 4.7 where blue circles represents the CoM of each leg with mass, m, and the red circle represents the CoM of the hip with mass, M. Once the infinitesimal foot touches the slope, the system switches

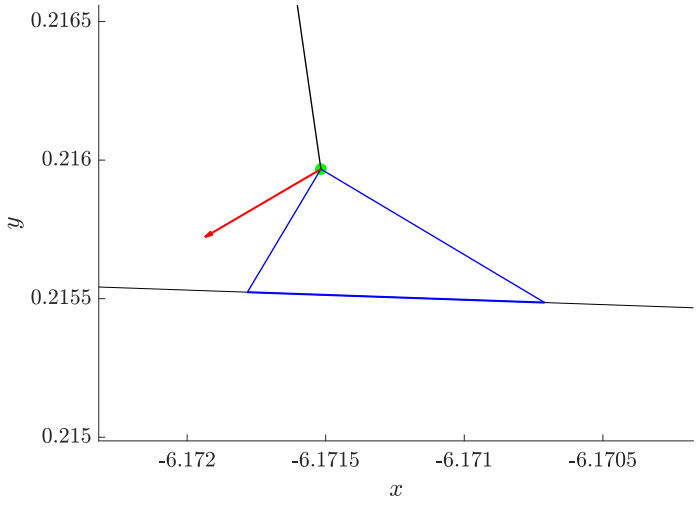

(a) Initial condition for the second impact phase

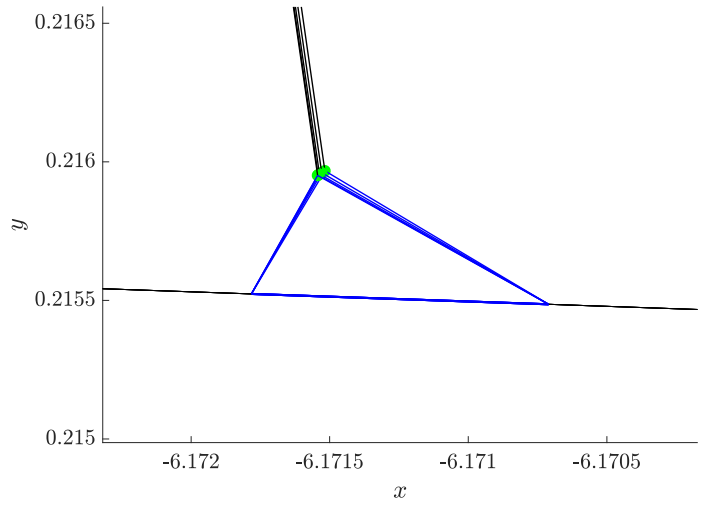

(b) Compression phase

Figure 4.8: Simulation of impact phase

to impact phase, and the initial condition is shown in Figure 4.8a, where the green circle represents the tipping point, the red arrow represents the initial tipping point velocity, and the blue triangle represents the foot model as in Figure 4.6. The simulation in the impact phase is shown in Figure 4.8b. Once the velocity of the tipping point reached zero, the system switches back to swinging phase with updated generalized velocity for $\dot{\theta}_{sw}$ and $\dot{\theta}_{st}$.

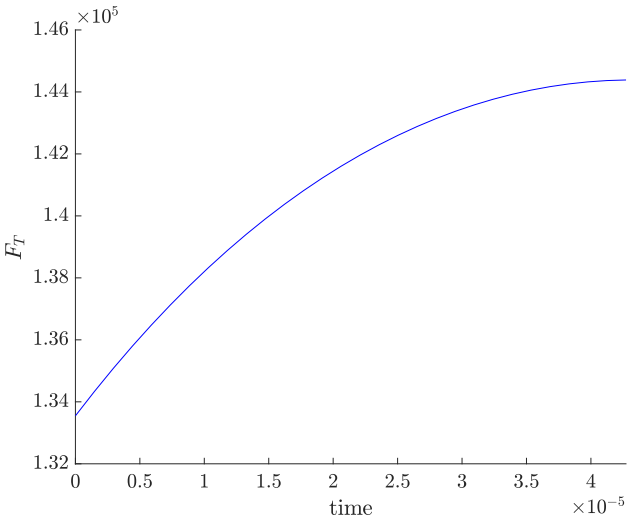

(a) Tangent force, F_T

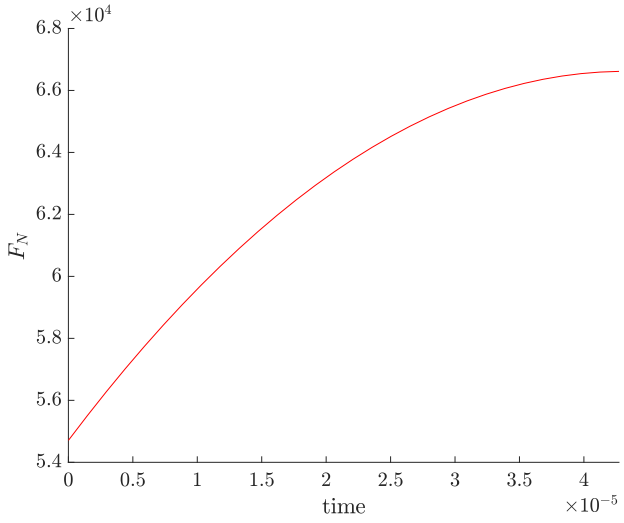

(b) Normal force, F_N

Figure 4.9: Force acting on the tipping point on second impact phase

The duration to stop the tipping point is numerically computed as

$$t_1(0.001) = 4.272 \times 10^{-5}.$$

The corresponding normal force and tangent force in that impact phase are shown in Figure 4.9. By normalizing the area to be one, the singular shape function can be obtained for each F_N and F_T. Different from the example in the bouncing ball problem in § 4.3.1,the

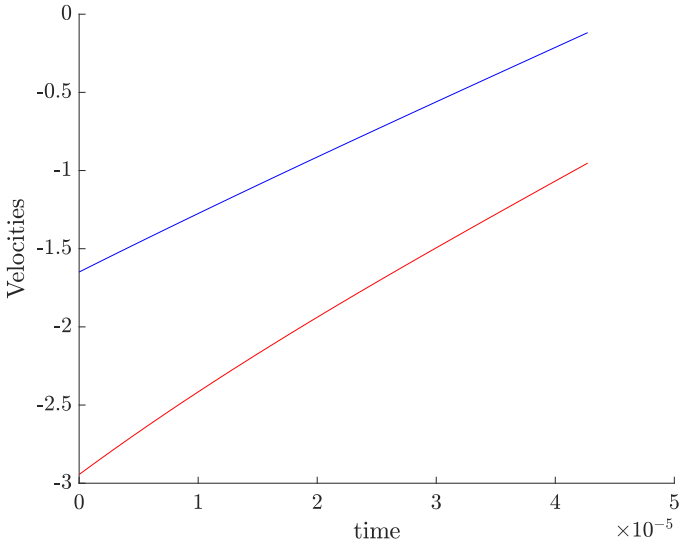

(a) Generalized velocities

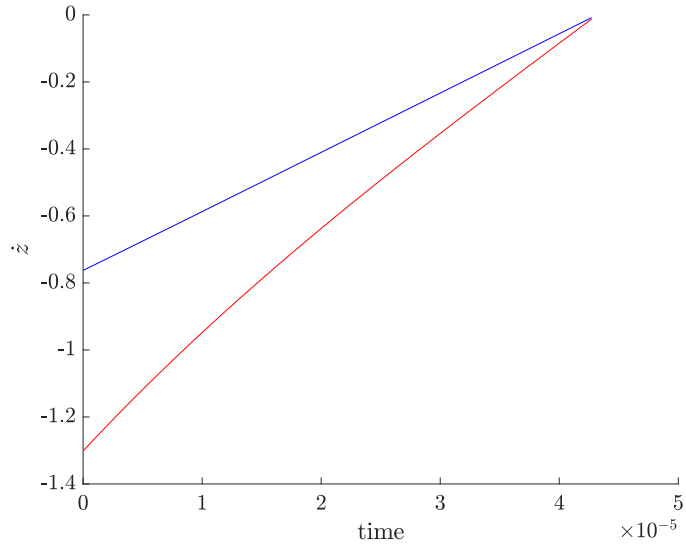

(b) Tipping point velocity

Figure 4.10: Continuization during the second impact phase

singular shape function is no longer constant as shown in Figure 4.9.

The corresponding continuous change in the tipping point velocity, and the generalized coordinates, $\dot{\theta}_{sw}$ and $\dot{\theta}_{st}$, are shown in Figure 4.10. The tipping point velocity goes to zero at t_1 as shown in Figure 4.10b where red and blue curves represent the x and y components of the velocity, respectively. The continuous change in the generalized velocities are shown in Figure 4.10a where the red and blue curves represent $\dot{\theta}_{sw}$ and $\dot{\theta}_{st}$, respectively.

Step	θ_{sw}	θ_{st}	$\dot{\theta}_{sw}$ (Effect)	$\dot{\theta}_{st}$ (Effect)	$\dot{\theta}_{sw}$ (Causal)	$\dot{\theta}_{st}$ (Causal)
1.	0.2048	-0.2736	-1.1947	-0.4596	-1.1943	-0.4588
2.	0.1427	-0.2100	-0.9335	-0.1029	-0.9524	-0.1181
3.	0.1473	-0.2155	-1.0431	-0.4778	-1.0572	-0.4953
4.	0.1543	-0.2238	-1.0909	-0.5885	-1.1056	-0.6211
5.	0.1602	-0.2296	-1.0926	-0.5557	-1.1055	-0.5843
6.	0.1603	-0.2289	-1.0621	-0.4618	-1.0754	-0.4817
7.	0.1551	-0.2234	-1.0379	-0.4189	-1.0604	-0.4469
8.	0.1557	-0.2241	-1.0570	-0.4734	-1.0582	-0.4749
9.	0.1530	-0.2215	-1.0425	-0.4540	-1.0425	-0.4537
10.	0.1507	-0.2191	-1.0393	-0.4643	-1.0600	-0.4911
11.	0.1551	-0.2241	-1.0744	-0.5354	-1.0969	-0.5747
12.	0.1599	-0.2290	-1.0850	-0.5321	-1.0909	-0.5433
13.	0.1577	-0.2261	-1.0506	-0.4442	-1.0667	-0.4662
14.	0.1550	-0.2232	-1.0446	-0.4424	-1.0559	-0.4570
15.	0.1536	-0.2221	-1.0477	-0.4633	-1.0778	-0.5037

Table 4.2: Comparison of the reset between the effect model and the causal model

The updated generalized velocities for all 15 gaits are given in Table 4.2. The reset acquired from the reset map in (2.18) is shown in fourth and fifth columns, and the new generalized velocities at the end of the compression are shown in the last two columns. The new reset does not significantly change but it differs by the order of 10^{-2}, which is still considerably large since the integral duration of the impulse is in the order of 10^{-5}.

Finally, the overlaid simulation for 15 walks is shown in Figure 4.11a, and the phase portrait on the projected state space, $(\theta_{sw}, \theta_{st})$ is shown in Figure 4.11b, which graphically show that the new velocity reset is within the basin of attraction of the original compass gait periodic orbit.

In contrast to the effect modeling, by using the causal analysis of the model, the new reset map is proposed to better approximate the soft landing behavior during the impact with an infinitesimally small deformable foot.

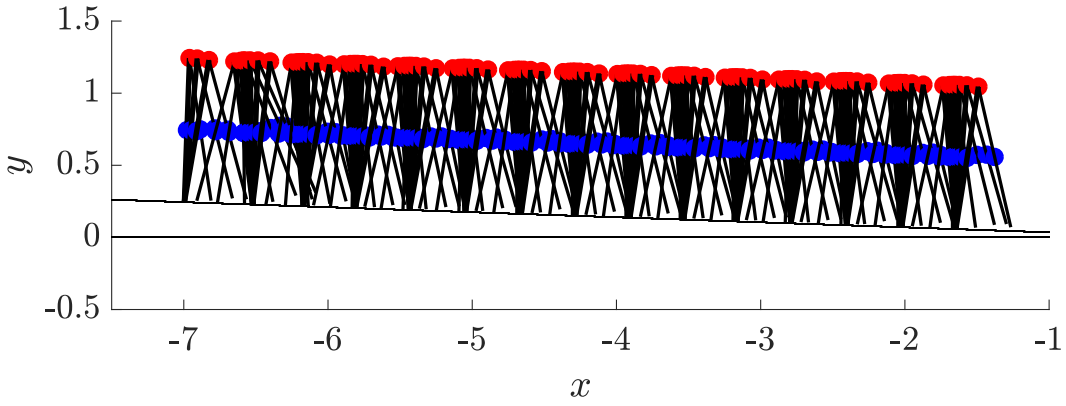

(a) Overlaid walking gaits

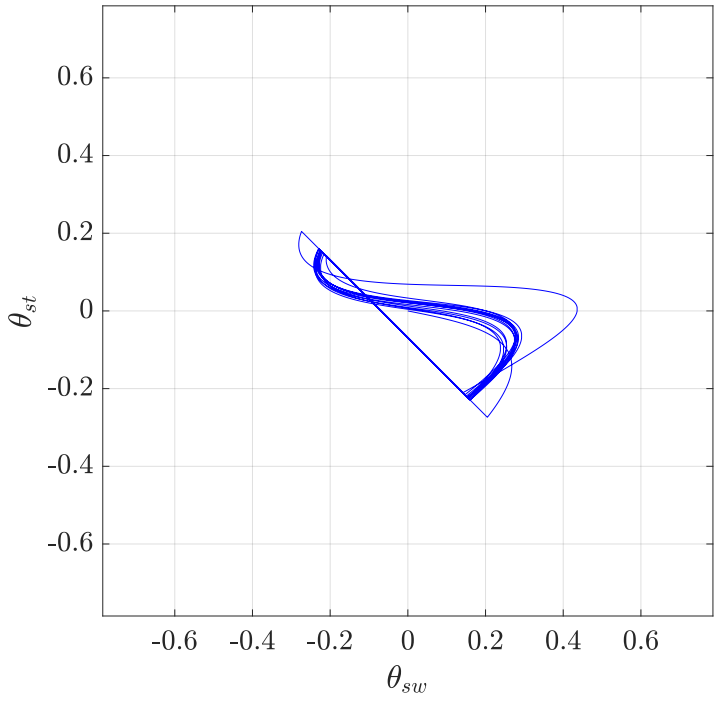

(b) Phase Portrait

Figure 4.11: Simulation of 15 steps

Part II

Safe Trajectory Planning using Polynomials: Algebra to Geometry

CHAPTER 5

ALGEBRA: POINT MASS ROBOTS PATH PLANNING

In contrast to the infinitesimal modeling of the motion in *insensible time*, a trajectory generation of point mass robots in the planar space in *sensible time* is considered in this chapter using the algebraic properties of the polynomials. The (x, y) coordinate of the point mass robot is identified with a unique complex number using the standard conversion from $\mathbb{R}^2$ to $\mathbb{C}$. The trajectory of a single robot and the trajectories of multiple robots are then generated by tracking the roots of smoothly varying polynomials.

This chapter is organized as follows. In 5.1, a background of the trajectory generation problem is introduced. An obstacle avoidance problem for a single point mass robot is reviewed in 5.1.1, and multi-agent safe formation control problem is reviewed in 5.1.2. A generalized root locus (GRL) method is introduced and analyzed in 5.2. The proposed algorithm using GRL method for a single robot path planning is introduced in 5.3, and its extended usage in multi-agent formation control is proposed in 5.4.

5.1 Introduction

The fundamental technique in this chapter relies on the classical root locus (RL) principle in the linear system theory but the objective of the usage of RL is completely different, and the generalized root locus is used instead.

5.1.1 Obstacle Avoidance Trajectory Generation

Path planning in the presence of obstacles has been analyzed intensively in the past decades. One of the most studied method is the potential field method (PFM) [68]. An obstacle-detouring path can be obtained by placing a fixed positive charge on the obstacles, and a fixed negative charge on the goal stage in order to create a force field. By tracking the

trajectory of a movable positive charge, one can easily find the collision free trajectories [69]. However, the PFM may create local minima at points of force equilibria, whereby the robot stops moving prior to arriving at the goal stage.

Using gradient descent on a harmonic potential field solves the problem of local minima [70, 71], since a harmonic function does not contain extremal valued points inside the domain. The problem for the local minimum is resolved by placing the goal at the minimum point on the boundary. Through gradient descent, the path converges to the minimum point of the harmonic function, which is the goal state. For obstacle avoidance, the obstacles are designed to be maximal points of the harmonic function. Extensive work using the harmonic field method (HFM) can be found in [72, 73, 70, 74]. The early work in [71, 75] presents the fundamental solution of the Laplace equation [76] with the poles having a fractional order of multiplicity less than 1 in the harmonic function. The fractional order pole warps the whole plane so that $\lim_{|s|\to\infty} |H(s)| \to \infty$ where H is the harmonic function in $\mathbb{C}$. By changing the fractional order of the pole at the obstacle location, the author controls the safety guard of the obstacles. Most previous work using the HFM focuses on finding a particular vector field satisfying the obstacle avoidance constraints but not on finding a set of all possible obstacle avoiding trajectories given a flow vector field. A notable exception is [74] proposing a method based on the heat transfer equation, which initially propagates in omnidirectional ways by modeling the starting point as a heat source. However, full analysis of the gradient dynamics is not performed, nor has the set of possible trajectories been formally defined. In this section, a new framework to define a set of trajectories evolving from a fixed starting point to the end point is proposed, where all the paths meet the obstacle avoidance constraints.

Another approach, similar to the HFM, and proposed in [77] uses the reciprocal root locus method to find a non-colliding path for the mobile vehicles. Instead of harmonic functions, the work uses meromorphic functions for the potential field in the complex domain and suggests a path design following the root locus (RL). Heuristic approaches to using

the RL plot are given rather than the complete mathematical (gradient) dynamics of the path. Furthermore, since the reciprocal RL also creates artificial poles and zeros that are not real obstacles nor targets, the path dynamics are affected by the undesired obstacles and targets. In addition, the reciprocal RL only produces at most two paths since it only uses 180 or 0 degree RL path. It is also not guaranteed that either path will converge to the desired zero since there are multiple zeros in different locations. Therefore, in this section, the full dynamics of the root locus path is analyzed, and a new framework to define the set of trajectories is proposed not by using the classical root locus but by evolving the generalized root locus driven from complex coefficient characteristic equations. Furthermore, it is also shown that the generalized root locus path actually follows the gradient descent of some harmonic function, which infers that following the RL path is a special form of the HFM method.

The generalized root locus has been studied in [78, 79, 61], with [80] explaining the fundamental rules for the generalized root locus (GRL). The paper [79] presents the potential field which creates a particle motion on root locus path, and formally gives a set theoretic definition. Building from the definition of GRL from [79], an alternative definition is proposed which regards the GRL as a set of curves parameterized by the gain k, and which gives a non-unique means to define the GRL by reparameterizing with a different speed. The multi-definition of the curve will be used in solving an optimization problem with a state dependent speed constraint.

The research literature on finding optimal, obstacle avoiding paths is extensive. Related papers are [81, 82, 83, 84]. The papers [81] and [82] propose a minimum length path problem with circular shaped obstacles. In both papers, the map of the obstacles are binary so that outside of the boundary there is no effect nor cost on moving in any direction. However, in the case when the robots needs to navigate through the diffusion type of hazard such as a fire or radiation exposure [85], one cannot strictly define the binary border of which states are safe and which are not. Other related research in optimization can be

found in [83] and [84]. In both cases, the authors focused on feasible parametrization of the trajectory with kinematic constraints. Both papers presented the problem of the constant kinematic constraint due to the configuration of the robot. In this section, the minimum time problem under a speed constraint due to obstacles or hazards in the scene is considered.

5.1.2 Multi-Agent Formation Control

In a multi-agent system, the formation control problem is defined as follows: Given N robots in the space, find a trajectory for each robot such that they reaches to M targets asymptotically or in a finite time. Solutions to this problem have broad applications in a flight and traffic control [86], and the swarm behavior of birds [87]. In order to find such control, two question need to be answered. The first one is to find which one of M targets, each robot should arrive at. This problem is the *assignment problem* (or *perfect matching problem* in the graph theory). The second question is to design a trajectory for each robot to avoid collisions with other known obstacles (other robots) and to reach to the assigned target position. Depending on the available resources for each robot, the level of centralization or decentralization can be defined. A centralized method usually has a single global planner who assigns each robot to a particularly ordered target, and determines the trajectory of all the robots. This usually assumes perfect knowledge of the global coordination of each robot. In contrast, a decentralized method relies only on more relaxed assumptions on the resource and the algorithm is based on the local interaction in between each agent. In this section, a new framework for formation control is proposed where each robot only requires to know the relative position but not the global coordinate and does not require a predefined assignment to the target (decentralized), and each robot should agree on the definition of the shape or formation (centralized).

The first problem, assigning robots to the target formation while minimizing some cost, has been researched extensively in the past years. There are centralized methods such as a Hungarian method in [88] which maximizes the linear sum of the weights of the matching

edges in polynomial time, a time complexity of order $O(N^3)$. Other centralized perfect matchings are also available such as a stable matching in [89] or a gravitational allocation in [90]. There are also decentralized methods for finding assignments, such as using an auction-based method in [91], and using a decentralized Hungarian method in [92]. See the references therein. However, the decentralized algorithms require a communication channel between neighboring agents, so it is hard to apply in the absence of a communication link. In this section, an extended GRL method is used to eventually find a perfect matching which do not depend on the communication channel but only using the relative position sensing from other agents.

Full solutions to the formation control problem, where the control protocol allocates each robot to one of the targets, and solves the necessary control for each robot to reach its specific target, are widely researched. The recent survey on the formation control can be found in [93]. Instead of reaching to the fixed formation on the global coordinates, the definition of formation is relaxed to a certain level of invariant structures. Different definitions of the invariant set can be given: in [94], it is for a rotation, translation and permutation invariant formation to a given target position; in [95], it is for any permutation invariant formation satisfying a inter-robot distance condition; in [96, 97] it is for any permutation invariant formation to a given target position; and in [98, 99, 100], it is the exact given target position. Excepting [96], although the formation is permutation invariant, the solutions require for a robot to solve the assignment problem at least locally to be determined which target is locally best to follow in a given network condition. Amongst these papers, the safety property on avoiding collision between robots is considered in [96, 98, 99, 97]. In this section, the goal formation is defined as a permutation invariant shape, and a set of possible inter-robot collision free trajectories is generated by following the generalized root locus paths.

In the proposed framework, a representation space for the robots in a planar space is modeled as a space of polynomials where the roots of given polynomial are the locations of

the robots. Similarly, the target location can be modeled with another polynomial, and by following the root locus principle in § 5.2, a set of collision free trajectory which all converges to permutation invariant target formation is constructed. Therefore, the formation control can be designed in the space of polynomials, and the trajectory can be generated with a gradient flow in § 5.2. Notably, the authors of [96] have also proposed a framework for formation control problem using a linear transformation in a monic polynomial space. However, the method needed to use heuristics to compensate for existing problems: the nominal paths are sensitive to perturbations in the vector field, and the robots following the nominal paths may collide to each other at break points. The main reason why the nominal paths are perturbation sensitive is that the suggested trajectories are actually equivalent to following the subset of the root locus going from gain 0 to 1. By setting the target polynomial to be exactly at gain 1 makes convergence to the desired target points sensitive to disturbances. This is mainly due to the initial assumption on the formation space in [96] that the space is defined on a set of monic polynomial. In the proposed framework, a general polynomial space is used, and the generalized root locus is utilized to generate a set of trajectories. The asymptotic convergence to the goal of root locus method in [101] is guaranteed since the zeros are modeled as a target location, and the gain k goes to infinity.

5.2 Generalized Root Locus

Consider the open loop transfer function $H(s) := \frac{b(s)}{a(s)}$ where $s \in \mathbb{C}$, and $b(s)$ and $a(s)$ are monic polynomials with an order m and n, respectively. The values $\{p_i\}_{i=1}^{n}$ and $\{z_i\}_{i=1}^{m}$ are the corresponding poles and zeros of the open loop system. The closed loop transfer function with constant gain feedback $k \in \mathbb{R}$ is $H_{cl}(s) := \frac{H(s)}{1+kH(s)} = \frac{b(s)}{a(s)+kb(s)}$. The root locus plot is the trajectory of the solution of

$$a(s) + kb(s) = 0 \quad \text{or} \quad H(s) = -1/k \tag{5.1}$$

as k changes from 0 to ∞. In classical root locus plots, the characteristic equation from Eqn (5.1) has real coefficients. The generalized root locus extends the set of characteristic equations to those with complex coefficients [79] and the gain k to complex values. With this generalization, the closed loop system can theoretically have a non-conjugated poles and zeros. As the classical RL is obtained by sweeping the k values, the generalized root locus involves increasing $|k|$ in a certain direction (determined by the phase). The generalized characteristic equation can be written as

$$a(s) + ke^{j\theta}b(s) = 0 \quad \text{or} \quad H(s) = -e^{-j\theta}/k \tag{5.2}$$

where k changes from 0 to ∞ for any given $\theta \in [-\pi, \pi)$.

Definition 22 (Generalized root locus (GRL)[79])**.** *Given a* $\theta \in [-\pi, \pi]$. $GRL(\theta)$ *is a subset of* $\mathbb{C}$ *such that* $GRL(\theta) = \{s \in \mathbb{C} : a(s) + k_c b(s) = 0, k_c = k \cdot e^{j\theta}, k \in \mathbb{R}^+\}$.

The set $GRL(\theta) \subset \mathbb{C}$ is well defined, with $GRL(0)$ and $GRL(\pi)$ being the classical 0 and π root locus trajectories. Since $H(s)$ is a finite order rational function, it is also analytic. Using, then, the fact that $H(s)$ is first continuously differentiable, leads to an alternative definition of a GRL:

Definition 23 (GRL_θ as a parameterized curve)**.** *Given* $\theta \in [-\pi, \pi]$*, a function* $GRL_\theta : \mathbb{R}^+ \to \mathbb{R}^2$ *is defined as a parameterized differentiable curve,* $GRL_\theta(k) := \{(\mathrm{Re}(s), \mathrm{Im}(s)) \in \mathbb{R}^2 : a(s) + ke^{j\theta}b(s) = 0\}$.

Define $s(\theta, k) := GRL_\theta(k)$ as a generalized root locus branch parameterized by k at a given θ. Once θ has been chosen, there exists an intrinsic property that the generalized root locus follows.

Theorem 7 (The fundamental root locus angular equation)**.** *The following equation is true*

for all $k \in \mathbb{R}+$, where the equality is the 2π modulus equality.

$$\theta = \pi - \sum_{i=1}^{m} \angle(s(\theta, k) - z_i) + \sum_{i=1}^{n} \angle(s(\theta, k) - p_i). \tag{5.3}$$

Proof. Using (5.1) to solve for the angle, $\angle H(s) = \angle \frac{-1}{ke^{\theta}} = \pi - \theta + 2\pi \cdot r$ for any integer r. Thus, the equation holds and is k independent. □

The theorem shows that θ completely characterizes the curve. If $\theta_1 \neq \theta_2$, then

$$GRL(\theta_1) \cap GRL(\theta_2) = \phi.$$

In other words, two curves, GRL_{θ_1} and GRL_{θ_2}, do not intersect. The generalized fundamental angular equation follows a similar rule. Here, two important properties for solving the path planning problem are presented. More rules can be found in [80].

Proposition 6 (Angle equation of GRL[80])**.** *Let GRL_θ is given for some $\theta \in [-\pi, \pi]$. The angle of departure from a pole p_j and the angle of arrival to a zero z_j can be expressed as θ_d and θ_r respectively.*

$$\begin{aligned} n_p\theta_d &= \pm r\pi + \theta + \sum_{i=1}^{m} \angle(p_j - z_i) - \sum_{i=1}^{*n} \angle(p_j - p_i) \\ n_z\theta_r &= \pm r\pi - \theta - \sum_{i=1}^{*m} \angle(z_j - z_i) + \sum_{i=1}^{n} \angle(z_j - p_i) \end{aligned} \tag{5.4}$$

The n_p and n_z are the multiplicity of each poles and zeros, and r is an odd integers. The $*$ indicates the summation except when $i = j$.

Proof. Follows directly from the fundamental root locus angular equation. □

Note that the angle of departure and the angle of arrival can also be defined in terms of the new GRL_θ definition, assuming that the desired root locus arrives at the given zero.

Otherwise the limit can be the asymptotic direction.

$$\begin{aligned}\theta_d &= \arctan \frac{\partial}{\partial k} s(\theta, k)_{k=0} \\ \theta_r &= \lim_{M\to\infty} \arctan \frac{\partial}{\partial k} s(\theta, k)_{k=M}\end{aligned}$$

Definition 24 (Break point)**.** *A point, $s_b \in \mathbb{C}$, is called a break point if s_b is a root of (5.2) and its order of multiplicity is greater than 1 for some $\theta \in [-\pi, \pi)$ and $k \in (0, \infty)$.*

Different from the classical root locus, the next theorem holds for the GRL.

Theorem 8 (Existence of a break point)**.** *Let $a(s)$ and $b(s)$ are monic polynomials with degree N, relatively prime and all roots have multiplicity of 1, then there exist a break point s_b, and the total number of break points is less than or equal to $2N - 2$.*

Proof. If $N = 1$, then obviously there is no break point. Let $N > 2$. A necessary condition for s_b to become a break point is that it should be a root from $a'(s)b(s) - a(s)b'(s) = 0$. Since $a(s)$ and $b(s)$ are monic, relatively prime and all roots have multiplicity of 1, there exist $2N - 2$ possible roots to this equation, and the candidate roots s_b is not a root for $a(s)$ and $b(s)$. Let s_b satisfies $a'(s_b)b(s_b) - a(s_b)b'(s_b) = 0$, and let $k = |\frac{a(s_b)}{b(s_b)}|$. Now with this k value solve the (5.2), then $|H(s)| = \frac{1}{k} = |\frac{a(s_b)}{b(s_b)}|$ holds and so s_b is a candidate of the roots in Eqn (5.2). By choosing $\theta := \pi - \sum_{i=1}^{m} \angle(s_b - z_i) + \sum_{i=1}^{n} \angle(s_b - p_i)$, it can be shown that s_b is the roots of (5.2) for such k and θ, and so it is a break point. This was true for any roots s_b, and so the total number of break points are less than or equal to $2N - 2$. □

Directly from the theorem, a set of break points is defined.

Definition 25 (Set of break point angles)**.** *Let $a(s)$ and $b(s)$ are given as in Theorem 8. A set $B = \{\theta_1, \cdots, \theta_m\}$ is the set of angles θ_i which creates a break point, where $m \leq 2N - 2$.*

This theorem infers that there is a set, $B = \{\theta_{b1}, \cdots, \theta_{bm}\}$, where $m \leq 2N - 2$, such that if $\theta \notin B$, then all the trajectories $s(\theta, \cdot)$ will not intersect each other.

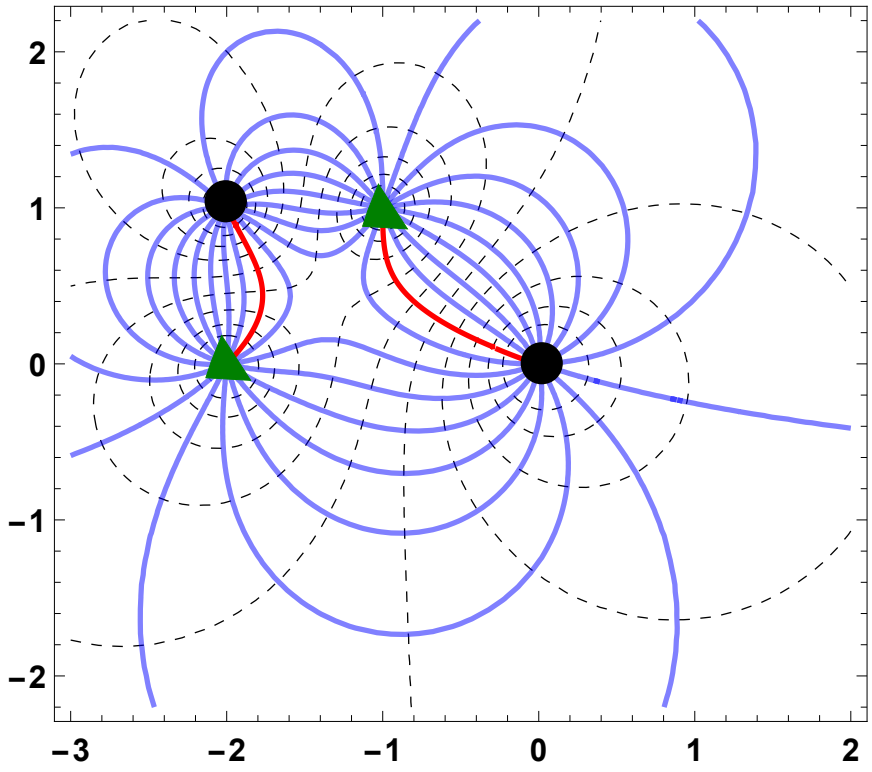

Figure 5.1: Multiple trajectories of GRL by different θ

Figure 5.1 graphically shows the example of a set of GRL when there exist two poles at $p_1 = -2$, $p_2 = -1 + i$ and two zeros at $z_1 = 0$ and $z_2 = -1 + i$. The blue curves represent the GRL with a θ value sampled by $\theta_i = \frac{i\pi}{9}$ for $i = \{1, \cdots, 18\}$, and the red curve shows the GRL with $\theta = 0$ (which are the classical root locus paths). As expected, no blue curve intersects. While it is not shown in the figure, one can see that there exist 2 break points located at $s_{b1} = -1.356 + 0.446i$ and $s_{b2} = -2.643 + 3.553i$. The corresponding θ values are $\theta_1 = -0.162\pi$ and $\theta_2 = 0.957\pi$. By using (5.4), two critical departure angle for p_1 and p_2 are found. Those angles are $\theta_{d1}(p_1) = 0.198\pi, \theta_{d2}(p_1) = -0.79\pi, \theta_{d1}(p_2) = -0.66\pi$ and $\theta_{d2}(p_2) = 0.45\pi$. The total number break points verifies the upper bound in Theorem 8 since the upper bound was $4 - 2 = 2$.

5.2.1 Gradient Flow

Define the function $F : \mathbb{R}^2 \to \mathbb{R}$ using the open loop transfer function as follows:

$$F(x, y) := \ln |H(s)| = \ln(\prod_{i=1}^{m} |(s - z_i)|) - \ln(\prod_{i=1}^{n} (s - p_i)) \tag{5.5}$$

whereby, with $s = x + jy$, the function is well defined except at the poles and zeros. Those points attain the supremum and infimum values of F, respectively. In this section, it is shown that the root locus always follows the negative gradient of F by deriving the dynamics of the generalized root locus, $s(\theta, \cdot)$. Here, $\cong$ is used instead of $=$ where $\cong$ indicates equality after the identification of $s \in \mathbb{C}$ and $(x, y) \in \mathbb{R}^2$. The isometry between two spaces preserves the topological structures. The level curves are shown in Figure 5.1. The dashed black curves are the level set of the F function, and as it is shown in [101], all the root locus path are orthogonal to the level curve of F function. A detailed analysis on F with the classical RL approach can be found in [61].

Define $\Omega = \mathbb{R}^2 \backslash \bigcup_{i \in \{1,\cdots,n\}, j \in \{1,\cdots,m\}} \{p_i, z_j\}$. Since the Laplace operator is linear, translation invariant, and F is a summation of translated fundamental solutions of the Laplace's equation, it satisfies $\Delta F(x, y) = 0$ on $(x, y) \in \Omega$ [76].

Further, let $C(k) := \{(x, y) \in \mathbb{R}^2 : F(x, y) = -\ln(k)\}$ be the $-\ln(k)$ level set of F. Then $(x, y) \in C(k)$ satisfies $F(x, y) = -\ln(k)$, so $|H(s)| = \frac{1}{k}$ for any given $k \in \mathbb{R}^+$. In other words,

$$C(k) \equiv \bigcup_{\theta \in [-\pi, \pi]} (\mathrm{Re}(s(\theta, k)), \mathrm{Im}(s(\theta, k))) \,. \tag{5.6}$$

The rational function $H(s)$ and the (natural) logarithm functions are conformal mappings, so the mapping $s \mapsto F(s)$ preserves the angle. Observe that $|F(s)| = k$ is a circle in $F(s)-$domain, and the set $\{F(s) \in \mathbb{C} : H(s) = ke^{j\theta}, \forall k \in \mathbb{R}+\}$ is a straight line from the origin in $F(s)-$ domain. The angle between the tangent of $C(k)$ and the straight line from the origin are always orthogonal. By properly defining the inverse of F locally, there

exist a unique inverse image of $C(k)$, and a unique inverse image of the straight line, which are orthogonal in the $s-$domain. Applying this insight properly over the complex domain leads to the conclusion that the root locus path and the level curves are always orthogonal.

Lemma 5. **(a)** $\nabla_{(x,y)} \ln|s-a| \cong \frac{s-a}{||s-a||^2}$ *holds for all* $s \in \mathbb{C}\backslash\{a\}$ *given* $a \in \mathbb{C}$.
(b) $\nabla_{(x,y)} F(s) \cong \overline{\sum_{i=1}^{m} \frac{1}{s-z_i} - \sum_{i=1}^{n} \frac{1}{s-p_i}}$ *for all* $s \in \Omega$.

Proof. (a) The following holds by by the chain rule:

$$\frac{\partial}{\partial x} \ln|x+jy-a| = \frac{1}{2}\frac{\partial}{\partial x} \ln|x+jy-a|^2 = \frac{\mathrm{Re}(s-a)}{||s-a||^2}$$

and

$$\frac{\partial}{\partial y} \ln|x+jy-a| = \frac{\mathrm{Im}(s-a)}{||s-a||^2}.$$

(b) It follows from (a) since

$$\frac{s-a}{||s-a||^2} = \frac{s-a}{(s-a)\overline{(s-a)}} = \frac{1}{\overline{s-a}},$$

and the linearity of differentiation, and the definition of F. □

The (gradient) dynamics of the generalized root locus are given in the next theorem.

Theorem 9 (Dynamics of the generalized root locus)**.** *Given the root locus,* $s(\theta,\cdot)$*, and let* $N(s(\theta,k)) := \frac{\nabla_{(x,y)} F(s(\theta,k))}{||\nabla_{(x,y)} F(s(\theta,k))||}$ *be the unit normal direction of the level curve* $C(k)$*, then*

$$\frac{\partial}{\partial k} s(\theta,k) = -\frac{1}{k||\nabla_{(x,y)} F(s(\theta,k))||} N(s(\theta,k)). \tag{5.7}$$

Proof. By taking the derivative of the characteristic equation (5.1) at some $k \in (0,\infty)$, it follows that $a'(s(\theta,k)) \cdot \frac{\partial}{\partial k} s(\theta,k) + b(s(\theta,k)) + kb'(s(\theta,k)) \cdot \frac{\partial}{\partial k} s(\theta,k) = 0$ and so the

derivative of $s(\theta, k)$,

$$\begin{aligned}
\frac{\partial}{\partial k} s(\theta, k) &= -b(s(\theta, k))/(a'(s(\theta, k)) + kb'(s(\theta, k))) \\
&= -b(s(\theta, k))/(a'(s(\theta, k)) - a(s(\theta, k))b'(s(\theta, k))/b(s(\theta, k))) \\
&= 1/(k \cdot (a'(s(\theta, k))/a(s(\theta, k)) - b'(s(\theta, k))/b(s(\theta, k)))).
\end{aligned}$$

Since $a(s)$ and $b(s)$ are a product of monic polynomials, $\frac{a'(s)}{a(s)} = \sum_{i=1}^{n} \frac{1}{s-p_i}$ and $\frac{b'(s)}{b(s)} = \sum_{i=1}^{m} \frac{1}{s-z_i}$, and so $\frac{a'(s)}{a(s)} - \frac{b'(s)}{b(s)} = -(\sum_{i=1}^{m} \frac{1}{s-z_i} - \sum_{i=1}^{n} \frac{1}{s-p_i})$. Therefore, by the previous lemmas,

$$\begin{aligned}
\frac{\partial}{\partial k} s(\theta, k) &= -1/(k\sum_{i=1}^{m} 1/(s(\theta, k) - z_i) - \sum_{i=1}^{n} 1/(s(\theta, k) - p_i)) \\
&= -1/(k\overline{\nabla_{(x,y)} F(s(\theta, k))}) \\
&= -\nabla_{(x,y)} F(s(\theta, k))/(k||\nabla_{(x,y)} F(s(\theta, k))||^2) \\
&= -N(s(\theta, k))/(k||\nabla_{(x,y)} F(s(\theta, k))||).
\end{aligned}$$

□

The root locus follows the negative gradient of F, confirming that the level lines and the root locus path are orthogonal. Figure 5.2 graphically illuminates the result of the theorem. The open loop transfer function was chosen to have $p_1 = -2$, $p_2 = -1+i$ and double zeros at the origin. The black dashed curves represents the level curves of F, and the blue curves represent the root loci with different angles $\theta_i = \frac{i\pi}{8}$ for $i = \{1, \cdots, 15\}$ counterclockwise from the one above the red curve. The red curve corresponds to $\theta = 0$. Observe that $H(s)$ has a non-conjugated pole (p_2) not allowed in the classical root locus. In addition, the change of the angle θ smoothly changes the direction of the path.

Note that given $K \in (0, \infty)$, the trajectory of the $s(\theta, K)$ for all θ was equal to $C(K)$ by (5.6). This shows that if the motion of the robot follows the (5.7), then all the root loci paths arrive at the level set $C(K)$ at the same time. Although the arrival times are all same

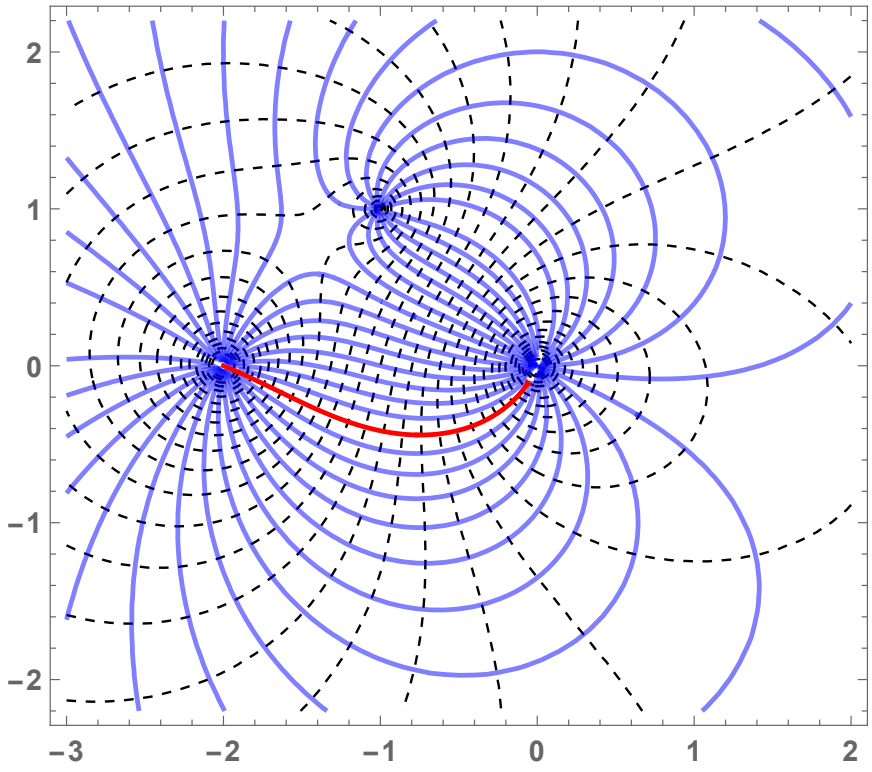

Figure 5.2: Level lines of F (black) and trajectories of GRL_θ (blue).

for every path, the lengths traveled are different since the speed is not uniform for the paths. The next subsection covers how to change the speed of the curve while following the same root locus path.

5.2.2 Reparametrization of the generalized root locus

Here three reparameterizations of the root locus curve are presented. The first rescales the k by $t := \ln(k)$ where $\frac{dt}{dk} = \frac{1}{k}$. Since the logarithmic function is strictly increasing and continuously differentiable in $(0, \infty)$, by the inverse function theorem, the inverse is also continuously differentiable, and so it can be used as a reparameterization of the differentiable curve. Suppose that $s_t(\theta, t) := s(\theta, e^t)$ where the lower subscript t represents time, then

$$\frac{\partial}{\partial t} s_t(\theta, t) = \frac{\partial s(\theta, k)}{\partial k} \frac{dk}{dt} = -\frac{N(s_t(\theta, t))}{||\nabla_{(x,y)} F(s_t(\theta, t))||}. \tag{5.8}$$

The new parameterized curve $s_t(\theta, \cdot) : \mathbb{R} \to \mathbb{R}^2$ has its domain in the entire $\mathbb{R}$, and it starts from $p \cong \lim_{t\to-\infty} s_t(\theta, t)$ to $z \cong \lim_{t\to\infty} s_t(\theta, t)$ if the root locus traverses from the pole p to the zero z.

The second reparameterization is by arc length. By the fundamental theorem of the local theory of curves [102], there exists an arc length reparameterization of the regular curve $s(\theta, \cdot)$. Since the arc-length parameterized curve has unit speed, the dynamics can be expressed as

$$\frac{\partial}{\partial r} s_a(\theta, r) = -N(s_a(\theta, r)), \tag{5.9}$$

where the lower subscript a represents arc length. The $s_a(\theta, r)$ are defined on $(0, L(\theta))$ where $L(\theta)$ is the length of the curve.

Lastly, let the curve $s_a(\theta, r)$ start from $s_a(\theta, 0+) = p_j$ for some j, and $0+$ represents an infinitesimally small positive number. Suppose that the speed of the curve is given to be $\frac{1}{||\nabla_{(x,y)} F_j(s)||}$ where $F_j(s) := -\ln(\prod_{i=1, i\neq j}^{n} |s - p_i|)$. Geometrically F_j is same as F except the pole at p_j and zeros have been removed. Therefore $||\nabla_{(x,y)} F_j(s)||$ is bounded along any given root locus path, $s(\theta, \cdot)$. This specific speed profile will be chosen as a state dependent constraint in the optimization section. More details will be explained in the next section; here the existence of such reparameterization is verified.

Theorem 10 (Reparameterization with a state dependent speed $||\nabla_{(x,y)} F_j(s)||^{-1}$)**.** *Given the arc-length parameterized root locus, $s_a(\theta, \cdot)$, where $s_a(\theta, 0+) = p_j$, then there exist a monotonically increasing function $g : [0, a] \to [0, L(\theta)]$ in $C^1([0, a], [0, L(\theta)])$ for some $a > 0$ such that $s_{new}(\theta, p) = s_a(\theta, g(p))$ and*

$$\frac{\partial}{\partial p} s_{new}(\theta, p) = -\frac{1}{||\nabla_{(x,y)} F_j(s_{new}(\theta, p))||} N(s_{new}(\theta, p)). \tag{5.10}$$

Proof. Let $J(p) := \int_0^p ||\nabla_{(x,y)} F_j(s_a(\theta, r))|| dr$. The function J is well defined on $[0, a]$ for any given $a > 0$ since $||\nabla_{(x,y)} F_j(s_a(\theta, r))||$ is bounded. Note that J is monotonically increasing and continuously differentiable by the fundamental theorem of calculus (FTC).

In addition, by the inverse function theorem, there exist a continuously differentiable inverse, J^{-1}, and it is also a monotonically increasing function. Let $a = J(L(\theta))$, and define $g : [0, a] \to [0, L(\theta)]$ where $g(p) := J^{-1}(p)$, then g is also a monotonically increasing function in $C^1([0, a], [0, L(\theta)])$. By definition, $J(g(p)) = p$, and so $J'(g(p))g'(p) = 1$. This shows that $g'(p) = \frac{1}{J'(g(p))}$. By invoking FTC again, $J'(g(p)) = ||\nabla_{(x,y)} F_j(s_a(\theta, g(p)))||$ holds, and so $g'(t) = \frac{1}{||\nabla_{(x,y)} F_j(s_a(\theta, g(p)))||}$. This shows that $s_{new}(\theta, p) := s_a(\theta, g(p))$ is a well defined parameterized curve.

Now, by taking derivative of $s_a(\theta, g(p))$ in p, the speed of parameterized curve is as desired,

$$\frac{\partial}{\partial p} s_{new}(\theta, p) = \frac{\partial}{\partial r} s_a(\theta, g(p))g'(p) = -\frac{1}{||\nabla_{(x,y)} F_j(s_{new}(\theta, p))||} N(s_{new}(\theta, p)).$$

□

5.3 A Single Robot Path Planning

5.3.1 Optimal Obstacle Avoidance Path Planning

This section presents a solution to the path planning problem in the $2-$dimensional plane where the locations of the obstacles are fixed.

Generating a set of trajectories

Suppose that there exist $n - 1$ obstacles with their center of mass are located at $p_i \in \mathbb{C}$ for each $i = \{1, \cdots, n - 1\}$, then the objective is to determine a trajectory which goes from $p_n \in \mathbb{C}$ to $z \in \mathbb{C}$ while avoiding the obstacle locations. Start by placing a single pole at all p_i for all obstacles, and n zeros at z. By using the harmonic field method (HFM), following the negative gradient will guarantee that starting from any non-singular point, p_n, will converge to the zero location.

Different from classical HFM, a singular point p_n is assumed at the start location by

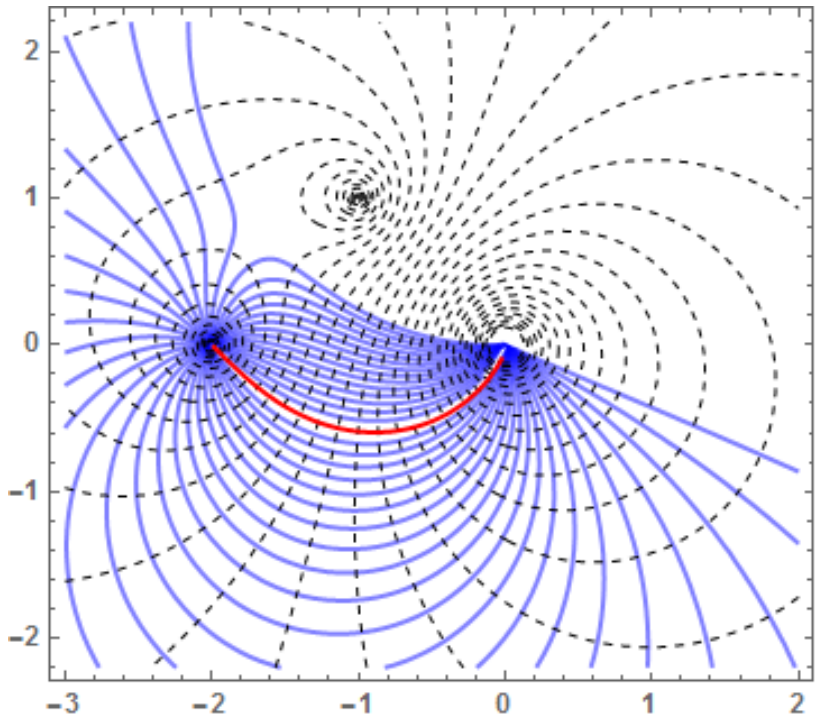

Figure 5.3: Set of admissible trajectories.

placing an additional pole there. The main advantage of this modification is the additional freedom it gives to chose the departure direction. By Theorem 9, it is shown that every root locus follows the negative gradient direction, and it can be fully characterized by its angle of departure, θ_d. Furthermore, Proposition 6 shows that θ_d can be uniquely identified with θ, Therefore, any generalized root locus path, GRL_θ starting from p_n, converges to the goal state while avoiding the center of the mass location of the obstacles. The convergence occurs since the transfer function has an equal number of poles and zeros. Figure 5.3 has a graphical picture of the set of trajectories. In this example, the starting point is at $p_2 = -2$, an obstacle is at $p_1 = -1 + j$, and the goal state is located at $z = 0$. The blue lines represent possible obstacle avoiding trajectories. The start direction has been sampled to show 41 trajectories. The black dashed lines represents the level lines of F.

There are multiple means to evaluate the trajectories, all depending on the speed of propagation (which is parametrization dependent). From the discussion in §5.2.2, four

such families of trajectories are:

$$
\begin{aligned}
U_k &:= \{s(\theta,\cdot) : \text{(5.7) holds } \forall\, \theta \in [-\pi,\pi]\};\\
U_t &:= \{s_t(\theta,\cdot) : \text{(5.8) holds } \forall\, \theta \in [-\pi,\pi]\};\\
U_a &:= \{s_a(\theta,\cdot) : \text{(5.9) holds } \forall\, \theta \in [-\pi,\pi]\};\ \text{and}\\
U_p &:= \{s_{new}(\theta,\cdot) : \text{(5.10) holds } \forall\, \theta \in [-\pi,\pi]\}.
\end{aligned}
\tag{5.11}
$$

Every root locus for each family starts at the pole p_n. From a set theoretic point of view, all four definitions are equivalent, however, the trajectory speeds are different. The different definition of the above sets will be useful in solving the path optimization problem in the next section.

Shadow zones

As the root locus paths do not intersect, there exists a region near the obstacles where the admissible paths cannot enter. Figure 5.3 graphically shows that the region outside of the boundary of the blue curves cannot be reached if the robot departs from the pole at -2. The region, which is denoted as *the shadow zone*, can be defined by using the set of trajectories starting from the obstacle poles. The shadow zone plays a role as a safety guard surrounding the obstacles, which the path must not enter. The size of the shadow zone can be controlled by having a multiple poles at the obstacles, and the fractional order obstacles have been studied in [71] to contorl the size. More analysis on the shadow zone can be done by using the invariance of the saddle point behavior in [103, 104].

5.3.2 Suboptimal Minimum Time Problem

A minimum time problem with the obstacle avoidance and the state dependent speed constraints is considered in this section. A typical example can be found in undulatory locomotion (such as snakes) where the amplitude of body motion (and therefore the body's envelope) of the snake depends on the average speed of motion. In the case of undulation

through a narrow region, the lower amplitude motions needed to clear the gap would induce a slower averaged velocity. Therefore, there exists a correlation between the speed and the obstacle location. A similar consideration might be needed for stealthy movement past adversarial obstacles.

General minimum time Problem for a single integrator

Suppose that the objective is to find the minimum time path starting from p_n to z with state dependent speed constraint, $P : \mathbb{R}^2 \to \mathbb{R}^+$, and the state constraint such that the path should not cross the obstacles located at p_i for $i \in \{1, \cdots, n-1\}$. In summary, the following minimization problem is sought,

$$\min_{u(\cdot)} T \tag{5.12}$$

with the constraints,

- $\dot{s} = u$
- $s(0) = p_n, s(T) = z, ||u|| = P(s)$
- $s(t) \notin \bigcup_{i=1}^{n-1} \{B(p_i, r_i)\}$

where r_i is the radius of the safety guard to avoid the collision with the obstacle at p_i, The case $P(s) = 1$ is the problem of path length minimization. If $P(s) := \frac{1}{||\nabla_{(x,y)} F_j(s)||}$ from Theorem 10, then the speed of the robot should be slow near an obstacle and increases as it moves away from the obstacle.

Modified minimum time Problem

In general, finding the optimal path satisfying the inequality constraints for the safety could be difficiult due to the possible non-convex shape of the obstacles. Assuming that enough poles are selected on the obstacles where the shadow zone fully contains the whole body

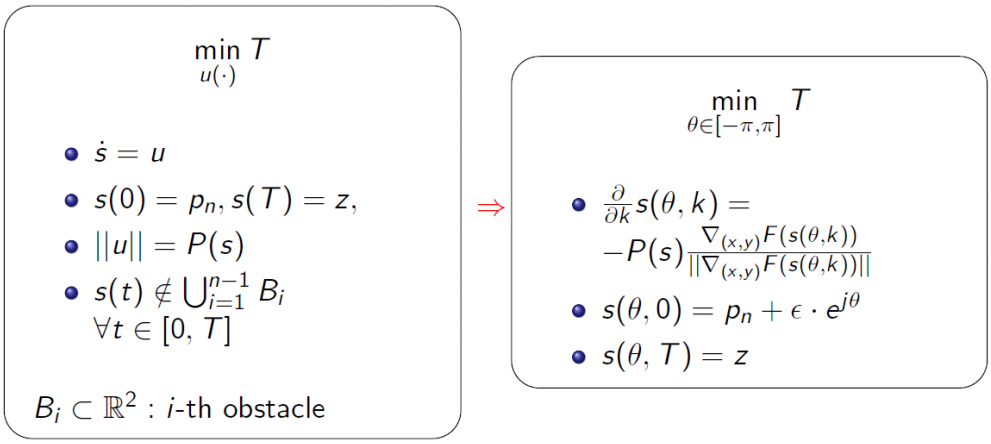

Figure 5.4: Suboptimal minimum time problem.

of the obstacles, the *sub-optimal* problem can be considered by removing the inequality constraints in (5.12), and making the dynamics restricted to the GRL path. The reduced problem is not equivalent to the problem in (5.12) since the trajectory only follows the negative gradient direction of F. However, the computation would be much simpler since the original infinite dimensional problem is transformed to the parameter optimization problem:

$$\min_{\theta \in [-\pi, \pi]} T \tag{5.13}$$

with the constraints $s(\theta, \cdot) \in U_p$ where U_p was chosen such that $s(0) = p_n, s(T) = z$. As each speed constraint can be involved in the admissible set definition, one can change the speed constraint by choosing different admissible sets from one of U_k, U_t, U_a and U_p as defined in §5.3.1. The summary of the suboptimal problem is shown in Fig 5.4.

Here, the algorithm to find the optimal θ is explained. First, observe that the level lines close to singularity have a circular shape, and so without loss of generality, it is assumed that the robot start from an ϵ apart from the starting pole. Let the initial set be the points $\{(x, y) : x + jy = s = p_n + \epsilon \cdot e^{j\theta}, \ \forall \theta \in [-\pi, \pi]\}$. One can construct a time map $T : \mathbb{C} \to \mathbb{R}^+$ where $T(q)$ is the arrival time from the initial curve to the point $q \in \mathbb{C}$. The time function is well defined since the root locus does not intersect.

The optimal solution θ can be obtained by finding the minimum T point around the ϵ

circle centered at the goal z. The argument for the approximate ϵ distance from the goal state is similar to the initial departure approximation. The problem is now stated as

$$\min_{\theta_r} T(s)$$

with the constraints, $||s - z||^2 = 2\epsilon^2$ or $s := z + \sqrt{2}\epsilon e^{j\theta_r}$.

Assuming that ϵ is small, θ_r is the approximation of the angle of arrival at the zero. Now, invoke Proposition 6, to compute θ or the angle of departure, θ_d. This will give the solution for the modified suboptimal problem, (5.13).

5.3.3 Example

Suppose that four obstacles are at $p_1 = (-1.2, 1.5), p_2 = (-1.4, 0.2), p_3 = (-1.2, -0.5)$ and $p_4 = (-1.2, -1.5)$, and the goal is to design a path from $p_5 = -3$ to the origin $z = 0$. There exist three gaps created by the obstacles, which the robot must pass through in order to reach the goal. Besides those gaps, there also exist two possible areas which are not surrounded by the obstacles but detour all the obstacles. The width of the gap between p_1 and p_2 is 1.3153, and the width of the gap between p_2 and p_3 is 0.7280. The GRL will be used to solve two problems. One is the original minimum length problem, when $P(s) = 1$ for all $s \in \mathbb{C}$. The other problem is the minimum time problem with the state dependent constraint, $P(s) := \frac{1}{||\nabla_{(x,y)} F_j(s)||}$ where $F_j(s) = \log(|\frac{1}{(s-p_1)(s-p_2)(s-p_3)(s-p_4)}|)$. Figure 5.5a shows both optimal path solutions. Black curves represent the sampled admissible paths in U_a, and the red path represents the shortest path solution without the speed constraint. The blue curve is the solution when there is a constraint on the speed. The constraint is such that the robot should slow down as it approaches an obstacle. Therefore, the entering speed near the smaller width gap is slower than the one for the larger width gap.

Figure 5.5b shows the arrival times with the speed constraint. The x axis shows the different angle of departures after using the Proposition 6. The minimum time angle of de-

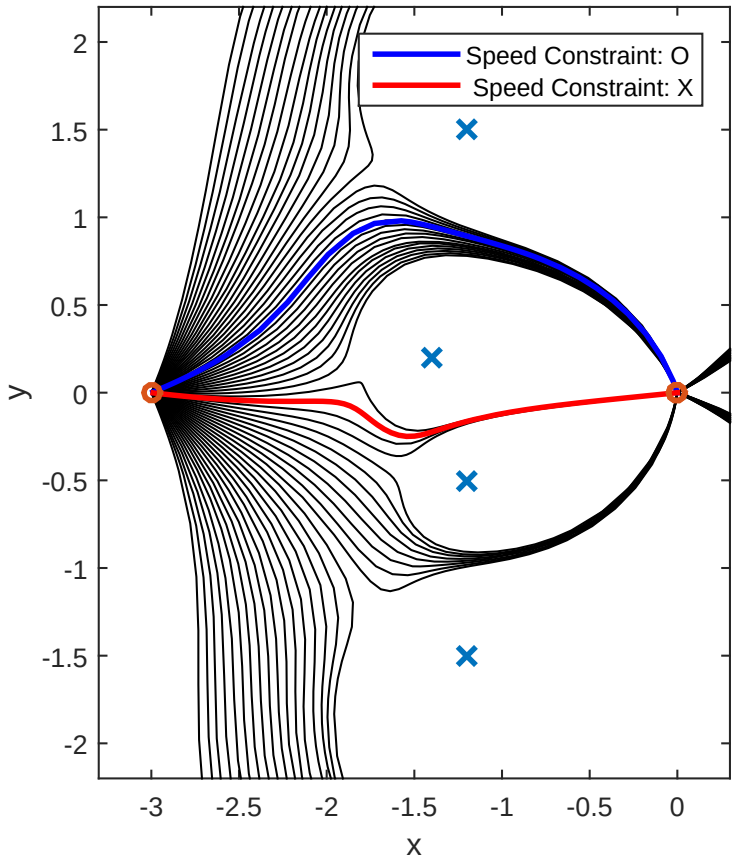

(a) Minimum time solution with (blue) and without (red) the state dependent speed constraint.

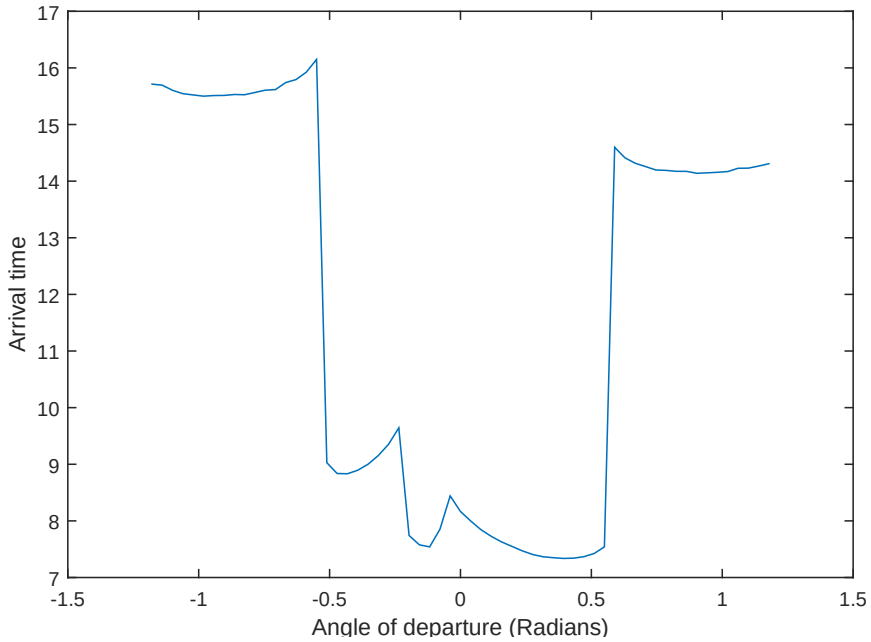

(b) Arrival time plot over different angle of departure.

Figure 5.5: Example for the sub-optimal minimum time solution.

parture in this example is 0.3927 in radians. The discontinuity in Figure 5.5b also confirms the existence of the shadow zone.

The shortest path, red curve, is not the exact straight line path since the obstacles warp the space slightly so that the straight line path is not within the family of paths U_a. In addition, the solution with the speed constraint, blue curve, also coincides with intuition since it enters the gap with width larger than the one entered by the red curve. The solver tends to find the path with faster motion along the path in order to minimize the total time. This example illuminates the optimal average motion of the undulatory locomotion.

5.4 Multi-Agent Formation Control

Multiple robot path planning can be designed using GRL, motivated by the fact that, given θ, a root locus path contains all continuous trajectories from each p_i to some z_i. Since $\mathbb{R}^2$ and $\mathbb{C}$ are isomorphic, each root, $s(\theta, k)$, of (5.2) can be identified with a location of a robot in $\mathbb{R}^2$ at time k. For example, suppose that two green triangle in Figure 5.1 are the starting points of two robots located at $(-2, 0)$ and $(-1, 1)$. Let the goal to be finding the control of these robots which makes them to asymptotically converge to two target points located at $(0, 0)$ and $(-2, 1)$. By choosing any angle of departure $\theta_d(p_1) \notin \{0.198\pi, -0.66\pi\}$ and $\theta_d(p_2) \notin \{-0.79\pi, 0.45\pi\}$, the figure graphically shows that each path arrives at one of the target points without colliding with other robots. Therefore, a set of trajectories from a given pole p_i, such that by following the path it is guaranteed that collision will never occur and the robots arrive at the goal location asymptotically, is defined.

Definition 26 (Set of collision-free paths)**.** *Let p_i be a root in $a(s)$. A set*

$$S(p_i) := \{(\theta, s(\theta, \cdot)) \in [-\pi, \pi) \times C^1(\mathbb{R}^+, \mathbb{C}) | s(\theta, \cdot) \subset GRL(\theta) \wedge s(\theta, 0) = p_i, \forall \theta \notin B\},$$

is a set of all collision free root locus trajectories from p_i labeled with corresponding θ.

Furthermore, it is shown in next proposition that by keeping the same $\theta \notin B$, the GRLs

indeed converges to all of the zeros.

Proposition 7. *Let $a(s)$ and $b(s)$ be two monic polynomials, relatively prime, and all roots are simple, then the roots of (5.2) asymptotically converge to the roots of $b(s)$.*

Proof. Let $C(s,k) = \frac{1}{1+ke^{j\theta}}(a(s) + ke^{j\theta}b(s))$. Since the roots do not change by scaling every coefficient with a same factor, $C(s,k)$ and (5.2) with same k have the same roots. It was shown in [105], that the roots of monic polynomial vary continuously as a function of its coefficients if the monic property doesn't change by the function. Observe that $C(s,k)$ is a monic polynomial by construction, and its coefficients are continuous for $k > 1$. Taking the limit $k \to \infty$, $C(s,k) - b(s) = \frac{1}{1+ke^{j\theta}}(a(s) - b(s))$, and so $\lim_{k\to\infty}(C(s,k) - b(s)) = 0$. Therefore, as $k \to \infty$, the roots of $C(s,k)$ converge to the roots of $b(s)$. □

5.4.1 Problem Statement

In this section, the formation control problem is stated. First, targets in some global coordinate system are defined as a set of distinct vectors, $\{y_1, \cdots, y_N\} \subset \mathbb{C}^N$. Let $\overline{y} = \frac{1}{N}\sum_{i=1}^{N} y_i$ be its center of mass. The definition of the shape is the relative position from its center of mass, and it is written as $z_i = y_i - \overline{y}$. Now, let N non-distinguishable robots initially located at $\{r_{10}, \cdots, r_{N0}\} \subset \mathbb{C}^N$. Let $\{r_1(t), \cdots, r_N(t)\} \subset \mathbb{C}^N$ be the location of each robot in the global coordinate at time t, and $\overline{r}(t) = \frac{1}{N}\sum_{i=1}^{N} r_i(t)$ be the center of mass of the robots at time t. Since $r_i(0) = r_{i0}$ for all i, the center of mass can be found by $\overline{r}(0) = \frac{1}{N}\sum_{i=1}^{N} r_i(0)$. Lastly, let $s_i(t) = r_i(t) - \overline{r}(t)$ be the relative vector from the center of mass of robots.

Information structure

Let $V = \{1, \cdots, N\}$. Here are two assumptions on the resources which each robot can have.

Assumption 4. *(Limited information) There is no communication link between robots, and the other robots are indistinguishable (no labeling).*

Assumption 5. *(Sensing) The robot can measure the relative displacement from other robots,* $\{r_i(t) - r_k(t)\}_{k=1}^N$*, but not the global coordinate.*

Assumption 6. *(Controller) A single integrator is used to generate the trajectory:* $\dot{s}_i = u_i$*.*

Assumption 7. *(Memory) Each robot has memory.*

By using the relative measurement, $s_i(t)$ can be known by taking a linear combination of the relative distances as

$$s_i(t) = r_i(t) - \overline{r}(t) = \frac{1}{N}\sum_{k=1}^{N}(r_i(t) - r_k(t)).$$

In addition, $s_i(t) - s_j(t)$ can also be known since

$$s_i(t) - s_j(t) = r_i(t) - \overline{r}(t) - (r_j(t) - \overline{r}(t)) = r_i(t) - r_j(t).$$

Lastly, all $s_j(t)$ can be computed by $s_j(t) = s_i(t) - (s_i(t) - s_j(t))$. In summary, i-th robot can compute $s_i(t)$, $s_j(t)$, and $s_i(t) - s_j(t)$ for all j at each time t. Furthermore, suppose that the robots were initially at rest, then i-th robot can store the values of $\{s_j(0)\}_{j=1}^N$, and so at any given time t, the robot can compute $s_i(t) - s_j(0)$ for all $j \in V$.

Problem statement

1. (Translation and Permutation Invariant control) Assume that all the nodes have agreed on the shape definition of $\{z_i\}_{i=1}^N$. Find a control u_i for each robot r_i such that the generated paths are collision free, and there exist a permutation $\pi : V \to V$ such that by evolving $\dot{r}_i(t) = u_i(t)$, the robots asymptotically converge to $\lim_{t\to\infty} r_i(t) = z_{\pi(i)} + v$ for some $v \in \mathbb{C}$.

2. (Permutation Invariant control) Assume that all the nodes have agreed on the shape definition of $\{z_i\}_{i=1}^N$. In addition, assume that all the nodes agreed on the initial

displacement of the center of masses, $\overline{r}(0) - \overline{y}(0)$. Find a control u_i for each robot r_i such that the generated path are collision free, and there exist a permutation $\pi : V \to V$ such that by evolving $\dot{r_i}(t) = u_i(t)$, the robots asymptotically converge to $\lim_{t\to\infty} r_i(t) = y_{\pi(i)}$.

5.4.2 Representation Space

In this section, the polynomial based representation space of robots in a planar space is defined. Pick $N \in \mathbb{N}$ such that N will be the number of robots. Let

$$P_m(N) = \{f(s) | f(s) = s^N + \sum_{i=1}^{N} a_i s^{N-i}, \forall a_i \in \mathbb{C}\} \tag{5.14}$$

$$P(N) = \{f(s) | f(s) = a_0 s^N + \sum_{i=1}^{N} a_i s^{N-i} \text{ where } a_0 \neq 0 \text{ and } \forall a_i \in \mathbb{C}\}. \tag{5.15}$$

$P_m(N)$ is a set of monic polynomial with an order N where the subscript m stands for monic, and $P(N)$ is a set of all polynomial with an order N. It is shown in [105] such that $\mathbb{C}^N$is isomorphic to $P_m(N)$. Since $P_m(N) \subset P(N)$, $P(N)$ also includes $\mathbb{C}^N$ but the representation is not unique. However, $P(N)$ can still be uniquely identified with $\mathbb{C}^N$ by taking a quotient, $\mathbb{C}^N \cong P(N)/\sim$, where $\sim$ is defined by dividing the highest coefficient. The proposed representation space is in $P(N)$, and the quotient operation is used whenever the the roots need to be uniquely identified.

Configuration space

Here the notion of representation space is formally defined.

Definition 27 (Configuration space)**.** *A polynomial subset, $CP(N)$, of $P(N)$ is called a configuration space where $CP(N) = \{f(s) \in P(N) |$ where $a_1 = 0\}$.*

Let $f(s) \in CP(N)$, then the property of $a_1 = 0$ represents that if $\{p_i\}_{i=1}^N$ are the roots of $f(s)$, then $\sum_{i=1}^N p_i = 0$. In other words, the center of mass of the roots is at the origin.

Also, observe that $CP(N)$ is almost closed under addition since if $\{a_i\}_{i=0}^N$ and $\{b_i\}_{i=0}^N$ are in $CP(N)$ and $a_0 + b_0 \neq 0$, then $a_1 = b_1 = 0$ and so $a_1 + b_1 = 0$. Furthermore, the coefficients of $f(s)$ from order 0 to $N-1$, say $\{a_i\}_{i=1}^N$, can be uniquely defined with elementary symmetric polynomials and a_0, by $a_i = a_0 e_i(p_1, \cdots, p_N)$ for $i \geq 1$ where $e_i(p_1, \cdots, p_N)$ is an i-th elementary symmetric polynomial.

Invariance properties

There are two invariant properties for $CP(N)$.

Proposition 8. *Let $a(s) = a_0(s-p_1)\cdots(s-p_N)$ and $b(s) = b_0(s-z_1)\cdots(s-z_N)$ be two polynomials in $CP(N)$, associated respectively with the coefficient representation , $\{a_i\}_{i=0}^N$ and $\{b_i\}_{i=0}^N$.*
(a) If π is a permutation operator, $\pi : \{1, \cdots, N\} \to \{1, \cdots, N\}$, and $c(s)$ represents the root-shuffled polynomial of $b(s)$ with a permutation π, and $\{c_i\}_{i=0}^N$ is its coefficient representation, then $b_i = c_i$ for all i.
(b) If α and β is in $\mathbb{C}\backslash\{0\}$ such that $\alpha a_0 + \beta b_0 \neq 0$, then $\alpha a(s) + \beta b(s) \in CP(N)$.

Proof. (a) By using the elementary symmetric polynomials, $b_i = b_0 e_i(z_1, \cdots, z_N)$ and $c_i = c_0 e_i(z_{\pi(1)}, \cdots, z_{\pi(N)})$ for all $i \geq 1$ holds. Since the coefficient of highest order is invariant under permutation, $b_0 = c_0$ holds. By the definition of elementary symmetric polynomial, it can be shown that $e_i(z_1, \cdots, z_N) = e_i(z_{\pi(1)}, \cdots, z_{\pi(N)})$. Therefore, $b(s) = c(s)$ holds.
(b) Since $\alpha+\beta \neq 0$, the coefficient of highest order in $\alpha a(s)+\beta b(s)$ is non zero. Therefore, $\alpha a(s) + \beta b(s) \in P(N)$. Now since $a_1 = 0$ and $b_1 = 0$, any linear combination is also zero. Hence, $\alpha a(s) + \beta b(s) \in CP(N)$ □

The first part of the proposition implies that even if the $b(s)$ in the GRL have a target configuration different from the original, the GRL will assign the robots to all permuted target positions. The second part of the proposition shows that if $a(s)$ and $b(s)$ of GRL are

both in $CP(N)$, then $a(s) + ke^{j\theta}b(s)$ is also in $CP(N)$ for all $k \in (0, \infty)$. Therefore, the root locus transition is made in $CP(N)$, and following corollary holds.

Corollary 1. *Let $a(s)$ and $b(s)$ are in $CP(N)$. Suppose that $\{s_i(\theta, \cdot)\}_{i=1}^N$ is a set of GRL which solves Eqn (5.2), then $\sum_{i=1}^N s_i(\theta, k) = 0$ for all $k \in (0, \infty)$.*

5.4.3 Formation Control

Based on the analysis for the representation space in § 5.4.2, this section describes a root locus control solution for the formation control problem.

Translation and permutation invariance

Let $\{z_i\}_{i=1}^N$ be the desired shape. Suppose $p_i = s_i(0)$ for all i, then $\{p_i\}_{i=1}^N$ are distinct poles, and $\{z_i\}_{i=1}^N$ are distinct zeros. The corresponding $a(s)$ and $b(s)$ in $CP(N)$ such that

$$a(s) = (s - p_1) \cdots (s - p_N) \tag{5.16}$$

$$b(s) = (s - z_1) \cdots (s - z_N) \tag{5.17}$$

can be defined. Pick $\theta \notin B$. Suppose that $s_i(t) := s_i(\theta, t)$ where $\{s_i(\theta, \cdot)\}_{i=1}^N$ is N GRL which solves $a(s) + ke^{j\theta}b(s) = 0$ such that $s_i(\theta, 0) = p_i$, then by using the Proposition 7, there exist a permutation operator $\pi : V \to V$ such that $\lim_{t\to\infty} s_i(t) = z_{\pi(i)}$.

Pick $u_i(t)$ as the right hand side of (5.9). The computation is feasible since i-th robot knows $s_i(t) - p_j$ and $s_i(t) - z_j$ for all j at each time t. By following the GRL solution, $r_i(t) = s_i(t) + c_i$ is achieved for some constant c_i. By using the Corollary 1, $\frac{1}{N}\sum_{i=0}^N s_i(t) = 0$ holds for all t, and so $c_i = \overline{r}(0)$ for all i is found. In other words, using the GRL control, the center of mass does not change, and also, by taking the path generated by the root locus, it is guaranteed that there is no collision. Hence, $\lim_{t\to\infty} r_i(t) = z_{\pi(i)} + \overline{r}(0)$ holds.

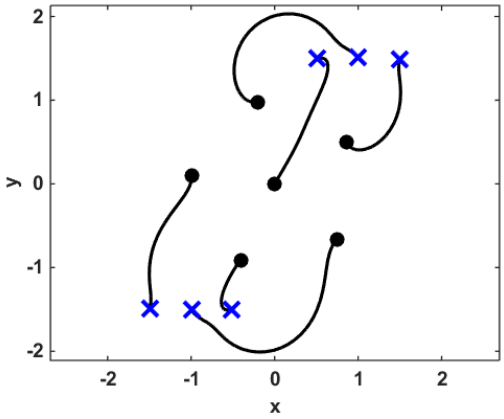

(a) Translation and permutation invariant formation control for $\theta = -0.25\pi$.

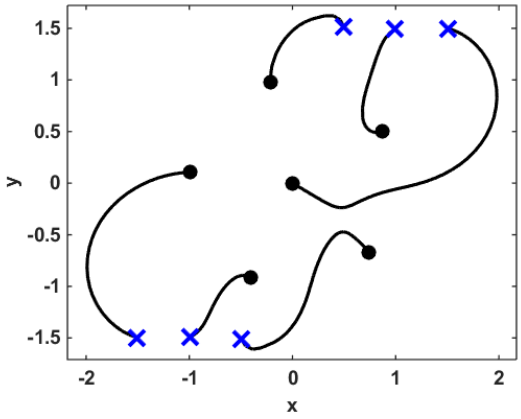

(b) Translation and permutation invariant formation control for $\theta = 0.25\pi$.

Figure 5.6: Example for the formation control in configuration space.

Permutation invariance

Let $v = \overline{y}(0) - \overline{r}(0)$. Compute the same $s_i(t)$ in the previous problem. Now, pick $u_i(t) = \dot{s}_i(t) + ve^{-t}$, then $r_i(t) := s_i(t) + v(1 - e^{-t}) + c_i$ for some $c_i \in \mathbb{R}$. Since $s_i(0) = r_i(0) - \overline{r}(0)$, the displacement $c_i = \overline{r}(0)$ is found. Substitute v with $\overline{y}(0) - \overline{r}(0)$, then $r_i(t) = s_i(t) + \overline{y}(0) - (\overline{y}(0) - \overline{r}(0))e^{-t}$ holds. In this case, the center of mass of the robot configuration is now changing with time, $\overline{r}(t) = \overline{y}(0) - (\overline{y}(0) - \overline{r}(0))e^{-t}$. Since $\lim_{t\to\infty} s_i(t) = z_{\pi(i)}$ for some permutation π, asymptotically $\lim_{t\to\infty} r_i(t) = z_{\pi(i)} + \overline{y}(0) = y_{\pi(i)}$ holds. Since all $r_i(t)$ are translated equally from the original root locus $s(t)$, the collision free property still

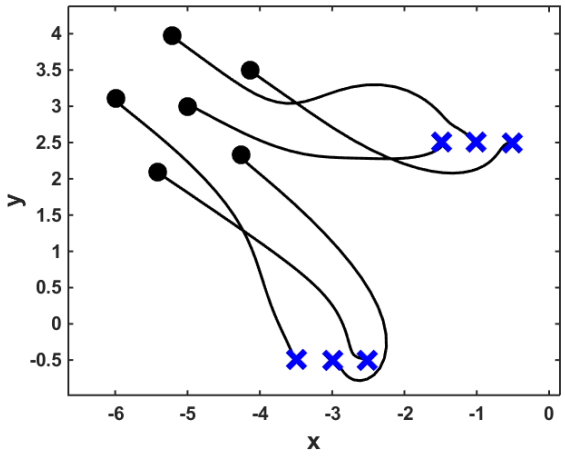

Figure 5.7: Permutation invariant formation control.

holds. Hence, $\lim_{t\to\infty} r_i(t) = y_{\pi(i)}$ holds, which solves the problem.

5.4.4 Example

Here is an example for six robots. The objective is to make a pentagon shape with a center node. Suppose that 6 robots are placed at $p_1 = (-1.5, -1.5)$, $p_2 = (-1, -1.5)$, $p_3 = (-0.5, -1.5)$, $p_4 = (0.5, 1.5)$, $p_5 = (1, 1.5)$, and $p_6 = (1.5, 1.5)$ in its configuration space, and have $\overline{r} = (-2, 1)$ as its center of mass. The targets are located at $z_i = (\cos(\frac{\pi(2i-1)}{5}), \sin(\frac{\pi(2i-1)}{5}))$ for $i = \{1, \cdot, 5\}$ and $z_6 = (0, 0)$ in its configuration space, and have $\overline{y} = (-5, 3)$ as its center of mass. In this example θ is chosen to be -0.25π for Figure 5.6a, and $\theta = 0.25\pi$ for Figure 5.6b. First, make all robots and goal formation into its configuration space, and let $\{p_i\}_{i=1}^6$ be 6 poles location, and $\{z_i\}_{i=1}^6$ be 6 zeros location. In Figure 5.6 these poles and zeros are marked with blue crosses and black circles, respectively. Following the root locus, provides a trajectory for each robot in its configuration space. As expected, each robot is assigned to a unique target position in the shape. By changing the θ values in B^c, a different assignment can be found with a safe trajectory. Figure 5.6b shows that the assignment of the robots are changed by having a different θ from Figure 5.6a.

The second example of finding the permutation free formation control is shown in Figure 5.7. The blue cross and black circle marks represents the robots and the target location in the global frame. Using the method in Section 5.4.3, leads to 6 trajectories which converge to each target position. In this example, the angle $\theta = -0.25\pi$ was chosen in B^c. The collision-free property holds for the second example. The intersection shown in the figure is not a collision. Rather, it shows that by using the root locus and translation method, there may exist a point in space which is visited by two robots at different times.

CHAPTER 6

GEOMETRY 1: RECTANGULAR ROBOTS PATH PLANNING

In this chapter, a new framework for modeling the optimal path planning problem of full body robots, especially, rectangular robots in $\mathbb{R}^2$, are considered. Typically, constraints for the safe, obstacle-avoiding path involve a set of inequalities expressed using logical OR operations, which makes the problem difficult to solve using existing optimization algorithms. Inspired by the geometry of the unit sphere in the weighted L_p norm, an exact and approximate constraints for safe configurations using only logical AND operations are pursued. The proposed method does not require integer programming nor computation of a Minkowski sum in the configuration space.

A direct approach for safety is considered by finding analytic collision constraints for each corner of the robot and obstacles. In particular, two different cases of obstacle geometry are considered: circular obstacles and rectangular obstacles. Using the weighted L_p norm requires six inequalities to represent the exact constraints for collision avoidance of circular obstacles using AND operations, and eight inequalities for rectangular obstacles.

This chapter is organized as follows. In § 6.1, the background of safe path planning for full body problem is reviewed. In § 6.2, a motivating example of the safety constraint using L_p norm is covered, and the formal definition of weighted L_p norm is introduced in § 6.3, with the problem statement formulated afterwords in § 6.4. Next, the framework for constructing the safe configuration constraints using L_p norm is illustrated in § 6.5, and four interesting simulations are given in § 6.6.

6.1 Introduction

In this section, the problem of safe trajectory generation for a robot through the synthesis of cost minimizing optimal controls (e.g., arrival time or path length), also known as robot

motion planning, is considered. A classical and well-known approach to robot motion planning is the *configuration space approach*, which converts the rigid body path planning problem into a simpler point mass robot problem in the higher dimensional space, denoted as the C-space [106]. Transforming the rigid body to a point mass equivalent involves applying the Minkowski sum, defined by $A \oplus B = \{q \in \mathbb{R}^n : q = x + y, \forall x \in A \wedge \forall y \in B\}$ for two given sets $A, B \subset \mathbb{R}^n$. The process creates obstacles representations in the C-space, so called C-obstacles, when computed via the Minkowski summation for each robot orientation. Once the C-obstacles are constructed, the set of collision free configurations, called the C-free space, is obtained via the complement of the $C-$obstacles in C-space. An algorithm to find the C-free space for two polygon shaped robot and obstacle is shown in [107] and an algorithm for the exact Minkowski sum of convex polyhedra is given in [108]. More details of the motion planning on the configuration space, and the numerical algorithms can be found in [109, 10, 110].

Analytic expressions for the $C-$free space involve a set of inequalities combined by the logical OR operation when the robot or the obstacle are polygon shaped [10]. The use of the logical OR causes a major problem in applying general optimization algorithms since they are constructed based on AND operations applied to the constraints; constraints with OR operations are analytically intractable [111]. One way to avoid the OR operation for the rectangular obstacle with a point mass robot is to use mixed integer programming (MIP) by introducing artificial integer valued variables [112, 113]. However, integer programing is known to be NP-hard [114]. Recently, an efficient way of reducing the number of integers in the optimal path planning problem was given in [115]. The method improves on the scaling of the NP-hard problem at the expense of a decreased probability of finding a feasible solution.

As an alternative method, without using integer variables, a new weighted L_p norm based framework to find the constraints for safe configurations through the use of the logical AND operations for the case of a rectangular robot is proposed. The new framework to

formulate the equivalent constraints of a safe configuration is inspired by the geometry of unit spheres for weighted L_p norms. The unit level set of the L_p norm with different p values forms different shapes that converge to the square as $p \to \infty$. Thus weighted L_p norms lead to exact and approximated implicit equations for the boundaries of rectangles. Taking advantage of this observation, a detailed method to synthesize a collection of mixed L_p norms that implicitly define safe configurations is described in this section.

Work related to the proposed framework exploring non-circular robots includes [116], which gives the analytic formulation of the exact boundary for the Minkowski sum of two ellipses through affine transformations. Follow-up work applied this formulation to the path planning problem with elliptic obstacles in the C-space by providing the exact boundaries for the C-obstacles [117]. Although ellipses arise through weighted L_2 norms, the approach here is essentially different from- and complementary to- [117]. First, the method here considers rectangular robots and a mixture of rectangular and circular obstacles (it also holds for circular robots). Second, the goal of current work is to find the implicit constraints for the center of the robot without constructing the Minkowski sum between the robot and the obstacles. As will be shown, the synthesis of these implicit constraints is computationally simple since all that is required is to define 8 different weighted L_p norms for the rectangular obstacle case, and 6 for the circular obstacle case. In addition, the primary interest is in solving the optimization problem by analytically setting up a Bolza type optimal control problem [118], rather than constructing C-obstacles.

6.2 Motivating Example

To motivate the solution, consider the shortest path problem for a square shaped unicycle robot avoiding a point obstacle. This problem can be formulated equivalently with a point-mass unicycle robot and the square obstacle after constructing the configuration space. Let the unicycle robot travel from the starting configuration $g = (\mathbf{x_i}, \mathbf{y_i}, \theta_\mathbf{i})$ to the final position $(x, y) = (\mathbf{x_f}, \mathbf{y_f})$, irrespective of orientation, in the planar space $SE(2)$. As per Figure 6.1,

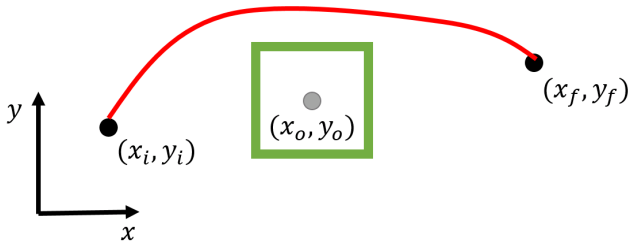

Figure 6.1: Single square obstacle avoidance example.

let there be a single square obstacle centered at (x_o, y_o) with edge length 2 between the initial and the final positions of the robot, so that a detour is needed to avoid collisions. A formulation of the shortest safe path problem is

$$\arg\min_{u_1,u_2} \int_0^T \sqrt{\dot{x}^2(t) + \dot{y}^2(t)}dt \quad \text{subject to} \tag{6.1}$$

$$\begin{cases} \dot{x} = u_1(t)\cos(\theta(t)) \\ \dot{y} = u_1(t)\sin(\theta(t)) \\ \dot{\theta} = u_2(t) \end{cases}, \tag{6.2}$$

$$(x(0), y(0), \theta(0)) = (\mathbf{x_i}, \mathbf{y_i}, \theta_\mathbf{i}), \tag{6.3}$$

$$(x(T), y(T)) = (\mathbf{x_f}, \mathbf{y_f}), \tag{6.4}$$

$$|x - x_o| > 1 \quad \text{OR} \quad |y - y_o| > 1, \tag{6.5}$$

where (6.1) is the cost, and (6.2-6.5) are constraints of the optimization problem. The safe trajectory constraints (6.5) are a set of inequalities with the logical OR operation. However, the OR condition is known to be analytically intractable, [111]. To solve with mathematical programming algorithms, a conversion to equivalent AND operations is considered in this chapter.

The idea is to find a function $V : \mathbb{R}^2 \to \mathbb{R}$ such that there exist a constant $c \in \mathbb{R}$, which makes the superlevel set $\{(x, y) = q \in \mathbb{R}^2 : V(x, y) \geq c\}$ equivalent to the OR

conditioned constraint in (6.5). The function V for the square obstacle centered at (x_o, y_o) will be formulated by the L_∞ norm in L_p theory [119]. Define V by

$$V(x,y) := ||(x - x_o, y - y_o)||_\infty = \lim_{p\to\infty} (|x - x_o|^p + |y - y_o|^p)^{\frac{1}{p}}. \tag{6.6}$$

Since the L_∞-norm unit sphere in $\mathbb{R}^2$ is a square centered at the origin, the inequality constraint $V(x, y) > 1$ replaces the OR conditions in (6.5).

6.3 Weighted Norm

Let $x = (x_1, \cdots, x_n)$ be a vector in $\mathbb{R}^n$ for $n \in \mathbb{N}$, with x being positive (e.g., $x_i > 0$ for all i).

Definition 28 (Weighted L_p norm)**.** *Let $\sigma \in \mathbb{R}^n$ be a positive vector, and $0 < p < \infty$, then $||\cdot||_{\sigma,p} : \mathbb{R}^n \to \mathbb{R}_{\geq 0}$ is the σ-weighted L_p norm such that*

$$||x||_{(\sigma,p)} := \left(\sum_{i=1}^{n} (|x_i|/\sigma_i)^p \right)^{\frac{1}{p}},$$

for all $x \in \mathbb{R}^n$ where $\sigma = (\sigma_1, \cdots, \sigma_n)$. Furthermore the level set $\{x \in \mathbb{R}^n : ||x||_{(\sigma,p)} = 1\}$ is called the unit sphere *of the $L_{\sigma,p}$ norm.*

With a slight abuse of notation, if σ is a scalar but x is a vector, then the division by σ is applied across all coordinates. Another way of defining the σ-weighted L_p norm is by $||x||_{\Sigma,p} := ||\Sigma^{-1}x||_p$, where $\Sigma = \mathrm{diag}(\sigma_1, \cdots, \sigma_\mathrm{n})$, which shows that it is a generalization of the usual L_p norm. A major benefit of this generalization is that by choosing different σ or p, the unit sphere of usual L_p norm can be continuously deformed. For any given positive σ, as p increases, the unit sphere of $L_{(\sigma,p)}$ approaches the unit sphere of $L_{(\sigma,\infty)}$.

The collection of unit spheres for $n = 2$ and $\sigma = (2, 1)$, where each closed curve represents the unit sphere for different p values, are shown in Figure 6.2. The blue curves corresponds to the case when p changes from 0.5 (innermost) to 1.9 (outermost) with step

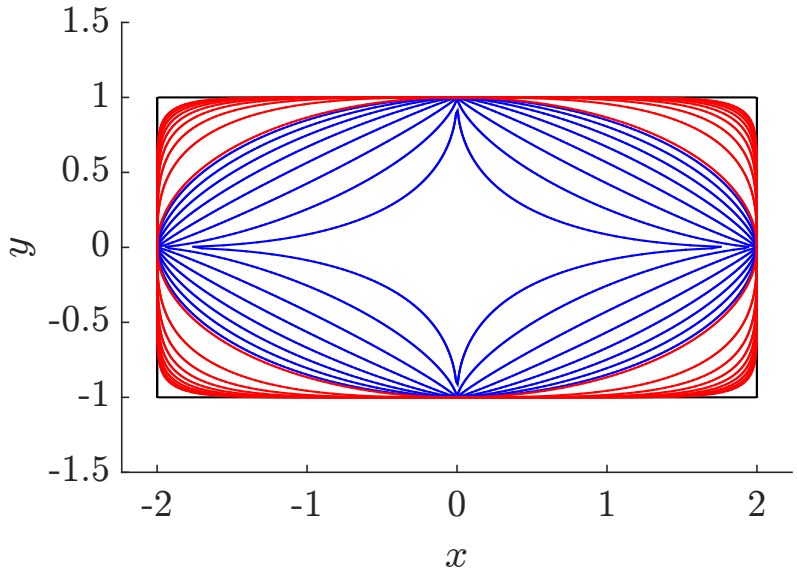

Figure 6.2: Unit sphere of $(2, 1)$-weighted L_p norms with different p values.

size 0.2. Similarly, the red curves represent corresponding changes as p increases from 2 (innermost) to 10 (outermost) with step size 1. The black curve corresponds to $p = \infty$, where it is equivalent to the supremum norm.

6.4 Problem Statement

This section generalizes the motivational problem to consider a rectangular robot navigating through a space with rectangular and circular obstacles. The geometry of the rectangular body is described by $\sigma := (\sigma_1, \sigma_2)$, where σ_1 and σ_2 are the half lengths of each edge. There are N_c circular obstacles centered at $o_c^i := (x_o^i, y_o^i) \in \mathbb{R}^2$ with radius $r_i > 0$ for each $i \in \{1, \cdots, N_c\}$, and there are N_r rectangular obstacles whose frame is $g_r^j := (x_r^j, y_r^j, \theta_r^j) \in SE(2)$, where the coordinate frame is centered in the square. The rectangular obstacle half lengths are $\sigma^j := (\sigma_1^j, \sigma_2^j)$ for each $j \in \{1, \cdots, N_r\}$. Without loss of generality, the problem will be formulated using an initial $SE(2)$ configuration and a final position, $\mathbb{R}^2 \subset SE(2)$, as the path boundary conditions. The arrival time, $T_f > 0$, is fixed.

Here, $g(q) \in \mathbb{R}^2$ denotes the transformation of coordinates of $q \in \mathbb{R}^2$ according to $g \in SE(2)$. The inverse g^{-1} would perform the change of coordinates in the inverse direction.

The collision-free spaces for the circular and rectangular obstacles are

$$C_i := \{q \in \mathbb{R}^2 : \left|\left|q - o_c^i\right|\right|_2^2 > r_i^2\}, \text{ and} \tag{6.7}$$

$$R_j := \{q \in \mathbb{R}^2 : \left|\left|[g_r^j]^{-1}(q)\right|\right|_{\Sigma,\infty} > 1\}, \tag{6.8}$$

respectively, in the world frame for all i and j (see §6.3 regarding $||\cdot||_{\Sigma,\infty}$). As the robot moves, the collision constraints in the robot's body frame will change. With g defining the robot's body frame relative to the world frame, the collision-free space in robot body coordinates is:

$$C_i^{\mathcal{R}} := \{q \in \mathbb{R}^2 : \left|\left|g(q) - o_c^i\right|\right|_2^2 > r_i^2\}, \text{ and} \tag{6.9}$$

$$R_j^{\mathcal{R}} := \{q \in \mathbb{R}^2 : \left|\left|[g_r^j]^{-1} \circ g(q)\right|\right|_{\Sigma,\infty} > 1\}. \tag{6.10}$$

Let $B \subset \mathbb{R}^2$ describe the subset of $\mathbb{R}^2$ containing the robot's full body in the robot's body frame, then the optimal safe path planning problem formulation is

$$\arg\min_u \int_0^{T_f} L(g, \dot{g}, u)dt \text{ subject to} \tag{6.11}$$

$$\begin{cases} \dot{g} = f(g, u), \\ g(0) = (\mathbf{x_i}, \mathbf{y_i}, \theta_\mathbf{i}), \\ p\left(g(T_f)\right) = (\mathbf{x_f}, \mathbf{y_f}), \end{cases} \tag{6.12}$$

$$\begin{cases} B \subset (\bigcap_{i=1}^{N_c} C_i^{\mathcal{R}}), \\ B \subset (\bigcap_{j=1}^{N_r} R_j^{\mathcal{R}}), \end{cases} \tag{6.13}$$

where $p(\cdot)$ gives the translation coordinates of $SE(2)$, $u(t) \in \mathbb{R}^2$ is the control of the

robot, f are the control equations of motion, and $L(g, \dot{g}, u)$ is some physically meaningful cost such as control energy or path length. Since the constraints in (6.13) typically require OR operations, the goal is to first convert them into a new set of constraints with AND operations.

Remarks. Once the problem is reformulated with AND operations, numerical solutions to Bolza type path planning problems [118] no longer require explicit construction of the C-obstacles nor the C-free space. The problem in (6.11-6.13) generalizes to admit other constraints such as free final time or fixed final orientation.

6.5 Collision Avoidance Constraints

The motivational example, with a point mass robot and a square obstacle, demonstrated that the weighted L_p norm can be used to analytically define the free space with the implicit inequality constraint (using $p = \infty$). However, for full body robots, imposing a single point-based L_∞ inequality constraint will not be sufficient. All boundary points of the robot must be considered to define a collision between the robot and an obstacle. Similar to the configuration space approach, the goal is to convert the collision-free space determination into an equation of the position of the robot frame or obstacle frame, but there is the additional objective to avoid explicit computation of the boundary points. Instead, this section seeks to define value functions as in (6.6) that provide implicit inequalities, and that compose using logical AND operations. Two cases are considered: the collision avoidance between a circular object and a rectangular object, and the collision avoidance between two rectangular objects.

6.5.1 Circular obstacles

The case of circular obstacles will be examined by converting the Minkowski sum of a rectangle with a circle into a set of inequality constraints (or of super-level set definitions) that must all be met. Define the collision space for the circular obstacle given relative to its

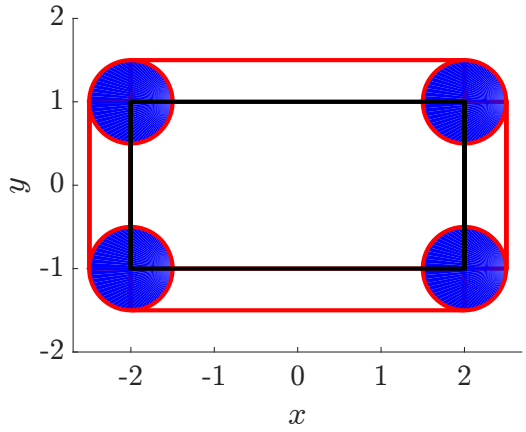

(a) Exact constraints

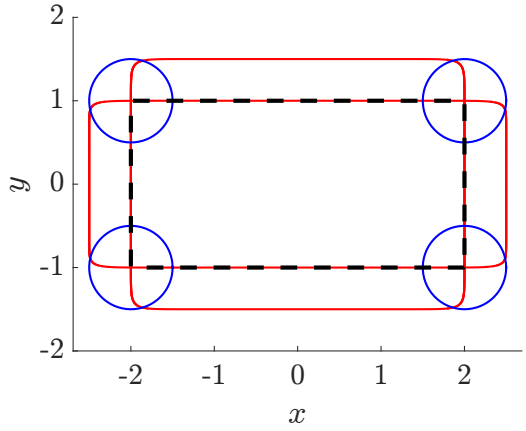

(b) 6 constraints

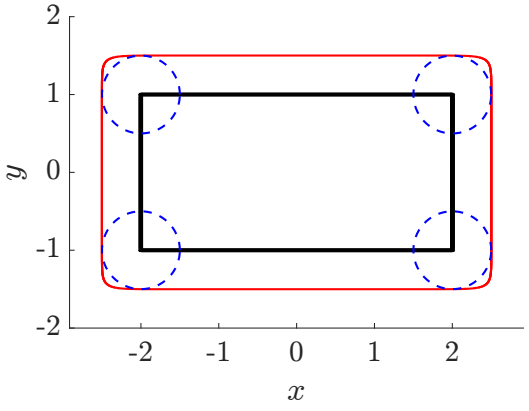

(c) 1 constraint

Figure 6.3: Weighted L_p constraints method for a rectangular robot and a circular obstacle.

own frame by

$$\overline{C}_i^{\mathcal{O}} := \{q \in \mathbb{R}^2 : ||q||_2^2 \leq r_i^2\}. \tag{6.14}$$

Robot collides with the obstacles if the distance of the robot body to the circular obstacle is less than r_i. The boundary of Minkowski sum $B \oplus \overline{C}_i^{\mathcal{O}}$ is depicted in Figure 6.3a by the outer boundary of the graphed shapes (coordinates in the robot's body frame). Since the robot is rectangular, the set B is a rectangular shape with half lengths $\sigma = (\sigma_1, \sigma_2)$. For the figure, $\sigma = (2, 1)$ and $r = 1$. The figure also depicts 6 shapes whose union is equal to the Minkowksi sum. These sums define the 6 value functions to be constructed.

Using the σ-weighted L_p norm of Definition 28, the value functions for the i^{th} circular obstacle are

$$
\begin{aligned}
V_1^i(q; g) &:= ||g^{-1}(q)||_{(\sigma_1 + r_i, \sigma_2), p} \\
V_2^i(q; g) &:= ||g^{-1}(q)||_{(\sigma_1, \sigma_2 + r_i), p} \\
V_3^i(q; g) &:= ||g^{-1}(q) - (\sigma_1, \sigma_2)^T||_{r_i, 2} \\
V_4^i(q; g) &:= ||g^{-1}(q) + (-\sigma_1, \sigma_2)^T||_{r_i, 2} \\
V_5^i(q; g) &:= ||g^{-1}(q) + (\sigma_1, -\sigma_2)^T||_{r_i, 2} \\
V_6^i(q; g) &:= ||g^{-1}(q) + (\sigma_1, \sigma_2)^T||_{r_i, 2}
\end{aligned}
$$

where g defines the current robot rigid body frame relative to the world frame. If g is omitted, then it is presumed to be the identity (e.g., the robot and world frames align).

Proposition 9. *If $p = \infty$, then $B \oplus \overline{C}_i^{\mathcal{O}}$ is equal to $\bigcup_{j=1}^{6} \{q \in \mathbb{R}^2 : V_j^i(q) \leq 1\}$.*

Proof. The proof is immediate since $\{q : V_1^i(q) \leq 1\} \cup \{q : V_2^i(q) \leq 1\}$ contains all the points inside the robot. It also contains the points located along the rays orthogonal to the edges (and pointing outwards), such that their distance is less than r_i. What remains are the set of points missed near the rectangle corners. These are covered by the four circles of radius r_i. Taking the union of the circles with radius r_i centered at four vertices of B, corresponds to the inequalities for V_3^i, V_4^i, V_5^i and V_6^i. The union of all these sub-level sets is equivalent to the Minkowski sum of the two shapes, $B \oplus C_i^{\mathcal{O}}$. □

The proposition indicates that the proposed six constraints are exactly equivalent to the C-obstacles constructed by the Minkowski sum, given that $p = \infty$. Furthermore, the collision-free space is the negation of the union, which leads to intersections of super level-sets. Intersections of spaces are described through logical AND operators in the optimal control formulation. However, since the gradient of the maximum operator does not have an analytic formula, using L_∞ norm in the optimization problem may not be a good choice. Differentiable, alternative or approximate formulations are sought.

The discussion of § 6.3 and visualization of unit L_p spheres showed that as p gets larger the unit sphere of L_p approaches that of L_∞. Although it is not a perfect rectangle, the benefit of having large p is an analytically computable gradient for the inequality constraint, and use it in the optimization problem. An example for the case $p = 20$ is shown in Fig 6.3b. The parameters in the examples are $\sigma = (2, 1)$ and $r = 1$. The black dotted line represents the robot body in its coordinate frame, and two horizontally long and vertically long rectangles represent the unit level sets of V_1^i and V_2^i, respectively. The four blue circles at each corner represents the unit level set of V_3^i, V_4^i, V_5^i and V_6^i. The approximate nature means that there will be some part of the collision-free space that is actually a collision, or conversely, some part of the collision space will return as collision-free. There are eight such regions, two at each corner. They are the dimples formed at the outer intersections of the approximately rectangular boundaries with the circular boundaries.

A simpler, conservative approximation of the Minkowski sum may be defined using a single value function instead of six. Let V_7^i be another value function defined as

$$V_7^i(q; g) := ||g^{-1}(q)||_{(\sigma_1+r_i+\epsilon,\sigma_2+r_i+\epsilon),p} \tag{6.15}$$

By choosing a large p and a small $\epsilon > 0$, the Minkowski sum is confined to the sub level-set $\{(x, y) : V_7^i(x, y) \leq 1\}$. An example for $p = 20$ and $\epsilon = 0.01$ is shown in Fig 6.3c, where red curve represents the unit level set of V_7^i, and dashed blue represents the circle with

radius $r = 1$ at each corner. In this case, the opposite situation occurs. The extra collision regions at the rounded corners means that some parts of the collision-free space evaluate to collisions.

As noted earlier, the main result of this section is that the OR condition in (6.13) due to the rectangular body of the robot is now changed to the AND condition. In summary, the anti-collision condition for the circular obstacle may be replaced by one of the two logical expressions,

$$\wedge_{i=1}^{N_c} \wedge_{k=1}^{6} \{q \in \mathbb{R}^2 : V_k^i(q) > 1\} \tag{6.16}$$

$$\wedge_{i=1}^{N_c} \{q \in \mathbb{R}^2 : V_7^i(q) > 1\}, \tag{6.17}$$

where $\wedge$ stands for the logical AND operation. The number of inequalities required for the circular obstacles will be $6N_c$ if only the former expression is used, N_c if only the latter expression is used (or some mix if one of either two is selected per circular obstacle). The constraint (6.16) is more accurate in capturing the collision at the corner of the robot, while (6.17) is more beneficial numerically since the formulation has less inequality constraints.

6.5.2 Rectangular obstacles

For two rectangular obstacles, the collision space is trickier to compute with the Minkowski sum since the obstacles orientations modify the sum. In order to construct a full C-obstacle, it is necessary to compute the Minkowski sum at every orientation of the robot and the obstacles. Fortunately, the weighted L_p method to find the equivalent set of inequalities composed with logical AND operation is simpler than computing the Minkoswski sum in C-space.

The contact of two polygons in $\mathbb{R}^2$ is categorized into two types: one is the *robot vertex to obstacle edge* and the other is *robot edge to obstacle vertex* [10], which are denoted as *Type A* and *Type B* collisions, respectively, in [109]. Since the robot and the obstacle are

both rectangular, there will be eight different types of possible contact.

Define the 8 corners from the robot and the j^{th} obstacle, in the world frame, by

$$A = g\left(\begin{bmatrix} \sigma_1 & \sigma_1 & -\sigma_1 & -\sigma_1 \\ \sigma_2 & -\sigma_2 & -\sigma_2 & \sigma_2 \end{bmatrix}\right) \tag{6.18}$$

$$A_j = g_r^j\left(\begin{bmatrix} \sigma_1^j & \sigma_1^j & -\sigma_1^j & -\sigma_1^j \\ \sigma_2^j & -\sigma_2^j & -\sigma_2^j & \sigma_2^j \end{bmatrix}\right) \tag{6.19}$$

where each column of A and A^j represents the coordinate of corners of the robot and each obstacle, respectively. The obstacle corners in the robot frame are $A_j^{\mathcal{R}} = g^{-1}(A_j)$. Denote the columns of $A_j^{\mathcal{R}}$ at time t by $\psi_k(t) \in \mathbb{R}^2$ for each $k \in \{1,2,3,4\}$. The anti-collision condition of *robot edge to obstacle vertex* contact consists of four AND operations,

$$\wedge_{k=1}^{4}\{||\psi_k(t)||_{(\sigma_1,\sigma_2),p} > 1\}. \tag{6.20}$$

The $L_{(\sigma_1,\sigma_2),p}$ distance from the center of the robot to the obstacle corners should be greater than one.

Now, consider the matrix of the four corner coordinates of the robot in the j^{th} obstacle frame, $A^{\mathcal{O},j} = [g_r^j]^{-1}(A)$. Denote its columns at time t by $\psi_k^j(t) \in \mathbb{R}^2$ for each $k \in \{1,2,3,4\}$, then the anti-collision conditions of *robot vertex to obstacle edge* comprise of four AND operations,

$$\wedge_{k=1}^{4}\{||\psi_k^j(t)||_{(\sigma_1^j,\sigma_2^j),p} > 1\}. \tag{6.21}$$

The union of (6.20) and (6.21) gives eight inequality constraints,

$$\wedge_{j=1}^{N_2}\wedge_{k=1}^{4}\left(\{||\psi_k(t)||_{(\sigma_1^j,\sigma_2^j),p} > 1\} \wedge \{||\psi_k^j(t)||_{(\sigma_1,\sigma_2),p} > 1\}\right), \tag{6.22}$$

which represent the avoidance of both Type A and Type B collisions. For N_r rectangular obstacles, there will be $8N_r$ inequality constraints. They will be somewhat permissive,

indicating that a configuration may be collision-free when it indeed collides. An ϵ-hedge gives conservative constraints.

6.6 Optimal Path Planning

This section solves several optimal path planning problems for a unicycle robot with the rectangular body shape using the L_p constraints defined in the previous section. The cost function (6.11) choice is $L(g, \dot{g}, u) := \sqrt{\dot{x}^2 + \dot{y}^2}$, to give a shortest path problem. The control equations of motion are those from (6.2). Assume that the control inputs, $u_1, u_2 \in C([0, T_f], \mathbb{R})$, are bounded by $u_1(t) \in [\underline{u}_1, \overline{u}_1]$ and $u_2(t) \in [\underline{u}_2, \overline{u}_2]$. The final arrival time $T_f > 0$ is fixed in each problem except for §6.6.2.

The MATLAB-based numerical optimal control solver OPTRAGEN [120], converts the Bolza type optimal control problem into a nonlinear programming problem (NLP) by using the collocation method. The NLP is then soved using an interior point method by invoking IPOPT 3.12.6 [121]. For all of the following solution figures, the red curves represent the obstacle boundaries, the blue curve represents the trajectory of the center position of the robot, and the black curves shows the shape of the robot at each sampled collocation time.

6.6.1 Circular Obstacles

Thin rectangular robot

This example involves a thin robot, $\sigma = (2, 1)$, with two circular obstacles both of radius $r = 1$, centered at $(2, -1.6)$ and $(-1, 1.5)$. The initial orientation is $\theta_{\mathbf{i}} = -\pi/4$. The direction of motion is in the direction of the shorter edge. The initial robot position is $(-3.11, 0.11)$, and the objective is to reach $(3.52, -0.22)$ at time $T_f = 3.667\pi$. The control upper and lower bounds are $u_1(t) \in [-2\pi, 2\pi]$ and $u_2(t) \in [-\pi/2, \pi/2]$. The simpler inequality constraint, (6.17), for the obstacles (2 constraints) is used with $p = 8$ for the approximation. The optimal control result depicted in Fig 6.4 shows that the shortest path involved moving the robot through the narrow gap.

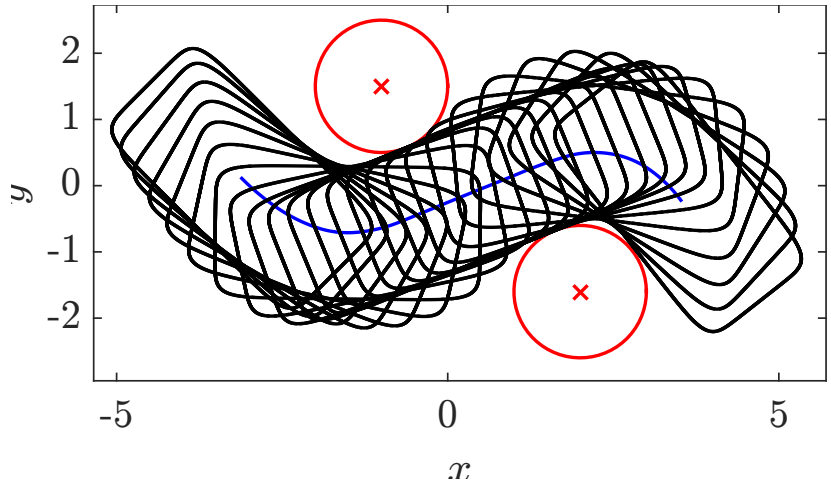

Figure 6.4: Shortest path solution for the thin robot.

Wide rectangular robot

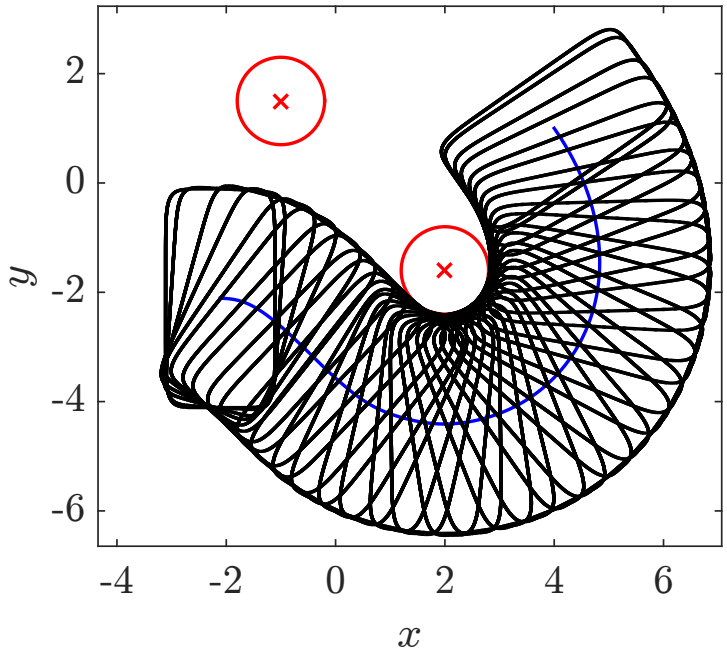

Figure 6.5: Shortest path solution for the wide robot

Here, the wide robot has $\sigma = (1, 2)$. The obstacles are centered at the same location as in the skinny case but the radii are changed to $r = 0.8$. The initial orientation is $\theta_{\mathrm{i}} = 0$. The direction of motion is in the direction of the longer edge. The initial robot position is $(-2.11, -2.11)$, and the objective is to reach $(2.52, 2.22)$ at time $T_f = 7\pi$, with the same

control bounds as for the thin robot. Again, the simpler inequality constraint (6.17) for the obstacles (2 constraints) are used with $p = 8$ for the approximation. The optimal control result depicted in Fig 6.5 shows that the shorted path involved circumnavigating the two obstacles, as the gap was not wide enough.

6.6.2 Rectangular obstacles

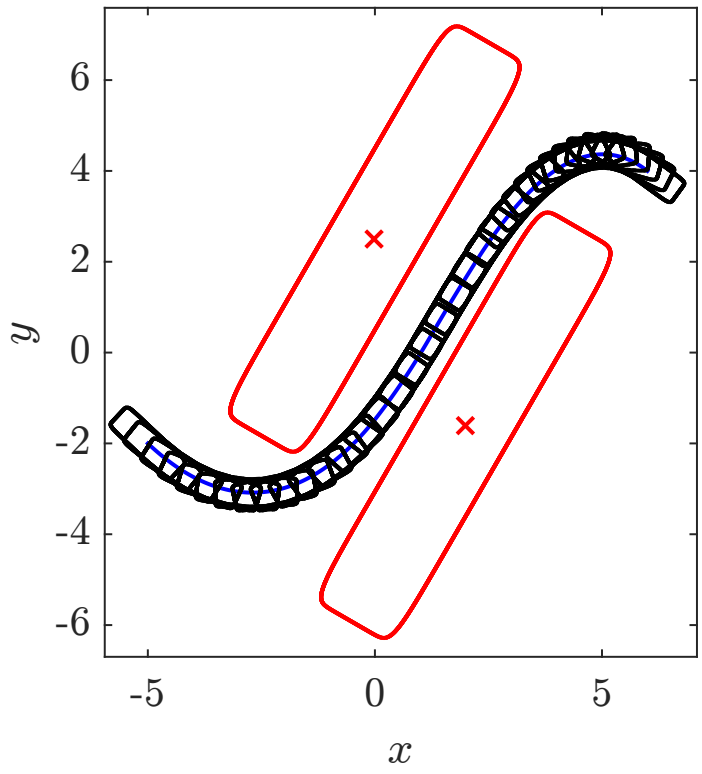

Figure 6.6: Shortest path between rectangles for a thin robot with a fixed final orientation and free final time constraints

This example considers two rectangular obstacles whose frames are $g_r^1 = (2, -1.6, \pi/3)$ and $g_r^2 = (0, 2.5, \pi/3)$, in $SE(2)$. Both rectangles have the shape half-lengths $\sigma^j = (5, 1)$. The rectangular robot has $\sigma = (0.9, 0.3)$ with initial orientation $\theta_{\mathbf{i}} = -\pi/4$. In addition, a final orientation constraint, $\theta_{\mathbf{f}} = -\pi/4$, is imposed with free final arrival time, T_f. The bounds for the controls are $u_1(t) \in [-5, 5]$ and $u_2(t) \in [-0.5\pi, 0.5\pi]$. The initial position of the robot is $(-5, -2)$, with the final position $(6, 4)$ at T_f. The L_p constraints for the safe

path (8 constraints for each obstacle) using (6.22) with $p = 10$ for the approximation is used. The optimal control result is depicted in Fig 6.6 and shows that the shortest path for the robot went through the hallway created by two rectangular obstacles.

6.6.3 Dual problem: circular robot with rectangular obstacle

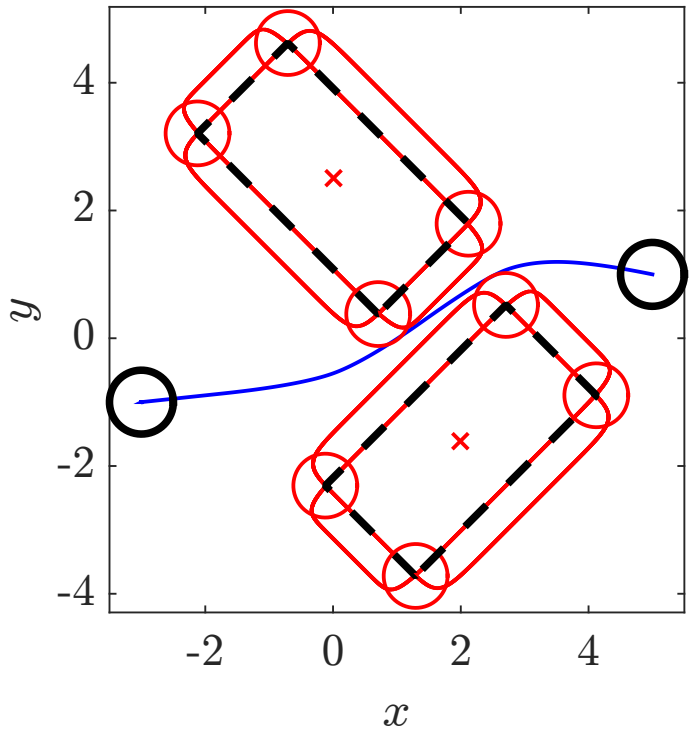

Figure 6.7: Shortest path using 6 constraints obstacle

The last example demonstrates the dual problem of a circular robot navigating around rectangular obstacles. The example is included since it is easier to visualize the 6 constraints in this dual problem. The robot has a radius of 0.5, and starts with the initial configuration, $g(0) = (-3, -1, \pi/4)$. The robot final position is $(5, 1)$ with final time $T_f = 11.6\pi$. The obstacles are centered at the same location as for the thin rectangular robot case (§6.6.2), with half side lengths $(2, 1)$, and orientations $\pi/4$ and $-\pi/4$, respectively. The bounds for the controls are $u_1(t) \in [-15, 15]$ and $u_2(t) \in [-0.5\pi, 0.5\pi]$. The L_p constraints for the safe path (6 constraints for each obstacles) with a modified version of

(6.16) is used. The value $p = 10$ is chosen for the approximation.

The optimal control result is depicted in Fig 6.7 where the two black circles represent the robot at the initial and the final position. Like Fig 6.3b, the unit spheres of the six L_p constraints are overlaid on the obstacles. Examination of the numerical output confirms that the robot trajectory does not enter the region generated by the six constraints for each obstacle.

CHAPTER 7

GEOMETRY 2: BENDABLE CUBOID ROBOTS PATH PLANNING

In this chapter, the safety constraint proposed in Chapter 6 is generalized to rigid and deformable (bendable) cuboid robots in $\mathbb{R}^3$. For regular cuboid robots, level sets of weighted L_p norms generate implicit approximations of their surfaces. For bendable cuboid robots a weighted L_p norm in polar coordinates implicitly approximates the surface boundary through a specified level set. Obstacle volumes, in the environment to navigate within, are presumed to be approximately described as sub-level sets of weighted L_p norms. Using these approximate surface models, the optimal safe path planning problem is reformulated as a two stage optimization problem, where the safety constraint depends on the point on the robot which is closest to the obstacle in the obstacle's distance metric. A set of equality and inequality constraints is derived to replace the closest point problem, which is then defines additional analytic constraints on the original path planning problem. Combining all the analytic constraints with logical AND operations leads to a general optimal safe path planning problem. Numerically solving the problem involves conversion to a nonlinear programing problem.

This chapter is organized as follows. In § 7.1, the background of the safe path planning for rigid or bendable robot in $\mathbb{R}^3$ is reviewed. The cuboid model is introduced in § 7.2, and the optimal path planning problem is stated in § 7.3. The approximation of bendable cuboid is proposed in § 7.4, and the analytic conditions for collision avoidance are derived in § 7.5. Finally, the proposed generalized weighted L_p method is used in the optimal path planning problem in § 7.6.

7.1 Introduction

Inspired by the geometry of level sets of L_p norms, the direct approach in Chapter 6 proposed a new framework based on analytic inequalities combined with AND operations that represent the C-free space of a rectangular robot with rectangular or ellipsoidal obstacles in the case of planar $SE(2)$ models. This new framework does not requires integer variables but is restricted to the planar model since *edge to edge* collision in $\mathbb{R}^3$ cannot be captured.

In this section, a further generalization of this framework is studied by analytically approximating the $SE(3)$ C-free space for regular rigid cuboid robots (which can be relaxed to ellipsoid or circular robots) with cuboid obstacles (which can also be relaxed to ellipsoid or spherical shapes). The safety constraint is reformulated by introducing an inner optimization to find the closest point on the cuboid robot to the obstacle in the obstacle's distance metric. The challenge of extending the method in Chapter 6 to $SE(3)$ is that *edge to edge* collisions in three dimensional space are difficult to model. Instead of fixing the candidate points of collision as per § 6.5, an auxiliary optimization problem is introduced, which finds the point on the robot with a minimum distance to the obstacle, then checks whether the point belongs to the obstacle or not. Since the surface of the obstacle is also modeled by the 1-level set of weighted L_p norm, a minimum distance greater than 1 implies that the shape and configuration of the robot is safe.

The challenge is that, now the constraints of the original path planning problem require the solution of another optimization problem. This, so called *two-staged optimization*, is avoided by analytically deriving the necessary and sufficient conditions for the closest point problem for both regular and bent cuboid robots. In the end, a total of four equality and two inequality constraints represent the safety constraint of a rigid cuboid robot, and four equality and ten inequality constraints for a bendable cuboid robot.

Continuing, there are many mechanical robots with non-rigid (deformable or soft) bodies. These robots can change their body shape during navigation or while executing a

movement. For example, robotic fish bend their bodies to maneuver under water [122, 123], and a finger shaped manipulator using fiber-reinforced soft actuators in [13] bends, twists and enlarges its body. Bending robots figure extensively as models for continuum manipulators [11, 12], where a multi-segment cylinder-shaped robot is controlled by a constant curvature bend in each segment [124].

However, the difficulty of applying rigid motion theory to the non-rigid motion directly is the lack of a meaningful joint space to describe the deformable motion [125]. Therefore, most research in controlling deformable robots first approximates the deformable surfaces. Deformation of solid geometric objects has been studied extensively in computer graphics [126]. One popular non-physical model uses the free form deformation technique, where the surface deformations use a trivariate tensor product Berstein polynomial with a discrete set of control points in $\mathbb{R}^3$ describing the deformations. This method has been extensively used in computer graphics but the control points lack physical meaning for robotics applications. As a result, much path planning research on deformable robots uses a physically grounded deformation model acting on sampled points of the surface [127]. More accurate approximation of the surface can be obtained by solving the partial differential equation (PDE) governing dynamic elastic equation using finite element methods (FEM) [128, 129]. The surface is discretized by the meshes (elements), and the PDE is converted to the algebraic equations of the node points. The original continuous shape function of meshes are then approximated by basis functions using the node values. Despite the accuracy of the model, the computation load for solving FEM is very high. Alternatively, a mass-spring system is widely used to represent the surface by discretizing the surface with a finite set of point masses which are connected with spring [130, 131]. Benefits of having this model is that the governing dynamics equation become ordinary differential equations, in contrast to FEM where the planner needs to solve PDE. The challenge in path planning using the sample based deformable surface lies in the collision checking part since the planner needs to consider every possible collision on the discrete surfaces. For deformable robots, since

safety constraint cannot be expressed analytically, the planning research is mostly limited to sample based planning methods such as probabilistic roadmap (PRM) [130, 131] or rapidly-exploring random tree (RRT) [128] planners.

This chapter includes an analytic approximation for the deformable surface of a bendable cuboid robot. It lies in the middle ground between physical and non-physical approximations since the control parameter of the deformable shape is the curvature of bending (which can be controlled in many applications, [11, 132, 133]) but is not influenced by external forces. This analytic model allows the construction of a set of equality and inequality constraints combined with logical AND operations as a function of the configuration of the robot in $SE(3)$ and the curvature control parameter, which altogether represent the safety constraints for the bendable cuboid robot. The proposed bendable cuboid model can be used for the deformable safety guard of a continuum manipulator [11], a soft fiber-reinforced bending actuator [132], and an average snake body frame [133].

7.2 Model

In this section, the kinematics of rigid body motion is reviewed, and the cuboid robot models are introduced.

7.2.1 Kinematics

A kinematic model for cuboid robots in $SE(3) := \mathbb{R}^3 \times SO(3)$ where $SO(3)$ is the special orthogonal group in $\mathbb{R}^{3\times3}$ is studied in this section. See more details of rigid body motion in [18]. Let $g(t) \in SE(3)$ be the robot frame at time t,

$$g(t) := (x(t), y(t), z(t), R(t))^T, \tag{7.1}$$

where $p\,(t) := (x(t), y(t), z(t))$ is the center of mass (CoM) position of the robot in the world frame, and $R(t) \in SO(3)$ is the rotation matrix describing the orientation

of robot frame relative to the world frame. This kinematic model assumes that the robot controls the speed of the CoM, $u(t) \in \mathbb{R}$, and the instantaneous angular velocity, $\omega(t) := (\omega_1(t), \omega_2(t), \omega_3(t)) \in \mathbb{R}^3$, in the body frame. These kinematics are

$$\dot{p}(t) = R(t)e_0u(t) \tag{7.2}$$

$$\dot{R}(t) = R(t)\hat{\omega}(t) \tag{7.3}$$

where $\hat{\omega}(t)$ maps ω to a 3×3 skew-symmetric matrix in $so(3)$,

$$\hat{\omega}(t) := \begin{pmatrix} 0 & -\omega_3 & \omega_2 \\ \omega_3 & 0 & -\omega_1 \\ -\omega_2 & \omega_1 & 0 \end{pmatrix}, \tag{7.4}$$

and $e_0 \in \mathbb{R}^3$ is the linear velocity direction in the body frame.

7.2.2 Cuboid Robot Model

The two types of robot geometries considered. One is a rigid model where the geometry of the robot does not change, and the other is a bendable model where the robot is assumed to be bendable in one of the axis in the robot's frame. The former is the *regular cuboid* geometry where the rigid shape is fully determined by the half lengths, $\sigma := (\sigma_1, \sigma_2, \sigma_3)$, on each axis in the robot frame. Figure 7.1a depicts an example with $\sigma = (2, 1, 1)$. The latter is the bent cuboid geometry where the bending is along the x-y plane with the constant curvature, $\kappa \in \mathbb{R}$. The full geometry of the *bent cuboid* requires the half lengths, $\sigma := (\sigma_1, \sigma_2, \sigma_3)$, the curvature, κ, and the bending angle θ_κ. Figure 7.1b depicts an example with $\sigma = (2, 1, 1)$, $\kappa = 0.3927$, and $\theta_\kappa = \pi/2$. For both geometries, there exists a curve passing through the robot which serves as an axis of symmetry for its surface.

Definition 29. *The* centerline *of the robot is a curve satisfying the following: 1) An intersection between a normal plane of the curve with the robot at any point on the curve*

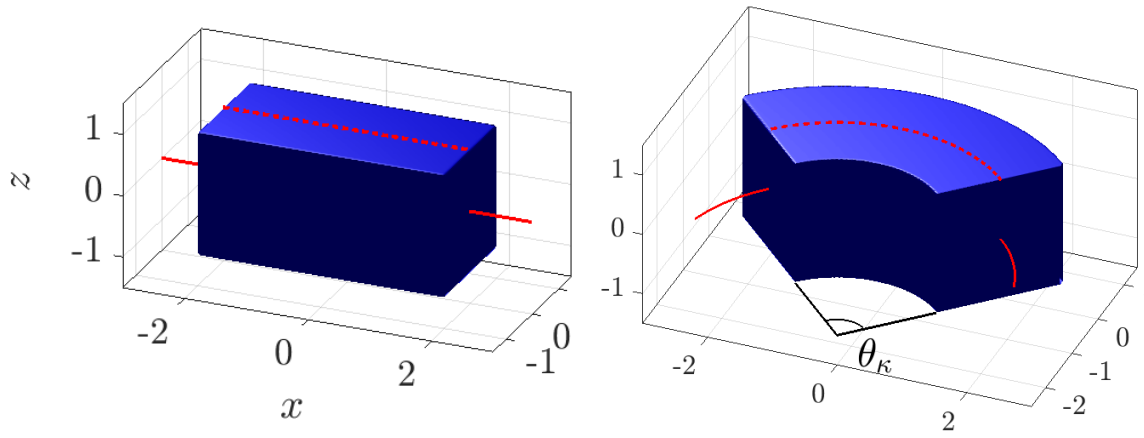

(a) Regular cuboid robot (b) Bent cuboid robot

Figure 7.1: Two types of geometries for cuboid robots in $SE(3)$

creates a rectangle with half lengths (σ_2, σ_3)*; and 2) The curve passes through the center of all such rectangles.*

The depictions in Figure 7.1 include the robot centerlines, drawn as solid red curves penetrating the robot. The dashed red line on the top surface visualizes the shape of the centerline inside the robot. The length of the centerline inside the robot is $2\sigma_1$ for the regular cuboid, and $1/\kappa \cdot \theta_\kappa$ for the bent cuboid. Inspired by the fact that the bent cuboid can be generated by bending the regular cuboid, the next invariant property for centerline is assumed.

Assumption 8 (Invariant property)**.** *The length of the centerline (LoC) captured in the bent cuboid is equal to the LoC of the original regular cuboid.*

The LoC of the examples in Figure 7.1 are both 4. The invariant property implies that the bending angle can be explicitly expressed by the curvature and the half-lengths as

$$\theta_\kappa = 2\sigma_1|\kappa|, \tag{7.5}$$

indicating that the half lengths and the curvature fully characterize the geometry of the bending robot. Therefore, the *shape parameters* are defined by σ for the regular cuboid,

and (σ, κ) for the bent cuboid.

Rigid model

The rigid model shape is time invariant. Therefore, the shape parameters σ and κ are fixed, and the required controls for rigid body kinematics are u and ω. The regular cuboid model could represent a box shaped furniture in the 3D space, and the bent cuboid model could be used as an surface model for a boomerang.

Bendable model

The bendable model admits time variable shape parameters. Therefore, the shape parameters $\sigma(t)$ and $\kappa(t)$ become additional control parameters besides u and ω. For the length preserving robots, the following assumptions holds:

Assumption 9 (Constant length assumption)**.** *The half lengths of the robot $\sigma > 0$ are fixed, and the robot can be bent by controlling the curvature $\kappa(t)$.*

Though the robot may bend with different curvatures, the above assumption means that the LoC is constant and equal to $2\sigma_1$ for all time, due to (7.5).

The bendable cuboid robot is directly related to the fundamental segment of finger motion using fiber-reinforced soft actuators in [13], and it is also related to the bending motion of the black knifefish in [134].

Remark 1 The volume of the regular cuboid robot, $V_r > 0$, with σ, is

$$V_r = 8\sigma_1\sigma_2\sigma_3. \tag{7.6}$$

From (7.6), the volume of a bent cuboid with the same half-lengths and satisfying Assump-

tion 9 is

$$\begin{aligned} V_b(t) &= ((1/|\kappa(t)| + \sigma_2)^2 - (1/|\kappa(t)| - \sigma_2)^2)\theta_\kappa(t)\sigma_3 \\ &= 4(1/|\kappa(t)|)\sigma_2\theta_\kappa(t)\sigma_3 \\ &= V_r, \end{aligned}$$

where the last equality holds by using (7.5). Therefore, the volume is invariant during bending, and the length preserving robot satisfying Assumption 9 also preserves the volume of the robot. This could be important for liquid filled robots. The proposed algorithm works equally in the case of a time varying half-length (i.e., a volume changing robot) without modifying any key result in this chapter.

7.3 Problem Statement

Consider the optimal path planning problem for cuboid robots navigating through a region containing regular cuboid obstacles. The robot state includes its frame $g(t) \in SE(3)$ and its shape parameters $(\sigma(t), \kappa(t))$, which satisfy Assumption 8. There are N_r regular cuboid obstacles each of whose frames and half-lengths are $g_r^j := (x_r^j, y_r^j, z_r^j, R_r^j) \in SE(3)$ and $\sigma^j := (\sigma_1^j, \sigma_2^j, \sigma_3^j)$, respectively, for $j \in \{1, \cdots, N_r\}$. The origin of each obstacle frame is at the center of cuboid. An initial $SE(3)$ configuration and a final $SE(3)$ configuration are given as the path boundary constraints. The arrival time, $T_f > 0$, is free.

Let $g(q) \in \mathbb{R}^3$ denote the transformation of coordinates of $q \in \mathbb{R}^3$ according to $g \in SE(3)$. The inverse g^{-1} would perform the change of coordinates in the inverse direction. Per §6.3, the σ^j-weighted L_∞ norm represents the regular cuboid with half lengths, σ^j, and the collision-free spaces of the regular cuboid obstacles are given by the super-level sets

$$R_j := \{q \in \mathbb{R}^3 : \left|\left|[g_r^j]^{-1}(q)\right|\right|_{\sigma^j,\infty} > 1\},$$

in the world frame for all i and j. As the robot moves, the collision constraints in the robot's body frame will change. The collision-free space in robot body coordinates is

$$R_j^{\mathcal{R}} := \{q \in \mathbb{R}^3 : \left|\left|[g_r^j]^{-1} \circ g(q)\right|\right|_{\sigma^j,\infty} > 1\}.$$

Let $B(\sigma(t), \kappa(t)) \subset \mathbb{R}^3$ describe the robot's full body in the robot frame at time t. The optimal safe path planning problem formulation is

$$\arg \min_{u,\omega,\sigma(t),\kappa(t)} \int_0^{T_f} L(g, \dot{g}, u, \kappa)dt \text{ subject to} \tag{7.7}$$

$$\begin{cases} \dot{g} = f(g, u, \omega), \\ g(0) = (\mathbf{x_i}, \mathbf{y_i}, \mathbf{z_i}, \mathbf{R_i}), \\ g(T_f) = (\mathbf{x_f}, \mathbf{y_f}, \mathbf{z_f}, \mathbf{R_f}), \end{cases} \tag{7.8}$$

$$B(\sigma(t), \kappa(t)) \subset (\bigcap_{j=1}^{N_r} R_j^{\mathcal{R}}), \tag{7.9}$$

where the vector field f is given by the kinematic equations (7.2-7.3), $u \in \mathbb{R}$ and $\omega \in \mathbb{R}^3$ are the control inputs, and $L(g, \dot{g}, u)$ is some physically meaningful cost such as control energy or path length. Depending on the flexibility of the robot, $B(\sigma(t), \kappa(t))$ would be constant (rigid model) or be time varying (bendable model).

The optimization problem will be solved for the two cases:

1. (Rigid robot) Find the kinematic controls for fixed shape parameters.
2. (Bendable robot) Find the kinematic controls and the curvature control, $\kappa(t)$, subject to Assumption 9.

Since the constraints in (7.9) typically require OR operations using the hyperplanes of the faces, the goal is to first find a set of inequality and equality constraints with AND operations for the safety constraints. Since the constraints in (7.9) typically require OR operations using the hyperplanes of the faces, the goal is to first find a set of inequality and

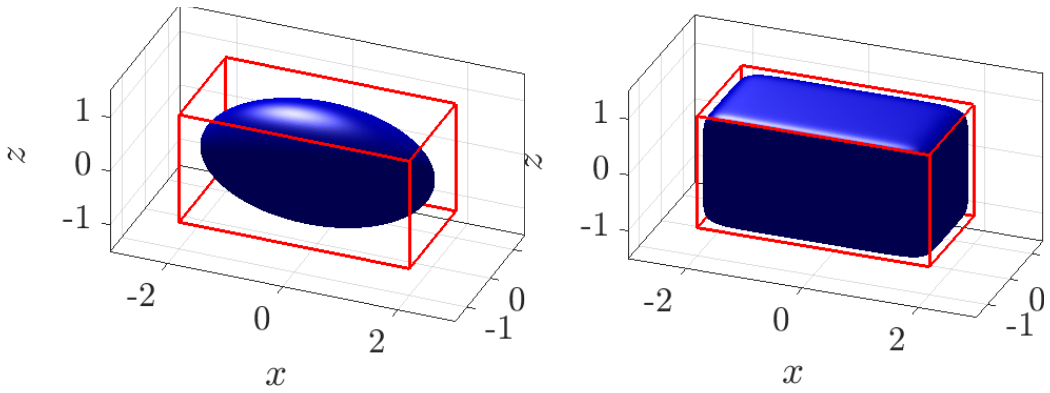

(a) 1-levelset with $p = 2$ (b) 1-levelset with $p = 10$

Figure 7.2: Approximated surface for regular and bent cuboid

equality constraints with AND operations for the safety constraints.

Remark 2. The obstacles are not restricted to cuboid shapes, rather any 1-level set of different σ^j and p value serves to model an obstacle. For example, an ellipsoidal obstacle has $p = 2$ and $\sigma^j = (a, b, c)$ for distinct $a, b, c > 0$, while a spherical obstacle further constrains the a, b, c to be equal. Since safety conditions are derived based on the abstract shape parameters, σ^j, and p, the results naturally applies to ellipsoidal and spherical obstacles.

7.4 Approximation of Cuboid Robots

In this section, the regular cuboid is approximated by the weighted L_p norm in Cartesian coordinate, and a new positive definite function is proposed, whose $|\kappa|$-level set approximates the bent cuboid.

7.4.1 Regular cuboid approximation

The rectangular robot surface in $\mathbb{R}^2$ approximated by the 1-level set of a weighted L_p norm in [135], generalizes to $\mathbb{R}^3$. Choosing the positive half lengths $\sigma := (\sigma_1, \sigma_2, \sigma_3)$, the cuboid surface description is

$$B_{(\sigma,p)} := \{v \in \mathbb{R}^3 | \; ||v||_{(\sigma,p)} = 1\}. \tag{7.10}$$

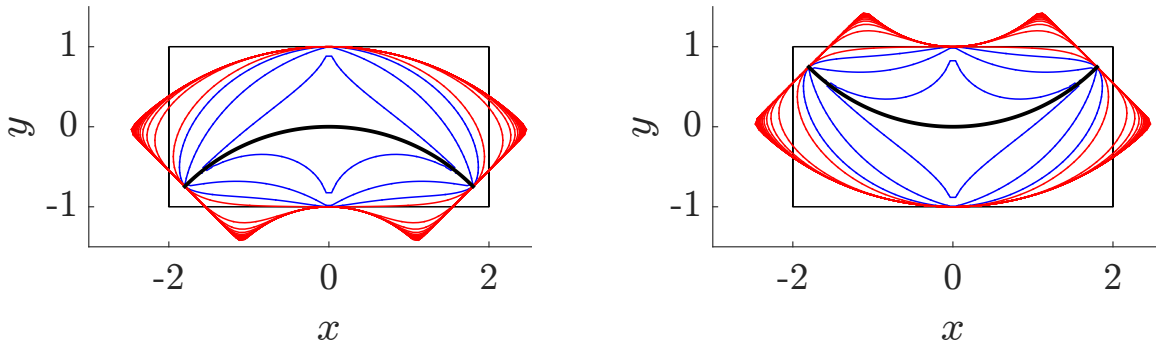

(a) $\kappa > 0$ (b) $\kappa < 0$

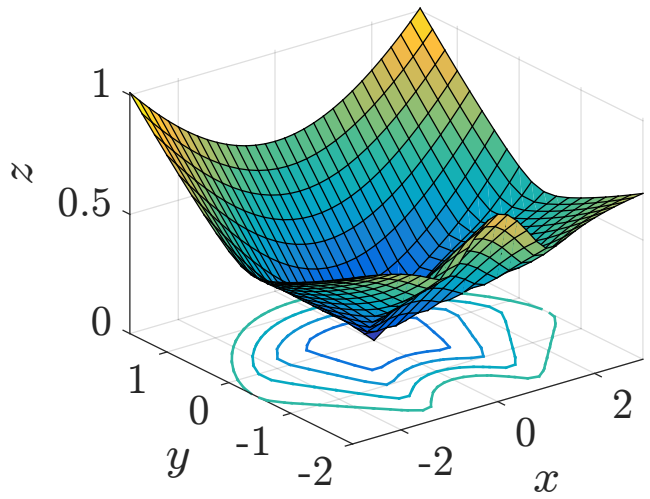

(c) Level sets for $p = 10$

Figure 7.3: Geometrical interpretation of weighted polar L_p in $2D$

Equation (7.10), evaluated in the robot frame, will play a role in formalizing the safety constraint (7.9) using inequality constraints. Figure 7.2 consists of several examples of cuboid approximations using the weighted L_p approximation with different p values. The half lengths are chosen as $\sigma = (2, 1, 1)$, with Figure 7.2a visualizing an ellipsoid for the choice $p = 2$, and Figure 7.2b an approximate cuboid for the choice $p = 10$. The surface model approaches that of a regular cuboid (the red boundaries in Figure 7.2) as the value of p increases. The example of Figure 7.1a uses $p = 200$.

7.4.2 Bent cuboid approximation

To approximate bent cuboids, this section introduces a weighted L_p norm expressed in polar coordinates. Analysis of the planar bent rectangle case establishes the important geometry associated to the polar space and its connection to the original shape. Extending the planar results to $\mathbb{R}^3$ will then involve extruding the planar bent rectangle in the vertical direction, normal to the plane. A modified weighted, polar L_p norm recovers the $3D$ surface for bent cuboids.

Bent rectangle

Bent rectangle

Let $\kappa \neq 0$ be given, and σ be fixed. Define the coordinate transformation $\mathcal{T}_\kappa : \mathbb{R}^2 \to \mathbb{R}^2$ to be

$$\mathcal{T}_\kappa(\begin{pmatrix} v_x \\ v_y \end{pmatrix}) := \begin{pmatrix} \kappa v_x \\ \kappa v_y + 1 \end{pmatrix}, \tag{7.11}$$

for every $v := (v_x, v_y) \in \mathbb{R}^2$. The polar coordinates of v, transformed by $\mathcal{T}_\kappa$, are

$$R_{\mathcal{T}_\kappa}(v) := \sqrt{(\kappa v_x)^2 + (\kappa v_y + 1)^2}, \tag{7.12}$$

$$\theta_{\mathcal{T}_\kappa}(v) := \arctan\left((\kappa v_y + 1)/\kappa v_x\right). \tag{7.13}$$

Definition 30 (Weighted polar L_p)**.** *The* (σ, κ)-weighted polar L_p *function is the positive definite function* $\Phi_{(\sigma,\kappa,p)} : \mathbb{R}^2 \to \mathbb{R}$*,*

$$\Phi_{(\sigma,\kappa,p)}(v) := ((|R_{\mathcal{T}_\kappa}(v) - 1|/\sigma_2)^p + (|\theta_{\mathcal{T}_\kappa}(v) - \theta_0|/\sigma_1)^p)^{1/p}, \tag{7.14}$$

where $\theta_0 = \mathrm{sign}(\kappa) \cdot \pi/2$*.*

The function $\mathrm{sign}(\kappa) = 1$ if $\kappa \geq 0$ and -1 if $\kappa < 0$. When the parameters (σ, κ) are known, the value function of Definition 30 is denoted as the weighted polar L_p function.

The surface of the bent rectangular robot is approximated by the $|\kappa|$-level set of $\Phi_{(\sigma,\kappa,p)}$. Several examples of the $|\kappa|$-level set of $\Phi_{(\sigma,\kappa,p)}$ with different p values are shown in Figure 7.3a and figure 7.3b, where $\sigma = (2,1)$ is chosen with $\kappa = 0.3927$ and $\kappa = -0.3927$, respectively. The blue contours represents the p value changes from 0.6 (innermost) to 1.6 (outermost) with step size 0.5, and the red contours represents the changes from 2 (innermost) to 40 (outermost) with step size 2.

The $((2,1), 0.3927)$-weighted polar L_p function with $p = 10$ and its different level sets are shown in Figure 7.3c where the contours projected on (x, y) plane corresponds to the levels from 0.2 (innermost) to 0.5 (outermost).

Lemma 6. *(a) For $p \geq 2$ even, $\Phi_{(\sigma,\kappa,p)}$ is a positive definite function*
(b) $\Phi_{(\sigma,\kappa,p)}$ is not positive homogeneous with respect to to scalar multiplication. In other words, there exist $\alpha > 0$ such that $\Phi_{(\sigma,\kappa,p)}(\alpha v) \neq \alpha v$ for some $v \in \mathbb{R}^2$.

Proof. Since p is even number, $\Phi_{(\sigma,\kappa,p)}(v) \geq 0$ holds for every $v \in \mathbb{R}^2$. Also $\Phi_{(\sigma,\kappa,p)}(\mathbf{0}) = 0$ holds for zero vector, $\mathbf{0} \in \mathbb{R}^2$ from $\lim_{\alpha\to\infty} \arctan\alpha = \pi/2$. Now, suppose that $\Phi_{(\sigma,\kappa,p)}(v) = 0$ holds, then $\theta_{\mathcal{T}_\kappa}(v) = \theta_0$ and $R_{\mathcal{T}_\kappa}(v) = 1$ follows from p even. From the first observation $\arctan\left((\kappa v_y + 1)/\kappa v_x\right) = \text{sign}(\kappa)\pi/2$, which implies $v_x = 0$. From the second observation, $v_y = 0$. Therefore, $\Phi_{(\sigma,\kappa,p)}(v) = 0$ holds if and only if $v = \mathbf{0}$. Hence, $\Phi_{(\sigma,\kappa,p)}$ is a positive definite function.
(b) Pick $p = 2$ and $v = (1,0)^T$, $\kappa = 1$, and $\sigma = (1,1)$, then $\Phi_{((1,1),1,2)}(v) = 0.8879$. Let $\alpha = -1$ and $\overline{v} = \alpha v$, then $\Phi_{((1,1),1,2)}(\overline{v}) = 2.3923$, which shows that

$$\Phi_{((1,1),1,2)}(\overline{v}) \neq |\alpha|\Phi_{((1,1),1,2)}(v).$$

Hence, $\Phi_{(\sigma,\kappa,p)}$ is not positive homogeneous with respect to scalar multiplication. □

With regards to collision detection, evaluation of the weighted polar L_p function at a point inside the robot is less than $|\kappa|$, and at a point outside is greater than $|\kappa|$. Additionally, the $|\kappa|$-level curves do not self intersect. Therefore, all safe configurations of the bent

rectangular robot to a point obstacle are simply obtained by evaluating the weighted L_p function at the obstacle point in the robot frame and checking if it is greater than $|\kappa|$. The $|\kappa|$-level set of (σ, κ)-weighted polar L_p function approaches the bent rectangular robot for $p \to \infty$.

Theorem 11. *The boundary of the bent rectangular robot, $\partial B_{((\sigma_1,\sigma_2),\kappa)}$, is equivalent to the $|\kappa|$-level set of $\Phi_{(\sigma,\kappa,p)}$,*

$$\partial B_{((\sigma_1,\sigma_2),\kappa,p)} := \{v \in \mathbb{R}^2 | \Phi_{(\sigma,\kappa,p)}(v) = |\kappa|\}, \tag{7.15}$$

as p approaches ∞

Proof. Let $\mathcal{R}_\kappa = 1/|\kappa|$ be the radius of curvature. The regular rectangle approximated by the (σ_1, σ_2)-weighted L_p norm is

$$B((\sigma_1, \sigma_2), p) := \{u \in \mathbb{R}^2 |\ ||u||_{(\sigma_1,\sigma_2),p} \leq 1\} \tag{7.16}$$

where $u = (u_x, u_y)$ such that $u_x \in [-\sigma_1, \sigma_1]$ and $u_y \in [-\sigma_2, \sigma_2]$.

Now define the mapping $\mathcal{B}_\kappa : B((\sigma_1, \sigma_2), p) \to \mathbb{R}^2$,

$$\mathcal{B}_\kappa(u) := \begin{pmatrix} (\mathcal{R}_\kappa + u_y)\cos(\alpha\pi/2 + (\theta_\kappa/2)(u_x/\sigma_1)) \\ (\mathcal{R}_\kappa + u_y)\sin(\alpha\pi/2 + (\theta_\kappa/2)(u_x/\sigma_1)) - \alpha\mathcal{R}_\kappa \end{pmatrix} \tag{7.17}$$

for all $u \in B((\sigma_1, \sigma_2), p)$, where $\alpha = \text{sign}(\kappa)$.

Observe that $\mathcal{B}_\kappa(\cdot)$ is invertible on its image, with said inverse $\mathcal{B}_\kappa^{-1} : \mathcal{B}_\kappa(B((\sigma_1, \sigma_2), p)) \to B((\sigma_1, \sigma_2), p)$ given by

$$\begin{pmatrix} u_x \\ u_y \end{pmatrix} = \begin{pmatrix} 2(\arctan((\overline{u}_y + \alpha\mathcal{R}_\kappa)/\overline{u}_x) - \alpha\pi/2)\sigma_1/\theta_\kappa \\ \sqrt{\overline{u}_x^2 + (\overline{u}_y + \alpha\mathcal{R}_\kappa)^2} - \mathcal{R}_\kappa \end{pmatrix} \tag{7.18}$$

where $(\overline{u}_x, \overline{u}_y) \in \mathcal{B}_\kappa(B((\sigma_1, \sigma_2), p))$, and θ_κ is the bending angle of constant curvature

(see Figure 7.1b). By using Assumption 8 and (7.5), with the coordinate transformation in (7.11), it holds that

$$\begin{pmatrix} |\kappa| u_x \\ |\kappa| u_y \end{pmatrix} = \begin{pmatrix} (\theta_{\mathcal{T}_\kappa}(\overline{u}) - \alpha\pi/2) \\ R_{\mathcal{T}_\kappa}(\overline{u}) - 1 \end{pmatrix}. \tag{7.19}$$

Since $u \in B((\sigma_1, \sigma_2), p)$, $|||\kappa|u||_{(\sigma_1,\sigma_2),p} \leq |\kappa|$ holds. Therefore, by computing $|||\kappa|u||_{(\sigma_1,\sigma_2),p}$,

$$\Phi_{(\sigma,\kappa,p)}(\overline{u}) \leq |\kappa|, \tag{7.20}$$

for all $\overline{u} \in \mathcal{B}_\kappa(B((\sigma_1, \sigma_2), p))$. Let the approximated bent rectangular be

$$B((\sigma_1, \sigma_2), \kappa, p) := \{\overline{u} \in \mathbb{R}^2 | \Phi_{(\sigma,\kappa,p)}(\overline{u}) \leq |\kappa|\}. \tag{7.21}$$

Since the mapping, $\mathcal{B}_\kappa$, is diffeomorphic, $B((\sigma_1, \sigma_2), \kappa, p)$ and $B((\sigma_1, \sigma_2), p)$ have a one to one correspondence for all p. Furthermore, the boundary of $B((\sigma_1, \sigma_2), \kappa, p)$ and the boundary of $B((\sigma_1, \sigma_2), p)$ can be induced by each other as well. Therefore, it is now obvious that $\partial B((\sigma_1, \sigma_2), \kappa, p)$ approaches the bent rectangular robot as $p \to \infty$ by computing (7.17) for the actual bent rectangular robot.

Remark. The centerline of $B((\sigma_1, \sigma_2), p)$ is on the x-axis, and is given by a parameterized curve $C(s) = (s, 0)$ for $s \in [-\sigma_1, \sigma_1]$. Transforming the curve $C(\cdot)$ using $\mathcal{B}_\kappa$, leads to an arc passing through zero with constant curvature κ,

$$\begin{pmatrix} (\mathcal{R}_\kappa) \cos(\alpha\pi/2 + (\theta_\kappa/2)(s/\sigma_1)) \\ (\mathcal{R}_\kappa) \sin(\alpha\pi/2 + (\theta_\kappa/2)(s/\sigma_1)) - \alpha\mathcal{R}_\kappa \end{pmatrix}. \tag{7.22}$$

This shows that the x-axis has been deformed to an arc after the transformation $\mathcal{B}_\kappa$, and that the new bent axis corresponds to $\mathcal{B}_\kappa(C(\cdot))$, which serves as a centerline of the bent robot. Two examples of bent centerlines are shown as black curves in Figure 7.3a and Figure 7.3b for positive and negative curvature, respectively. □

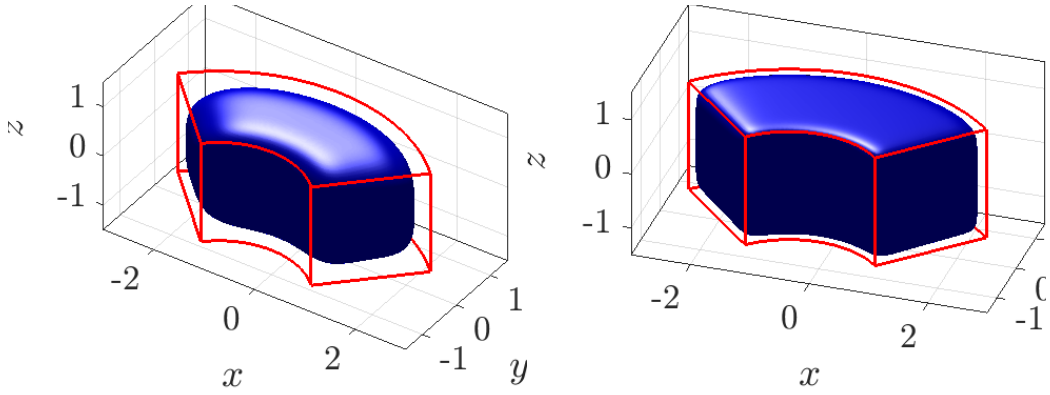

(a) $|\kappa|$-levelset with $p = 4$ (b) $|\kappa|$-levelset with $p = 10$

Figure 7.4: Approximated surface for bent cuboid

The following proposition shows that Assumption 8 holds for the approximate, weighted polar L_p model.

Proposition 10. *The LoC of $\partial B_{((\sigma_1,\sigma_2),\kappa,p)}$ is equal to the LoC of original rectangular robot with half-lengths (σ_1, σ_2).*

Proof. The centerline for the $((\sigma_1, \sigma_2), \kappa)$-weighted polar L_p function is defined as a parameterized curve, (7.22). The centerline is an arc with radius of curvature $1/|\kappa|$, whose polar angle varies in the range $[\text{sign}(\kappa)\pi/2 - \theta_\kappa/2, \text{sign}(\kappa)\pi/2 + \theta_\kappa/2]$ with θ_κ the desired angle of curvature in (7.5). Computing the length of the arc, the LoC of $\partial B_{((\sigma_1,\sigma_2),\kappa,p)}$ is found to be $2\sigma_1$, as needed by Assumption 8. □

Centerlines examples are shown as black curves in Figure 7.3a and Figure 7.3b for positive and negative curvatures, respectively.

Bent cuboid

In this section, the bent cuboid surface model is approximated by vertically expanding the bent rectangle in the robot's frame. Inspired by the fact that the different level sets still preserve the shape of the bending effect as shown in Figure 7.3c, the multiple level of $\Phi_{(\sigma,\kappa,p)}$ will be considered as a $X - Y$ section at different z values.

Without loss of generality, let the bent rectangular robot with the shape parameters, $((\sigma_1, \sigma_2), \kappa)$, be the $X - Y$ section at $z = 0$ of the bent cuboid robot with the shape parameters, $((\sigma_1, \sigma_2, \sigma_3), \kappa)$ in the robot's frame.

A new positive definite function is given as follows.

Definition 31 (Weighted polar L_p in $3D$)**.** *The* (σ, κ)-weighted polar L_p function in $3D$. *is the positive definite function,* $\Psi_{(\sigma,\kappa,p)} : \mathbb{R}^3 \to \mathbb{R}$,

$$\Psi_{(\sigma,\kappa,p)}(v) := ((\Phi_{((\sigma_1,\sigma_2),\kappa,p)}(v_x, v_y))^p + (|\kappa| v_z/\sigma_3)^p)^{1/p}, \tag{7.23}$$

where $v = (v_x, v_y, v_z) \in \mathbb{R}^3$.

Similar to the bent rectangle case, the $|\kappa|$-level set of $\Psi_{(\sigma,\kappa,p)}$ represents the approximated bent cuboid. Several examples of the $|\kappa|$- level sets of $\Psi_{((2,1,1),\kappa,p)}$ for $\kappa = 0.3927$ with different p values are shown in Figure 7.4a-7.4b. The red boundary represents the original bent cuboid robot, and the blue surface represents the approximation with different p values. As p increases higher, the approximated bent cuboid model approaches closer to the original bounds. An example when $p = 200$ is shown in Figure 7.1b. The $|\kappa|$-level set of $\Psi_{(\sigma,\kappa,p)}$ is a proper approximation to the bent cuboid robot in the robot's frame.

Theorem 12. *The surface of the bent cuboid robot,* $\partial B_{((\sigma_1,\sigma_2,\sigma_3),\kappa)}$*, is equivalent to the* $|\kappa|$*-level set of* $\Psi_{(\sigma,\kappa,p)}$*,*

$$\partial B_{((\sigma_1,\sigma_2,\sigma_3),\kappa,p)} := \{v \in \mathbb{R}^3 | \Psi_{(\sigma,\kappa,p)}(v) = |\kappa|\}, \tag{7.24}$$

as p *approaches* ∞

Proof. It is enough to show that, for every $v_z \in [-\sigma_3, \sigma_3]$, the approximated surface $\partial B^{v_z}_{((\sigma_1,\sigma_2),\kappa,p)}$ defined by

$$\{v \in \mathbb{R}^3 | \Phi_{((\sigma_1,\sigma_2),\kappa,p)}(v_x, v_y) = |\kappa|(1 - (v_z/\sigma_3)^p)^{1/p}\} \tag{7.25}$$

is a bent rectangle with shape parameters $((\sigma_1, \sigma_2), \kappa)$, as $p \to \infty$. If $|v_z|/\sigma_3 < 1$, then

$$\lim_{p\to\infty} |\kappa|(1 - (v_z/\sigma_3)^p)^{1/p} = |\kappa|,$$

and so $\partial B^{v_z}_{((\sigma_1,\sigma_2),\kappa,p)}$ is the $|\kappa|$-level set of $\Phi_{((\sigma_1,\sigma_2),\kappa,p)}$. Therefore, by Theorem 11, the level set is the bent rectangle with the desired shape parameters.

If $|v_z|/\sigma_3 = 1$, then

$$\lim_{p\to\infty} \Psi_{(\sigma,\kappa,p)}(v) = \max\left(\Phi_{((\sigma_1,\sigma_2),\kappa,p)}(v_x, v_y), |\kappa v_z|/\sigma_3\right),$$

by using the fact the L_∞ norm is equivalent to the maximum absolute coordinate. Therefore, the approximated surface, $\partial B^{v_z}_{((\sigma_1,\sigma_2),\kappa,p)}$, is equal to the sublevel set,

$$\{v \in \mathbb{R}^3 | \Phi_{((\sigma_1,\sigma_2),\kappa,\infty)}(v_x, v_y) \leq |\kappa| \ \ \wedge \ |v_z|/\sigma_3 = 1\},$$

which consists of the top and bottom faces of the bent cuboid as $p \to \infty$. □

It follows that the approximated bent cuboid satisfies Assumption 8.

Corollary 2. *The LoC of $\partial B_{((\sigma_1,\sigma_2,\sigma_3),\kappa,p)}$ is equal to the LoC of original regular cuboid robot with half-lenghts $(\sigma_1, \sigma_2, \sigma_3)$.*

Proof. The proof is immediate from Theorem 12 and Proposition 10, as it was shown that each $X - Y$ section for a given Z level of the approximated robot is equivalent to the approximated bent rectangle. □

7.5 Collision Avoidance Constraints

In this section, the safety conditions for regular cuboid and bent cuboid in (7.9) are analyzed, and transformed into a set of equality and inequality constraints using the weighted L_p norm, and the weighted polar L_p function proposed in the previous section.

7.5.1 Two stage optimization

The geometry explored in the previous sections will serve to convert the safety constraint expressed as a set inclusion in (7.9) into several set exclusion inequality constraints to be met simultaneously. In doing so the equivalent formulation of the constraints will involve the solution to an optimization problem. Suppose that the surface of robot is modeled as in (7.10) for a regular cuboid, and (7.24) for bent cuboid with some even number p_r. In addition, the surface of j-th rectangular obstacle is modeled with 1-level set of σ^j-weighted L_p norm with some even number p_o. Given this analytic surface model of the robot, the safey constraint between a robot and a single obstacle is

$$\left|\left|[g_r^j]^{-1} \circ g_t(\overline{v}^j)\right|\right|_{\sigma^j,p_o} > 1 \tag{7.26}$$

$$\text{such that} \quad \overline{v}^j := \arg\min_{v^j \in \mathbb{R}^3} \left|\left|[g_r^j]^{-1} \circ g_t(v^j)\right|\right|_{\sigma^j,p_o} \tag{7.27}$$

$$\text{subject to} \quad \left|\left|v^j\right|\right|_{\sigma,p_r} = 1, \tag{7.28}$$

$$\text{or subject to} \quad \Psi_{(\sigma,\kappa,p_r)}(v^j) = |\kappa|, \tag{7.29}$$

following the notation of §7.3. The closest point $\overline{v}^j$ in (7.27) is on the surface of the robot given by (7.28) for the regular cuboid or (7.29) for the bent cuboid in the robot frame. This closest point minimizes the σ^j-weighted L_p obstacle distance in the obstacle frame. Therefore, the safety constraint is equivalent to (7.26), since the surface of the obstacle is given by the 1-level set of σ^j-weighted L_p norm. This formulation is only valid when the closest point, $\overline{v}^j$ is available. The subsequent sections identify necessary and sufficient conditions for the closest point $\overline{v}^j$ optimization problem.

7.5.2 Regular Cuboid Robots

First, the necessary condition for $v := (v_x, v_y, v_z)$ to be a stationary solution to (7.27) subject to (7.28) is analyzed. Let $w = (w_x, w_y, w_z) := [g_r^j]^{-1} \circ g_t(v)$ be transformation of

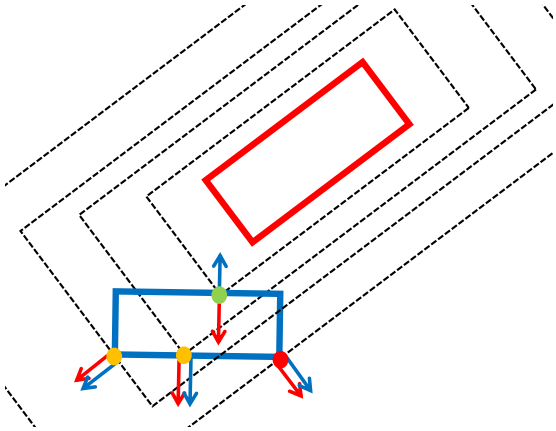

(a) Regular cuboid.

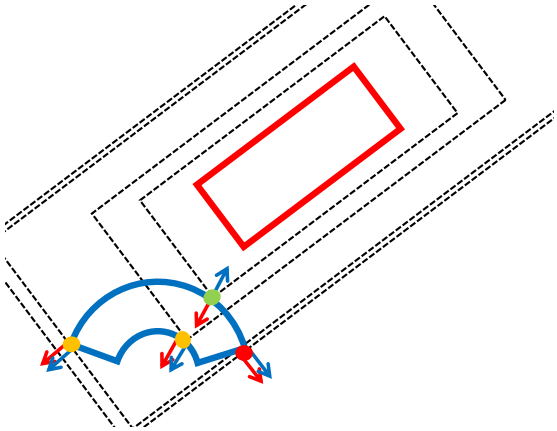

(b) Case 1 : Bent cuboid

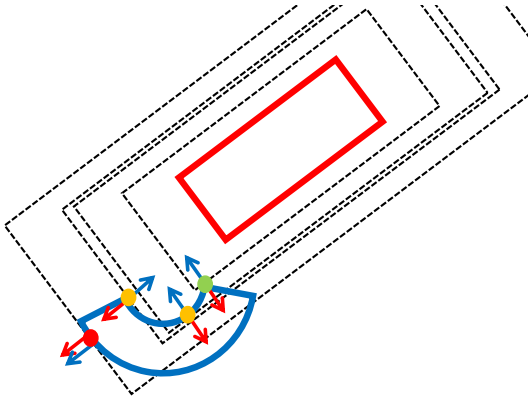

(c) Case 2 : Bent cuboid

Figure 7.5: Geometric interpretation of stationary points.

v to the j-the obstacle frame. The gradient of the cost function in (7.27) with respect to w, and the gradient of the equality constraint in (7.28) with respect to v are

$$\mathcal{W}_v := (w_x^{p-1}/(\sigma_1^j)^p, w_y^{p-1}/(\sigma_2^j)^p, w_z^{p-1}/(\sigma_3^j)^p)^T \tag{7.30}$$

$$\mathcal{V}_v := (v_x^{p-1}/(\sigma_1)^p, v_y^{p-1}/(\sigma_2)^p, v_z^{p-1}/(\sigma_3)^p)^T. \tag{7.31}$$

Theorem 13. *The first order necessary condition for $\overline{v}$ to be minimizer of (7.27) is*

$$P_{\overline{v}}([g_t]^{-1} \circ g_r^j(\mathcal{W}_{\overline{v}})) = 0, \tag{7.32}$$

where

$$P_{\overline{v}} = I_{3\times 3} - \mathcal{V}_{\overline{v}}\overline{v}^T, \tag{7.33}$$

with $I_{3\times 3}$ an identity matrix.

Proof. Let $H(v_x, v_y, v_z, \lambda)$ be a Hamiltonian of the problem in (7.27),

$$H(v_x, v_y, v_z, \lambda) := ||w(v)||_{\sigma^j, p_o} + \lambda(||v||_{\sigma, p_r} - 1), \tag{7.34}$$

where $w(v) := (w_x, w_y, w_z)$. The gradient of H is

$$\nabla_v H = ||w(v)||_{\sigma^j, p_o}^{1-p_o} \left([g_t]^{-1} \circ g_r^j(\mathcal{W})\right)^T + \lambda \, ||v||_{\sigma, p_r}^{1-p_r} \left(\mathcal{V}_{\overline{v}}\right)^T. \tag{7.35}$$

Then the necessary condition for a stationary point is

$$\nabla_v H = 0 \tag{7.36}$$

with the equality constraint in (7.28). By multiplying $\overline{v}$ to the right and using (7.28), λ is computed to be

$$\lambda = -(||w(v)||_{\sigma^j, p_o}^{1-p_o} \,/\, ||v||_{\sigma, p_r}^{1-p_r})([g_t]^{-1} \circ g_r^j(\mathcal{W}))^T \overline{v},$$

and by replacing λ in (7.35), the necessary condition in (7.36) is equivalent to (7.32). □

The structure of $P_{\overline{v}}$ provides a geometric interpretation for the necessary condition.

Proposition 11. *$P_{\overline{v}}$ is a projection matrix.*

Proof. It suffices to show that $P_{\overline{v}}$ is idempotent since $P_{\overline{v}}$ is a linear transformation. By computing $P_{\overline{v}}^2$, the following holds,

$$P_{\overline{v}}^2 = (I_{3\times 3} - \mathcal{V}_{\overline{v}}\overline{v}^T)^2 = I_{3\times 3} - 2\mathcal{V}_{\overline{v}}\overline{v}^T + \mathcal{V}_{\overline{v}}\overline{v}^T\mathcal{V}_{\overline{v}}\overline{v}^T = P_{\overline{v}},$$

since $\overline{v}^T \mathcal{V}_{\overline{v}} = 1$ by (7.28). □

The next corollary investigatess the range space of $P_{\overline{v}}$.

Corollary 3. *The dimension of the range space of $P_{\overline{v}}$, is 2.*

Proof. Since $P_{\overline{v}}$ is idempotent, each eigenvalue of $P_{\overline{v}}$ is either 0 or 1 [26]. The trace of $P_{\overline{v}}$ is given by,

$$Tr(P_{\overline{v}}) = 3 - \overline{v}^T \mathcal{V}_{\overline{v}} = 2.$$

Hence, there exist two eigenvalues of 1. □

The next theorem follows immediately.

Theorem 14. *(Geometric interpretation) The necessary condition in (7.32) holds for v if and only if the vector $([g_t]^{-1} \circ g_r^j(\mathcal{W}))$ is orthogonal to the two dimensional tangent space of the boundary of the robot, $\partial B_{((\sigma_1,\sigma_2,\sigma_3),p)}$, at v.*

Proof. Since $\mathcal{V}_{\overline{v}}$ is a gradient vector, it is orthogonal to the tangent space of $\partial B_{((\sigma_1,\sigma_2,\sigma_3),p)}$, at v. In addition, observe that $\mathcal{V}_{\overline{v}}$ is in the nullspace of $P_{\overline{v}}$. Therefore, the row space of $P_{\overline{v}}$ represents the two dimensional tangent space by Corollary 3. Hence, the necessary condition in (7.32) holds if and only if the vector $([g_t]^{-1} \circ g_r^j(\mathcal{W}_{\overline{v}}))$ is aligned with $\mathcal{V}_{\overline{v}}$. □

Instead of examining the Hessian of the Hamiltonian in (7.34), the following proposition provides a sufficient condition for global minima of (7.27).

Proposition 12. *A sufficient condition for $\overline{v}$ to be a global minimum is*

$$([g_t]^{-1} \circ g_r^j(\mathcal{W}_{\overline{v}}))^T \overline{v} < 0. \tag{7.37}$$

Proof. First, observe that the regular cuboid robot, $B_{((\sigma_1,\sigma_2,\sigma_3),p)}$, is convex, and the (σ^j, p)-weighted L_p norm is a convex function. The necessary condition in (7.32) shows that $\mathcal{V}_{\overline{v}}$ and $([g_t]^{-1} \circ g_r^j(\mathcal{W}_{\overline{v}}))$ are aligned. If these two vectors point in the same direction, in other

words $([g_t]^{-1} \circ g_r^j(\mathcal{W}_{\overline{v}}))^T \mathcal{V}_{\overline{v}} > 0$, then there is a point interior to $B_{((\sigma_1,\sigma_2,\sigma_3),p)}$ for which the cost is smaller. Since the level curves of (σ^j, p)-weighted L_p norm are continuous, there exist a point on the boundary $\partial B_{((\sigma_1,\sigma_2,\sigma_3),p)}$ with smaller cost. Therefore,

$$([g_t]^{-1} \circ g_r^j(\mathcal{W}_{\overline{v}}))^T \mathcal{V}_{\overline{v}} < 0$$

should hold for a global minimum point.

By using (7.36), the inner product between two normal vectors is explicitly computed as

$$([g_t]^{-1} \circ g_r^j(\mathcal{W}_{\overline{v}}))^T \mathcal{V}_{\overline{v}} = ([g_t]^{-1} \circ g_r^j(\mathcal{W}_{\overline{v}}))^T v ||\mathcal{V}_{\overline{v}}||_2.$$

Since $||\mathcal{V}_{\overline{v}}||_2$ is not equal to zero for every v on the surface of the robot, (7.37) only holds at the minimum. □

Interestingly, the inequality constraint in (7.37) is equivalent to $\lambda > 0$, where λ is the Lagrange multiplier in the Hamiltonian (7.34). This condition is similar to the Karush-Kuhn-Tucker (KKT) condition in the sense that the sign of the Lagrange multiplier must be non-negative.

A geometric explanation of Theorem 14 and Proposition 12 is demonstrated in Figure 7.5a. The example depicted is in planar space in order to better explain the direction of the normal vectors of the surface. The blue weighted L_p rectangle represents the robot's boundary, and the red weighted L_p rectangle represents the obstacle's boundary. The figure is drawn in the robot frame. The black dashed lines represent the level sets of the obstacle's weighted L_p norm, where the level value gets smaller closer to the red rectangle. The blue arrows represent the outward normal to the surface of the robot, and the red arrows represent the outward normal to the level curves of the obstacle's weighted L_p norm. In this example, there exist four points, two orange circles, one green circle, and one red circle on the robot's boundary. The green circle is the desired closest point, and the red circle is the maximum distance in terms of obstacle's weighted L_p norm. All four circles are statio-

nary solutions satisfying the necessary condition in (7.32). In all cases, the normal vectors are aligned. The blue arrow and the red arrow are pointing in the same direction for all three circles except for the green circle, which is the desired closest point. This graphically verifies the Proposition 12.

Therefore, the original optimization problem is replaced by introducing an auxiliary closest point $\overline{v}$ which satisfies four equality conditions, (7.32) and (7.28), and one inequality condition (7.37). By combining these constraints with inequality condition in (7.26), the safety condition for the regular cuboid can be given by four equality constraints and two inequality constraints.

7.5.3 Bent Cuboid Robots

Here, the necessary condition for v to be a stationary solution to (7.27) subject to (7.29) is considered. Let $w = (w_x, w_y, w_z) := [g_r^j]^{-1} \circ g_t(v)$ be the transformation of v to the j-th obstacle frame. The gradient of the cost function in (7.27) with respect to w is the same as in (7.30), and the gradient of the equality constraint in (7.29) with respect to v is

$$\mathcal{U}_v := \mathcal{V}_v^T \overline{Q}^{-1}, \tag{7.38}$$

where

$$\mathcal{V}_v := \begin{pmatrix} (R_{\mathcal{T}_\kappa}(v) - 1)^{p-1}/(\sigma_2)^p \\ (\theta_{\mathcal{T}_\kappa}(v) - \theta_0)^{p-1}/(\sigma_1)^p \\ (|\kappa| v_z)^{p-1}/(\sigma_3)^p)^T \end{pmatrix} \tag{7.39}$$

$$\overline{Q} := \begin{pmatrix} Q & \mathbf{0} \\ \mathbf{0}^T & 1 \end{pmatrix} \tag{7.40}$$

such that **0** is a zero vector in $\mathbb{R}^2$, and

$$Q = \begin{pmatrix} \cos(\theta_{\mathcal{T}_\kappa}(v)) & R_{\mathcal{T}_\kappa}(v)\sin(\theta_{\mathcal{T}_\kappa}(v)) \\ \sin(\theta_{\mathcal{T}_\kappa}(v)) & -R_{\mathcal{T}_\kappa}(v)\cos(\theta_{\mathcal{T}_\kappa}(v)) \end{pmatrix}. \tag{7.41}$$

Now, define ν as follows,

$$\nu := (R_{\mathcal{T}_\kappa}(v) - 1, \theta_{\mathcal{T}_\kappa}(v) - \theta_0, |\kappa| v_z)^T.$$

Using the equality constraint in (7.29), it holds,

$$\nu^T \mathcal{V}_v = |\kappa|^p. \tag{7.42}$$

Theorem 15. *The first order necessary condition for $\overline{v}$ to be minimizer of (7.27) is*

$$P_{\overline{v}}([g_t]^{-1} \circ g_r^j(\mathcal{W}_{\overline{v}})) = 0, \tag{7.43}$$

where

$$P_{\overline{v}} = I_{3\times 3} - (1/|\kappa|^p)\overline{Q}^{-T}\mathcal{V}_{\overline{v}}\nu^T\overline{Q}^T, \tag{7.44}$$

with $\overline{Q}^{-T}$ as an inverse transpose of $\overline{Q}$.

Proof. Let $H(v_x, v_y, v_z, \lambda)$ be a Hamiltonian of the problem in (7.27),

$$H(v_x, v_y, v_z, \lambda) := ||w(v)||_{\sigma^j, p_o} + \lambda(\Psi_{(\sigma,\kappa,p_r)}(v) - |\kappa|), \tag{7.45}$$

where $w(v) := (w_x, w_y, w_z)$. The gradient of H is

$$||w(v)||_{\sigma^j,p_o}^{1-p_o}([g_t]^{-1} \circ g_r^j(\mathcal{W}))^T + \lambda|\kappa|\Psi_{(\sigma,\kappa,p_r)}(v)^{1-p_r}(\mathcal{U}_{\overline{v}}). \tag{7.46}$$

Then the necessary condition for a stationary point is

$$\nabla_v H = 0 \tag{7.47}$$

with the equality constraint in (7.28). By multiplying $\overline{Q}\nu$ to the right and using (7.28) and (7.42), λ is computed to be

$$\lambda = -(||w(v)||_{\sigma^j,p_o}^{1-p_o} \Psi_{(\sigma,\kappa,p_r)}(v)^{p_r-1}/|\kappa|^{p_r+1})([g_t]^{-1} \circ g_r^j(\mathcal{W}))^T \overline{Q}\nu, \tag{7.48}$$

and by replacing λ in (7.46), the necessary condition in (7.47) is equal to (7.43). □

Similar to the regular cuboid case, $P_{\overline{v}}$ is also a projection matrix, which provides the geometric interpretation of the necessary condition.

Proposition 13. *$P_{\overline{v}}$ is a projection.*

Proof. Follows the proof of Proposition 11 but using (7.42). □

Corollary 4. *The dimension of the range space of $P_{\overline{v}}$ is 2.*

Proof. Similar to the proof of Corollary 3, it follows by explicitly computing the trace, and using the fact that $P_{\overline{v}}$ is idempotent. □

Furthermore, $\mathcal{V}_{\overline{v}}$ is an outward normal vector to the level set of the polar coordinate $(R_{\mathcal{T}_\kappa}(v), \theta_{\mathcal{T}_\kappa}(v))$, followed by the coordinate transformation explained in §7.4.2. The interchange between the polar coordinate and the original coordinate in the robot's frame is governed by Q^{-T} operator.

Remark 3. A similar matrix to Q or Q^{-T} appears in the coordinate transformations of velocity vectors as a near-identity diffeomorphism (NID) [136]. Although the usage of NID is different from here, the Q matrix has useful properties such as that Q^T is almost

equivalent to the Q^{-1}. It is easy to check that $\det Q = -R_{\mathcal{T}_\kappa}(v)$, and the inverse, Q^{-1}, is

$$\begin{pmatrix} \cos(\theta_{\mathcal{T}_\kappa}(v)) & \sin(\theta_{\mathcal{T}_\kappa}(v)) \\ (1/R_{\mathcal{T}_\kappa}(v))\sin(\theta_{\mathcal{T}_\kappa}(v)) & -(1/R_{\mathcal{T}_\kappa}(v))\cos(\theta_{\mathcal{T}_\kappa}(v)) \end{pmatrix}.$$

Since $\det Q < 0$, it is an orientation reversing transformation.

The geometric interpretation of the necessary condition in (7.43) is similar to the one in the regular cuboid case.

Theorem 16. *(Geometric interpretation) The necessary condition in (7.43) holds for v if and only if the vector $([g_t]^{-1} \circ g_r^j(\mathcal{W}_{\overline{v}}))$ is orthogonal to the two dimensional tangent space of the boundary of the robot, $\partial B_{((\sigma_1,\sigma_2,\sigma_3),\kappa,p)}$, at v.*

Proof. Since $\overline{Q}^{-T}\mathcal{V}_{\overline{v}}$ is in the null space of $P_{\overline{v}}$, and it is a gradient vector, then, by using Corollary 4, the row space of $P_{\overline{v}}$ is found to be equal to the tangent space of the boundary of the robot, $\partial B_{((\sigma_1,\sigma_2,\sigma_3),\kappa,p)}$, at v. Therefore, the necessary condition in (7.43) holds if and only if the vector $([g_t]^{-1} \circ g_r^j(\mathcal{W}_{\overline{v}}))$ is aligned with $\overline{Q}^{-T}\mathcal{V}_{\overline{v}}$. □

The examples of the stationary points are demonstrated in Figure 7.5b and figure 7.5c, where all four circles in each figure show the stationary points. The green circle is the point with minimum cost, and the red circle is the one with maximum cost. As confirmed in Theorem 16, the normal vectors to each level sets of robot's boundary and extended obstacle's boundary in robot's frame, $\overline{Q}^{-T}\mathcal{V}_{\overline{v}}$ and $([g_t]^{-1} \circ g_r^j(\mathcal{W}_{\overline{v}}))$, are aligned at the stationary points.

However, different from the regular cuboid case, there exist a case when two normal vectors at the non-minimal stationary point are pointing in opposite directions. In Figure 7.5c, all three stationary points have the opposite normal vectors including the green circle. This is due to the nonconvex shape of the robot, and so the Proposition 12 does not hold for every configuration of the bent robot.

Nevertheless, checking whether two normal vectors are pointing opposite direction is

important since it eliminates the possibility of finding the maximum point (shown as red circles in Figrue 7.5c), and it is necessarily true that the globally minimum point should satisfy this property. Furthermore, in many cases as in Figure 7.5b, only the globally minimum point attains this property among the other candidates.

Therefore, a similar inequality test to (7.37) is proposed by using the gradient of the Hamiltonian in (7.46) and (7.48),

$$(1/|\kappa|^{p_r})([g_t]^{-1} \circ g_r^j(\mathcal{W}_{\overline{v}}))^T \overline{Q} \nu < 0, \tag{7.49}$$

which is also can be viewed as the Lagrange multiplier λ needs to be positive in the Hamiltonian (7.45).

In addition, observe that all the faces of the bent cuboid robot, $\partial B_{((\sigma_1,\sigma_2,\sigma_3),\kappa,p)}$, have a convex shape except the face with the shorter arch which has a concave shape. Therefore, if there exist a minimum point on the seven convex faces (including edges), the obstacle weighted L_p norm distance should be smaller than all four corners of the faces.

As a result, the following eight inequalities are imposed to the candidate $\overline{v}$ in addition to the inequality condition in (7.49). All eight corners of the bent cuboid in robot's frame are represented by

$$\xi^i := \begin{pmatrix} \mathcal{B}_\kappa(u_i) \\ \sigma_3 \end{pmatrix}, \chi^i = \begin{pmatrix} \mathcal{B}_\kappa(u_i) \\ -\sigma_3 \end{pmatrix},$$

where $\mathcal{B}_\kappa(u_i)$ is the mapping from the regular cuboid to the bent cuboid with curvature, κ, (7.17), and $u_i \in \mathbb{R}^2$ for $i \in \{1, 2, 3, 4\}$ represents the four corners of the regular rectangle with half lengths, (σ_1, σ_2). The eight inequality constraints combined with AND operation are given as

$$\wedge_{i=1}^4 (|||[g_r^j]^{-1} \circ g_t(\xi^i)||_{\sigma^j,p_o} > |||[g_r^j]^{-1} \circ g_t(\overline{v})||_{\sigma^j,p_o}) \tag{7.50}$$

$$\wedge_{i=1}^4 (|||[g_r^j]^{-1} \circ g_t(\chi^i)||_{\sigma^j,p_o} > |||[g_r^j]^{-1} \circ g_t(\overline{v})||_{\sigma^j,p_o}). \tag{7.51}$$

In order to find the closest point, the four equality constraints (necessary conditions in (7.43) and (7.29)), and nine inequality constraints (sign of λ condition in (7.49), and eight constraints for the corners in (7.50-7.51)) are considered in this chapter.

Lastly, by combining these constraints with the inequality condition in (7.26), the safety conditions for bent cuboids are given by four equality constraints and ten inequality constraints.

Remark 4. Although the idea of considering the eight corners is similar to [135], doing so serves a different purpose as the eight corners are not regarded as candidate collision points but used to find the closest point to the obstacle (by avoiding local minima). Therefore, the edge to edge collision is naturally captured by the proposed method, which was not available in [135].

Remark 5. If the global minimum point occurs in the concave face (excluding the edges), then there exist at most two points, the true minimum point and the one on the edges of the concave face, which satisfy above necessary constraint and the eight inequalities. The only scenario when this could be a problem is the false positive case when the optimizer finds the local minimum on the edge while the obstacle intrudes the robot. However, it does not mean that the worst case always happens, and even it does, one could escape from the local minima by providing an additional inequality constraint for checking if the weighted polar L_p distance from each corner of the obstacle to the CoM of the robot is greater than $|\kappa|$. Nevertheless, the full analysis of this worst case is important, and is left for a future task.

7.6 Optimal Path Planning

This section solves several optimal path planning problems proposed in §7.3 for a rigid and soft cuboid robot using the L_p constraints proposed in the previous section. The equations of motion are those from (7.2-7.3) where the rotational matrix is represented by the unit quaternion [137, 138]. Assume that the control inputs, $u, \omega_1, \omega_2, \omega_3 \in C([0, T_f], \mathbb{R})$, are

bounded by $u(t) \in [-30, 30]$ and $\omega_i(t) \in [-\pi/2, \pi/2]$ for each i. In addition, the curvature, $\kappa \in C([0, T_f], \mathbb{R})$, is a time-varying control variable bounded by $[-1, 1]$ for the bendable cuboid case.

The MATLAB-based numerical optimal control solver OPTRAGEN [120], converts the Bolza type optimal control problem into a nonlinear programming problem (NLP) by approximating the trajectories using B-splines, and sample at each provided collocation points. After converting the optimal control problem to a NLP, invoking a numerical NLP solver using an interior point method, IPOPT 3.12.6 [121], finds the numerical solution.

The rectangular obstacle with half length $\sigma^1 = (10, 2, 5)$ is located at the origin of the world frame, $(0, 0, 0)$, and it is rotated by $\pi/4$ along the axis of $(1, 1, 0)$. In the rigid regular cuboid model, the cost function is chosen, $L(g, \dot{g}, u) := \sqrt{\dot{x}^2 + \dot{y}^2 + \dot{z}^2}$, to give a shortest path problem. The half length of the rigid regular cuboid robot is given by $(2, 1, 1)$, and the CoM of robot is initially located at $(-4, -4, -4)$. The robot is initially rotated by $\pi/4$ along the axis of $(1, 0, 0)$. The desired final CoM position is $(4, 4, 4)$ with the rotation of $\pi/4$ along the axis of $(0, 0, 1)$.

In the bendable cuboid model, a regularization term is added to the cost to minimize the bending effort assuming that the cost of bending is proportional to $|\kappa|$,

$$L(g, \dot{g}, u) := \sqrt{\dot{x}^2 + \dot{y}^2 + \dot{z}^2} + \lambda|\kappa|.$$

The regularization parameter $\lambda = 0.1$. The half length of the bendable cuboid robot is given by $(5, 1, 1)$, and the initial and final curvature is given as $\kappa(0) = 0.5$ and $\kappa(T_f) = -0.5$, respectively.

For all of the following solution figures in Figure 7.6, the red surface represents the obstacle boundaries, the blue surface represents the robot boundaries at initial configuration, and the green surface represents the robot boundary at final configuration. The black surfaces are used to demonstrate the approximated shape of the robot at each sampled col-

location time point. The solid blue curve represents the trajectory of CoM.

7.6.1 Rigid model

The numerical result is shown in Figure 7.6a-7.6b. It is confirmed numerically at each collocation time that the closest point has been correctly captured, and the edge-to-edge collision is avoided by the proposed safety constraint. In addition, the necessary and sufficient condition for the closest point is also verified in Figure 7.6b, where the blue and red arrow represent the outward normal of the robot and the extended level set of L_p at the closest point, respectively. In addition, the green arrows show the basis vectors of the tangent space at the closest point. The corresponding numerical solution of four controls are shown in Figure 7.6c. The result suggests that the robot should first focus on rotating without moving the CoM excessively, and then once it points toward the right direction, it navigates close to the final position. After reaching a neighborhood of the final position, the robot should focus again on rotating to meet the final orientation constraint. The result is intuitively understandable since the cost was to minimize the traveled length of the CoM.

7.6.2 Bendable model

In addition to the kinematic controls, u and ω, a continuous curvature which connects initial and final curvature is sought, and the result are shown in Figure 7.7a-7.7b. Similar to the rigid model, the orthogonality condition, and the opposite sign condition for normal vectors are confirmed. The continuous change in the curvature deforms the cuboid robot in Figure 7.7a. Since the cost consists of the traveled length of the CoM, and the integral of the absolute curvature, $|\kappa|$, the numerical solution finds a path where the trajectory of the CoM turns close to the obstacle, and flattens out the robot to maintain the low curvature during the navigation. The simulation numerically and graphically verifies that the computed path avoids the collision. The corresponding numerical solution of five controls are shown in Figure 7.7c. Similar to the result in the cuboid case, the result suggests that the robot

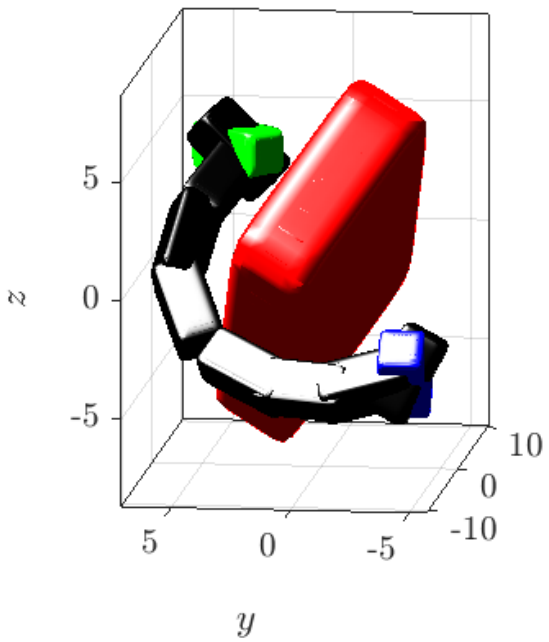

(a) Path snapshots

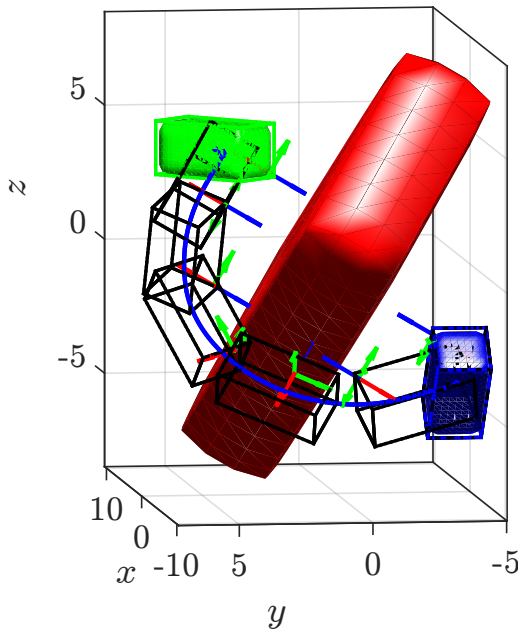

(b) Normal vectors

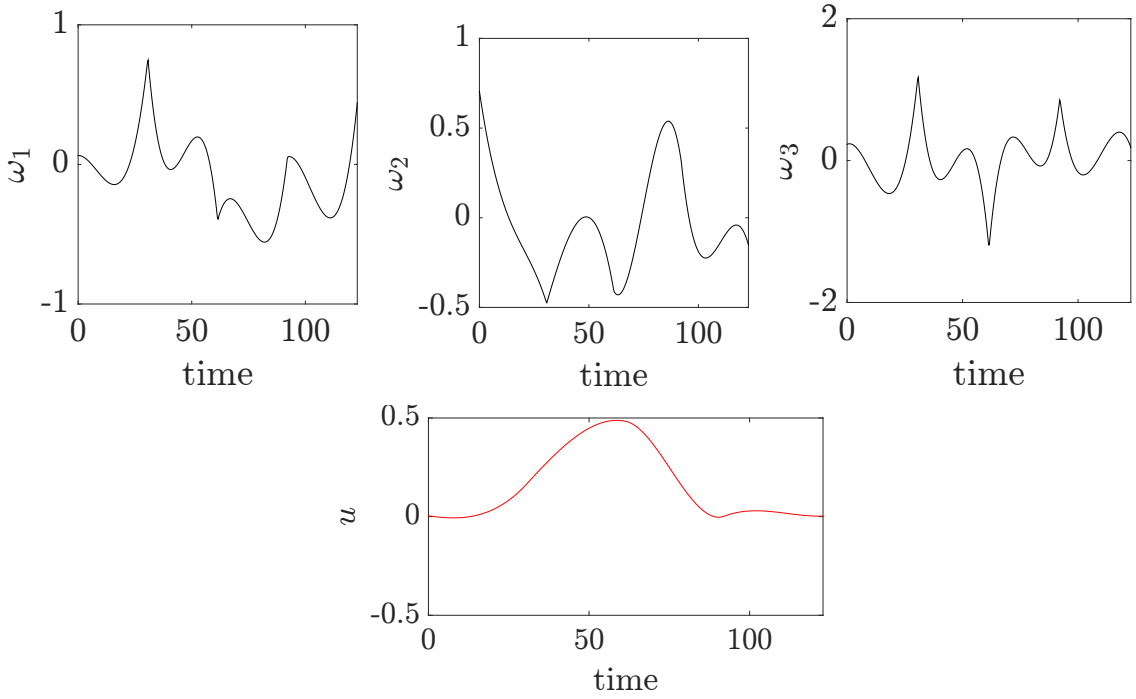

(c) Controls for regular cuboid

Figure 7.6: Shortest path example for rigid regular cuboid in $SE(3)$

should turn first, and move towards to the final position, and then rotate back to meet the final orientation constraint. In addition, in order to minimize the norm of the curvature, the

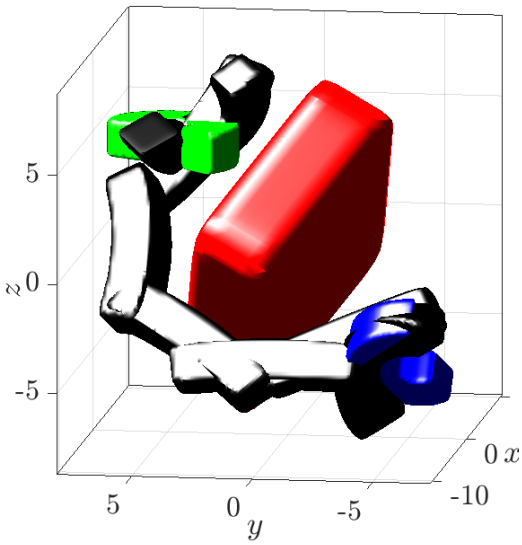

(a) Path snapshots

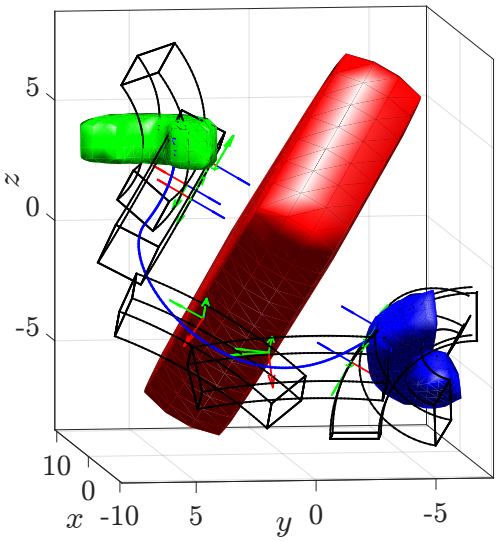

(b) Normal vectors

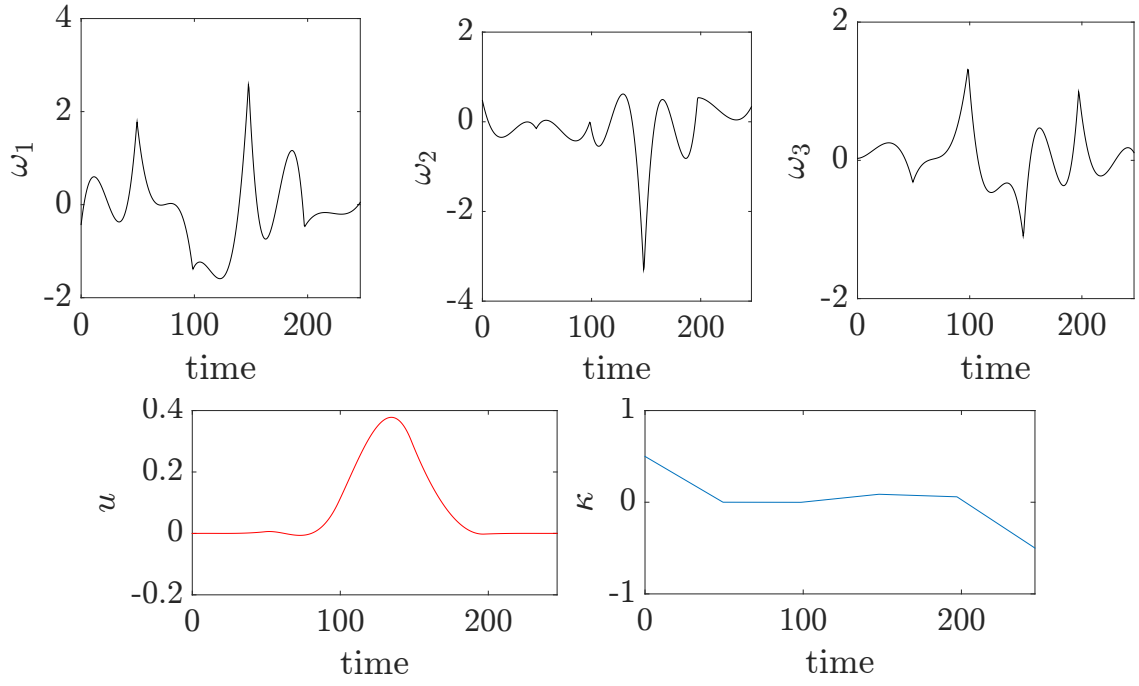

(c) Controls for bendable cuboid

Figure 7.7: Shortest path with curvature cost example for bendable cuboid in $SE(3)$

numerical planner first decreases the curvature to near zero and stays close to zero, then changes to the final negative curvature at the end.

Part III

Conclusions

CHAPTER 8
CONCLUSIONS AND FUTURE RESEARCH

In the first part of the thesis, causal modeling of the impulsive affine systems is studied with the applications to the multi-body mechanical systems which interact with the rigid environment. In such systems, the dynamics are nonsmooth, and some trajectories even have discontinuities. The causes of the jump in the state are usually neglected in the impulsive affine systems modeling, and it is assumed that those jumps are given a priori. The objective of the first part is to properly model the impulsive contact force to generate physically meaningful state jumps. First, a new generalized function theory, denoted as Krylov generalized function (KGF) theory is constructed, which is based on the hyperreals in nonstandard analysis. An algebraically structured infinite-dimensional space is proposed which consists of the sensible part, which is the usual standard time, and the insensible part, which represents the time like infinitesimals. The regular functions and singular functions defined on the Krylov space are generated by three fundamental shape functions using scaling and translation operators. The shape functions represent the continuization process of discontinous functions or the force profile of singular functions in insensible time. Next, the generalized ordinary differential equation is studied within the KGF theory. An equivalent causal impulsive system is sought which generates the same jumps as given in the impulsive effect model. Several cases are analyzed to verify the causal representation problem. Finally, a singular contact force is found within the Lagrangian mechanics framework. A singular contact force for the horizontal bouncing ball is proposed using a nonlinear visco-elasctic model with the stiffness constant designed by the square of delta function. The powers of singular function are ill-posed in the usual distributional theory, but all well-defined in the KGF theory. Lastly, a new reset map for compass gait walker is proposed by introducing the infinitesimal foot modeling the softness of the human skin.

In the second part of the thesis, a safe optimal path planning problem is considered for the point mass robot and the full body robot. In both cases, polynomials are used to either generate the trajectories or finding the analytic safety conditions. In the case of point mass robot, algebraic properties of single variable polynomial are considered. The roots of polynomial are considered as the positions of the robots in two dimensional space, and by following generalized root locus principles, a safe trajectory is generated. The convergence to the final target position is dictated by the root locus principles. In addition, this generalized root locus solves the assignment free formation control problem. The target formation and the initial configurations of the robots are modeled with polynomials of the same order, and the collision avoidance trajectories are found by only using the displacement information. Furthermore, the safety conditions for the full body robot are considered using the geometric properties of the weighted L_p norm. The boundary or surface of the robot is modeled by the one level set of weighted L_p norm, and the collision avoidance constraints are approximated by the set of inequality constraints. The expression does not require any OR operation nor integer slack variable, which makes the algorithm difficult to solve numerically. A further generalization to three dimensional space is also considered, and the approximated surface model for the bendable cuboid robot is proposed. The safety condition is generalized by solving two-staged optimization problem. Three shape parameters are used as the control, and the safety constraints are proposed with a set analytic constraints, which is a function of the shape parameters. Finally, a general Bolza type of optimal path planning problem is formulated and the numerical solution is sought by converting into nonlinear programming problem

Future Research

In the first part, a generalized function theory is introduced to find the solution of the impulsive affine systems containing the singular function in the vector field. The formulation is new and the theory can be extended to solve many interesting problems in mathema-

tical system theory. In this section, several open problems are illustrated to motivate the potential future directions of the research using the KGF theory.

1. (Extended Krylov space) As mentioned in § 3.1, the Krylov space can be extended to contain *infinitely large numbers* by extending the Krylov basis to include e_n for negative n, which is a sequence blows up to infinity since $\alpha > 1$ is assumed. By containing these elements for every negative integers n, the extended Krylov space $\overline{K}$ can be proved to be a subfield of ${}^*\mathbb{R}$ using the fact that the ring of formal Laurent series over a field is a field. A evaluation at *infinity* could be then formally defined in KGF theory which may be used to analyze the stability of the system. This extension could be later verified and compared to the globally asymptotically stability definition studied within the nosntandard analysis framework in [59].

2. (Instantaneous reachability) An instantaneous reachability condition can be also studied. Chow's theorem shows the conditions for the controllability of the driftless nonlinear systems which are composed with smooth vector fields. The question is how this theorem can be generalized to the nonsmooth vector field cases. The task is to extend Lie bracket to non-smooth vector fields. Consider the following example.

$$\begin{cases} \dot{x} = u_1 \\ \dot{v} = 0 \end{cases} \quad \text{if } x < 0 \tag{8.1}$$

$$\begin{cases} \dot{x} = u_1 \\ \dot{v} = u_2 \end{cases} \quad \text{if } x > 0 \tag{8.2}$$

where u_1 and u_2 is the generalized control which could be singular functions. By using the generalized Heaviside function, $H(x)$, it can be reformulated as

$$\begin{pmatrix} \dot{x} \\ \dot{v} \end{pmatrix} = \begin{pmatrix} 1 \\ 0 \end{pmatrix} u_1 + \begin{pmatrix} 0 \\ H(x) \end{pmatrix} u_2. \tag{8.3}$$

Let g_1 and g_2 be the the actuation vector fields for u_1 and u_2, respectively, and $X = [x, v]$. By using the generalized derivative, the Lie bracket can be defined as

$$\begin{aligned}
[g_1, g_2] &:= \nabla g_2(X) g_1(X) - \nabla g_1(X) g_2(X) \\
&= \begin{pmatrix} 0 & 0 \\ \delta(x) & 0 \end{pmatrix} \begin{pmatrix} 1 \\ 0 \end{pmatrix} \\
&= \begin{pmatrix} 0 \\ \delta(x) \end{pmatrix}
\end{aligned}$$

where $\delta(x)$ is generalized derivative of $H(x)$. This example illustrates that the system is controllable in insensible time where $\delta(x)$ is not equal to zero, and so any state is instantaneously reachable. The further analysis of this example will be useful to generalize the existing reachability conditions for smooth vector fields to the non-smooth ones.

3. (Composition of generalized functions) In this thesis, the impact time is first computed to define the singular function which generates the jump. If the impact time is implicitly defined by the *discontinuous function* such as the velocity dependent switching surface, then the problem is in general very difficult to analyze. However, it is still possible by considering the composition in the higher insensible dimension, which the composition could be well defined. There are many physical application to the generalization of the composition functions including the instantaneous kicker model by Van der Meer in [139].

Furthermore, in the second part, a new framework of generating the safe trajectories and formulating analytic safety condition is proposed. This new framework can be extended, and used in many motion planning problem.

1. (Algebra) The root locus principle follows the gradient descent of the harmonic landscape function which can only be defined in the two dimensional space. The ex-

tension to the three dimensional space is still open. However, an interesting extension of the harmonic function inspired by the electrostatic field in three dimensional space shows that the assignment free formation control can be found using the electrostatic forces, which is similar to the root locus path if it is restricted to two dimensional space.

2. (Geometry) The weighted L_p method is a new framework to define the safety condition. There are numerous applications directly using so called the L_p box such as controlling the average body frame of the snake locomotion in [140]. The concatenation of bendable L_p can be also used to find an approximated surface for continuum mechanical chains.

REFERENCES

[1] J. W. Grizzle, C. Chevallereau, A. D. Ames, and R. W. Sinnet, "3d bipedal robotic walking: Models, feedback control, and open problems," *IFAC Proc. Vol.*, vol. 43, no. 14, pp. 505–532, 2010.

[2] I. Halperin and L. Schwartz, *Introduction to the Theory of Distributions*, ser. Canadian Mathematical Congress. University of Toronto Press, 1968.

[3] P. A. M. Dirac, *The principles of quantum mechanics*, 27. Oxford university press, 1981.

[4] T. Kailath, *Linear Systems*, ser. Information and System Sciences Series. Prentice-Hall, 1980.

[5] A. Robinson, "Nonstandard arithmetic," *Bulletin of the American Mathematical Society*, vol. 73, no. 6, pp. 818–843, 1967.

[6] R. Goldblatt, *Lectures on the Hyperreals: An Introduction to Nonstandard Analysis*, ser. Graduate Texts in Mathematics. Springer New York, 1998.

[7] R. Kalman, "On the general theory of control systems," *IRE Transactions on Automatic Control*, vol. 4, no. 3, pp. 110–110, 1959.

[8] J. C. Willems and J. W. Polderman, *Introduction to mathematical systems theory: a behavioral approach*. Springer Science & Business Media, 2013, vol. 26.

[9] M. Elbanhawi and M. Simic, "Sampling-based robot motion planning: A review," *IEEE Access*, vol. 2, pp. 56–77, 2014.

[10] S. M. LaValle, *Planning Algorithms*. Cambridge University Press, 2006.

[11] J. Li and J. Xiao, "Task-constrained continuum mnipulation in cluttered space," in *Proc. IEEE Int. Conf. Robot Autom.*, May 2014, pp. 2183–2188.

[12] I. S. Godage, E. Guglielmino, D. T. Branson, G. A. Medrano-Cerda, and D. G. Caldwell, "Novel modal approach for kinematics of multisection continuum arms," in *IEEE/RSJ Int. Conf. Intell. Robots Syst.*, Sep. 2011, pp. 1093–1098.

[13] F. Connolly, C. J. Walsh, and K. Bertoldi, "Automatic design of fiber-reinforced soft actuators for trajectory matching," *Proc. Nat. Academy of Sci.*, vol. 114, no. 1, pp. 51–56, 2017.

[14] A. Goswami, B. Thuilot, and B. Espiau, "Compass-like biped robot part i: Stability and bifurcation of passive gaits," PhD thesis, INRIA, 1996.

[15] J. W. Grizzle, G. Abba, and F. Plestan, "Asymptotically stable walking for biped robots: Analysis via systems with impulse effects," *IEEE Transactions on Automatic Control*, vol. 46, no. 1, pp. 51–64, Jan. 2001.

[16] H. Goldstein, *Classical mechanics*. Pearson Education India, 2011.

[17] M. Levi, *Classical mechanics with calculus of variations and optimal control: an intuitive introduction*. American Mathematical Soc., 2014, vol. 69.

[18] R. M. Murray, Z. Li, and S. S. Sastry, *A Mathematical Introduction to Robotic Manipulation*. CRC press, 1994.

[19] Y. Hurmuzlu and D. B. Marghitu, "Rigid body collisions of planar kinematic chains with multiple contact points," *The international journal of robotics research*, vol. 13, no. 1, pp. 82–92, 1994.

[20] F. Grognard, "Feedback stabilization of predator-prey systems for impulsive biological control," in *Proc. of the IFAC World Congress*, vol. 19, IFAC, 2014, pp. 5264–5269.

[21] E. Verriest, "Regularization method for optimally switched and impulsive systems with biomedical applications," in *Proc. IEEE Int. Conf. on Decision and Control*, vol. 3, IEEE, Dec. 2003, pp. 2156–2161.

[22] A. Baños and A. Barreiro, *Reset Control Systems*, ser. Advances in Industrial Control. Springer London, 2011.

[23] B. Brogliato, *Nonsmooth mechanics*. Springer, 2016.

[24] A. D. Ames, K. Galloway, K. Sreenath, and J. W. Grizzle, "Rapidly exponentially stabilizing control lyapunov functions and hybrid zero dynamics," *IEEE Transactions on Automatic Control*, vol. 59, no. 4, pp. 876–891, 2014.

[25] M. Posa, M. Tobenkin, and R. Tedrake, "Stability analysis and control of rigid-body systems with impacts and friction," *IEEE Transactions on Automatic Control*, vol. 61, no. 6, pp. 1423–1437, 2016.

[26] R. A. Horn and C. R. Johnson, *Matrix Analysis*. Cambridge university press, 2012.

[27] V. Lakshmikantham, D. Bainov, and P. Simeonov, *Theory of Impulsive Differential Equations*, ser. Series in modern applied mathematics. World Scientific, 1989, vol. 6.

[28] S. Zavalishchin and A. Sesekin, *Dynamic Impulse Systems: Theory and Applications*, ser. Mathematics and Its Applications. Springer Netherlands, 1997, vol. 394.

[29] W. Haddad, V. Chellaboina, and S. Nersesov, *Impulsive and Hybrid Dynamical Systems: Stability, Dissipativity, and Control: Stability, Dissipativity, and Control*, ser. Princeton Series in Applied Mathematics. Princeton University Press, 2014.

[30] T. Yang, *Impulsive control theory*. Springer Science & Business Media, 2001, vol. 272.

[31] A. Haron and K. Ismail, "Coefficient of restitution of sports balls: A normal drop test," in *IOP Conference Series: Materials Science and Engineering*, IOP Publishing, vol. 36, 2012, p. 012 038.

[32] C. D. Remy, "Ambiguous collision outcomes and sliding with infinite friction in models of legged systems," *The International Journal of Robotics Research*, vol. 36, no. 12, pp. 1252–1267, 2017.

[33] P. Flores and H. Lankarani, *Contact Force Models for Multibody Dynamics*, ser. Solid Mechanics and Its Applications. Springer International Publishing, 2016.

[34] F. Plestan, J. W. Grizzle, E. R. Westervelt, and G. Abba, "Stable walking of a 7-dof biped robot," *IEEE Transactions on Robotics and Automation*, vol. 19, no. 4, pp. 653–668, Aug. 2003.

[35] I. Gelfand and G. Shilov, *Generalized Functions. Vol. 1: Properties and Operations*. Academic Press, 1964.

[36] L. Schwartz, "Sur limpossibilit de la multiplication des distributions," *C. R. Acad. Sci. Paris*, vol. 239, pp. 847–848, 1954.

[37] J. Colombeau, *Multiplication of distributions: a tool in mathematics, numerical engineering, and theoretical physics*, ser. Lecture notes in mathematics. Springer-Verlag, 1992.

[38] ——, *New Generalized Functions and Multiplication of Distributions*, ser. North-Holland Mathematics Studies. Elsevier Science, 2000.

[39] ——, *Elementary Introduction to New Generalized Functions*, ser. North-Holland Mathematics Studies. Elsevier Science, 2011.

[40] M. Kunzinger and R. Steinbauer, "A rigorous solution concept for geodesic and geodesic deviation equations in impulsive gravitational waves," *Journal of Mathematical Physics*, vol. 40, no. 3, pp. 1479–1489, 1999.

[41] T. D. Todorov, "Colombeau's generalized functions and non-standard analysis," in *Generalized Functions Convergence Structures and Their Applications*. Boston, MA: Springer US, 1988, pp. 327–339.

[42] M. Oberguggenberger, "Products of distributions: Nonstandard methods," *Zeitschrift für Analysis und ihre Anwendungen*, vol. 7, no. 4, pp. 347–365, 1988.

[43] R. S. Baty, F. Farassat, and J. Hargreaves, "Nonstandard analysis and shock wave jump conditions in a one-dimensional compressible gas," Los Alamos National Laboratory (LANL), Los Alamos, NM, Tech. Rep., 2007.

[44] S. N. Simić, K. H. Johansson, S. Sastry, and J. Lygeros, "Towards a geometric theory of hybrid systems," in *Int. Workshop on Hybrid Systems: Computation and Control*, Springer, 2000, pp. 421–436.

[45] J. Kim, H. Cho, A. Shamsuarov, H. Shim, and J. H. Seo, "State estimation strategy without jump detection for hybrid systems using gluing function," in *Proc. IEEE Int. Conf. on Decision and Control*, 2014, pp. 139–144.

[46] J. Cortes, "Discontinuous dynamical systems," *IEEE control Systems*, vol. 28, no. 3, pp. 36–73, 2008.

[47] A. Filippov, *Differential equations with discontinuous righthand sides*, ser. Mathematics and Its Applications Soviet. Kluwer Academic Publishers, 1988, vol. 18.

[48] Y. Orlov, "Nonlinear control systems with impulsive inputs," in *Proc. of IEEE Conf. on Decision and Control*, vol. 1, Dec. 1997, pp. 630–635.

[49] M. S. Aronna and F. Rampazzo, "A note on systems with ordinary and impulsive controls," *IMA Journal of Mathematical Control and Information*, vol. 33, pp. 147–162, 2016.

[50] B. Miller, "Controllable systems with impacts," *Journal of Mathematical Sciences*, vol. 199, no. 5, pp. 571–582, 2014.

[51] A. Bressan and F. Rampazzo, "On differential systems with vector-valued impulsive controls.," *Bolletino U.M.I*, vol. 7, 1987.

[52] A. Arutyunov, D. Karamzin, and F. L. Pereira, "On a generalization of the impulsive control concept: Controlling system jumps," *Discrete and Continuous Dynamical Systems*, vol. 29, pp. 403–415, 2011.

[53] M. Nedeljkov and M. Oberguggenberger, "Ordinary differential equations with delta function terms," *Publ. Inst. Math.(Beograd)(NS)*, vol. 91, no. 105, pp. 125–135, 2012.

[54] E. I. Verriest, "Nonlinear impulsive systems: A causal model," in *Proc. of the Int. Symposium on Mathematical Theory of Networks and Systems,*, 2014.

[55] J. Bentsman and B. M. Miller, "Dynamical systems with active singularities of elastic type: A modeling and controller synthesis framework," *Automatic Control, IEEE Transactions on*, vol. 52, no. 1, pp. 39–55, 2007.

[56] N. J. Cutland, "Infinitesimal methods in control theory: Deterministic and stochastic," *Acta Applicandae Mathematica*, vol. 5, no. 2, pp. 105–135, 1986.

[57] C. Lobry, T. Sari, and S. Touhami, "Fast and slow feedback in systems theory," *Journal of Biological Systems*, vol. 7, no. 03, pp. 307–331, 1999.

[58] M. Diener, "The canard unchained or how fast/slow dynamical systems bifurcate," *The Mathematical Intelligencer*, vol. 6, no. 3, pp. 38–49, 1984.

[59] C. Lobry and T. Sari, "Non-standard analysis and representation of reality," *International Journal of Control*, vol. 81, no. 3, pp. 519–536, 2008.

[60] T Todorov, "Steady-state solutions in an algebra of generalized functions: Lightning, lightning rods and superconductivity," *Novi Sad Journal of Mathematics*, vol. 45, no. 1, 2015.

[61] E. I. Verriest, *Lecture notes on Signals, Systems and Control, ECE3550*. In preparation to publish, 2014.

[62] F. H. Clarke, Y. S. Ledyaev, R. J. Stern, and P. R. Wolenski, *Nonsmooth analysis and control theory*. Springer Science & Business Media, 2008, vol. 178.

[63] G. Folland, *Real analysis: modern techniques and their applications*, ser. Pure and applied mathematics. Wiley, 1999.

[64] A. Lightstone, "Infinitesimals and integration," *Mathematics Magazine*, vol. 46, no. 1, pp. 20–30, 1973.

[65] M. Artin, *Algebra*, second. Prentice Hall, 1991.

[66] S. N. Simić, K. H. Johansson, S. Sastry, and J. Lygeros, "Towards a geometric theory of hybrid systems," in *Int. Workshop on Hybrid Systems: Computation and Control*, Springer, 2000, pp. 421–436.

[67] N. s.P. Hyun and E. I. Verriest, "Causal impact modeling of state dependent impulsive affine systems using non-standard analysis," in *Proc. IEEE Int. Conf. on Decision and Control*, Dec. 2016, pp. 3024–3029.

[68] O. Khatib, "Real-time obstacle avoidance for manipulators and mobile robots," *The international journal of robotics research*, vol. 5, no. 1, pp. 90–98, 1986.

[69] E. Rimon and D. E. Koditschek, "Exact robot navigation using artificial potential functions," *Robotics and Automation, IEEE Transactions on*, vol. 8, no. 5, pp. 501–518, 1992.

[70] J.-O. Kim and P. K. Khosla, "Real-time obstacle avoidance using harmonic potential functions," *Robotics and Automation, IEEE Transactions on*, vol. 8, no. 3, pp. 338–349, 1992.

[71] J. Guldner and V. I. Utkin, "Sliding mode control for gradient tracking and robot navigation using artificial potential fields," *Robotics and Automation, IEEE Transactions on*, vol. 11, no. 2, pp. 247–254, 1995.

[72] C. I. Connolly, J. Burns, and R Weiss, "Path planning using laplace's equation," in *Proc., IEEE Int. Conf. on Robotics and Automation*, IEEE, 1990, pp. 2102–2106.

[73] A. Ferrara and M. Rubagotti, "Sliding mode control of a mobile robot for dynamic obstacle avoidance based on a time-varying harmonic potential field," in *ICRA 2007 workshop: planning, perception and navigation for intelligent vehicles*, vol. 160, 2007.

[74] Y. Wang and G. S. Chirikjian, "A new potential field method for robot path planning," in *Proc., IEEE Int. Conf. on Robotics and Automation*, IEEE, vol. 2, 2000, pp. 977–982.

[75] J. Guldner, V. I. Utkin, and H. Hashimoto, "Robot obstacle avoidance in n-dimensional space using planar harmonic artificial potential fields," *Journal of dynamic systems, measurement, and control*, vol. 119, no. 2, pp. 160–166, 1997.

[76] L. Evans, *Partial Differential Equations*, ser. Graduate studies in mathematics. American Mathematical Society, 1998.

[77] A Landi and F Paoletti, "Reciprocal root locus approach to path planning for multiple mobile robots," in *Proc. of the INRIA/IEEE Symposium on Emerging Technologies and Factory Automation*, IEEE, vol. 2, 1995, pp. 345–352.

[78] J. Mitchell and J. McDaniel W., "A generalized root locus following technique," *Automatic Control, IEEE Transactions on*, vol. 15, no. 4, pp. 483–486, 1970.

[79] C.-D. Yang and F.-B. Yeh, "On modeling root-locus behavior," in *Proc. of the IEEE Conf. on Decision and Control*, vol. 3, 1994, pp. 2151–2156.

[80] A. Doria-Cerezo and M. Bodson, "Root locus rules for polynomials with complex coefficients," in *Mediterranean Conf. on Control & Automation (MED),*, IEEE, 2013, pp. 663–670.

[81] Y.-H. Liu and S. Arimoto, "Proposal of tangent graph and extended tangent graph for path planning of mobile robots," in *Proc., IEEE Int. Conf. on Robotics and Automation*, IEEE, 1991, pp. 312–317.

[82] S. Sundar and Z. Shiller, "Optimal obstacle avoidance based on the hamilton-jacobi-bellman equation," *Robotics and Automation, IEEE Transactions on*, vol. 13, no. 2, pp. 305–310, 1997.

[83] J. Yang, Z. Qu, J. Wang, and K. Conrad, "Comparison of optimal solutions to real-time path planning for a mobile vehicle," *Systems, Man and Cybernetics, Part A: Systems and Humans, IEEE Transactions on*, vol. 40, no. 4, pp. 721–731, 2010.

[84] I. Arvanitakis and A. Tzes, "Trajectory optimization satisfying the robot's kinodynamic constraints for obstacle avoidance," in *Mediterranean Conference on Control & Automation (MED)*, IEEE, 2012, pp. 128–133.

[85] M. Schwager, P. Dames, D. Rus, and V. Kumar, "A multi-robot control policy for information gathering in the presence of unknown hazards," in *Int. Symposium on Robotics Research*, 2011.

[86] B. Chen and H. H. Cheng, "A review of the applications of agent technology in traffic and transportation systems," *Intelligent Transportation Systems, IEEE Transactions on*, vol. 11, no. 2, pp. 485–497, 2010.

[87] H. Weimerskirch, J. Martin, Y. Clerquin, P. Alexandre, and S. Jiraskova, "Energy saving in flight formation," *Nature*, vol. 413, no. 6857, pp. 697–698, 2001.

[88] H. W. Kuhn, "The hungarian method for the assignment problem," *Naval research logistics quarterly*, vol. 2, no. 1-2, pp. 83–97, 1955.

[89] D. Gale and L. S. Shapley, "College admissions and the stability of marriage," *The American Mathematical Monthly*, vol. 69, no. 1, pp. 9–15, 1962.

[90] N. Holden, Y. Peres, and A. Zhai, "Gravitational allocation for uniform points on the sphere," *arXiv preprint arXiv:1704.08238*, 2017.

[91] M. M. Zavlanos, L. Spesivtsev, and G. J. Pappas, "A distributed auction algorithm for the assignment problem," in *Proc., IEEE Conf. on Decision and Control*, 2008, pp. 1212–1217.

[92] S. Chopra, G. Notarstefano, M. Rice, and M. Egerstedt, "A distributed version of the hungarian method for multirobot assignment," *IEEE Transactions on Robotics*, vol. 33, no. 4, pp. 932–947, Aug. 2017.

[93] K.-K. Oh, M.-C. Park, and H.-S. Ahn, "A survey of multi-agent formation control," *Automatica*, vol. 53, pp. 424–440, 2015.

[94] M. Ji, S.-i. Azuma, and M. B. Egerstedt, "Role-assignment in multi-agent coordination," *International Journal of Assistive Robotics and Mechatronics*, vol. 7, no. 1, pp. 32–40, 2006.

[95] M. M. Zavlanos and G. J. Pappas, "Distributed formation control with permutation symmetries," in *Proc. IEEE Conf. on Decision and Control*, 2007, pp. 2894–2899.

[96] S. Kloder and S. Hutchinson, "Path planning for permutation-invariant multirobot formations," *Robotics, IEEE Transactions on*, vol. 22, no. 4, pp. 650–665, 2006.

[97] K. Solovey, J. Yu, O. Zamir, and D. Halperin, "Motion planning for unlabeled discs with optimality guarantees," *arXiv preprint arXiv:1504.05218*, 2015.

[98] M. Turpin, K. Mohta, N. Michael, and V. Kumar, "Goal assignment and trajectory planning for large teams of aerial robots.," in *Robotics: Science and Systems*, 2013.

[99] M. Turpin, N. Michael, and V. Kumar, "Trajectory planning and assignment in multirobot systems," in *Algorithmic foundations of robotics X*, Springer, 2013, pp. 175–190.

[100] M. M. Zavlanos and G. J. Pappas, "A dynamical systems approach to weighted graph matching," *Automatica*, vol. 44, no. 11, pp. 2817–2824, 2008.

[101] N. P. Hyun, E. Verriest, and P. Vela, "Optimal obstacle avoidance trajectory generation using the root locus principle," in *Proc., IEEE Conf. on Decision and Control*, 2015, pp. 626–631.

[102] M. do Carmo, *Differential Geometry of Curves and Surfaces*. Prentice-Hall, 1976.

[103] U. Helmke and P. A. Fuhrmann, "Bezoutians," *Linear Algebra and its Applications*, vol. 122, pp. 1039–1097, 1989.

[104] P. Crouch and T. Cheng, "Root-locus invariants for output feedback stabilization," *IMA Journal of Mathematical Control and Information*, vol. 6, no. 1, pp. 71–79, 1989.

[105] G. Harris and C. Martin, "Shorter notes: The roots of a polynomial vary continuously as a function of the coefficients," *Proc. of the American Mathematical Society*, pp. 390–392, 1987.

[106] T. Lozano-Perez, "Spatial planning: A configuration space approach," *IEEE Trans. Comput.*, vol. 100, no. 2, pp. 108–120, 1983.

[107] F. Avnaim and J.-D. Boissonnat, "Polygon placement under translation and rotation," in *Proc. Annu. Symp. Theoretical Aspects of Comput. Sci.*, Springer-Verlag, 1988, pp. 322–333.

[108] E. Fogel and D. Halperin, "Exact and efficient construction of minkowski sums of convex polyhedra with applications," *Computer-Aided Design*, vol. 39, no. 11, pp. 929–940, 2007.

[109] J.-C. Latombe, *Robot Motion Planning*. Springer Science & Business Media, 2012, vol. 124.

[110] C. Goerzen, Z. Kong, and B. Mettler, "A survey of motion planning algorithms from the perspective of autonomous uav guidance," *J. Intell. Robot. Syst.*, vol. 57, no. 1-4, pp. 65–100, 2010.

[111] H. A. Taha, *Operations Research: An Introduction*, 8th ed. Prentice-Hall, Inc., 2006.

[112] T. Schouwenaars, B. De Moor, E. Feron, and J. How, "Mixed integer programming for multi-vehicle path planning," in *Proc. European Control Conf.*, IEEE, 2001, pp. 2603–2608.

[113] A. Richards and J. How, "Mixed-integer programming for control," in *Proc. Amer. Control Conf.*, IEEE, 2005, pp. 2676–2683.

[114] R. M. Karp, "Reducibility among combinatorial problems," in *50 Years of Integer Programming 1958-2008: From the Early Years to the State-of-the-Art*. Springer Berlin Heidelberg, 2010, pp. 219–241.

[115] R. Deits and R. Tedrake, "Efficient mixed-integer planning for uavs in cluttered environments," in *Proc. IEEE Int. Conf. Robot Autom.*, 2015, pp. 42–49.

[116] Y. Yan and G. S. Chirikjian, "Closed-form characterization of the Minkowski sum and difference of two ellipsoids," *Geometriae Dedicata*, vol. 177, no. 1, pp. 103–128, 2015.

[117] Y. Yan, Q. Ma, and G. S. Chirikjian, "Path planning based on closed-form characterization of collision-free configuration-spaces for ellipsoidal bodies, obstacles, and environments," in *Proc. Int. Workshop on Robot Learning and Planning*, 2016.

[118] A. Bryson, *Applied Optimal Control: Optimization, Estimation and Control*, ser. Halsted Press book. Taylor & Francis, 1975.

[119] A. Naylor and G. Sell, *Linear Operator Theory in Engineering and Science*, ser. Applied Mathematical Sciences. Springer New York, 2000.

[120] R. Bhattacharya, "OPTRAGEN: A MATLAB toolbox for optimal trajectory generation," in *Proc. Conf. Decision and Control*, IEEE, 2006, pp. 6832–6836.

[121] A. Wächter and L. T. Biegler, "On the implementation of an interior-point filter line-search algorithm for large-scale nonlinear programming," *Mathematical Programming*, vol. 106, no. 1, pp. 25–57, 2006.

[122] A. D. Marchese, C. D. Onal, and D. Rus, "Autonomous soft robotic fish capable of escape maneuvers using fluidic elastomer actuators," *Soft Robotics*, vol. 1, no. 1, pp. 75–87, 2014.

[123] O. M Curet, N. A. Patankar, G. V. Lauder, and M. A. MacIver, "Mechanical properties of a bio-inspired robotic knifefish with an undulatory propulsor," *Bioinspiration and biomimetics*, vol. 6, no. 2, p. 026 004, 2011.

[124] J. Burgner-Kahrs, D. C. Rucker, and H. Choset, "Continuum robots for medical applications: A survey," *IEEE Trans. Robot.*, vol. 31, no. 6, pp. 1261–1280, Dec. 2015.

[125] S. Joshua, M. Yiit, T. Michael, and V. Bram, "What is the path ahead for soft robotics?" *Soft Robotics*, vol. 3, no. 4, pp. 159–160, 2016.

[126] P. Moore and D. Molloy, "A survey of computer-based deformable models," in *Proc. Int. Mach. Vision and Image Process.*, Sep. 2007, pp. 55–66.

[127] A. Nealen, M. Müller, R. Keiser, E. Boxerman, and M. Carlson, "Physically based deformable models in computer graphics," in *Computer graphics forum*, Wiley Online Library, vol. 25, 2006, pp. 809–836.

[128] S. Rodriguez, J.-M. Lien, and N. M. Amato, "Planning motion in completely deformable environments," in *Proc. IEEE Int. Conf. Robot Autom.*, May 2006, pp. 2466–2471.

[129] R. Gayle, M. C. Lin, and D. Manocha, "Constraint-based motion planning of deformable robots," in *Proc. IEEE Int. Conf. Robot Autom.*, 2005, pp. 1046–1053.

[130] E. Anshelevich, S. Owens, F. Lamiraux, and L. E. Kavraki, "Deformable volumes in path planning applications," in *Proc. IEEE Int. Conf. Robot Autom.*, vol. 3, 2000, pp. 2290–2295.

[131] R. Gayle, P. Segars, M. C. Lin, and D. Manocha, "Path planning for deformable robots in complex environments," in *Robotics: science and systems*, 2005, pp. 225–232.

[132] P. Polygerinos, Z. Wang, J. T. B. Overvelde, K. C. Galloway, R. J. Wood, K. Bertoldi, and C. J. Walsh, "Modeling of soft fiber-reinforced bending actuators," *IEEE Trans. Robot.*, vol. 31, no. 3, pp. 778–789, Jun. 2015.

[133] A. H. Chang and P. A. Vela, "Closed-loop path following of traveling wave rectilinear motion through obstacle-strewn terrain," in *Proc. IEEE Int. Conf. Robot. Autom.*, May 2017, pp. 3532–3537.

[134] C. M Postlethwaite, T. M. Psemeneki, J. Selimkhanov, M. Silber, and M. A. MacIver, "Optimal movement in the prey strikes of weakly electric fish: A case study of the interplay of body plan and movement capability," *Journal of The Royal Society Interface*, vol. 6, no. 34, pp. 417–433, 2009.

[135] N. P. Hyun, P. A. Vela, and E. I. Verriest, "A new framework for optimal path planning of rectangular robots using a weighted l_p norm," *IEEE Robot. Autom. Lett.*, vol. 2, no. 3, pp. 1460–1465, Jul. 2017.

[136] R. Olfati-Saber, "Near-identity diffeomorphisms and exponential epsilon-tracking and epsilon-stabilization of first-order nonholonomic se(2) vehicles," in *Proc. Amer. Control Conf.*, vol. 6, May 2002, pp. 4690–4695.

[137] J. B. Kuipers, *Quaternions and Rotation Sequences*. Princeton university press Princeton, 1999, vol. 66.

[138] Y.-B. Jia, "Quaternions and rotations," *Com S*, vol. 477, no. 577, p. 15, 2008.

[139] S. Van Der Meer, "Stochastic cooling and the accumulation of antiprotons," *Reviews of Modern Physics*, vol. 57, no. 3, p. 689, 1985.

[140] A. H. Chang, N.-s. P. Hyun, E. I. Verriest, and P. A. Vela, "Optimal trajectory planning and feedback control of lateral undulation in snake-like robots," in *Proc., American Control Conf.*, IEEE, 2018.